Physics of intraband quantum dot optoelectronic devices

Nenad Vukmirović BSc (Hons)

The University of Leeds
School of Electronic and Electrical Engineering
Institute of Microwaves and Photonics

June 2007

Submitted in accordance with the requirements for the degree of Doctor of Philosophy.

The candidate confirms that the work submitted is his own and that appropriate credit has been given where reference has been made to the work of others.

Acknowledgments

I would like to gratefully acknowledge the excellent supervision of Professor Paul Harrison and Dr Dragan Indjin during this work. I also thank Dr Zoran Ikonić for sharing his strong experience in physics of nanostructures. Both friendship and scientific support of Dr Ivana Savić and Dr Vladimir Jovanović made me feel a member of the group from the first day I arrived at Leeds. I would also like to thank all my office mates for providing a pleasant research atmosphere.

The work presented in this thesis would be impossible without the strong theoretical background in physics, mathematics and programming. I am grateful to all my teachers from Mathematical High School, Belgrade, as well as Faculty of Physics and Faculty of Electrical Engineering, University of Belgrade. Special thanks to Professor Vitomir Milanović, Faculty of Electrical Engineering, who encouraged me to pursue a PhD in the field of nanostructures at Leeds.

Thanks are also due to researchers from other institutions, that I visited or collaborated with. Joint work with colleagues from the Electronic Materials Engineering Department at the Australian National University, Greg Jolley, Satya Barik, Dr Fu Lan and Professor Chennupati Jagadish, during my stay in Canberra in summer 2005, gave me an important insight into the experimental procedures for growth and characterisation of realistic quantum dot infrared photodetectors and inspired some of the theoretical works done later. Many useful discussions with Sven Höfling, University of Würzburg, regarding the possibility of realisation of quantum dot based cascade structures are also acknowledged. The work presented in Sec. 7.2 was done in collaboration

with Pantelis Aivaliotis, Dr Evgeny Zibik and Dr Luke Wilson, University of Sheffield. I would also like to thank Dr Stanko Tomić, CCLRC Daresbury Laboratory, for enlightening discussions regarding the methods for quantum dot electronic structure calculations. Thanks also to my friend and colleague Žarko Gačević for working on his Diploma thesis at the Faculty of Electrical Engineering, University of Belgrade, under my co-supervision, and providing his MATLAB code for comparison.

My PhD research was funded by the Overseas Research Students Award Scheme (ORSAS), University of Leeds Tetley and Lupton Scholarship, and the Maintenance grant from the School of Electronic and Electrical Engineering. Additional financial support was obtained from the Institute of Electrical Engineers (IEE) in the form of Leslie H Paddle Fellowship and from the Lasers and Electro Optics Society of the Institute of Electrical and Electronics Engineers (IEEE-LEOS) in the form of LEOS Graduate Student Fellowship.

Finally, I am indebted to my parents for their understanding and encouragement when it was most required.

Abstract

In last two decades, semiconductor nanostructures, such as quantum wells, wires and dots, have been recognised as sources and detectors of radiation in the mid- and far-infrared region of the spectrum. Much of a success has been obtained with quantum well based intraband devices, such as quantum cascade lasers and quantum well infrared photodetectors. However due to longer carrier lifetimes in quantum dots, it is expected that optoelectronic devices based on intraband transitions in self-assembled quantum dots would have superior performance to their quantum well counterparts. In order to fully exploit this prospect, appropriate theoretical models describing electronic, optical and transport properties of the active region of these devices need to be developed, which was the subject of this thesis.

It was shown how symmetry of the dot shape can be exploited to efficiently calculate the energy levels within the framework of the multiband envelope function method. The implementation of the method in the plane wave representation of the Hamiltonian eigenvalue problem and the results of its application to square based pyramidal InAs/GaAs quantum dots and hexagonal III-nitride quantum dots were given.

A semiclassical model of intraband carrier dynamics in quantum dots was then developed and applied to design an optically pumped long wavelength mid-infrared laser based on intersublevel transitions in InAs/GaAs quantum dots. Two orders of magnitude lower pumping flux was predicted than in similar quantum well based devices.

Next, simulations of the optical absorption spectrum in the existing quantum dot infrared photodetector structures were performed. A special emphasis

was put into quantum dots-in-a-well structures and explanation of the effect of well width on the detection wavelength.

A theory of transport in quantum dot infrared photodetectors starting from the energy levels and wavefunctions obtained by solving the envelope Hamiltonian, yielding as output the device characteristics such as dark current and responsivity, was then developed. The comparison with experimental data available in the literature was made, yielding a good agreement.

Finally, the theory of electron transport through arrays of closely stacked quantum dots, where coherent and polaronic effects become important, therefore requiring the treatment within the formalism of the nonequilibrium Green's functions, rather than the semiclassical approach, was presented. A design of a structure promising to act as a terahertz quantum dot cascade laser was given.

Contents

Publications

Papers in peer reviewed journals [1]

1. ⋆ **N. Vukmirović**, D. Indjin, V. D. Jovanović, Z. Ikonić, and P. Harrison, "Symmetry of $k \cdot p$ Hamiltonian in pyramidal InAs/GaAs quantum dots: Application to the calculation of electronic structure", *Phys. Rev. B* **72**, 075356 (2005).

2. ⋆ **N. Vukmirović**, Z. Ikonić, D. Indjin, and P. Harrison, "Symmetry-based calculation of single-particle states and intraband absorption in hexagonal GaN/AlN quantum dot superlattices", *J. Phys.: Condens. Matter* **18**, 6249 (2006).

3. ⋆ **N. Vukmirović**, Z. Ikonić, V. D. Jovanović, D. Indjin, and P. Harrison, "Optically pumped intersublevel mid-infrared lasers based on InAs/GaAs quantum dots", *IEEE J. Quantum Electron.* **41**, 1361 (2005).

4. ⋆ **N. Vukmirović**, Ž. Gačević, Z. Ikonić, D. Indjin, P. Harrison, and V. Milanović, "Intraband absorption in InAs/GaAs quantum dot infrared photodetectors - effective mass vs. $k \cdot p$ modelling", *Semicond. Sci. Technol.* **21**, 1098 (2006).

5. ⋆ **N. Vukmirović**, D. Indjin, Z. Ikonić, and P. Harrison, "Origin of detection wavelength tuning in quantum-dots-in-a-well infrared photodetectors", *Appl. Phys. Lett.* **88**, 251107 (2006).

[1] Key journal papers are marked with ⋆

6. ⋆ **N. Vukmirović**, Z. Ikonić, I. Savić, D. Indjin, and P. Harrison, "A microscopic model of electron transport in quantum dot infrared photodetectors", *J. Appl. Phys.* **100**, 074502 (2006).

7. ⋆ **N. Vukmirović**, Z. Ikonić, D. Indjin, and P. Harrison, "Inelastic quantum transport in semiconductor quantum dot superlattices: electron-phonon resonances and polaron effects", submitted.

8. ⋆ **N. Vukmirović**, D. Indjin, Z. Ikonić, and P. Harrison, "Electron transport and terahertz gain in quantum dot cascades", submitted.

9. **N. Vukmirović**, V. D. Jovanović, D. Indjin, Z. Ikonić, P. Harrison, and V. Milanović, "Optically pumped terahertz laser based on intersubband transitions in a GaN/AlGaN double quantum well", *J. Appl. Phys.* **97**, 103106 (2005).

10. P. Aivaliotis, **N. Vukmirović**, E. A. Zibik, J. W. Cockburn, L. R. Wilson, D. Indjin, P. Harrison, C. Groves, J. P. R. David, and M. Hopkinson, "Stark shift of the spectral response in quantum dots-in-a-well infrared photodetectors", submitted.

11. I. Savić, Z. Ikonić, V. Milanović, **N. Vukmirović**, V. D. Jovanović, D. Indjin, and P. Harrison, "Electron transport in quantum cascade lasers in a magnetic field", *Phys. Rev. B* **73**, 075321 (2006).

12. S. Barik, H. H. Tan, C. Jagadish, **N. Vukmirović**, and P. Harrison, "Selective wavelength tuning of self-assembled InAs quantum dots grown on InP", *Appl. Phys. Lett.* **88**, 193112 (2006).

13. I. Savić, Z. Ikonić, **N. Vukmirović**, D. Indjin, P. Harrison, and V. Milanović, "Design of a ZnMnSe/ZnMgSe spin-polarized terahertz quantum cascade laser tunable by magnetic field", *Appl. Phys. Lett.* **89**, 011109 (2006).

14. V. D. Jovanović, S. Höfling, D. Indjin, **N. Vukmirović**, Z. Ikonić, P. Harrison, J. P. Reithmaier, and A. Forchel, "Influence of doping density on electron dynamics in GaAs/AlGaAs quantum cascade lasers", *J. Appl. Phys.* **99**, 103106 (2006).

15. L. Fu, H. H. Tan, I. McKerracher, J. Wong-Leung, C. Jagadish, **N. Vukmirović**, and P. Harrison, "Effects of rapid thermal annealing on device characteristics of InGaAs/GaAs quantum dot infrared photodetectors", *J. Appl. Phys.* **99**, 114517 (2006).

16. S. Höfling, V. D. Jovanović, D. Indjin, J. P. Reithmaier, A. Forchel, Z. Ikonić, **N. Vukmirović**, P. Harrison, A. Mirčetić, and V. Milanović, "Dependence of saturation effects on electron confinement and injector doping in GaAs/$Al_{0.45}Ga_{0.55}$As quantum-cascade lasers", *Appl. Phys. Lett.* **88**, 251109 (2006).

17. I. Savić, V. Milanović, **N. Vukmirović**, V. D. Jovanović, Z. Ikonić, D. Indjin, and P. Harrison, "Magnetic-field tunable terahertz quantum well infrared photodetector", *J. Appl. Phys.* **98**, 084509 (2005).

18. V. D. Jovanović, D. Indjin, **N. Vukmirović**, Z. Ikonić, P. Harrison, E. H. Linfield, H. Page, X. Marcadet, C. Sirtori, C. Worrall, H. E. Beere, D. A. Ritchie, "Mechanisms of dynamic range limitations in GaAs/AlGaAs quantum cascade lasers: Influence of injector doping", *Appl. Phys. Lett.* **86**, 211117 (2005).

19. D. Indjin, Z. Ikonić, V. D. Jovanović, **N. Vukmirović**, P. Harrison, and R. W. Kelsall, "Relationship between carrier dynamics and temperature in terahertz quantum cascade structures: simulation of GaAs/AlGaAs, SiGe/Si and GaN/AlGaN devices", *Semicond. Sci. Technol.* **20**, S237 (2005).

20. I. Savić, **N. Vukmirović**, Z. Ikonić, D. Indjin, R. W. Kelsall, P. Harrison, and V. Milanović, "Density matrix theory of transport and gain in

quantum cascade lasers in a magnetic field", accepted for publication in *Phys. Rev. B*.

Papers in conference proceedings issues of peer reviewed journals

1. **N. Vukmirović**, Z. Ikonić, I. Savić, D. Indjin, and P. Harrison, "Theoretical modelling of electron transport in InAs/GaAs quantum dot superlattices", *Phys. Status Solidi C* **3**, 3770 (2006).

2. **N. Vukmirović**, Z. Ikonić, D. Indjin, and P. Harrison, "Symmetry based calculation of electronic structure and intraband absorption in GaN/AlN hexagonal quantum dot superlattices", *Phys. Status Solidi C* **3**, 3939 (2006).

3. I. Savić, Z. Ikonić, **N. Vukmirović**, V. Milanović, D. Indjin, and P. Harrison, "Lasing in spin-polarized terahertz quantum cascade structures", *Phys. Status Solidi C* **3**, 4401 (2006).

4. D. Indjin, S. Höfling, A. Mirčetić, V. D. Jovanović, J. Radovanović, Z. Ikonić, **N. Vukmirović**, P. Harrison, R. W. Kelsall, V. Milanović, J. P. Reithmaier, and A. Forchel, "Comparative analysis of $\lambda \approx 9\mu$m GaAs/AlGaAs quantum cascade lasers with different injector doping", *Mat. Sci. Forum* **518**, 29 (2006).

5. S. Höfling, D. Indjin, V. D. Jovanović, A. Mirčetić, J. P. Reithmaier, A. Forchel, Z. Ikonić, **N. Vukmirović**, P. Harrison, V. Milanović, "Influence of injector doping density and electron confinement on the properties of GaAs/$Al_{0.45}Ga_{0.55}$As quantum cascade lasers", *Phys. Status Solidi C* **3**, 411 (2006).

6. P. Harrison, D. Indjin, V. D. Jovanović, A. Mirčetić, Z. Ikonić, R.W. Kelsall, J. McTavish, I. Savić, **N. Vukmirović** and V. Milanović, "Carrier

Dynamics in Quantum Cascade Lasers", *Acta Physica Polonica A* **107**, 75 (2005).

7. P. Harrison, D. Indjin, V. D. Jovanović, A. Mirčetić, Z. Ikonić, R. W. Kelsall, J. McTavish, I. Savić, **N. Vukmirović**, and V. Milanović, "A physical model of quantum cascade lasers: Application to GaAs, GaN and SiGe devices", *Phys. Status Solidi A* **202**, 980 (2005).

Invited seminars

1. "Optically pumped lasers based on quantum wells and quantum dots", Centre for Nanostructures, Nanoelectronics and Nanophotonics (C3N) seminar series, Faculty of Electrical Engineering, University of Belgrade, 20 December 2004.

2. "Theoretical modelling of quantum dot intraband optoelectronic devices", Computational Materials Science Group seminar series, CCLRC Daresbury Laboratory, Warrington, UK, 23 August 2006.

3. "Electronic, optical and transport properties of quantum dot intraband devices", Scientific Computing Seminars, Lawrence Berkeley National Laboratory, Berkeley, US, 14 May 2007.

Conference publications

1. **N. Vukmirović**, Z. Ikonić, I. Savić, D. Indjin, and P. Harrison, "Carrier transport in quantum dot infrared photodetectors", One day quantum dot meeting, Nottingham, UK, 19 January 2007.

2. **N. Vukmirović**, Z. Ikonić, D. Indjin, V. D. Jovanović, and P. Harrison, "Design and simulation of an optically pumped intraband InAs/GaAs quantum dot laser", Semiconductor and integrated opto-electronics conference, Cardiff, Wales, UK, 10-12 April 2006.

3. **N. Vukmirović**, Z. Ikonić, I. Savić, D. Indjin, and P. Harrison, "Theoretical modelling of electron transport in InAs/GaAs quantum dot superlattices", The 4th International Conference on Quantum Dots, Chamonix-Mont Blanc, France, 1-5 May 2006.

4. **N. Vukmirović**, Z. Ikonić, D. Indjin, and P. Harrison, "Symmetry based calculation of electronic structure and intraband absorption in GaN/AlN hexagonal quantum dot superlattices", The 4th International Conference on Quantum Dots, Chamonix-Mont Blanc, France, 1-5 May 2006.

5. **N. Vukmirović**, Z. Ikonić, D. Indjin, and P. Harrison, "The use of hexagonal symmetry for the calculation of single-particle states in III-nitride quantum dots", The 14th International Symposium - Nanostructures: Physics and Technology, St. Petersburg, Russia, 26-30 June 2006.

6. **N. Vukmirović**, D. Indjin, Z. Ikonić, and P. Harrison, "Theoretical modelling of the effect of well width on the absorption spectrum of quantum dots-in-a-well infrared photodetectors", Quantum Electronics and Photonics QEP-17, Manchester, UK, 4-7 September 2006.

7. **N. Vukmirović**, Z. Ikonić, I. Savić, D. Indjin, and P. Harrison, "Theoretical modelling of quantum dot infrared photodetectors", The 210th Meeting of The Electrochemical Society, Cancun, Mexico, 29 October-3 November 2006.

8. **N. Vukmirović**, D. Indjin, V. D. Jovanović, Z. Ikonić, and P. Harrison, "Design of an optically pumped intersublevel laser based on InAs/GaAs quantum dots", The 8th International Conference on Intersubband Transitions in Quantum Wells, Cape Cod, USA, 11-16 September 2005.

9. **N. Vukmirović**, D. Indjin, V. D. Jovanović, and P. Harrison, "Application of symmetry in $k \cdot p$ calculations of the electronic structure of pyramidal self-assembled InAs/GaAs quantum dots", The 13th International

Symposium - Nanostructures: Physics and Technology, St. Petersburg, Russia, 20-25 June 2005.

10. **N. Vukmirović**, V. D. Jovanović, D. Indjin, Z. Ikonić, P. Harrison, and V. Milanović, "Quantum fountain terahertz laser based on intersubband transitions in a GaN/AlGaN double quantum well", UK Nitrides Consortium, Nottingham, UK, 14 June 2005.

11. **N. Vukmirović**, D. Indjin, V. D. Jovanović, and P. Harrison, "Application of symmetry in $k \cdot p$ calculations of the electronic structure of pyramidal vertically stacked InAs/GaAs quantum dots", One day quantum dot meeting, Nottingham, UK, 5 April 2005.

12. **N. Vukmirović**, D. Indjin, V. D. Jovanović, P. Harrison, and Ž. Gačević, "Symmetry based $k \cdot p$ calculations of the electronic structure of pyramidal self-assembled InAs/GaAs quantum dots", The 1st International Workshop on Nanoscience and Nanotechnology, Belgrade, Serbia and Montenegro, 15-18 November 2005.

13. S. Barik, H. H. Tan, C. Jagadish, **N. Vukmirović**, and P. Harrison, "The Emission Wavelength Tailoring of Self-assembled InAs/InP Quantum Dots Grown on GaInAsP and InP Buffers", MRS Fall Meeting, Boston, USA, 27 November - 1 December 2006.

14. I. Savić, Z. Ikonić, **N. Vukmirović**, V. Milanović, D. Indjin, and P. Harrison, "Lasing in spin-polarized terahertz quantum cascade structures", The 4th International Conference on Physics and Applications of Spin-Related Phenomena in Semiconductors, Sendai, Japan, 15-18 August 2006.

15. P. Harrison, D. Indjin, V. D. Jovanović, Z. Ikonić, R. W. Kelsall, I. Savić, J. McTavish, C. A. Evans, **N. Vukmirović**, and V. Milanović, "Theoretical modelling and design of mid-infrared and terahertz quantum cascade lasers and quantum well infrared photodetectors", The 16th Ural Winter

School on the Physics of Semiconductors, Ekaterinsburg, Russia, February 2006.

16. P. Harrison, Z. Ikonić, **N. Vukmirović**, D. Indjin, and V. D. Jovanović, "On the incoherence of quantum transport in semiconductor heterostructure optoelectronic devices", The 10th Biennial Baltic Electronic Conference, Tallinn, Estonia, 2-4 October 2006.

17. S. Höfling, D. Indjin, V. D. Jovanović, A. Mirčetić, J. P. Reithmaier, A. Forchel, Z. Ikonić, **N. Vukmirović**, P. Harrison, V. Milanović, "Influence of injector doping density and electron confinement on the properties of GaAs/$Al_{0.45}Ga_{0.55}As$ quantum cascade lasers", International Symposium on Compound Semiconductors, Rust, Germany, 18-22 September 2005.

18. D. Indjin, S. Höfling, A. Mirčetić, V. D. Jovanović, Z. Ikonić, **N. Vukmirović**, P. Harrison, R. W. Kelsall, V. Milanović, J. P. Reithmaier, A. Forchel, "$\lambda \sim 9\mu$m GaAs/AlGaAs quantum cascade laser based on double-phonon resonance depopulation mechanism with diagonal optical transitions", The Mid-Infrared Optoelectronics - Materials and Devices conference, Lancaster, UK, 12-14 September 2005.

19. I. Savić, V. Milanović, Z. Ikonić, V. D. Jovanović, **N. Vukmirović**, D. Indjin, and P. Harrison, "A model of quantum cascade lasers in a magnetic field", The 8th International Conference on Intersubband Transitions in Quantum Wells, Cape Cod, USA, 11-16 September 2005.

20. I. Savić, V. Milanović, V. D. Jovanović, **N. Vukmirović**, Z. Ikonić, D. Indjin, and P. Harrison, "Magnetic field tunable Terahertz QWIP", The 8th International Conference on Intersubband Transitions in Quantum Wells, Cape Cod, USA, 11-16 September 2005.

21. V. D. Jovanović, D. Indjin, **N. Vukmirović**, Z. Ikonić, P. Harrison, S. Höfling, J. P. Reithmaier, and A. Forchel, "Influence of injector doping

on the performance and electron heating in midinfrared GaAs/AlGaAs quantum cascade lasers", The 8th International Conference on Intersubband Transitions in Quantum Wells, Cape Cod, USA, 11-16 September 2005.

22. D. Indjin, V. D. Jovanović, C. Worrall, H. E. Beere, Z. Ikonić, **N. Vukmirović**, P. Harrison, R. W. Kelsall, E. H. Linfield, H. Page, C. Sirtori, D. A. Ritchie, V. Milanović. S. Tomić, and S. Kočinac, "Electroluminescence from a mid-infrared digitally graded GaAs/AlGaAs quantum cascade structure", The 8th International Conference on Intersubband Transitions in Quantum Wells, Cape Cod, USA, 11-16 September 2005.

23. C. A. Evans, V. D. Jovanović, D. Indjin, **N. Vukmirović**, and P. Harrison, "Modelling of InGaAs/AlAsSb quantum cascade lasers", The 8th International Conference on Intersubband Transitions in Quantum Wells, Cape Cod, USA, 11-16 September 2005.

24. D. Indjin, S. Höfling, A. Mirčetić, V. D. Jovanović, J. Radovanović, Z. Ikonić, **N. Vukmirović**, P. Harrison, R. W. Kelsall, V. Milanović, J. P. Reithmaier, and A. Forchel, "Comparative analysis of $\lambda \approx 9\mu$m GaAs/AlGaAs quantum cascade lasers with different injector doping", The 7th Yugoslav Materials Research Society Conference, Herceg Novi, Serbia and Montenegro, 12-16 September 2005.

25. V. D. Jovanović, D. Indjin, **N. Vukmirović**, Z. Ikonić, H. Page, C. Sirtori, C. Worrall, H. E. Beere, and D. A. Ritchie, "Effect of injector doping on non-equilibrium electron dynamics in mid-infrared GaAs/AlGaAs quantum cascade lasers", 14th International Conference on Nonequilibrium Carrier Dynamics in Semiconductors, Chicago, USA, 24-29 July 2005.

26. P. Harrison, D. Indjin, V. D. Jovanović, I. Savić, **N. Vukmirović**, J. P. McTavish, R. W. Kelsall, Z. Ikonić, and V. Milanović, "Carrier dynamics

in quantum cascade lasers", Latin American Symposium on Solid State Physics, Havana, Cuba, 6-9 December 2004.

27. P. Harrison, V. D. Jovanović, **N. Vukmirović**, M. Erić, I. Savić, A. Mirčetić, J. P. McTavish, C. A. Evans, Z. Ikonić, R. W. Kelsall, V. Milanović, and D. Indjin, "A physical model and scattering dynamics engineering for intersubband lasers and photodetectors", Conference on Optoelectronic and Microelectronic Materials and Devices, Brisbane, Australia, 8-10 December 2004.

28. **N. Vukmirović** and G. Poparić, "Determination of ground state of H_2^+ molecule ion using diffusion Monte Carlo method", 11th Conference of General Physics, Petrovac, Serbia and Montenegro, 3-5 June 2004.

29. D. Indjin, V. D. Jovanović, Z. Ikonić, A. Mirčetić, J. Radovanović, I. Savić, P. Harrison, R.W. Kelsall, **N. Vukmirović**, V. Milanović, M. Giehler, R. Hey, and H. T. Grahn, "Physical modelling, design, optimization and experimental realization of quantum cascade lasers and quantum-well infrared photodetectors", XVI National Symposium on Condensed Matter Physics, Sokobanja, Serbia and Montenegro, 20-23 September 2004.

30. P. Harrison, D. Indjin, V. D. Jovanović, J. P. McTavish, R. W. Kelsall, Z. Ikonić, I. Savić, **N. Vukmirović**, and V. Milanović, "Carrier Dynamics in Quantum Cascade Lasers", 12th International Symposium on Ultrafast Phenomena in Semiconductors, Vilnius, Lithuania, 22-25 August 2004.

31. P. Harrison, D. Indjin, V. D. Jovanović, J. P. McTavish, R. W. Kelsall, Z. Ikonić, I. Savić, **N. Vukmirović** and V. Milanović, "A physical model of quantum cascade lasers: Application to GaAs, GaN and SiGe devices", International Conference on Superlattice, Nanostructures and Nanodevices, Cancun, Mexico, 19-23 July 2004.

32. P. Harrison, D. Indjin, V. D. Jovanović, J. P. McTavish, R. W. Kelsall, Z. Ikonić, I. Savić, **N. Vukmirović**, and V. Milanović, "The electron temperature and mechanisms of hot carrier generation in quantum cascade lasers", Nanostructures: Physics and Technology, St. Petersburg, Russia, 21-25 June 2004.

33. D. Indjin, V. D. Jovanović, A. Mirčetić, J. Radovanović, P. Harrison, Z. Ikonić, R. W. Kelsall, **N. Vukmirović**, V. Milanović, M. Giehler, R. Hey, and H. T. Grahn, "GaAs-and GaN-based intersubband quantum emitters and detectors: from physical model to working devices", 11th Conference of General Physics, Petrovac, Serbia and Montenegro, 3-5 June 2004.

34. P. Harrison, D. Indjin, V. D. Jovanović, J. P. McTavish, R. W. Kelsall, Z. Ikonić, I. Savić, and **N. Vukmirović**, "A physical model of quantum cascade lasers: Application to GaAs, GaN and SiGe devices", Quantum Cascade Laser Workshop, Seville, Spain, 4-8 January 2004.

List of Figures

List of Tables

List of Principal Abbreviations

MBE	Molecular Beam Epitaxy
MOCVD	Metalorganic Chemical Vapour Deposition
QD	Quantum Dot
LO	Longitudinal Optical
DFT	Density Functional Theory
VFF	Valence Force Field
CM	Continuum Mechanical
WEM	Wavefunction Expansion Method
FDM	Finite Difference Method
LA	Longitudinal Acoustic
SCBA	Self-consistent Born Approximation
QDIP	Quantum Dot Infrared Photodetector
QCL	Quantum Cascade Laser
QWIP	Quantum Well Infrared Photodetector
DWELL	Quantum Dots-in-a-well
IR	Irredicible representation
VCSEL	Vertical Cavity Surface Emitting Laser
LPE	Liquid Phase Epitaxy
ML	Monolayer
WL	Wetting Layer

Chapter 1

Introduction

1.1 Semiconductor quantum dots and their importance

In last three decades, remarkable progress in technology has been made, enabling the production of semiconductor structures of nanometer size. This is the length scale where the laws of quantum mechanics rule and a range of new physical effects is manifested. Fundamental laws of physics can be tested on the one hand, while on the other hand many possible applications are rapidly emerging.

The ultimate nanostructure where carriers are confined in all three spatial dimensions is called a *quantum dot*. In the last 15 years quantum dots have been produced in several different ways in a broad range of semiconductor material systems. The properties of quantum dots and their possible applications are largely dependent on the method they have been obtained, which can therefore be used as a criterion for classification of different types of quantum dots:

- **Electrostatic quantum dots**. One can fabricate quantum dots by restricting the two dimensional electron gas in a semiconductor heterostructure laterally by electrostatic gates, or vertically by etching techniques [5, 6]. The properties of this type of quantum dots, sometimes termed as *electrostatic quantum dots*, can be controlled by changing the applied potential at gates, the choice of the geometry of gates or by external magnetic field.

- **Nanocrystals**. A very different approach to obtain quantum dots is to synthesise single crystals of the size of a few nanometers, via chemical methods. The dots obtained this way are called *nanocrystals* or colloidal quantum dots [7]. Their size and shape can be controlled by the duration, temperature and ligand molecules used in the synthesis [8].

- **Self-assembled quantum dots**. The quantum dots that will be the main interest in this thesis are *self-assembled quantum dots*. They are obtained in heteroepitaxial systems with different lattice constants. During the growth of a layer of one material on top of another, the formation of nanoscale islands takes place [9], if the width of the layer (so called wetting layer) is larger than a certain critical thickness. This growth mode is called Stranski-Krastanov mode. The most common experimental techniques of the epitaxial nanostructure growth are Molecular Beam Epitaxy (MBE) and Metalorganic Chemical Vapour Deposition (MOCVD) [10, 11].

Quantum dots have enabled the study of many fundamental physical effects. Electrostatic quantum dots can be controllably charged with a desired number of electrons and therefore the whole periodic system [12] of *artificial atoms* created, providing a wealth of data from which an additional insight into the many-body physics of fermion systems could be obtained [5]. Single electron transport and Coulomb blockade effects on the one hand, and the regime of Kondo physics on the other hand, have been investigated [13, 14].

One of the most exciting aspects of quantum dot research is certainly the prospect of using the state of the dot (spin state, exciton or charged exciton) as a qubit in quantum information processing. Coherent control of an exciton state in a single dot selected from an ensemble of self-assembled quantum dots has been achieved [15], as well as the manipulation of the spin state in electrostatic quantum dots [16, 17]. These results appear promising, although the control of a larger number of quantum dot qubits is not feasible yet, mainly due to difficulty of controlling qubit-qubit interactions.

Cavity quantum electrodynamics experiments with quantum dots have been performed demonstrating strong coupling of the exciton state in a quantum dot with the mode of the surrounding cavity [18]. This has motivated quantum computing architecture proposals [19] where quantum information is converted from stationary quantum dot qubits to flying photonic qubits, which are ideal information transmitters. Most recent technological advances have enabled the realisation of quantum dots (QDs) doped with a single magnetic ion [20], as well as to controllably populate these dots with selected numbers of electrons. If the dot were placed within the appropriate cavity (microdisk, micropost or photonic crystal), the realised system would enable a highly fundamental study of physical interaction between a single charge, single spin and a single photon.

The practical applications of quantum dots certainly do not lag behind these exciting areas of fundamental science with quantum dots. For example, colloidal quantum dots have found several cutting-edge applications such as fluorescent biological labels [21], highly efficient photovoltaic solar cells [22], and nanocrystal based light emitting diodes [7].

Self-assembled quantum dots find the main application as optoelectronic devices - lasers, optical amplifiers, single photon sources and photodetectors. The following section will cover their use in this field.

1.2 Optoelectronic devices based on self-assembled quantum dots

Most of the semiconductor optoelectronic devices utilise transitions between the state in the conduction band and the state in the valence band, so called *interband* transitions, illustrated in Fig. 1.1. Electrons and holes created by injection recombine and emit photons. The active medium can in principle be just a bulk semiconductor, but it is widely understood that much better performance of the devices can be achieved if heterostructures, where a material of lower value of bandgap is embedded within the larger bandgap material, are

used.

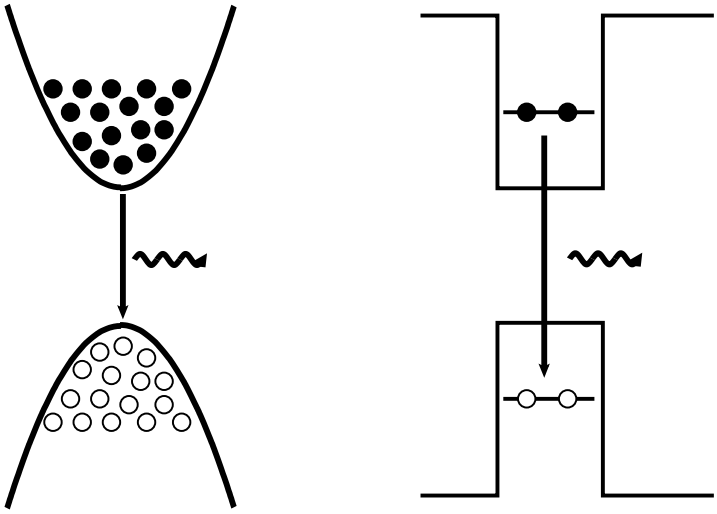

Figure 1.1: Schematic description of interband optical transition in bulk semiconductor (left) and quantum dot (right).

The main advantage in using low dimensional heterostructures as active medium of lasers stems from the increased density of states near the band edges, compared to the bulk case [23]. The degradation of device performance at higher temperatures is caused by carriers effectively populating higher energy states, reducing the population of near band edge states responsible for lasing [24]. The increased density of states near the band edge clearly suppresses this effect, and as a consequence, concentrates injected carriers near the bottom of the conduction band and the top of the valence band. Quantum dots, where the density of states has the form of a delta function, is an ultimate system where the above effect is fully exploited.

Following the initial idea to use quantum heterostructures in semiconductor lasers [25] reported by Dingle and Henry in 1976, rapid progress was made in the development of quantum well based devices [26–28]. In 1982 Arakawa and Sakaki analysed the influence of dimensionality on the threshold current [29]. They have predicted that its temperature sensitivity is much smaller for highly

confined structures and is nearly temperature independent in the case of three dimensionally confined structures - quantum dots. Furthermore, these predictions were confirmed experimentally by placing a quantum well laser in a magnetic field, mimicking the effect of additional quantum confinement. Asada *et al.* [30] also predicted a significant reduction of the threshold current and gain in quantum dot structures, termed as quantum boxes at the time. However, for the realisation of realistic devices it was necessary to enable fabrication of high density ensembles of relatively uniform quantum dots, with low defect densities. This was possible only when the growth of self-assembled quantum dots in the Stranski-Krastanov mode was developed, leading to the demonstration of quantum dot lasers [31]. The most investigated material system for quantum dot lasers is certainly In(Ga)As/GaAs on GaAs substrate covering mainly the wavelength range $1 - 1.3\,\mu$m. This wavelength range was extended to longer wavelengths with InAs dots grown on InP [32]. Shorter wavelengths in the red part of the visible spectrum were achieved with InP/InGaP dots grown on InP [33].

While nonuniformity of quantum dots leading to spectrally broad gain is a disadvantage for the development of lasers, it can be very useful for the design of optical amplifiers [34]. Due to the promise for use in photonic networks and expected advantages over quantum well and bulk amplifiers [35], optical amplifiers have been developed at telecommunication wavelengths of $1.3\,\mu$m and $1.55\,\mu$m [32, 36].

The applications of quantum dots mentioned thus far in this section involve ensembles of quantum dots. On the other hand, it has become possible to isolate individual quantum dots for example by etching mesas in the sample grown by MBE [37]. These dots can be used as single photon sources for applications in the field of quantum cryptography. Indeed, sources of triggered single photons from InAs/GaAs quantum dots employing the excitonic transition have been realised [38, 39], and most recently sources of triggered entangled photons employing biexcitonic cascade decay [40, 41].

1.3 Intraband transitions in quantum nanostructures

The operating wavelength of the interband devices mentioned in Sec. 1.2 is mainly determined by the bandgap of the material employed and is therefore limited to the near-infrared and visible part of the spectrum. However, if one wishes to access longer wavelengths, a different approach is necessary, i.e. the transitions within the same band have to be used. These transitions are called *intraband* transitions. Intraband optical transitions in bulk are not allowed and therefore low dimensional nanostructures have to be used. Therefore, in the last two decades, semiconductor nanostructures, such as quantum wells, wires and dots [42, 43] have been recognised as sources and detectors of electromagnetic radiation in the mid- and far-infrared region of the spectrum. A brief note on terminology is in place here. In quantum wells, where the energy spectrum is still continuous and consists of subbands (Fig.1.2 - left), the appropriate term for intraband transitions is *intersubband*. On the other, in quantum dots where the spectrum is fully discrete (Fig.1.2 - right), more appropriate term is *intersublevel*, although sometimes the term intersubband is also used.

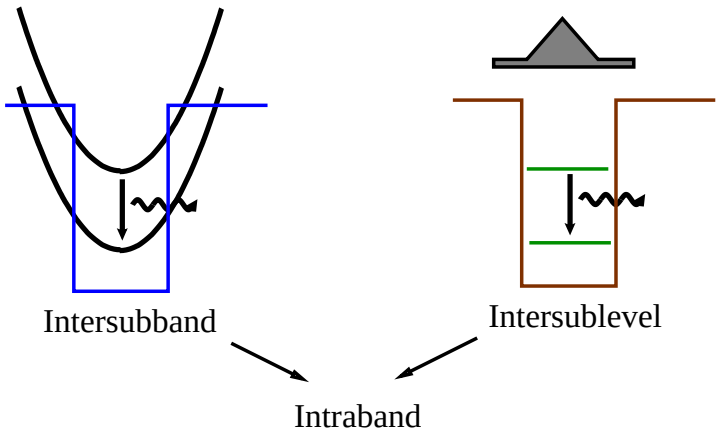

Figure 1.2: Intersubband optical transition in quantum well (left) and intersublevel optical transition in quantum dot (right).

Those spectral regions are interesting due to a range of applications. The two atmospheric windows at $3-5\,\mu$m and $8-13\,\mu$m where the atmosphere is transparent for electromagnetic radiation offer the possibility of free space optical communications, remote sensing and detection. Many molecular compounds have their vibrational modes in the $3-17\,\mu$m part of the spectrum and their detection enables the applications as measuring pollution, industrial process monitoring and detection of hidden explosives [44]. As many objects (including the human body) are the most emissive in this spectral region, corresponding detectors can be used for night vision. The far-infrared (terahertz) part of the spectrum can be potentially applied for medical imaging, astronomy and food quality control [45].

1.3.1 Quantum well intersubband devices

The historical development of intraband optoelectronic devices based on low dimensional heterostructures, has followed a similar path as in the case of interband devices. The first developments motivated by the theoretical proposal of Kazarinov and Suris [46] were achieved with quantum wells, and quantum dot based devices became possible only after the techniques of growth of high density ensembles of self-assembled quantum dots were developed.

The *quantum well infrared photodetector* (QWIP) consists of a periodic array of quantum wells subjected to an electric field perpendicular to the plane of the wells. Its operating principle is illustrated in Fig. 1.3. Carriers from the ground state are excited to a higher state by absorbing incident photons. If the structure is subjected to an electric field, these carriers are included in transport through continuum states and form a photocurrent. Such structures were first realised in the mid 1980s [47]. An impressive characteristic of all intersubband devices is that the operating wavelength can be designed by the choice of quantum well widths and material composition. Therefore, the mid-infrared part of the spectrum was covered within the next few years [48], and more recently terahertz QWIPs have been realised as well [49].

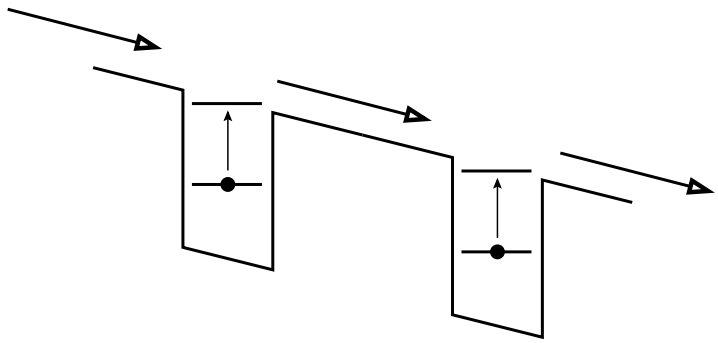

Figure 1.3: Principle of operation of quantum well infrared photodetectors.

In an *optically pumped intersubband laser* (also termed a quantum fountain laser) population inversion between the upper laser level (marked 3 in Fig. 1.4) and the lower laser level (marked 2 in Fig. 1.4) is achieved by optical pumping of carriers from the ground state (marked 1 in Fig. 1.4) to the upper laser level. The radiative transition between levels 3 and 2 then takes place. Depopulation of level 2 must be faster than the undesired nonradiative depopulation of level 3 in order to obtain gain. This is realised by designing the energy spacing between levels 2 and 1 to match an longitudinal optical (LO) phonon energy. While their operating principle is simple and it is relatively easy to design them, a clear disadvantage of this type of devices is that an external pumping source is necessary. The interest in these devices is therefore limited and this is probably the reason why they were realised for the first time [50] several years after electrically injected quantum cascade lasers, which have a more complicated structure.

The *quantum cascade laser* (QCL) is an intersubband semiconductor laser consisting of periodically repeated carefully engineered multiple quantum wells that direct the electronic transport along the desired path and enable gain in the structure. Following its first realisation in 1994 [51], a number of different designs has been realised in material systems such as InGaAs/AlInAs [51], AlGaAs/GaAs [1, 52], InGaAs/AlAsSb [53], InAs/AlSb [54]. The wavelength

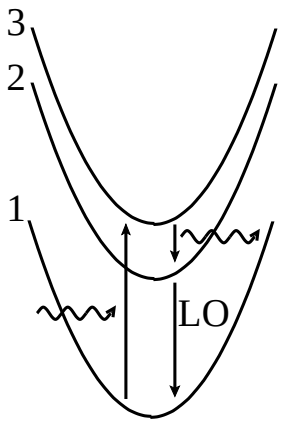

Figure 1.4: Energy level scheme of an optically pumped intersubband quantum well laser.

range spans the region from $\approx 3\,\mu$m to $\approx 190\,\mu$m [55] in the terahertz range [56], and up to $215\,\mu$m [57] in strong external magnetic fields, with a forbidden gap around $34\,\mu$m corresponding to LO phonon energy. The energy level scheme in the heart of the active region (Fig. 1.5) is similar to the one in optically pumped lasers, however one needs to ensure efficient injection of electrons into the upper laser level and extraction from the lower laser level and ground state. This is achieved by adding a so called injector region (Fig. 1.5) as an electron Bragg reflector.

1.3.2 Intraband quantum dot devices

While achievements in the realisation of a variety of quantum well intersubband devices are certainly impressive, the realised devices still have their limitations and one is facing the evergoing quest for the devices based on new concepts that would cover the so far unreachable parts of the spectrum and/or have an improved performance. Following the same idea in the development of the interband devices, improvements in performance can be achieved by using quantum dots in the active region of intraband devices.

Several limitations of QWIPs have motivated the development of *quan-*

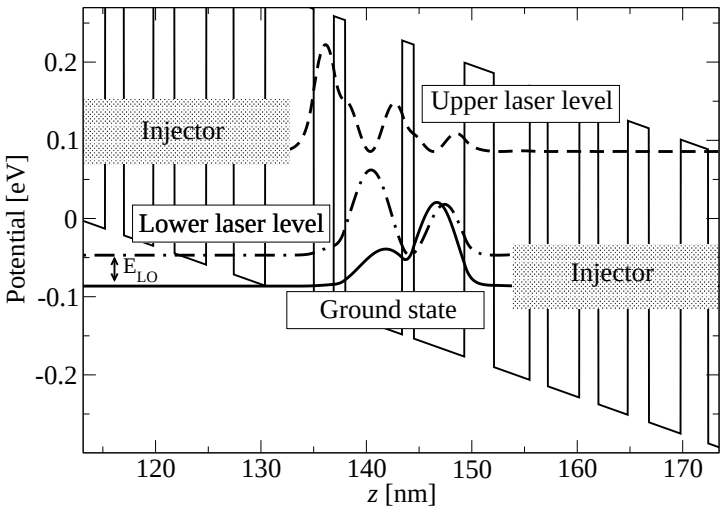

Figure 1.5: Scheme of the wavefunctions of most relevant levels in a quantum cascade laser structure from Ref. [1].

tum dot infrared photodetectors (QDIPs). The main origin of dark current in QWIPs is thermal excitation (due to interaction with phonons) of carriers from the ground state to continuum states. The discrete electronic spectrum of quantum dots as opposed to continuum spectrum of quantum wells significantly reduces the phase space for such processes and therefore reduces the dark current. Higher operating temperatures of QDIPs are therefore expected. Due to optical selection rules, QWIPs based on intersubband transitions in the conduction band interact only with radiation having the polarisation vector in the growth direction. This is not the case in quantum dots since these are three dimensional objects where such selection rules do not exist.

QDIPs comprising III-As self-assembled quantum dots have indeed become a very important technology for the detection of mid- and far-infrared electromagnetic radiation [58–72]. Since their initial realisation and demonstration [58–60], there has been a lot of experimental success leading to continuous improvements in their performance. For example, the concept of a current blocking layer [61, 62] was introduced to reduce the dark current. Quantum

dots-in-a-well (DWELL) photodetectors [63–65] provide a way to tailor the detection wavelength within a certain range by changing the well width and focal plane arrays based on QDIPs have also been demonstrated [66, 67, 73]. Most recently, room temperature operation of a resonant tunnelling QDIP with InGaAs quantum dots grown on GaAs substrate [68], as well as of QDIP comprising InAs quantum dots grown on InP substrate [74], has been achieved. These are probably the most exciting results, since room temperature operation of QWIPs has never been achieved.

Although In(Ga)As/GaAs quantum dots grown on GaAs substrates [59, 60, 63, 64, 68, 69, 71, 72, 75–81], being probably the most explored quantum dot material system, are typically used in QDIPs, other material systems have also attracted attention such as InAs quantum dots grown on InP [82], InGaAs/InGaP dots grown on GaAs substrate [83–85], InAs/InAlAs dots grown on InP [86], GaN/AlN [87, 88] and Ge/Si quantum dots [89]. QDIP devices utilise two different geometries - lateral conductivity QDIPs and vertical conductivity QDIPs [34]. Vertical QDIPs have been the subject of more intensive research due to their suitability for application as focal plane arrays [66,67], although lateral QDIPs have demonstrated excellent performance too [34]. The mentioned devices exhibit response in the mid-infrared range, but most recently the terahertz range was approached with QDIPs, as well [90].

On the other hand, there has been less success in the development of quantum dot intraband emitters. In quantum well based intersubband lasers the lasing threshold depends on the lifetime of the upper laser level which is determined by LO phonon scattering and is of the order of picoseconds. In order to have a lower threshold, LO phonon scattering needs to be reduced. Due to the discrete nature of states in quantum dots, electron relaxation due to the interaction with LO phonons has previously been considered to be vanishingly small unless the energy levels are separated by the energy of an LO phonon [91]. Consequently, a quantum dot cascade laser with six orders of magnitude lower threshold current than in quantum well based devices was expected [92]. How-

ever, current thought is that the electron – LO phonon interaction in quantum dots should be considered in the strong coupling regime [93,94], and theoretical predictions of relaxation due to LO phonon decay [95,96] have indicated relaxation times of the order of hundred of picoseconds, in accordance with experimentally measured values [97, 98]. This is still two orders of magnitude larger than in quantum wells and hence the latest theoretical proposals of quantum dot cascade lasers [99–101] still predict lower threshold currents. Electroluminescence from such structures has been observed [102–104] but lasing has not been observed yet. Experimental evidence that the system with truly discrete states should have a lower threshold current comes from extremely low threshold currents observed in quantum well based QCLs in strong magnetic fields [105]. From the commercial point of view it is necessary to avoid the use of high magnetic fields and have a system with truly discrete states.

As far as optically pumped intraband quantum dot lasers are concerned, prior to work reported here, there have been no reports on theoretical analysis of their feasibility or experimental attempts of their realisation.

1.4 Thesis outline

From the discussion presented in Sec. 1.3.2, one can see that the prospect of having quantum dot intraband devices superior to existing quantum well intersubband devices, has not been fully exploited. While this is partly due to difficulties in technological realisations of quantum dot structures with desired characteristics, there is also a lack of understanding of complex physical processes within the devices and the absence of appropriate device models. The goal of this thesis is to bridge the mentioned gap by developing the appropriate models of intraband quantum dot devices.

In Chapter 2 the theoretical framework used in this work will be presented. Chapters 3 and 4 will present efficient methods for electronic structure calculation in quantum dots, based on exploiting the symmetry of the dot shape, in the case of materials with zincblende and wurtzite crystal structure, respec-

tively. In Chapter 5 the design and simulation of an optically pumped laser based on InAs/GaAs quantum dots will be given. Calculations of the absorption spectrum of InAs/GaAs QDIPs and their comparison with experimental results from the literature will be presented in Chapter 6. Chapter 7 will be devoted to understanding the performance of DWELL detectors, namely the effect of wavelength tailoring by changing the well width and the Stark shift in these structures. A model of electron transport in QDIPs, capable of predicting the output device characteristics is presented in Chapter 8, and used to investigate a realistic device. In Chapter 9 the application of nonequilibrium Green's functions formalism to transport in quantum dot structures is introduced and transport through a superlattice of quantum dots is investigated. The prospect of realising quantum dot QCLs is analysed and one possible design is given. Finally, a summary of the work presented, along with the conclusion and suggestions for possible future direction of the research in this exciting area are given in Chapter 10.

Chapter 2

Theoretical framework

The theoretical framework used in the thesis will be presented in this Chapter. The discussion will start with an overview of the existing models used in the calculation of the electronic structure of quantum dots. The $\boldsymbol{k}\cdot\boldsymbol{p}$ model, which was mostly used in this work will be presented next, along with the ways to take into account the effects of strain and external electromagnetic field. Different numerical methods for solving the $\boldsymbol{k}\cdot\boldsymbol{p}$ Hamiltonian and finding the strain distribution in quantum dots, with a special emphasis on those exploited in this thesis, will be then presented. The following section will describe the interaction of carriers in quantum dot with phonons which is essential for understanding the dynamical and transport properties of quantum dot devices. Finally, the nonequilibrium Green's functions theory of transport in quantum dots, will be described in the last section of this Chapter.

2.1 Electronic structure of quantum dots

Self-assembled quantum dots typically have lateral dimensions of the order of $15-30\,\mathrm{nm}$ and height of the order $3-7\,\mathrm{nm}$. While on the one hand, they seem to be small and simple objects, a look at their structure from the atomistic side reveals their high complexity. Having in mind that the lattice constants of the underlying semiconductor materials are typically of the order of $0.5\,\mathrm{nm}$, one can estimate that a single quantum dot contains $\sim 10^6$ nuclei and even a larger number of electrons interacting among each other with long range Coulomb

forces. This clearly indicates that direct solution of the many body quantum dot Hamiltonian is not a feasible approach and that smart and efficient methods need to be developed. Fortunately, there is a wealth of theoretical methods that have been applied to the calculation of the electronic structure of bulk semiconductors, many of which can be appropriately extended to quantum dots.

The method that is closest to being able to be called *ab initio* and yet relatively efficient to provide some hope that it will be feasible for quantum dot systems is *density functional theory* (DFT). It is based on the theorem by Hohenberg and Kohn [106] of a unique correspondence between the electron density and the ground state of a many electron system. Furthermore, Kohn and Sham [107] showed how it is possible to replace the many electron problem by an equivalent set of self-consistent single particle equations. These equations contain the functional of exchange correlation potential, whose exact form is not known, and needs to be approximated. While the initially developed DFT treats ground state only, it was later developed to treat excited states as well. The method has been applied to a range of solid state systems [108], nevertheless despite its elegance it is still limited to systems of several thousands atoms. Calculations of the electronic structure and optical spectra of clusters and nanocrystals of the size up to $\sim$3 nm have indeed been performed [109–113], however much larger self-assembled quantum dots still seem to be out of the range of present day computational resources.

An approach that has been highly successful in modelling the bulk band structure of semiconductors is the *empirical pseudopotential method* [114, 115]. The method is based on the assumption that the effect of the nucleus, core electrons and potential of valence electrons on a single electron can be replaced by a single potential, therefore reducing the problem to a single particle problem. The mentioned potential is represented in plane wave expansion, and it turns out that only a small number of coefficients in the expansion (so called form factors) is necessary to accurately reproduce the band structure over a

wide range of energies and throughout the whole Brillouin zone. The empirical pseudopotential method can be extended to quantum dot structures. The pseudopotentials fitted to the experimental results of bulk materials consituting the quantum dot and embedding matrix are then used as known values and total potential experienced by an electron in quantum dot is expressed as a sum of pseudopotentials of each atom [116]. An additional complication is that in the strained structures the equilibrium positions of atoms are not known in advance, therefore the system of atoms has to be relaxed to its equilibrium position before the pseudopotential Hamiltonian is calculated and diagonalised [117, 118]. The corresponding eigenvalue problem is solved either by expanding the wavefunction in plane waves or in a linear combination of bulk Bloch bands [119]. The electronic structure calculation within the empirical pseudopotential method is computationally demanding, but it is feasible with present day computers. An interesting method that has been developed more recently is the *charge density patching method* [120]. Central quantities in this method are electronic charge densities, rather than pseudopotentials. Its main idea is to patch the charge densities calculated for smaller systems by DFT, to obtain the charge density of a bigger system.

Another method that was initially applied to bulk crystals, and then extended to quantum heterostructures is the *tight-binding method*. The method is atomistic in nature as it treats individual atoms. The model Hamiltonian of the structure is constructed by considering the interactions of electron orbitals originating from one atom with orbitals of its few nearest neighbours only. Similarly as in the empirical pseudopotential method, the parameters of the Hamiltonian are chosen to accurately fit the bulk band structure [121]. Although the resulting Hamiltonian matrix is large, it is sparse and can be diagonalised using efficient routines for such matrices, which has resulted in relatively frequent applications of the method to studies of quantum dot electronic structure [122–125].

For most of the electronic and optical properties of semiconductors and

nanostructures based upon them, it is only a certain region of momentum space where carriers reside. The idea of the $\boldsymbol{k}\cdot\boldsymbol{p}$ *method* and its simplest version *the effective mass method* is to exploit this fact and make an expansion of the wavefunction in a limited number of bulk Bloch bands at some characteristic point, usually the point $\boldsymbol{k}=0$, the so called Γ-point. While one can in principle form a $\boldsymbol{k}\cdot\boldsymbol{p}$ Hamiltonian from any number of bulk bands, the most popular is the 8-band Hamiltonian, which fairly well describes the top of the valence band and the bottom of the conduction band. It has therefore often been applied in quantum dot electronic structure calculations [126–131]. While possibly limited in the description of some subtle effects, the $\boldsymbol{k}\cdot\boldsymbol{p}$ method can inherently incorporate the effects of band mixing, strain, piezoelectricity, as well as the influence of external fields, keeping a lower computational cost compared to atomistic methods. It has therefore been the method of choice for the electronic structure calculations reported in this work and will be described in more detail in sections that follow.

2.2 $\boldsymbol{k}\cdot\boldsymbol{p}$ method

Let the Hamiltonian of an electron in a semiconductor be

$$\hat{H}=\frac{\hat{\boldsymbol{p}}^2}{2m_0}+V_0(\boldsymbol{r})+\hat{H}_{\mathrm{so}}, \tag{2.1}$$

where $\hat{\boldsymbol{p}}$ is the momentum operator, $V_0(\boldsymbol{r})$ the periodic crystal potential (including nuclei, core electrons and self-consistent potential of valence electrons), and $\hat{H}_{\mathrm{so}}$ the spin-orbit interaction Hamiltonian arising from relativistic corrections to Schrödinger equation given by

$$\hat{H}_{\mathrm{so}}=\frac{\hbar}{4m_0^2c^2}\left[\nabla V_0(\boldsymbol{r})\times\hat{\boldsymbol{p}}\right]\cdot\boldsymbol{\sigma}, \tag{2.2}$$

where $\boldsymbol{\sigma}$ is a vector of Pauli matrices

$$\sigma_x=\begin{bmatrix}0&1\\1&0\end{bmatrix},\sigma_y=\begin{bmatrix}0&-i\\i&0\end{bmatrix},\sigma_z=\begin{bmatrix}1&0\\0&-1\end{bmatrix}. \tag{2.3}$$

According to Bloch's theorem, the wavefunction of an electron in a periodic potential can be expressed as

$$\Psi(\boldsymbol{r}) = u_{n\boldsymbol{k}}(\boldsymbol{r})e^{i\boldsymbol{k}\boldsymbol{r}}, \tag{2.4}$$

where $\boldsymbol{k}$ is the wave vector from the first Brillouin zone and $u_{n\boldsymbol{k}}(\boldsymbol{r})$ is a periodic function, a so called *Bloch function*. The index n anticipates that for each $\boldsymbol{k}$ vector, there will be a discrete set of solutions of the Schrödinger equation (so called bands)

$$\hat{H}\Psi = E\Psi. \tag{2.5}$$

After substituting (2.4) into (2.5) one arrives at

$$\left(\frac{\hat{\boldsymbol{p}}^2}{2m_0} + V_0(\boldsymbol{r}) + \frac{\hbar^2k^2}{2m_0} + \hbar\frac{\boldsymbol{k}\cdot\hat{\boldsymbol{p}}}{m_0} + \frac{\hbar}{4m_0^2c^2}\left[\nabla V_0(\boldsymbol{r})\times\hat{\boldsymbol{p}}\right]\cdot\boldsymbol{\sigma} + \right. \tag{2.6}$$
$$\left. + \frac{\hbar^2}{4m_0^2c^2}\left[\nabla V_0(\boldsymbol{r})\times\boldsymbol{k}\right]\cdot\boldsymbol{\sigma}\right) u_{n\boldsymbol{k}}(\boldsymbol{r}) = E_{n\boldsymbol{k}}u_{n\boldsymbol{k}}(\boldsymbol{r}).$$

Due to the smallness of $\hbar\boldsymbol{k}$ compared with matrix elements of $\hat{\boldsymbol{p}}$, the last term in Eq. (2.6) will be neglected in further discussion. The solutions at the Γ point when spin-orbit interaction is excluded satisfy the eigenvalue problem of a Hermitian operator with periodic boundary conditions

$$\hat{H}_0u_{n0}(\boldsymbol{r}) = \left(\frac{\hat{\boldsymbol{p}}^2}{2m_0} + V_0(\boldsymbol{r})\right)u_{n0}(\boldsymbol{r}) = E_{n0}u_{n0}(\boldsymbol{r}), \tag{2.7}$$

and therefore form an orthonormal basis of functions with periodicity of the crystal lattice. At this place, one can see that the introduction of a discrete index n was justifiable. Since Bloch functions u_{n0} form an orthonormal basis, one can express the solution of (2.6) as their linear combination

$$u_{n\boldsymbol{k}}(\boldsymbol{r}) = \sum_n c_{n\boldsymbol{k}}u_{n0}(\boldsymbol{r}), \tag{2.8}$$

which leads to the eigenvalue problem of the Hamiltonian matrix whose elements are given as

$$h_{mn} = \langle u_{m0}|\left(\hat{H} + \frac{\hbar^2k^2}{2m_0} + \hbar\frac{\boldsymbol{k}\cdot\hat{\boldsymbol{p}}}{m_0}\right)|u_{n0}\rangle\,. \tag{2.9}$$

Using (2.7) and the orthonormality condition, one gets:

$$h_{mn} = \left(E_{n0} + \frac{\hbar^2 k^2}{2m_0}\right)\delta_{m,n} + \frac{\hbar}{m_0}\langle u_{m0}|\,\boldsymbol{k}\cdot\hat{\boldsymbol{p}}\,|u_{n0}\rangle + \langle u_{m0}|\,\hat{H}_{\mathrm{so}}\,|u_{n0}\rangle\,. \quad (2.10)$$

Since the second term in Eq. (2.10) is crucial in determining the Hamiltonian matrix, the method being described is called the $\boldsymbol{k}\cdot\boldsymbol{p}$ method. If infinitely many bands were taken, the solution of the eigenvalue problem of matrix h_{mn} would lead to exact eigenvalues of Hamiltonian (2.1). Clearly, in practice, one has to restrict it to a finite number of bands. Historically, it was first applied to valence band (6-band Hamiltonian) [132,133] and later on the conduction band was added (8-band Hamiltonian) [134]. In Secs. 2.2.1 and 2.2.2, the explicit forms of 8-band Hamiltonians in semiconductors with zincblende and wurtzite crystal structure, used in this work, will be derived.

2.2.1 The 8-band $\boldsymbol{k}\cdot\boldsymbol{p}$ Hamiltonian for semiconductors with zincblende crystal symmetry

Many of the technologically important semiconductors crystalise in zincblende structure. Apart from InAs and GaAs that are mostly of interest here, these are also AlSb, CdTe, GaP, GaSb, InP, InSb, ZnS, ZnSe, and ZnTe. Moreover, the point T_d symmetry group of the zincblende crystal is a subgroup of the diamond group of Ge and Si, and therefore the same $\boldsymbol{k}\cdot\boldsymbol{p}$ Hamiltonian, can be applied to these semiconductors, as well.

The first step in the construction of the explicit form of the $\boldsymbol{k}\cdot\boldsymbol{p}$ Hamiltonian is the choice of bands to be included in the expansion (2.8). A logical choice is to include the highest states in the valence band and the lowest states in the conduction band. Following the notation of Ref. [135], the point group T_d has five irreducible representations (IRs) Γ_1–Γ_5. The lowest state in the conduction band transforms under the operations of a symmetry group according to one dimensional representation Γ_1, and will be labelled as $|S\rangle$, while the highest states in the valence band transforms according to the three dimensional representation Γ_5, and will be labelled as $|X\rangle$, $|Y\rangle$, and $|Z\rangle$. While analogy of

these states with s and p_{x-z} orbitals of a spherically symmetric system (such as for example hydrogen atom) does exist, one should still have in mind that, for example Γ_1 state is not spherically symmetric and transforms as s only under the symmetry operations of group T_d, and similarly for Γ_5 states. The basis consisting of spin up and down states of the four selected Bloch functions

$$\{u_1,\ldots,u_8\}=\{|S\uparrow\rangle,|X\uparrow\rangle,|Y\uparrow\rangle,|Z\uparrow\rangle,|S\downarrow\rangle,|X\downarrow\rangle,|Y\downarrow\rangle,|Z\downarrow\rangle\} \tag{2.11}$$

is therefore chosen in expansion (2.8).

As a second step in the construction of the $\boldsymbol{k}\cdot\boldsymbol{p}$ Hamiltonian, one has to evaluate the matrix elements appearing in (2.10). The momentum operator $\hat{\boldsymbol{p}}$ transforms as Γ_5 under the operations of the symmetry group and this fact can be exploited to conclude that many of the matrix elements of the components of the $\hat{\boldsymbol{p}}$-operator are equal to zero. This stems from the theorem that says that the matrix element $\langle i|\hat{O}|f\rangle$ is non zero only if the product of the IRs of f and $\hat{O}$ contains the IR of i [136]. From multiplication tables [135] of IRs of the group T_d, and additional symmetry considerations, it follows that only the following matrix elements are non-zero and that they are mutually equal:

$$P_0=-i\frac{\hbar}{m_0}\langle S|\hat{p}_x|X\rangle=-i\frac{\hbar}{m_0}\langle S|\hat{p}_y|Y\rangle=-i\frac{\hbar}{m_0}\langle S|\hat{p}_z|Z\rangle, \tag{2.12}$$

where P_0 is the interband matrix element of the velocity operator [137] usually reported in energy units as $E_P=\frac{2m_0}{\hbar^2}P_0^2$.

The symmetry of the crystal also allows only certain matrix elements of the spin-orbit interaction operator to be non-zero, in particular these are

$$\begin{aligned}\frac{\Delta}{3} &= -i\frac{\hbar}{4m_0^2c^2}\langle X|\left[\nabla V_0(\boldsymbol{r})\times\hat{\boldsymbol{p}}\right]_y|Z\rangle=\\ &= -i\frac{\hbar}{4m_0^2c^2}\langle Y|\left[\nabla V_0(\boldsymbol{r})\times\hat{\boldsymbol{p}}\right]_z|X\rangle=\\ &= -i\frac{\hbar}{4m_0^2c^2}\langle Z|\left[\nabla V_0(\boldsymbol{r})\times\hat{\boldsymbol{p}}\right]_x|Y\rangle.\end{aligned} \tag{2.13}$$

The following discussion will make evident the fact that Δ is the spin splitting of the states in the valence band. After explicitly calculating all 64 matrix

elements in the 8-dimensional manifold of states (2.11), one obtains the 8-band Hamiltonian

$$\hat{H} = \begin{bmatrix} G + G_{\text{so}} & \Gamma \\ -\Gamma^* & G + G_{\text{so}}^* \end{bmatrix}, \tag{2.14}$$

where the respective blocks are given by

$$G = \begin{bmatrix} E_C' + \frac{\hbar^2 k^2}{2m_0} & ik_x P_0 & ik_y P_0 & ik_z P_0 \\ -ik_x P_0 & E_V' + \frac{\hbar^2 k^2}{2m_0} & 0 & 0 \\ -ik_y P_0 & 0 & E_V' + \frac{\hbar^2 k^2}{2m_0} & 0 \\ -ik_z P_0 & 0 & 0 & E_V' + \frac{\hbar^2 k^2}{2m_0} \end{bmatrix}, \tag{2.15}$$

where E_C' and E_V' are the conduction and valence band edges when spin orbit interaction is not included, and

$$G_{\text{so}} = \frac{\Delta}{3}\begin{bmatrix} 0 & 0 & 0 & 0 \\ 0 & 0 & -i & 0 \\ 0 & i & 0 & 0 \\ 0 & 0 & 0 & 0 \end{bmatrix}, \Gamma = \frac{\Delta}{3}\begin{bmatrix} 0 & 0 & 0 & 0 \\ 0 & 0 & 0 & 1 \\ 0 & 0 & 0 & i \\ 0 & -1 & i & 0 \end{bmatrix}. \tag{2.16}$$

The eigenvalues of the spin-orbit part of the Hamiltonian are 0 (doubly degenerate, with eigenvectors related to conduction band states), $\frac{\Delta}{3}$ (fourfold degenerate) and $-2\frac{\Delta}{3}$ (doubly degenerate). Therefore, the actual position of the conduction band edge at the Γ point is $E_C = E_C'$, but the position of the valence band edge is $E_V = E_V' + \frac{\Delta}{3}$. It is the difference of E_C and E_V that is equal to the experimentally measured energy gap, therefore these will be used, rather than E_C' and E_V'.

The Hamiltonian (2.14) represents the reduction of the total Hamiltonian of a zincblende semiconductor to an 8-dimensional space of states (2.11) and is therefore clearly only an approximation of the total Hamiltonian. One way to improve this approximation would be clearly to include more bands which would result in a matrix of larger dimensions. There is, however, a more attractive approach due to Löwdin [138], which allows one to perturbatively take into account the influence of the states outside the chosen manifold (so called

remote bands), and at the same time keep the size of the Hamiltonian matrix at the same value. Within Löwdin's perturbation theory, the Hamiltonian U with second-order perturbative corrections due to the influence of remote bands is given by

$$U_{\alpha\beta} = H_{\alpha\beta} + \sum_r \frac{H_{\alpha r} H_{r\beta}}{E - H_{rr}}, \tag{2.17}$$

where the indices α and β refer to states within the manifold, and r to all other states. The eigenvalue problem of U becomes a nonlinear problem since the energy E explicitly appears in the Hamiltonian. However, as is often done in perturbation expansions of this kind, one approximates E with a certain value. There is some ambiguity in the choice of this value, especially when corrections to off-diagonal matrix elements are concerned. Usually, in the corrections to all matrix elements among the valence band states, E is replaced with E'_V, and in the elements among conduction band states with E'_C. The ambiguity is pronounced when the elements between conduction and valence band states are concerned and then E is sometimes replaced with $\frac{1}{2}(E_C + E_V)$ [130]. After symmetry considerations of matrix elements between states in the manifold and remote bands and neglecting spin-orbit terms in the correction, one obtains the following additional terms to the Hamiltonian blocks G

$$G_r = \frac{\hbar^2}{m_0} \begin{bmatrix} A'k^2 & Bk_yk_z & Bk_xk_z & Bk_xk_y \\ Bk_yk_z & w_x & N'k_xk_y & N'k_xk_z \\ Bk_xk_z & N'k_xk_y & w_y & N'k_yk_z \\ Bk_xk_y & N'k_xk_z & N'k_yk_z & w_z \end{bmatrix}, \tag{2.18}$$

where $w_{xx} = M'(k_y^2 + k_z^2) + L'k_x^2$, $w_{yy} = M'(k_x^2 + k_z^2) + L'k_y^2$, and $w_{zz} = M'(k_x^2 + k_y^2) + L'k_z^2$. The B coefficient exactly vanishes in crystals with diamond structure, and in crystals with zincblende structure it appears to be very small and is usually neglected [139].

One can in principle work in the basis (2.11), although it is more usual to work in the basis of the total angular momentum operator $|JJ_z\rangle$ that diago-

nalises the Hamiltonian at $\boldsymbol{k}=0$, given by:

$$\begin{aligned}
|1\rangle &= |\frac{1}{2},-\frac{1}{2}\rangle = |S\downarrow\rangle,\\
|2\rangle &= |\frac{1}{2},\frac{1}{2}\rangle = |S\uparrow\rangle,\\
|3\rangle &= |\frac{3}{2},\frac{1}{2}\rangle = -\frac{i}{\sqrt{6}}|(X+iY)\downarrow\rangle + i\sqrt{\frac{2}{3}}|Z\uparrow\rangle,\\
|4\rangle &= |\frac{3}{2},\frac{3}{2}\rangle = \frac{i}{\sqrt{2}}|(X+iY)\uparrow\rangle,\\
|5\rangle &= |\frac{3}{2},-\frac{3}{2}\rangle = -\frac{i}{\sqrt{2}}|(X-iY)\downarrow\rangle,\\
|6\rangle &= |\frac{3}{2},-\frac{1}{2}\rangle = \frac{i}{\sqrt{6}}|(X-iY)\uparrow\rangle + i\sqrt{\frac{2}{3}}|Z\downarrow\rangle,\\
|7\rangle &= |\frac{1}{2},-\frac{1}{2}\rangle = -\frac{i}{\sqrt{3}}|(X-iY)\uparrow\rangle + \frac{i}{\sqrt{3}}|Z\downarrow\rangle,\\
|8\rangle &= |\frac{1}{2},\frac{1}{2}\rangle = -\frac{i}{\sqrt{3}}|(X+iY)\downarrow\rangle - \frac{i}{\sqrt{3}}|Z\uparrow\rangle.
\end{aligned} \tag{2.19}$$

The Bloch functions labelled by 1 and 2 correspond to electron states of spin down and spin up, those labelled by 3 and 6 to light-hole states, 4 and 5 to heavy-hole states and 7 and 8 to split-off band states. In this basis, the Hamiltonian acquires the form

$$\hat{H}_k = \tag{2.20}$$
$$\begin{bmatrix}
A & 0 & V^+ & 0 & \sqrt{3}V & -\sqrt{2}U & -U & \sqrt{2}V^+\\
0 & A & -\sqrt{2}U & -\sqrt{3}V^+ & 0 & -V & \sqrt{2}V & U\\
V & -\sqrt{2}U & -P+Q & -S^+ & R & 0 & \sqrt{\frac{3}{2}}S & -\sqrt{2}Q\\
0 & -\sqrt{3}V & -S & -P-Q & 0 & R & -\sqrt{2}R & \frac{1}{\sqrt{2}}S\\
\sqrt{3}V^+ & 0 & R^+ & 0 & -P-Q & S^+ & \frac{1}{\sqrt{2}}S^+ & \sqrt{2}R^+\\
-\sqrt{2}U & -V^+ & 0 & R^+ & S & -P+Q & \sqrt{2}Q & \sqrt{\frac{3}{2}}S^+\\
-U & \sqrt{2}V^+ & \sqrt{\frac{3}{2}}S^+ & -\sqrt{2}R^+ & \frac{1}{\sqrt{2}}S & \sqrt{2}Q & -P-\Delta & 0\\
\sqrt{2}V & U & -\sqrt{2}Q & \frac{1}{\sqrt{2}}S^+ & \sqrt{2}R & \sqrt{\frac{3}{2}}S & 0 & -P-\Delta
\end{bmatrix},$$

where

$$\begin{aligned}
A &= E_C + \frac{\hbar^2}{m_0}A'k^2 + \frac{\hbar^2k^2}{2m_0},\\
U &= \frac{1}{\sqrt{3}}P_0k_z,\\
V &= \frac{1}{\sqrt{6}}P_0(k_x - ik_y),\\
P &= -E_V + \gamma_1\frac{\hbar^2k^2}{2m_0},\\
Q &= \gamma_2\frac{\hbar^2}{2m_0}\left(k_x^2 + k_y^2 - 2k_z^2\right),\\
R &= -\frac{\sqrt{3}}{2}\frac{\hbar^2}{m_0}\left[\gamma_2\left(k_x^2 - k_y^2\right) - 2i\gamma_3k_xk_y\right],\\
S &= \sqrt{3}\gamma_3\frac{\hbar^2}{m_0}k_z(k_x - ik_y),
\end{aligned}$$

and $\gamma_1 = -1-\frac{4}{3}M'-\frac{2}{3}L'$, $\gamma_2 = \frac{1}{3}(M'-L')$, $\gamma_3 = -\frac{1}{3}N'$ are Luttinger parameters of the 8-band model. More experimentally accessible are the parameters of the 6-band model (M, L, and N, or γ_1^L, γ_2^L, and γ_3^L) as they are directly related to effective masses in the valence band. By applying Eq. (2.17) to the 6-band and 8-band model and subtracting these equations, one gets $M' = M$, $L' = L+\frac{1}{2}\frac{E_P}{E_g+\frac{\Delta}{3}}$, and $N' = N+\frac{1}{2}\frac{E_P}{E_g+\frac{\Delta}{3}}$, where $E_g = E_C - E_V$ is the energy gap. Consequently, one gets the relation for 8-band model Luttinger parameters expressed in terms of the parameters of the 6-band model

$$\begin{aligned}
\gamma_1 &= \gamma_1^L - \frac{E_P}{3E_g + \Delta},\\
\gamma_2 &= \gamma_2^L - \frac{1}{2}\frac{E_P}{3E_g + \Delta},\\
\gamma_3 &= \gamma_3^L - \frac{1}{2}\frac{E_P}{3E_g + \Delta}.
\end{aligned}$$

Furthermore, A' can be related to conduction band effective mass m^*. By calculating m^* considering all bands other than the conduction band as remote bands and applying Löwdin's perturbation theory, one gets

$$\frac{\hbar^2}{m_0}(\frac{1}{2} + A') = \frac{\hbar^2}{2m^*} - \frac{P_0^2}{E_g + \frac{1}{3}\Delta}. \tag{2.21}$$

In this work, however, it will be taken that $A' = 0$. One can see, for example from the matrix elements in Ref. [140] that conduction band is coupled most

strongly to the valence band and weakly to other bands, implying that the value of A' that measures the coupling to other bands is small.

2.2.2 The 8-band $\boldsymbol{k}\cdot\boldsymbol{p}$ Hamiltonian for semiconductors with wurtzite crystal symmetry

III-nitride semiconductor compounds such as GaN, AlN, and InN often crystalise in the wurtzite structure. The point symmetry group of this crystal is C_{6v} and has six IRs Γ_1 – Γ_6. The lowest state in the conduction band transforms as Γ_1 and will be labelled as $|S\rangle$. The two highest states in the valence band that transform according to two dimensional representation Γ_6, and will be labelled as $|X\rangle$ and $|Y\rangle$, are followed by a state that transforms as Γ_1 and is labelled as $|Z\rangle$. The 8-band Hamiltonian in the manifold (2.11) then takes the form (2.14) where the blocks in the Hamiltonian are given by

$$G = \frac{\hbar^2 k^2}{2m_0} + \begin{bmatrix} E'_C & ik_xP_\perp & ik_yP_\perp & ik_zP_\parallel \\ -ik_xP_\perp & E'_V+\Delta_1 & 0 & 0 \\ -ik_yP_\perp & 0 & E'_V+\Delta_1 & 0 \\ -ik_zP_\parallel & 0 & 0 & E'_V \end{bmatrix}, \tag{2.22}$$

$$G_{\mathrm{so}} = \Delta_2 \begin{bmatrix} 0&0&0&0 \\ 0&0&-i&0 \\ 0&i&0&0 \\ 0&0&0&0 \end{bmatrix}, \Gamma = \Delta_3 \begin{bmatrix} 0&0&0&0 \\ 0&0&0&1 \\ 0&0&0&i \\ 0&-1&i&0 \end{bmatrix}, \tag{2.23}$$

where

$$P_\perp = -i\frac{\hbar}{m_0}\langle S|\hat{p}_x|X\rangle = -i\frac{\hbar}{m_0}\langle S|\hat{p}_y|Y\rangle,$$

$$P_\parallel = -i\frac{\hbar}{m_0}\langle S|\hat{p}_z|Z\rangle,$$

$$E'_C = \langle S|\frac{\hat{\boldsymbol{p}}^2}{2m_0} + V_0(\boldsymbol{r})|S\rangle,$$

$$E'_V = \langle Z|\frac{\hat{\boldsymbol{p}}^2}{2m_0} + V_0(\boldsymbol{r})|Z\rangle,$$

$$E'_V+\Delta_1 = \langle X|\frac{\hat{\boldsymbol{p}}^2}{2m_0} + V_0(\boldsymbol{r})|X\rangle = \langle Y|\frac{\hat{\boldsymbol{p}}^2}{2m_0} + V_0(\boldsymbol{r})|Y\rangle,$$

where Δ_1 is called the crystal field splitting,

$$\Delta_2 = -i\frac{\hbar}{4m_0^2c^2}\langle Y|\left[\nabla V_0(\boldsymbol{r})\times\hat{\boldsymbol{p}}\right]_z|X\rangle,$$

$$\Delta_3 = -i\frac{\hbar}{4m_0^2c^2}\langle X|\left[\nabla V_0(\boldsymbol{r})\times\hat{\boldsymbol{p}}\right]_y|Z\rangle = -i\frac{\hbar}{4m_0^2c^2}\langle Z|\left[\nabla V_0(\boldsymbol{r})\times\hat{\boldsymbol{p}}\right]_x|Y\rangle.$$

The momentum matrix elements $P_\parallel$ and $P_\perp$ can be related to effective mass parameters by [141]

$$P_\parallel^2 = \frac{\hbar^2}{2m_0}\left(\frac{m_0}{m_\parallel}-1\right)\frac{(E_g+\Delta_1+\Delta_2)(E_g+2\Delta_2)-2\Delta_3^2}{E_g+2\Delta_2},$$
$$P_\perp^2 = \frac{\hbar^2}{2m_0}\left(\frac{m_0}{m_\perp}-1\right)\frac{(E_g+\Delta_1+\Delta_2)(E_g+2\Delta_2)-2\Delta_3^2}{(E_g+\Delta_2)(E_g+\Delta_1+\Delta_2)}E_g,$$

where $m_\perp$ and $m_\parallel$ are the transversal and longitudinal bulk conduction band effective mass, $\Delta_2=\Delta_3=\frac{1}{3}\Delta_{so}$ and E_g is the energy gap.

In principle, G should also contain terms linear in k that couple $|Z\rangle$ to $|X\rangle$ and $|Y\rangle$. However, the values of these terms extracted from empirical pseudopotentials in Ref. [142] are small, and these terms are not considered in the literature [141, 143, 144].

When the effect of remote bands is included the following additional terms appear

$$G_r = \frac{\hbar^2}{m_0}\begin{bmatrix} w_1 & B_1k_yk_z & B_1k_xk_z & B_2k_xk_y \\ B_1k_yk_z & w_2 & N_1'k_xk_y & N_2'k_xk_z \\ B_1k_xk_z & N_1'k_xk_y & w_3 & N_2'k_yk_z \\ B_2k_xk_y & N_2'k_xk_z & N_2'k_yk_z & w_4 \end{bmatrix}, \tag{2.24}$$

where $w_1 = A_\perp'(k_x^2+k_y^2)+A_\parallel'k_z^2$, $w_2 = M_1'k_y^2+M_2'k_z^2+L_1'k_x^2$, $w_3 = M_1'k_x^2+M_2'k_z^2+L_1'k_y^2$, and $w_4 = M_3'(k_x^2+k_y^2)+L_2'k_z^2$.

Several approximations can be made at this point. Spin-orbit splitting can be neglected, which is justified by its small value in nitrogen containing semiconductors ($\Delta_2=\Delta_3=\Delta_{so}/3 \lesssim 5\,\text{meV}$ [4]). This leads to block diagonalisation of the total 8-band Hamiltonian into two identical 4-band Hamiltonians. Next, B_1 and B_2 terms are neglected in a similar manner as in the case of zincblende crystals. Finally, it also turns out that in the $(1,1)$ term in (2.24), the coefficient after k^2 is small and can be omitted [141, 143].

After transforming to a new basis

$$\begin{aligned}
|1\rangle &= i|S\uparrow\rangle, \\
|2\rangle &= \frac{1}{\sqrt{2}}|(X+iY)\uparrow\rangle, \\
|3\rangle &= \frac{1}{\sqrt{2}}|(X-iY)\uparrow\rangle, \\
|4\rangle &= |Z\uparrow\rangle,
\end{aligned} \tag{2.25}$$

one obtains the following 4-band Hamiltonian

$$\hat{H}_k = \begin{bmatrix}
E_c + \frac{\hbar^2 k^2}{2m_0} & V & V^+ & U \\
V^+ & E_v + F & K^+ & H^+ \\
V & K & E_v + F & H \\
U & H & H^+ & E_v + \Lambda
\end{bmatrix}, \tag{2.26}$$

with

$$\begin{aligned}
H &= i\frac{\hbar^2}{2m_0}A'_6 k_z k_+, \\
K &= \frac{\hbar^2}{2m_0}A'_5\left(k_x^2 - k_y^2 + 2ik_x k_y\right), \\
\Lambda &= -\Delta_1 + \frac{\hbar^2}{2m_0}\left[A'_1 k_z^2 + A'_2\left(k_x^2 + k_y^2\right)\right], \\
\Theta &= \frac{\hbar^2}{2m_0}\left[A'_3 k_z^2 + A'_4\left(k_x^2 + k_y^2\right)\right], \\
F &= \Delta_1 + \Lambda + \Theta, \\
V &= \frac{1}{\sqrt{2}}P_\perp k_+, \\
U &= P_\parallel k_z,
\end{aligned} \tag{2.27}$$

and $A'_1 = 1 + 2L'_2$, $A'_2 = 1 + 2M'_3$, $A'_3 = 2M'_2 - 2L'_2$, $A'_4 = L'_1 + M'_1 - 2M'_3$, $A'_5 = N'_1$, $A'_6 = \sqrt{2}N'_2$. From Löwdin's perturbation formula one gets the relation between the parameters of the four and three band model $L'_1 = L_1 + \frac{m_0}{\hbar^2}\frac{P_\perp^2}{E_g}$, $L'_2 = L_2 + \frac{m_0}{\hbar^2}\frac{P_\parallel^2}{E_g}$, $M'_1 = M_1$, $M'_2 = M_2$, $M'_3 = M_3$, $N'_1 = N_1 + \frac{m_0}{\hbar^2}\frac{P_\perp^2}{E_g}$, $N'_2 = N_2 + \frac{m_0}{\hbar^2}\frac{P_\perp P_\parallel}{E_g}$, and consequently the relations between the A'_i $(i = 1, \ldots, 6)$ parameters in the four band model with the three band model parameters A_i

$(i = 1, \ldots, 6)$

$$\begin{aligned} A_1' &= A_1 + \frac{2m_0}{\hbar^2}\frac{P_\parallel^2}{E_g}, \\ A_2' &= A_2, \\ A_3' &= A_3 - \frac{2m_0}{\hbar^2}\frac{P_\parallel^2}{E_g}, \\ A_4' &= A_4 + \frac{m_0}{\hbar^2}\frac{P_\perp^2}{E_g}, \\ A_5' &= A_5 + \frac{m_0}{\hbar^2}\frac{P_\perp^2}{E_g}, \\ A_6' &= A_6 + \frac{\sqrt{2}m_0}{\hbar^2}\frac{P_\perp P_\parallel}{E_g}. \end{aligned} \tag{2.28}$$

2.3 The effect of strain

Strain has a strong effect on the electronic structure of semiconductors. The displacement of constituent atoms from their equilibrium positions changes the potential created by them and therefore the bandstructure is modified. The aim of this section will be to quantitatively describe how the effect of strain can be incorporated in the $\boldsymbol{k} \cdot \boldsymbol{p}$ model. The approach of Ref. [130] is mainly followed in this section.

Let the component of the displacement vector of a point in the semiconductor in the direction i be u_i. The strain tensor components are then defined as

$$e_{ij} = \frac{1}{2}\left(\frac{\partial u_i}{\partial x_j} + \frac{\partial u_j}{\partial x_i}\right). \tag{2.29}$$

Both the x, y, z and $1, 2, 3$ notation for the indices ij will be used. A case of the strain homogeneous in space will be assumed. The periodicity of the crystal is then still present, but with a different deformed unit cell whose basis vectors are related to the original basis vectors by

$$\boldsymbol{a}_i' = \sum_j (\delta_{ij} + e_{ij})\boldsymbol{a}_j. \tag{2.30}$$

The relation between the old and new coordinates is then

$$x_i = \sum_j (\delta_{ij} + e_{ij})x_j'. \tag{2.31}$$

The relationship between momentum operators in old and new coordinates is then up to terms linear in strain

$$\hat{p}_i = \sum_j (\delta_{ij} - e_{ij})\hat{p}'_j. \tag{2.32}$$

One should note that Bloch's theorem can now be applied only if the Hamiltonian (2.6) is expressed in new primed coordinates, since the system has the periodicity described by the vectors $\boldsymbol{a}'_i$, rather than $\boldsymbol{a}_i$. The crystal potential in the strained case is up to terms linear in strain then given by:

$$V(\boldsymbol{r}) = V_0(\boldsymbol{r}') + \sum_{ij} V_{ij}(\boldsymbol{r}')e_{ij}. \tag{2.33}$$

After replacing (2.31), (2.32) and (2.33) into (2.1) and applying Bloch's theorem in new coordinates, one obtains the eigenvalue problem for Bloch functions in the new coordinate system

$$\left(\hat{H}'_b + \hat{D}_0 + \hat{D}_1\right) v_{n\boldsymbol{k}}(\boldsymbol{r}') = E_{n\boldsymbol{k}} v_{n\boldsymbol{k}}(\boldsymbol{r}'), \tag{2.34}$$

where $\hat{H}'_b$ is the Hamiltonian on the left hand side of (2.6) with $\boldsymbol{r}$ and $\boldsymbol{p}$ replaced by $\boldsymbol{r}'$ and $\boldsymbol{p}'$

$$\hat{D}_0 = \sum_{ij} \left[-\frac{\hat{p}'_i \hat{p}'_j}{m_0} + V_{ij}(\boldsymbol{r}') \right] e_{ij} = \sum_{ij} \hat{D}_{ij} e_{ij}, \tag{2.35}$$

and

$$\hat{D}_1 = -\frac{\hbar}{m_0} \sum_{ij} k_i e_{ij} \hat{p}'_j. \tag{2.36}$$

The terms that couple the strain to the spin-orbit interaction have been neglected as is exclusively done in the literature [127, 131, 139, 145]. Next, the explicit forms of the strain part of the Hamiltonian in the case of crystals with zincblende and wurtzite symmetry will be derived.

2.3.1 Strain in zincblende crystals

For the case of crystals with zincblende symmetry, the appearance of additional terms $\hat{D}_0$ and $\hat{D}_1$ leads to additional contributions to the 4×4 blocks

of the Hamiltonian of the form

$$G_e = \begin{bmatrix} w_{ss} & w_x & w_y & w_z \\ w_x^* & w_{xx} & ne_{xy} & ne_{xz} \\ w_y^* & ne_{xy} & w_{yy} & ne_{yz} \\ w_z^* & ne_{xz} & ne_{yz} & w_{zz} \end{bmatrix}, \tag{2.37}$$

where $w_{ss} = a'(e_{xx} + e_{yy} + e_{zz})$, $w_{xx} = le_{xx} + m(e_{yy} + e_{zz})$, $w_{yy} = le_{yy} + m(e_{xx} + e_{zz})$, $w_{zz} = le_{zz} + m(e_{xx} + e_{yy})$, $w_x = b'e_{yz} - iP_0 \sum_j e_{xj}k_j$, $w_y = b'e_{xz} - iP_0 \sum_j e_{yj}k_j$, $w_z = b'e_{xy} - iP_0 \sum_j e_{zj}k_j$, $a' = \langle S|\hat{D}_{xx}|S\rangle$, $b' = 2\langle S|\hat{D}_{xy}|Z\rangle$, $l = \langle X|\hat{D}_{xx}|X\rangle$, $m = \langle Y|\hat{D}_{xx}|Y\rangle$, and $n = 2\langle X|\hat{D}_{xz}|Z\rangle$. The b' term is very small and is usually neglected [139].

The strain part of the Hamiltonian in the basis (2.19) is then

$$\hat{H}_s = \tag{2.38}$$
$$\begin{bmatrix} a_c e & 0 & -v^+ & 0 & -\sqrt{3}v & \sqrt{2}u & u & -\sqrt{2}v^+ \\ 0 & a_c e & \sqrt{2}u & \sqrt{3}v^+ & 0 & v & -\sqrt{2}v & -u \\ -v & \sqrt{2}u & -p+q & -s^+ & r & 0 & \sqrt{\frac{3}{2}}s & -\sqrt{2}q \\ 0 & \sqrt{3}v & -s & -p-q & 0 & r & -\sqrt{2}r & \frac{1}{\sqrt{2}}s \\ -\sqrt{3}v^+ & 0 & r^+ & 0 & -p-q & s^+ & \frac{1}{\sqrt{2}}s^+ & \sqrt{2}r^+ \\ \sqrt{2}u & v^+ & 0 & r^+ & s & -p+q & \sqrt{2}q & \sqrt{\frac{3}{2}}s^+ \\ u & -\sqrt{2}v^+ & \sqrt{\frac{3}{2}}s^+ & -\sqrt{2}r^+ & \frac{1}{\sqrt{2}}s & \sqrt{2}q & -p & 0 \\ -\sqrt{2}v & -u & -\sqrt{2}q & \frac{1}{\sqrt{2}}s^+ & \sqrt{2}r & \sqrt{\frac{3}{2}}s & 0 & -p \end{bmatrix},$$

where

$$\begin{aligned} e &= e_{11} + e_{22} + e_{33}, \\ p &= a_v e, \\ q &= b\left[e_{33} - \frac{1}{2}(e_{11} + e_{22})\right], \\ r &= \frac{\sqrt{3}}{2} b(e_{11} - e_{22}) - id e_{12}, \\ s &= -d(e_{13} - ie_{23}), \\ u &= \frac{1}{\sqrt{3}} P_0 \sum_{j=1}^{3} e_{3j} k_j, \\ v &= \frac{1}{\sqrt{6}} P_0 \sum_{j=1}^{3} (e_{1j} - ie_{2j}) k_j, \end{aligned}$$

where a_c and a_v are the conduction and valence band hydrostatic deformation potentials, respectively, b and d are the shear deformation potentials, related to previously introduced constants as $a_c = a'$, $a_v = -\frac{1}{3}(l + 2m)$, $b = \frac{1}{3}(l - m)$, $d = \frac{n}{\sqrt{3}}$.

2.3.2 Strain in wurtzite crystals

The strain part of the Hamiltonian in this case reads

$$G_e = \begin{bmatrix} w_1 & w_x & w_y & w_z \\ w_x^* & w_2 & n_1 e_{xy} & n_2 e_{xz} \\ w_y^* & n_1 e_{xy} & w_3 & n_2 e_{yz} \\ w_z^* & n_2 e_{xz} & n_2 e_{yz} & w_4 \end{bmatrix}, \tag{2.39}$$

where $w_x = b_\perp e_{yz} - i\sum_j P_j e_{xj} k_j$, $w_y = b_\perp e_{xz} - i\sum_j P_j e_{yj} k_j$, $w_z = b_\perp e_{xy} - i\sum_j P_j e_{zj} k_j$, with $P_1 = P_2 = P_\perp$, $P_3 = P_\parallel$, $w_1 = a_\perp(e_{xx} + e_{yy}) + a_\parallel e_{zz}$. $w_2 = l_1 e_{xx} + m_1 e_{yy} + m_2 e_{zz}$, $w_3 = l_1 e_{yy} + m_1 e_{xx} + m_2 e_{zz}$, $w_4 = l_2 e_{zz} + m_3(e_{xx} + e_{yy})$.

The deformation potentials in (2.39) are given by $a_\perp = \langle S|\hat{D}_{xx}|S\rangle$, $a_\parallel = \langle S|\hat{D}_{zz}|S\rangle$, $b_\perp = 2\langle S|\hat{D}_{yz}|X\rangle$, $b_\parallel = 2\langle S|\hat{D}_{xy}|Z\rangle$, $l_1 = \langle X|\hat{D}_{xx}|X\rangle$, $l_2 = \langle Z|\hat{D}_{zz}|Z\rangle$, $m_1 = \langle X|\hat{D}_{yy}|X\rangle$, $m_2 = \langle X|\hat{D}_{zz}|X\rangle$, $m_3 = \langle Z|\hat{D}_{xx}|Z\rangle$, $n_1 = 2\langle X|\hat{D}_{xy}|Y\rangle$, $n_2 = 2\langle X|\hat{D}_{xz}|Z\rangle$.

The strain terms that couple the conduction and valence bands are sometimes neglected [144] which can be justified by the fact that they are much smaller than the corresponding terms in the kinetic part of the Hamiltonian (typically 2 orders of magnitude smaller as they contain e_{ij} terms that are of the order of $\lesssim 0.01$). One then obtains the following Hamiltonian in basis (2.25)

$$\hat{H}_s = \begin{bmatrix} w_1 & 0 & 0 & 0 \\ 0 & f & k^* & h^* \\ 0 & k & f & h \\ 0 & h & h^* & \lambda \end{bmatrix}, \tag{2.40}$$

with

$$\begin{aligned} \lambda &= D_1 e_{zz} + D_2 \left(e_{xx} + e_{yy}\right), \\ \theta &= D_3 e_{zz} + D_4 \left(e_{xx} + e_{yy}\right), \\ f &= \lambda + \theta, \\ k &= D_5 \left(e_{xx} - e_{yy} + 2ie_{xy}\right), \\ h &= D_6 \left(e_{xz} + ie_{yz}\right), \end{aligned} \tag{2.41}$$

where D_i $(i = 1, \ldots, 6)$ are the deformation potentials given as $D_1 = l_2$, $D_2 = m_3$, $D_3 = m_2 - l_2$, $D_4 = \frac{1}{2}(l_1 + m_1) - m_3$, $D_5 = \frac{1}{2}n_1$, and $D_6 = \frac{n_2}{\sqrt{2}}$.

2.3.3 Piezoelectric effect

The main effect of strain on the electronic structure is through the strain part of the Hamiltonian. However, the strain also induces piezoelectric polarisation which further modifies the potential. Its components in a crystal of arbitrary symmetry are given as

$$P_i = \sum_{k,l=1}^{3} \epsilon_{ikl} e_{kl}, \tag{2.42}$$

where ϵ_{ikl} are the piezoelectric constants of the material. In a crystal with zincblende symmetry, the only nonzero components of ϵ_{ikl} are

$$\epsilon_{123} = \epsilon_{132} = \epsilon_{213} = \epsilon_{231} = \epsilon_{312} = \epsilon_{321}, \tag{2.43}$$

and will be denoted as ϵ_{14}. In the crystal with wurtzite lattice, the piezoelectric polarisation components are related to strain tensor components by [42, 146]

$$\begin{aligned} P_1^{pz} &= 2\epsilon_{15}e_{13}, \\ P_2^{pz} &= 2\epsilon_{15}e_{23}, \\ P_3^{pz} &= \epsilon_{31}(e_{11}+e_{22})+\epsilon_{33}e_{33}, \end{aligned} \tag{2.44}$$

where ϵ_{ij} are the piezoelectric constants.

2.4 Application of $\boldsymbol{k}\cdot\boldsymbol{p}$ Hamiltonian to quantum dot heterostructures

The $\boldsymbol{k}\cdot\boldsymbol{p}$ Hamiltonians derived in Sec. 2.2 apply to bulk semiconductors only, when Bloch's theorem is valid. In heterostructures, the periodicity is broken and these Hamiltonians cannot be applied directly. The wavefunction of the electron is not periodic any longer, it is modulated by a slowly varying function, the so called *envelope function*.

A heuristic way of obtaining the Hamiltonian for quantum dot heterostructures is simply to replace the wave vectors $\boldsymbol{k}$ by the operators $\hat{\boldsymbol{p}}$ acting on the envelope functions. Since material parameters in the Hamiltonian are now position dependent and the operators of momentum and coordinate do not commute, an ambiguity arises about the proper choice of operator ordering. It is necessary to choose the ordering in such a way that the Hamiltonian remains hermitian, however this condition still does not give a unique choice. The discussion of Ref. [147] will be followed to show how one can systematically introduce the appropriate ordering of operators.

The envelope representation of the wavefunction of an electron is given by

$$\Psi(\boldsymbol{r}) = \sum_i \psi_i(\boldsymbol{r})u_i(\boldsymbol{r}), \tag{2.45}$$

where $u_i(\boldsymbol{r})$ form the complete orthonormal set of functions with periodicity of the Bravais lattice and $\psi_i(\boldsymbol{r})$ are slowly varying envelope functions. The most

common choice of the functions u_i are bulk Bloch functions at the Γ point. It has been pointed out in Ref. [147] that (2.45) is an exact representation of the wavefunction $\Psi(\boldsymbol{r})$ if the same u_i functions are used throughout the whole space (i.e. both in the dot and the surrounding matrix) and a condition is imposed on $\psi_i(\boldsymbol{r})$ that their plane wave expansion contains only the contribution from the first Brillouin zone. After the replacement of (2.45) in the Schrödinger equation and making an approximation that eliminates the non-local terms that appear in the derivation, one arrives at [147, 148]

$$-\frac{\hbar^2}{2m_0}\nabla^2\psi_m(\boldsymbol{r})+\sum_n\frac{-i\hbar}{m_0}\boldsymbol{p}_{mn}\cdot\nabla\psi_n(\boldsymbol{r})+\sum_n H_{mn}(\boldsymbol{r})\psi_n(\boldsymbol{r})=E\psi_m(\boldsymbol{r}). \quad (2.46)$$

The terms in the previous equation are given by

$$\boldsymbol{p}_{mn}=\frac{1}{\Omega}\int u_m(\boldsymbol{r})^*\hat{\boldsymbol{p}}u_n(\boldsymbol{r})\mathrm{d}^3\boldsymbol{r}, \quad (2.47)$$

where the integration goes over the volume of the crystal unit cell Ω, and $H_{mn}(\boldsymbol{r})$ is the term that, away from the interfaces, reduces to the bulk matrix elements of the Hamiltonian

$$H_{mn}=\frac{1}{\Omega}\int u_m(\boldsymbol{r})^*\hat{H}u_n(\boldsymbol{r})\mathrm{d}^3\boldsymbol{r}. \quad (2.48)$$

The next step in the derivation of the $\boldsymbol{k}\cdot\boldsymbol{p}$ Hamiltonian for quantum dot heterostructures is to select the bands that will be included as the main bands for forming the Hamiltonian (which will be labelled with indices α and β) and to add the influence of remote bands (which will be labelled with r). After applying Eq. (2.46) to a remote band r and neglecting the first term in it, as well as much smaller terms containing other remote bands, one gets

$$\psi_r=\frac{1}{E-H_{rr}}\sum_\beta\left(\frac{-i\hbar}{m_0}\boldsymbol{p}_{r\beta}\cdot\nabla\psi_\beta+H_{r\beta}\psi_\beta\right). \quad (2.49)$$

The replacement of (2.49) into (2.46) applied to state α leads to

$$\begin{aligned} -\frac{\hbar^2}{2m_0}\left[\nabla^2\psi_\alpha + \frac{2}{m_0}\sum_{\beta,r}\boldsymbol{p}_{\alpha r}\cdot\nabla\left(\frac{1}{E-H_{rr}}\boldsymbol{p}_{r\beta}\nabla\psi_\beta\right)\right] &+ \\ +\sum_\beta \frac{-i\hbar}{m_0}\boldsymbol{p}_{\alpha\beta}\nabla\psi_\beta + \sum_\beta\left(H_{\alpha\beta}+\sum_r H_{\alpha r}\frac{1}{E-H_{rr}}H_{r\beta}\right)\psi_\beta &+ \\ +\sum_\beta\left[\sum_r \frac{-i\hbar}{m_0}\boldsymbol{p}_{\alpha r}\cdot\nabla\left(\frac{1}{E-H_{rr}}H_{r\beta}\right)\right]\psi_\beta &+ \\ +\sum_\beta\sum_r \frac{-i\hbar}{m_0}\frac{1}{E-H_{rr}}\left(\boldsymbol{p}_{\alpha r}H_{r\beta}+H_{\alpha r}\boldsymbol{p}_{r\beta}\right)\nabla\psi_\beta &= E\psi_\alpha \end{aligned} \tag{2.50}$$

The first term in (2.50) gives rise to terms quadratic in k in the bulk Hamiltonian, the second and the fifth term are related to the terms that couple the conduction and valence band, while the third term represents the band edges of appropriate zones. The fourth term that does not have its bulk counterpart can be neglected as a first approximation. By comparing the terms in (2.50) with the expressions for parameters of the bulk band structure, one can express all of them in terms of the bulk parameters, obtaining the Hamiltonian for heterostructures with appropriate operator ordering, as will now be shown.

The term connecting $|S\rangle$ states in (2.50) is

$$-\frac{\hbar^2}{2m_0}\nabla^2 - \frac{\hbar^2}{2m_0}\sum_r \boldsymbol{p}_{Sr}\cdot\nabla\frac{2}{m_0}\frac{1}{E-H_{rr}}\boldsymbol{p}_{rS}\nabla. \tag{2.51}$$

After introducing the notation $\hat{\boldsymbol{k}} = -i\nabla$, one gets the rule for operator ordering in the $(1,1)$ element of the Hamiltonian block G_r (Eq. (2.18)) as

$$A'k_i^2 \to \hat{k}_i A'\hat{k}_i. \tag{2.52}$$

The same rule is also obtained for other diagonal elements of G_r. It has been suggested in Ref. [149] that the rule for $(1,2)$, $(1,3)$ and $(1,4)$ elements og G_r is

$$Pk_i \to P\hat{k}_i. \tag{2.53}$$

It is most difficult to derive the rule for elements that connect the states in the valence band, such as for example the $(2,3)$ element of G_r. These elements

come from the first term in (2.50). One has to identify the contributions from remote bands of different symmetry in order to express this term in terms of Luttinger parameters. The result, when the influence of Γ_4 remote bands is neglected reads [149, 150]

$$N' k_x k_y \rightarrow \hat{k}_y M \hat{k}_x + \hat{k}_x \left(N' - M\right) \hat{k}_y. \tag{2.54}$$

Equations (2.52)–(2.54) give a systematically derived set of rules for operator ordering.

Many of the existing quantum dot electronic structure calculations [126, 127, 129, 131, 139] use heuristic, symmetrical arrangement of operators

$$\begin{aligned} f(\boldsymbol{r}) k_i k_j &\rightarrow \frac{1}{2}\left(\hat{k}_i f(\boldsymbol{r}) \hat{k}_j + \hat{k}_j f(\boldsymbol{r}) \hat{k}_i\right), \\ f(\boldsymbol{r}) k_i &\rightarrow \frac{1}{2}\left(\hat{k}_i f(\boldsymbol{r}) + f(\boldsymbol{r}) \hat{k}_i\right). \end{aligned} \tag{2.55}$$

It has been pointed out that such ordering of operators can lead to unphysical solutions in some circumstances [151]. On the other hand, the rules (2.52)–(2.54) have been derived for unstrained heterostructures in the absence of external static or time varying electromagnetic fields. A different set of rules has to be derived if one wants to include each of these effects, as well. This has been done only recently for the case of external magnetic fields [152]. Recently, it has been also argued that the existing derivations of envelope function theories (such as for example the one in Ref. [147]) do not take into account the perturbative corrections up to the same order, which lead to the development of a new, more systematic, envelope function theory for the case of unstrained structures [153].

The development of envelope function theories is therefore still an active area of research with questions that remain to be answered. The main interest of this work was, however, to predict the physical characteristics of intraband quantum dot optoelectronic devices, where it is necessary to include the effects of strain and external electromagnetic fields on the one hand, but where due to a lack of structural information about quantum dot characteristics and nonuniformity of quantum dot ensembles, a high level of precision is not essential.

Therefore, for the sake of consistency, throughout this work, the conventional but heuristic, symmetrical arrangement of operators as in (2.55) was used.

2.5 The influence of electromagnetic fields

2.5.1 Interaction with external electromagnetic radiation

It is essential for any theoretical description of optoelectronic devices to have an appropriate treatment of interaction of the active region of the device with electromagnetic radiation. Let the radiation be described classically by the magnetic vector potential $\boldsymbol{A}$ in the Coulomb gauge [154]. The microscopic Hamiltonian of interaction of electrons with electromagnetic radiation is obtained by substitution in the Hamiltonian [154, 155]

$$\hat{\boldsymbol{p}} \rightarrow \hat{\boldsymbol{p}} + |e|\boldsymbol{A}, \tag{2.56}$$

leading to a Hamiltonian of interaction

$$\hat{H}' = \frac{(\hat{\boldsymbol{p}} + |e|\boldsymbol{A})^2}{2m_0} - \frac{\hat{\boldsymbol{p}}^2}{2m_0}. \tag{2.57}$$

Throughout this work, the main interest will be in the linear response to external electromagnetic field, therefore the terms quadratic in $\boldsymbol{A}$ will be neglected. The wavelengths of interest will be those in the mid-infrared region of the spectrum, when the wavelength of the radiation is much larger than the size of the quantum dot. Therefore, in a certain moment of time, the dot effectively sees a constant electromagnetic field, and consequently the spatial dependence of $\boldsymbol{A}$ can be neglected (the dipole approximation). Within these approximations, the Hamiltonian of interaction reduces to

$$\hat{H}' = \frac{|e|}{m_0}\hat{\boldsymbol{p}} \cdot \boldsymbol{A}. \tag{2.58}$$

According to Fermi's Golden rule, the transition rate from an initial state $|i\rangle$ to a final state $|f\rangle$ due to the interaction with electromagnetic radiation of

angular frequency ω is given by

$$W_{if} = \frac{2\pi}{\hbar} \left| \left\langle i \left| \hat{H}' \right| f \right\rangle \right|^2 \delta \left(E_f - E_i \mp \hbar\omega \right), \tag{2.59}$$

where the '–' sign corresponds to absorption and '+' to emission, and E_f and E_i are the energies of the final and initial state, respectively.

Since $\boldsymbol{A}$ does not depend on the coordinate, one can first consider only the momentum operator in evaluation of the matrix elements between states. The matrix element of the momentum operator between two states i and f whose envelope function representations are given as

$$\begin{aligned} \Psi^{(i)}(\boldsymbol{r}) &= \sum_n \psi_n^{(i)}(\boldsymbol{r}) u_n(\boldsymbol{r}), \\ \Psi^{(f)}(\boldsymbol{r}) &= \sum_m \psi_m^{(f)}(\boldsymbol{r}) u_m(\boldsymbol{r}), \end{aligned} \tag{2.60}$$

is then given by

$$\mathcal{P}_{if} = \int \mathrm{d}^3\boldsymbol{r} \Psi^{(i)*}(\boldsymbol{r}) \hat{\boldsymbol{p}} \Psi^{(f)}(\boldsymbol{r}), \tag{2.61}$$

leading to

$$\mathcal{P}_{if} = \sum_{mn} \int \mathrm{d}^3\boldsymbol{r} \psi_n^{(i)*} u_n^* \left[u_m \hat{\boldsymbol{p}} \psi_m^{(f)} + \psi_m^{(f)} \hat{\boldsymbol{p}} u_m \right]. \tag{2.62}$$

The slowly varying envelope functions $F(\boldsymbol{r})$ feel only the average value over the unit cell of Bloch functions that vary rapidly, which can mathematically be expressed as

$$\int \mathrm{d}^3\boldsymbol{r} F(\boldsymbol{r}) u(\boldsymbol{r}) = \int \mathrm{d}^3\boldsymbol{r} F(\boldsymbol{r}) \langle u(\boldsymbol{r}) \rangle, \tag{2.63}$$

where $\langle u(\boldsymbol{r}) \rangle$ is the average value over unit cell of a rapidly varying function. After exploiting this relation, and using the condition of orthonormality of the Bloch functions, as well as Eq. (2.47), one arrives at

$$\mathcal{P}_{if} = \sum_{mn} \int \mathrm{d}^3\boldsymbol{r} \psi_n^{(i)*} \left(\delta_{nm} \hbar \hat{\boldsymbol{k}} + \boldsymbol{p}_{nm} \right) \psi_m^{(f)}, \tag{2.64}$$

with $\hat{\boldsymbol{k}} = \hat{\boldsymbol{p}}/\hbar$. Comparing the expression in brackets in (2.64) with the $\boldsymbol{k} \cdot \boldsymbol{p}$ Hamiltonian h given in Eq. (2.10), one gets

$$\mathcal{P}_{if} = \frac{m_0}{\hbar} \sum_{mn} \int \mathrm{d}^3\boldsymbol{r} \psi_n^{(i)*} \left(\frac{\partial h}{\partial \boldsymbol{k}} \right)_{nm} \psi_m^{(f)}, \tag{2.65}$$

or symbolically

$$\mathcal{P}_{if} = \frac{m_0}{\hbar}\langle i|\frac{\partial h}{\partial \boldsymbol{k}}|f\rangle. \tag{2.66}$$

Since this work will address the response of quantum dot ensembles, present in realistic devices, the linewidth of the transition is entirely determined by the nonuniformity in the sizes of the quantum dots in an ensemble. These linewidths are of the order of at least several meV and are much larger than the inherent homogeneous linewidths of a transition in a single dot. Therefore, the recipe is adopted to treat the inhomogeneous broadening due to size inhomogeneity of the quantum dot ensemble by replacing the delta function with a Gaussian, i.e.

$$\delta(x) \to g(x, 2\sigma) = \frac{1}{\sigma\sqrt{2\pi}} \exp\left(-\frac{x^2}{2\sigma^2}\right). \tag{2.67}$$

The optical cross section of the $i \to f$ transition is the quantity that normalises the transition probability to the flux of incident radiation and is therefore given by $\sigma_{if} = W_{if}/\Phi$, where Φ is the optical pump flux. Using the relation between the flux and the vector potential one gets

$$\sigma_{if}^{\boldsymbol{\varepsilon}}(\omega) = \frac{2\pi}{\overline{n}\varepsilon_0 c\omega} \left|\mathcal{M}_{if}^{\boldsymbol{\varepsilon}}\right|^2 g(E_f - E_i \mp \hbar\omega, 2\sigma), \tag{2.68}$$

where $\overline{n}$ is the refraction index. $\mathcal{M}_{if}^{\boldsymbol{\varepsilon}} = \left\langle i \left| \hat{H}' \right| f \right\rangle / A$ is the matrix element which depends only on the direction $\boldsymbol{\varepsilon}$ of light polarisation and not on the amplitude of A, related to $\mathcal{P}_{if}$ by

$$\mathcal{M}_{if}^{\boldsymbol{\varepsilon}} = \frac{|e|}{m_0}\mathcal{P}_{if} \cdot \boldsymbol{\varepsilon}. \tag{2.69}$$

2.5.2 Spontaneous emission of photons

The formalism describing the interaction of electrons with a classical external electromagnetic field, presented in Sec. 2.5.1 can reliably determine the transition rates due to the processes of absorption and stimulated emission. On the other hand, it is known [154] that the process of spontaneous emission can be described only if the electromagnetic field is quantised.

The formula for the transition rate from the initial state i to the final state f due to the spontaneous emission of photons will be derived in this section. The operator of the vector potential of quantum electromagnetic field is given by

$$\hat{\boldsymbol{A}} = i \sum_{\boldsymbol{k},\sigma} \sqrt{\frac{\hbar}{2\varepsilon\omega V}} \left(\hat{b}_{\boldsymbol{k},\sigma} e^{i\boldsymbol{k}\cdot\boldsymbol{r}} - \hat{b}^{+}_{\boldsymbol{k},\sigma} e^{-i\boldsymbol{k}\cdot\boldsymbol{r}} \right) \cdot \boldsymbol{\varepsilon}_{\sigma}, \tag{2.70}$$

where $\hat{b}_{\boldsymbol{k},\sigma}$ and $\hat{b}^{+}_{\boldsymbol{k},\sigma}$ are the annihilation and creation operators of a photon mode, ε is the dielectric constant at angular frequency ω, V the volume of the system, $\boldsymbol{k}$ the wave vector, σ the polarisation and $\boldsymbol{\varepsilon}_{\sigma}$ is the unit vector in the direction of polarisation. The Hamiltonian of the electron-photon interaction is given by

$$\hat{H}' = \hat{H}_k(\boldsymbol{k} + \frac{|e|}{\hbar}\hat{\boldsymbol{A}}) - \hat{H}_k(\boldsymbol{k}) \tag{2.71}$$

and the transition rate from the state $|i;0\rangle$ with no photons to the states $|f;1_{\boldsymbol{q},\sigma}\rangle$ with an electron in the state f and one photon in any of the states $(\boldsymbol{q},\sigma)$ is equal to

$$W_{if} = \frac{2\pi}{\hbar} \sum_{\boldsymbol{q},\sigma} \left| \langle i;0|\hat{H}'|f;1_{\boldsymbol{q},\sigma}\rangle \right|^2 \delta(E_i - E_f - \hbar\omega). \tag{2.72}$$

In the dipole approximation the exponential terms in (2.70) are equal to 1, the terms quadratic in $\hat{\boldsymbol{A}}$ are neglected and after putting (2.70) and (2.71) into (2.72) one gets

$$W_{if} = \frac{2\pi}{\hbar} \sum_{\boldsymbol{q},\sigma} \frac{\hbar}{2\varepsilon\omega V} |\mathcal{M}_{\boldsymbol{\varepsilon}_{\sigma}}|^2 \delta(E_i - E_f - \hbar\omega), \tag{2.73}$$

$$W_{if} = \frac{V}{(2\pi)^3} \int \mathrm{d}^3\boldsymbol{q} \frac{\pi}{\varepsilon\omega V} \delta(E_i - E_f - \hbar\omega) \sum_{\sigma} |\mathcal{M}_{\boldsymbol{\varepsilon}_{\sigma}}|^2. \tag{2.74}$$

One then has

$$W_{if} = \frac{V}{(2\pi)^3} \frac{2}{3} \int \mathrm{d}^3\boldsymbol{q} \frac{\pi}{\varepsilon\omega V} \delta(E_i - E_f - \hbar\omega) \left(|\mathcal{M}_{\boldsymbol{e}_x}|^2 + |\mathcal{M}_{\boldsymbol{e}_y}|^2 + |\mathcal{M}_{\boldsymbol{e}_z}|^2 \right),$$

$$W_{if} = \frac{1}{(2\pi)^3} \frac{2}{3} 4\pi \left(|\mathcal{M}_{\boldsymbol{e}_x}|^2 + |\mathcal{M}_{\boldsymbol{e}_y}|^2 + |\mathcal{M}_{\boldsymbol{e}_z}|^2 \right) \int q^2 \mathrm{d}q \frac{\pi}{\varepsilon\omega} \delta(E_i - E_f - \hbar\omega),$$

and using $\omega = cq/\overline{n}$ the final result yields

$$W_{if} = \frac{(E_i - E_f)\overline{n}}{3\hbar^2\varepsilon_0\pi c^3} \left(|\mathcal{M}_{\boldsymbol{e}_x}|^2 + |\mathcal{M}_{\boldsymbol{e}_y}|^2 + |\mathcal{M}_{\boldsymbol{e}_z}|^2 \right). \tag{2.75}$$

2.5.3 Static electric and magnetic fields

Realistic quantum dot optoelectronic devices operate under external bias and therefore quantum dot energy levels and wavefunctions are modified by the presence of an electric field. On a microscopic level, the external electric field is added simply by adding its corresponding potential $V_F(\boldsymbol{r}) = |e|\boldsymbol{F}\cdot\boldsymbol{r}$. One can easily verify that the things remain simple in the envelope representation as well, and that electric field can be included in $\boldsymbol{k}\cdot\boldsymbol{p}$ Hamiltonian by adding $V_F(\boldsymbol{r})$ to all diagonal elements of the Hamiltonian.

The effect of a magnetic field on quantum dot electronic structure is not as dramatic as in the case of quantum wells or wires where the spectrum is changed from a continuous one to a discrete set of so called Landau levels. In quantum dots, where the spectrum is discrete in the absence of magnetic field already, the magnetic field only splits otherwise degenerate states of opposite spin and shifts the energy levels. This is the reason why its influence on quantum dot optoelectronic devices has not been experimentally investigated much and therefore not much emphasis has been put on it in this work either. Nevertheless, for completeness the mathematical description of the effect of a magnetic field within the envelope function theory will be given here. There is certainly some prospect in using a magnetic field for fine tuning of the operating wavelength for example, although it is possible that the fields may be too large.

A magnetic field is added to the $\boldsymbol{k}\cdot\boldsymbol{p}$ Hamiltonian by making the minimal gauge substitution (2.56) and explicitly adding the Zeeman term. In the case of the axial magnetic field $\boldsymbol{B} = B\boldsymbol{e}_z$ (assuming the symmetric gauge for the vector potential $\boldsymbol{A} = \frac{1}{2}B\,(-y, x, 0)$) the nonzero elements of the Zeeman term

of the 8-band Hamiltonian in basis (2.19) are given by:

$$\begin{aligned}
\hat{H}_Z^{11} &= -\hat{H}_Z^{22} = -\frac{|e|\hbar}{2m_0}B, \\
\hat{H}_Z^{33} &= -\hat{H}_Z^{66} = -\kappa\frac{|e|\hbar}{2m_0}B, \\
\hat{H}_Z^{44} &= -\hat{H}_Z^{55} = -3\kappa\frac{|e|\hbar}{2m_0}B, \\
\hat{H}_Z^{77} &= -\hat{H}_Z^{88} = \left(\kappa+\frac{1}{2}\right)\frac{|e|\hbar}{m_0}B, \\
\hat{H}_Z^{83} &= \hat{H}_Z^{38} = -\frac{1}{\sqrt{2}}\left(\kappa+1\right)\frac{|e|\hbar}{m_0}B, \\
\hat{H}_Z^{76} &= \hat{H}_Z^{67} = -\frac{1}{\sqrt{2}}\left(\kappa+1\right)\frac{|e|\hbar}{m_0}B,
\end{aligned} \tag{2.76}$$

where κ is the modified Luttinger parameter related to the Luttinger parameter κ^L by

$$\kappa = \kappa^L - \frac{1}{2}\frac{E_P}{3E_g+\Delta}. \tag{2.77}$$

The matrix elements of the 8-band $\boldsymbol{k}\cdot\boldsymbol{p}$ Hamiltonian in the case of a magnetic field of arbitrary direction are given in [156, 157] for the bulk case and the Hamiltonian with proper ordering of operators for the case of heterostructures has recently been presented in Ref. [152] and applied to quantum dots.

2.6 Numerical methods

2.6.1 Methods for solving the $\boldsymbol{k}\cdot\boldsymbol{p}$ Hamiltonian

From the numerical point of view, the eigenvalue problem of the envelope function n-band Hamiltonian can be viewed as a set of n coupled partial differential equations for functions of three spatial variables. It is therefore a challenging numerical task to solve it. There are two overall strategies that one can accordingly employ:

- **Finite-difference method (FDM)**. Within the finite-difference method, the wavefunction is represented by points on a discrete three dimensional grid of size $N_xN_yN_z$, and partial derivatives are then re-

placed with finite differences. One therefore obtains the eigenvalue problem of a very large matrix, its dimension being given by $nN_xN_yN_z$. If $N_x \sim N_y \sim N_z \sim 50$ grid points are taken in each direction, the resulting matrix is of the order of $\sim 10^6$ already. Fortunately, the matrix is sparse, and specialised algorithms for the diagonalisation of sparse matrices can be employed [139]. FDM has therefore indeed been employed in several studies of quantum dot electronic structure using the multiband envelope function Hamiltonian [126, 128, 129, 158].

- **Wavefunction expansion methods (WEM)**. The idea of the wavefunction expansion method [159] is to expand the envelope functions as a linear combination of a certain set of orthonormal basis functions

$$\psi_j(\boldsymbol{r}) = \sum_l A_{jl} a_l(\boldsymbol{r}), \tag{2.78}$$

and find the coefficients A_{jn} in the expansion. After making the substitution of (2.78) into the Hamiltonian eigenvalue problem

$$\sum_j \hat{H}_{ij}\psi_j(\boldsymbol{r}) = E\psi_i(\boldsymbol{r}), \tag{2.79}$$

one gets

$$\sum_{jn} \mathcal{H}_{ij}(m,n) A_{jn} = EA_{im}, \tag{2.80}$$

where

$$\mathcal{H}_{ij}(m,n) = \int \mathrm{d}^3\boldsymbol{r}\, a_m(\boldsymbol{r})^* \hat{H}_{ij} a_n(\boldsymbol{r}). \tag{2.81}$$

Therefore, the eigenvalue problem (2.80) has to be solved. The matrix $\mathcal{H}$ is dense, but with a smart choice of basis functions, one can obtain the correct eigenvalues by employing a relatively small basis set (of the order of 10–20 basis functions per dimension). Present day personal computers can solve eigenproblems of dense matrices of the size ~ 10000 and parallel supercomputers even larger matrices ~ 50000, which makes this approach feasible, albeit still relatively computationally demanding. Several different choices of orthonormal basis functions have been used

in the literature to calculate the electronic properties of quantum dots. These include plane waves [131, 144, 160–162], the eigenfunctions of the particle in a cylinder with infinite walls (referred to as cylindrical basis in what follows) [145,163], and eigenfunctions of a harmonic oscillator [164].

While a claim is not made that the WEMs are better than FDMs, a few of their advantages will be mentioned here, which have led to them being made the method of choice for this work. It is not easy to give a fair comparison of two different sets of methods employed and say which one is better, i.e. faster. The time for diagonalising sparse matrices in FDM scales approximately as $\sim N$, and for dense matrices as $\sim N^3$. Therefore, if an extremely high precision solution of the eigenvalue problem were necessary, than the linear scaling offered by FDM would be more favourable. However, for the precision of eigenenergies of several meV, which is entirely sufficient for any analysis of optoelectronic devices, the number of necessary basis functions in WEM is small, making the calculations fully feasible. Another good side of WEM is that after the wavefunctions are calculated, other relevant physical quantities, such as for example optical matrix elements and carrier lifetimes, can be expressed from the coefficients in the expansion, rather than by performing three dimensional numerical integration.

Another important issue of WEM is that the elements of the Hamiltonian matrix $\mathcal{H}$ need to be calculated efficiently. This is fullfilled in the case of plane waves where the expressions for $\mathcal{H}_{ij}(m, n)$ are fully analytical, since differential operators act on plane waves as simple multiplication. In the case of a cylindrical basis, the expressions are not fully analytical, but these can be calculated efficiently as well. Finally, the methods developed in this work and presented in Chapters 3 and 4 enable additional significant speed-up of plane wave calculations in quantum dots with symmetric pyramidal shape, based on block diagonalisation of the matrix $\mathcal{H}$. Symmetry can also be exploited in dots with cylindrical symmetry and this fact has been implemented in the calculation in the cylindrical basis in Chapter 6. More technical details on

WEM methods will be given in sections where they are applied to particular problems.

2.6.2 Methods for finding the strain distribution

In Secs. 2.3.1 and 2.3.2, it has been described how one can include strain in the envelope function Hamiltonian. The aim of this section will be to describe how strain can actually be calculated in quantum dots. There are two overall groups of models [9] that are used to calculate the strain distribution in nanostructures

- **Atomistic models**. In atomistic models, each atom in a quantum dot is considered and the total elastic energy of the structure is expressed as a sum of interaction energies among atoms represented by a sum of classical $n-$ body interaction potentials

$$W = \sum_{i,j} V^{(2)}(\boldsymbol{r}_i - \boldsymbol{r}_j) + \sum_{i,j,k} V^{(3)}(\boldsymbol{r}_i - \boldsymbol{r}_j, \boldsymbol{r}_i - \boldsymbol{r}_k) + \cdots \tag{2.82}$$

  The energy can then be expressed in terms of the displacements of each individual atom from its equilibrium position and from its minimisation one finds new, relaxed, positions of atoms. Several different models of interaction potentials are available in the literature. In atomistic calculations of strain in quantum dots [116, 117, 126, 128, 139, 160, 165], the valence-force field (VFF) model of Keating [166] and Martin [167] is mostly used. The interaction of an atom with its nearest neighbours only are considered in the VFF model.

- **Continuum mechanical (CM) models**. In this group of models, the quantum dot structure is modelled by an elastic classical continuum medium whose elastic energy is given by

$$W = \frac{1}{2} \sum_{ijkl} \int \mathrm{d}^3\boldsymbol{r} \lambda_{ijkl} e_{ij} e_{kl}, \tag{2.83}$$

  where λ_{ijkl} is the elastic tensor relating the stress and strain tensor by Hooke's law

$$\sigma_{ij} = \sum_{kl} \lambda_{ijkl} e_{kl}. \tag{2.84}$$

There have been several comparisons in the literature between the VFF and CM models [126, 165, 168]. While certain differences have been obtained, the results of the two models give overall agreement. From the computational point of view, the VFF model is more demanding as the displacement of each atom is considered, in contrast to CM models where a grid of the size of lattice constant or even larger may be used, leading to a smaller number of variables to be handled. The minimisation of the VFF functional (2.82) leads to a system of nonlinear equations for atom displacements, while in the CM model where the strain functional (2.83) depends quadratically on displacements, a much less computationally demanding system of linear equations is obtained. Moreover, in several important cases, there are analytical or nearly analytical solutions of the CM model [169, 170]. On the other hand, from the fundamental point of view, the advantage of the VFF model is that it captures the atomistic symmetry of the crystal, while CM models have a higher symmetry group. Nevertheless, throughout this work, this weakness of the CM model will be exploited as a strength from the computational point of view, allowing the possibility to exploit the symmetry in the calculation, as will be shown in Chapters 3, 4, and 6. The CM model has therefore been adopted as a model of choice for this work, and therefore it will be presented in more detail in what follows.

The problem of finding the strain field of an inclusion in an infinite medium has been formulated and considered by Eshelby in 1957 [171] and it is therefore a classical problem that has found one of its important application in the calculation of strain in quantum dots. It will be shown here, following Ref. [9, 169], how analytical formulae for the Fourier transform of components of the strain tensor can be obtained in the case where the elastic constants of the dot and the surrounding matrix are the same.

Let the displacements u_i in the problem be defined with respect to the atomic sites of the undeformed matrix. The strain is then defined by Eq. (2.29) and related to stress via (2.84). The presence of the dot induces body forces

$\boldsymbol{f}$ that are related to stress via

$$\sum_k \frac{\partial \sigma_{jk}}{\partial x_k} + f_j = 0. \tag{2.85}$$

After the replacement of Hooke's law (2.84) and the expression for strain (2.29) into (2.85) one gets

$$\sum_{klm} \lambda_{jklm} \frac{\partial}{\partial x_k} \frac{\partial u_l}{\partial x_m} + f_j = 0. \tag{2.86}$$

Since the tensor e_{ij} is by the definition symmetric, one can assume that λ_{ijkl} is symmetric as well ($\lambda_{ijkl} = \lambda_{klij} = \lambda_{ijlk}$), since the contribution from its antisymmetric parts would give a vanishing contribution to stress. This fact, as well as the assumption that λ_{ijkl} is constant in space have been exploited to obtain (2.86). In order to find the displacement field in the medium a method of inclusions can be used [171]. The idea of this method is to find the response of the medium to a small point-like inclusion first, and then integrate the result over the volume of the dot to find the total displacements. Following this general idea, it is natural to introduce the Green's function

$$\sum_{klm} \lambda_{jklm} \frac{\partial}{\partial x_k} \frac{\partial G_{ln}(\boldsymbol{r} - \boldsymbol{r}')}{\partial x_m} + \delta_{jn} \delta(\boldsymbol{r} - \boldsymbol{r}') = 0, \tag{2.87}$$

representing the displacement in the direction l at point $\boldsymbol{r}$, due to a unit body force acting in the direction n at point $\boldsymbol{r}'$.

At this point the zincblende symmetry of the crystal will be assumed, and that the small inclusion of lattice constant a_{incl} is placed at point $\boldsymbol{r}'$, in medium with lattice constant a. In the crystals with zincblende lattice the elastic tensor is of the form

$$\lambda_{ijkl} = C_{12}\delta_{ij}\delta_{kl} + C_{44}(\delta_{ik}\delta_{jl} + \delta_{il}\delta_{jk}) + C_{an}\sum_{p=1}^{3} \delta_{ip}\delta_{jp}\delta_{kp}\delta_{lp}, \tag{2.88}$$

where C_{12}, C_{44} and $C_{an} = C_{11} - C_{12} - 2C_{44}$ are the elastic constants.

The inclusion then creates the strain $e_{ij} = e_0\delta_{ij}\delta(\boldsymbol{r}')$ (where $e_0 = -\frac{a - a_{incl}}{a}$), the stress $\sigma_{ij} = \lambda_{ijkl}e_{ij} = e_0(C_{11} + 2C_{12})\delta_{ij}\delta(\boldsymbol{r}')$, and consequently it acts as a body force

$$f_j(\boldsymbol{r}') = -\sum_k p_{jk} \frac{\partial \delta(\boldsymbol{r}')}{\partial x'_k}, \tag{2.89}$$

where $p_{jk} = e_0(C_{11} + 2C_{12})\delta_{jk}$. The displacement of the medium to this point inclusion is then

$$w_i(\boldsymbol{r}) = \sum_{jk} \int \mathrm{d}^3\boldsymbol{r}' G_{ij}(\boldsymbol{r} - \boldsymbol{r}') \left(p_{jk} \frac{\partial \delta(\boldsymbol{r}')}{\partial x'_k} \right) = -\sum_{jk} p_{jk} \frac{\partial G_{ij}(\boldsymbol{r})}{\partial x_k}, \quad (2.90)$$

and the displacement due to the presence of a quantum dot is consequently found by treating the dot as a superposition of small inclusions

$$u_i(\boldsymbol{r}) = \int \mathrm{d}^3\boldsymbol{r}' \chi_{\mathrm{QD}}(\boldsymbol{r}')\, w_i(\boldsymbol{r} - \boldsymbol{r}'), \quad (2.91)$$

where $\chi_{\mathrm{QD}}(\boldsymbol{r})$ is the quantum dot characteristic function equal to 1 inside the dot and 0 outside the dot. Since the displacements were defined with respect to the undeformed matrix, this has to be accounted for, and the expressions for strain tensor components that enter the $\boldsymbol{k}\cdot\boldsymbol{p}$ Hamiltonian are given by [172]

$$e_{ij} = \frac{1}{2}\left(\frac{\partial u_i}{\partial x_j} + \frac{\partial u_j}{\partial x_i} \right) - e_0 \chi_{\mathrm{QD}}(\boldsymbol{r})\, \delta_{ij}. \quad (2.92)$$

Equations (2.87), (2.90), (2.91), and (2.92) form the system of equations from which the strain distribution can be found. Transforming these equations into Fourier space, they reduce to a system of ordinary algebraic equations. Their solution for the strain distribution yields

$$\begin{aligned} e_{ij}(\boldsymbol{q}) \;=\; & \tfrac{a_M - a_{QD}}{a_{QD}} \chi_{QD}(\boldsymbol{q}) \;\; \left\{ \delta_{ij} - \frac{1}{2} \frac{(C_{11} + 2C_{12}) q_i q_j / q^2}{1 + (C_{12} + C_{44}) \sum_{p=1}^{3} \frac{q_p^2}{C_{44} q^2 + C_{an} q_p^2}} \times \right. \\ & \left. \times \left[\frac{1}{C_{44} + C_{an} q_i^2 / q^2} + \frac{1}{C_{44} + C_{an} q_j^2 / q^2} \right] \right\}, \end{aligned} \quad (2.93)$$

where a_M and a_{QD} are the lattice constants of the matrix and the dot material, where the following definition for the Fourier transform was used

$$F(\boldsymbol{q}) = \frac{1}{(2\pi)^3} \int \mathrm{d}^3\boldsymbol{r} \exp(-i\boldsymbol{q}\cdot\boldsymbol{r})\, F(\boldsymbol{r}). \quad (2.94)$$

As already mentioned, equation (2.93) is derived under the assumption of the elastic constants of the dot and the matrix both equal to the elastic constants of the matrix. The elastic constants of a material in a state of high strain may differ from those of the relaxed material and there is no obvious choice

for the values of the elastic constants. However, there are arguments [9, 169] that choosing the elastic constants of the barrier material for all the materials in the system is appropriate.

Along similar lines, one can also find the Fourier transform of the strain distribution in quantum dots made of crystals with wurtzite symmetry. The formula analogous to (2.93) for the case of crystals with wurtzite symmetry is derived in Ref. [144].

The approach described where an analytical formula for the strain distribution is obtained is highly attractive when combined with plane wave calculations of the electronic structure, where Fourier transforms of strain tensor components are required [131, 144] and the obtained formulae will therefore be used in Chapters 3 and 4.

On the other hand, if some other method for the electronic structure is used where the values of strain in real space are necessary, it may be more efficient to calculate the strain directly in real space, rather than to transform it from Fourier space to real space. Furthermore, if the dot is not embedded in an infinite medium and the effect of boundaries is important, then the derived formulae are not valid and real space approach might be more efficient. The finite element method [173] can be used for that purpose. The main approach in the finite element method is to minimise the total elastic energy given by [172]

$$W = \frac{1}{2}\int \mathrm{d}V \sum_{ijkl} \lambda_{ijkl} \left[e_{ij}(\boldsymbol{r}) - e_{ij}^{(0)}(\boldsymbol{r})\right] \left[e_{kl}(\boldsymbol{r}) - e_{kl}^{(0)}(\boldsymbol{r})\right], \tag{2.95}$$

where $e_{ij}(\boldsymbol{r})$ are the elastic strain tensor components, and $e_{ij}^{(0)}(\boldsymbol{r})$ the local intrinsic strain induced by the changes in the lattice constant

$$e_{ij}^{(0)}(\boldsymbol{r}) = \frac{a(\boldsymbol{r}) - a}{a}\delta_{ij}, \tag{2.96}$$

where $a(\boldsymbol{r})$ is the unstrained lattice constant at $\boldsymbol{r}$ and a the substrate lattice constant. The continuum space is then discretised on a nonuniform rectangular grid of the size $N_x \times N_y \times N_z$ and the components of the displacement in each point of space are expressed in terms of the displacements u_l^i ($l \in \{x, y, z\}$,

$i \in \{1, 2, \ldots, 8\}$) in the 8 neighbouring nodes of the grid, where first order Lagrange interpolation is used. i.e.

$$u_l(x, y, z) = \frac{1}{8} \sum_{i=1}^{8} u_l^i \left(1 + c_{xi}\eta_x\right) \left(1 + c_{yi}\eta_y\right) \left(1 + c_{zi}\eta_z\right), \tag{2.97}$$

where $\eta_x = 2(x - \overline{x})/d_x$, $\eta_y = 2(y - \overline{y})/d_y$, $\eta_z = 2(z - \overline{z})/d_z$, $(c_{x1}, c_{y1}, c_{z1}) = (1, -1, -1)$, $(c_{x2}, c_{y2}, c_{z2}) = (1, 1, -1)$, $(c_{x3}, c_{y3}, c_{z3}) = (-1, 1, -1)$, $(c_{x4}, c_{y4}, c_{z4}) = (-1, -1, -1)$, $(c_{x5}, c_{y5}, c_{z5}) = (1, -1, 1)$, $(c_{x6}, c_{y6}, c_{z6}) = (1, 1, 1)$, $(c_{x7}, c_{y7}, c_{z7}) = (-1, 1, 1)$, $(c_{x8}, c_{y8}, c_{z8}) = (-1, -1, 1)$, while $\overline{x}$, $\overline{y}$ and $\overline{z}$ are the coordinates of the centre of the rectangular box and d_x, d_y, d_z its dimensions (see Fig. 2.1). Consequently, the elastic energy of the system W is a quadratic functional of the $3N_xN_yN_z$ displacements at the nodes of the grid. Its minimisation therefore leads to a sparse system of linear equations for the displacements at the nodes, which is solved using the conjugate gradient method [174].

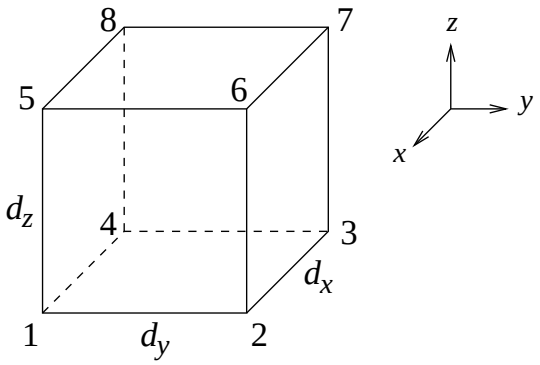

Figure 2.1: A rectangular finite element, d_x, d_y, d_z are its dimensions and $1 - 8$ its nodes.

2.7 Electron – phonon interaction and polarons

The theory presented in this chapter so far covered only the stationary electronic structure of quantum dots when atoms are in their equilibrium positions.

However, at finite temperatures atoms can vibrate around their equilibrium positions. These quantised lattice vibrations are called phonons. Phonons create additional potential that perturbs otherwise stationary electronic states and causes transitions among them. Depending on the type of crystal, there are several different types of electron – phonon interaction [175]

- **Deformation potential coupling to acoustic phonons**. Lattice deformations caused by vibration of atoms create an additional potential, in a similar way the strain does. It turns out that out of three acoustic phonon branches only the longitudinal phonons effectively create this potential.

- **Polar coupling to optical phonons**. This type of interaction is present in polar crystals only. The charged ions in a unit cell oscillate in opposite directions creating an effective electric field that electrons interact with. Again, only longitudinal optical phonons create this potential.

- **Deformation potential coupling to optical phonons**. This type of interaction is based on the same physical mechanism as coupling to acoustic phonons. In polar crystals, it is weaker than polar coupling to optical phonons and is therefore usually neglected.

- **Piezoelectric coupling to acoustic phonons**. The origin of this interaction is the creation of an effective field due to the piezoelectric effect, which is present in crystals lacking inversion symmetry. The matrix element for this interaction scales with phonon wave vector as $\sim 1/\sqrt{q}$, in contrast to deformation potential interaction where it scales as $\sim \sqrt{q}$. Therefore, for sufficiently large energy spacing, typically present in quantum nanostructures, deformation potential coupling to acoustic phonons is much stronger than piezoelectric coupling.

Throughout this work, only polar coupling to optical phonons and deformation potential coupling to acoustic phonons will therefore be considered. As it

is thought that the influence of phonon confinement is not so important in AlGaAs/GaAs and InGaAs/GaAs nanostructures [176, 177], bulk LO phonon modes are assumed.

The Frölich interaction Hamiltonian describing polar coupling to optical phonons is then given by [42, 175]

$$\hat{H}_{e-ph} = \sum_{ij\boldsymbol{q}} M_{ij}(\boldsymbol{q}) \hat{a}_i^+ \hat{a}_j \left(\hat{b}_{\boldsymbol{q}} + \hat{b}_{-\boldsymbol{q}}^+ \right), \tag{2.98}$$

where $\hat{b}_{\boldsymbol{q}}$ and $\hat{b}_{\boldsymbol{q}}^+$ are phonon annihilation and creation operators, $\hat{a}$ and $\hat{a}^+$ the same operators for electrons, $M_{ij}(\boldsymbol{q}) = \alpha(\boldsymbol{q}) F_{ij}(\boldsymbol{q})$,

$$\alpha(\boldsymbol{q}) = \frac{1}{q} \sqrt{\frac{e^2 \hbar \omega_{\mathrm{LO}}}{2V} \left(\frac{1}{\varepsilon_\infty} - \frac{1}{\varepsilon_{st}} \right)}, \tag{2.99}$$

and

$$F_{if}(\boldsymbol{q}) = \sum_{j=1}^{8} \int_V \mathrm{d}^3 \boldsymbol{r} \psi_j^f(\boldsymbol{r})^* e^{i\boldsymbol{q}\cdot\boldsymbol{r}} \psi_j^i(\boldsymbol{r}) \tag{2.100}$$

is the electron – phonon interaction form factor, and ε_∞ and ε_{st} are high frequency and static dielectric constants, respectively. Optical phonons are nearly dispersionless and for simplicity, a constant LO phonon energy ω_{LO} is assumed.

The Hamiltonian of the deformation potential interaction with acoustic phonons is given by the same formula (2.98) except that in this case

$$\alpha(\boldsymbol{q}) = \sqrt{\frac{D_A^2 \hbar q}{2\rho v_s V}}, \tag{2.101}$$

where D_A is the acoustic deformation potential, ρ the material density and v_s the longitudinal sound velocity. To a very good approximation, a linear and isotropic acoustic phonon dispersion relation $\omega(\boldsymbol{q}) = v_s q$ can be assumed.

2.7.1 Carrier lifetime in quantum dots

Electron – LO phonon interaction

In order to calculate transition rates among different electronic states due to the interaction with LO phonons, it is tempting to apply Fermi's Golden rule,

which is a good approximation in quantum wells, for example [42]. However, its direct application to quantum dots leads to the result that transition rates are zero unless two levels are separated by one LO phonon energy exactly [91]. Such an approach treats the electron and phonon systems separately with their interaction being only a perturbation. It is currently known that electrons and phonons in quantum dots form coupled entities – polarons and that the polaron lifetime is determined by anharmonic decay of an LO phonon into two low energy phonons [94–98]. A full description of processes in quantum dots would therefore require considerations in Hilbert space containing both electronic and phononic degrees of freedom and the problem would most likely become intractable. Since the electronic charge carries current and the external radiation mostly interacts with electronic degrees of freedom, an approach that will keep track of electronic states only would be useful. Such a description is derived here following Ref. [95].

The transition rate from the initial state of the electron – phonon system $|\Psi_i; \{n_{\boldsymbol{q}}\}\rangle$ with an electron in the state i and $n_{\boldsymbol{q}}$ LO phonons with the wave vector $\boldsymbol{q}$ (where $\boldsymbol{q}$ takes all possible values of the phonon wave vector) to the final state $|\Psi_f; \{n_{\boldsymbol{q}} \pm \delta_{\boldsymbol{q},\boldsymbol{k}}\}\rangle$ with an electron in the state f and one more (less) phonon with the wave vector $\boldsymbol{k}$ will be derived here. It is expected to be a good approximation to the transition rate from electron state i to state f, providing the contribution to polaron states from the electron states is mainly due to one electron state. It should be also mentioned that the following derivation is strictly valid for a two level system only. Nevertheless, the transition rates obtained can be used as a reasonable approximation in a multilevel system, too.

Let $|\Psi_i; \{n_{\boldsymbol{q}}\}\rangle$ be the initial state of the electron – phonon system. The time dependence of the state of the system is given by

$$|\Psi(t)\rangle = a(t)e^{-iE_i t/\hbar}|\Psi_i; \{n_{\boldsymbol{q}}\}\rangle + \sum_{\boldsymbol{k}} b_{\boldsymbol{k}}(t)e^{-i(E_f \pm \hbar\omega_{LO})t/\hbar}|\Psi_f; \{n_{\boldsymbol{q}} \pm \delta_{\boldsymbol{q},\boldsymbol{k}}\}\rangle,$$

where $|\Psi_f; \{n_{\boldsymbol{q}} \pm \delta_{\boldsymbol{q},\boldsymbol{k}}\}\rangle$ represents the state of the system with an electron in the state f and one more (less) phonon with the wave vector $\boldsymbol{k}$ and E_i and E_f

are the energies of the states i and f, respectively. The initial conditions are $a(t=0)=1$, $b_{\boldsymbol{k}}(t=0)=0$. The coefficients $a(t)$ and $b_{\boldsymbol{k}}(t)$ can be found by solving the time-dependent Schrödinger equation

$$i\hbar\frac{\mathrm{d}|\Psi(t)\rangle}{\mathrm{d}t}=\hat{H}|\Psi(t)\rangle, \tag{2.102}$$

where $\hat{H}$ is the Hamiltonian of the system given by

$$\hat{H}=\hat{H}_e+\hat{H}_{ph}+\hat{H}_{e-ph}, \tag{2.103}$$

where $\hat{H}_e$ is the Hamiltonian of electrons,

$$\hat{H}_e=\sum_i \varepsilon_i \hat{a}_i^+\hat{a}_i, \tag{2.104}$$

where ε_i are energies of the electron states, $\hat{H}_{ph}$ is the Hamiltonian of phonons

$$\hat{H}_{ph}=\sum_{\boldsymbol{q}}\left(\hat{b}_{\boldsymbol{q}}^+\hat{b}_{\boldsymbol{q}}+\frac{1}{2}\right)\hbar\omega_{LO}, \tag{2.105}$$

$\hat{H}_{e-ph}$ is the Frölich Hamiltonian of the electron – phonon interaction (2.98). After substituting (2.103) into (2.102) one arrives at

$$\begin{aligned}
&\left(i\hbar\frac{\mathrm{d}a}{\mathrm{d}t}+a(t)E_i\right)e^{-iE_it/\hbar}|\Psi_i;\{n_{\boldsymbol{q}}\}\rangle+\\
&+\sum_{\boldsymbol{k}}e^{-i(E_f\pm\hbar\omega_{LO})t/\hbar}\left[i\hbar\frac{\mathrm{d}b_{\boldsymbol{k}}}{\mathrm{d}t}+(E_f\pm\hbar\omega_{LO})\,b_{\boldsymbol{k}}(t)\right]|\Psi_f;\{n_{\boldsymbol{q}}\pm\delta_{\boldsymbol{q},\boldsymbol{k}}\}\rangle=\\
&=a(t)E_ie^{-iE_it/\hbar}|\Psi_i;\{n_{\boldsymbol{q}}\}\rangle+a(t)e^{-iE_it/\hbar}\hat{H}_{e-ph}|\Psi_i;\{n_{\boldsymbol{q}}\}\rangle+\\
&+\sum_{\boldsymbol{k}}(E_f\pm\hbar\omega_{LO})\,e^{-i(E_f\pm\hbar\omega_{LO})t/\hbar}b_{\boldsymbol{k}}(t)|\Psi_f;\{n_{\boldsymbol{q}}\pm\delta_{\boldsymbol{q},\boldsymbol{k}}\}\rangle+\\
&+\sum_{\boldsymbol{k}}e^{-i(E_f\pm\hbar\omega_{LO})t/\hbar}b_{\boldsymbol{k}}(t)\hat{H}_{e-ph}|\Psi_f;\{n_{\boldsymbol{q}}\pm\delta_{\boldsymbol{q},\boldsymbol{k}}\}\rangle,
\end{aligned}$$

i.e.

$$\begin{aligned}
&i\hbar\frac{\mathrm{d}a}{\mathrm{d}t}e^{-iE_it/\hbar}|\Psi_i;\{n_{\boldsymbol{q}}\}\rangle+\sum_{\boldsymbol{k}}i\hbar\frac{\mathrm{d}b_{\boldsymbol{k}}}{\mathrm{d}t}e^{-i(E_f\pm\hbar\omega_{LO})t/\hbar}|\Psi_f;\{n_{\boldsymbol{q}}\pm\delta_{\boldsymbol{q},\boldsymbol{k}}\}\rangle=\\
&=a(t)e^{-iE_it/\hbar}\hat{H}_{e-ph}|\Psi_i;\{n_{\boldsymbol{q}}\}\rangle\\
&+\sum_{\boldsymbol{k}}e^{-i(E_f\pm\hbar\omega_{LO})t/\hbar}b_{\boldsymbol{k}}(t)\hat{H}_{e-ph}|\Psi_f;\{n_{\boldsymbol{q}}\pm\delta_{\boldsymbol{q},\boldsymbol{k}}\}\rangle.
\end{aligned} \tag{2.106}$$

After multiplying (2.106) from the left by $\langle\Psi_i;\{n_{\boldsymbol{q}}\}|$, one obtains

$$i\hbar\frac{\mathrm{d}a}{\mathrm{d}t}=\sum_{\boldsymbol{k}}e^{-i(E_f-E_i\pm\hbar\omega_{LO})t/\hbar}b_{\boldsymbol{k}}(t)\langle\Psi_i;\{n_{\boldsymbol{q}}\}|\hat{H}_{e-ph}|\Psi_f;\{n_{\boldsymbol{q}}\pm\delta_{\boldsymbol{q},\boldsymbol{k}}\}\rangle \quad (2.107)$$

and after multiplying (2.106) from the left by $\langle\Psi_f;\{n_{\boldsymbol{q}}\pm\delta_{\boldsymbol{q},\boldsymbol{k}}\}|$

$$i\hbar\frac{\mathrm{d}b_{\boldsymbol{k}}}{\mathrm{d}t} \;=\; a(t)e^{i(E_f-E_i\pm\hbar\omega_{LO})t/\hbar}\langle\Psi_f;\{n_{\boldsymbol{q}}\pm\delta_{\boldsymbol{q},\boldsymbol{k}}\}|\hat{H}_{e-ph}|\Psi_i;\{n_{\boldsymbol{q}}\}\rangle.$$

Finally one gets the equations

$$\frac{\mathrm{d}a}{\mathrm{d}t}=-\frac{i}{\hbar}\sum_{\boldsymbol{k}}g_{\boldsymbol{k}}e^{i\Delta t/\hbar}b_{\boldsymbol{k}}(t), \quad (2.108)$$

$$\frac{\mathrm{d}b_{\boldsymbol{k}}}{\mathrm{d}t}=-\frac{i}{\hbar}g^*_{\boldsymbol{k}}e^{-i\Delta t/\hbar}a(t), \quad (2.109)$$

where $\Delta=E_i-E_f\mp\hbar\omega_{\mathrm{LO}}$ and

$$g_{\boldsymbol{k}}=\langle\Psi_i;\{n_{\boldsymbol{q}}\}|\hat{H}_{e-ph}|\Psi_f;\{n_{\boldsymbol{q}}\pm\delta_{\boldsymbol{q},\boldsymbol{k}}\}\rangle \quad (2.110)$$

is the electron – LO phonon coupling strength.

So far it has been assumed that LO phonons are stable. However due to cubic anharmonic terms in the crystal potential energy the LO phonons decay. It is thought that the physical process responsible for that decay process is either the decay to two LA phonons [95,178] or to one acoustic and one optical phonon [96]. Nevertheless, whatever the physical origin of the process is, it can be phenomenologically taken into account by adding an extra decay term $-\frac{\Gamma_{\boldsymbol{k}}}{\hbar}b_{\boldsymbol{k}}(t)$ into (2.109), i.e.

$$\frac{\mathrm{d}b_{\boldsymbol{k}}}{\mathrm{d}t}=-\frac{i}{\hbar}g^*_{\boldsymbol{k}}e^{-i\Delta t/\hbar}a(t)-\frac{\Gamma_{\boldsymbol{k}}}{\hbar}b_{\boldsymbol{k}}(t), \quad (2.111)$$

where $\Gamma_{\boldsymbol{k}}/\hbar$ is the inverse LO phonon lifetime. Taking the Laplace transform of (2.108) and (2.111) one arrives at

$$sA(s)-1=-\frac{i}{\hbar}\sum_{\boldsymbol{k}}g_{\boldsymbol{k}}B_{\boldsymbol{k}}(s-i\frac{\Delta}{\hbar}), \quad (2.112)$$

$$sB_{\boldsymbol{k}}(s)=-\frac{i}{\hbar}g^*_{\boldsymbol{k}}A(s+i\frac{\Delta}{\hbar})-\frac{\Gamma_{\boldsymbol{k}}}{\hbar}B_{\boldsymbol{k}}(s). \quad (2.113)$$

As shown in Ref. [178], the LO phonon lifetime is weakly dependent on the wave vector and it will therefore be considered to be a constant. Solving Eqs. (2.112) and (2.113) one gets

$$A(s) = \frac{s-\gamma}{s^2 - \gamma s + g^2}, \tag{2.114}$$

where $\gamma = \frac{-\Gamma + i\Delta}{\hbar}$ and $g^2 = \sum_{\boldsymbol{k}} |g_{\boldsymbol{k}}|^2$. Taking the inverse Laplace transform one obtains

$$a(t) = e^{\gamma t/2}\left(\cos\beta t - \frac{\gamma}{2\beta}\sin\beta t\right), \tag{2.115}$$

where $\beta^2 = \frac{g^2}{\hbar^2} - \frac{1}{4}\gamma^2$. The probability that the system stays in its initial state after time t is equal to

$$\begin{aligned} P(t) &= |a(t)|^2 = \frac{1}{16|\beta|^2}\Big[|2\beta - i\gamma|^2 e^{-(\frac{\Gamma}{\hbar} - 2\beta_2)t} + |2\beta + i\gamma|^2 e^{-(\frac{\Gamma}{\hbar} + 2\beta_2)t} + \\ &+ 2\cos(2\beta_1 t)e^{-\frac{\Gamma}{\hbar}t}\left(4|\beta|^2 - |\gamma|^2\right) + 8\sin(2\beta_1 t)e^{-\frac{\Gamma}{\hbar}t}(\frac{\Gamma}{\hbar}\beta_1 - \beta_2\frac{\Delta}{\hbar})\Big], \end{aligned} \tag{2.116}$$

where $\beta_1 = \mathrm{Re}\beta$ and $\beta_2 = \mathrm{Im}\beta$. It can be seen from (2.116) that the dominant exponentially decaying term is $e^{-(\frac{\Gamma}{\hbar} - 2\beta_2)t}$ and therefore the relaxation time is equal to $\tau^{-1} = \frac{\Gamma}{\hbar} - 2\beta_2$. After finding the explicit expression for β_2 one gets the approximate transition rate

$$W = \frac{\Gamma}{\hbar} - \frac{\sqrt{2(R-X)}}{\hbar}, \tag{2.117}$$

where $R = \sqrt{X^2 + Y^2}$, $X = g^2 + (\Delta^2 - \Gamma^2)/4$, $Y = \Gamma\Delta/2$.

Eq. (2.117) has been verified experimentally, as it was used to fit the experimental results on intraband carrier dynamics in quantum dots [98, 179].

Electron – acoustic phonon interaction

The interaction with acoustic phonons is much weaker than the interaction with optical phonons in semiconductor nanostructures [42]. Therefore, it can be satisfactorily treated perturbatively within Fermi's Golden rule. The transition rate from an initial state i to a final state f is then given by

$$\begin{aligned} W_{if} &= \frac{2\pi}{\hbar}\sum_{\boldsymbol{q}} |\langle\Psi_f; \{n_{\boldsymbol{k}} \pm \delta_{\boldsymbol{k},\boldsymbol{q}}\}| \left(\alpha(\boldsymbol{q})\hat{a}_{\boldsymbol{q}} e^{i\boldsymbol{q}\cdot\boldsymbol{r}} + \alpha(\boldsymbol{q})^* \hat{a}^+_{\boldsymbol{q}} e^{-i\boldsymbol{q}\cdot\boldsymbol{r}}\right) \\ &\qquad |\Psi_i; \{n_{\boldsymbol{k}}\}\rangle|^2 \, \delta(E_f - E_i \pm \hbar\omega(\boldsymbol{q})), \end{aligned} \tag{2.118}$$

where $\hbar\omega(\boldsymbol{q})$ is an LA phonon energy, implying

$$W_{if} = \frac{2\pi}{\hbar}\sum_{\boldsymbol{q}}(n_{\boldsymbol{q}} + \frac{1}{2} \pm \frac{1}{2})|\alpha(\boldsymbol{q})|^2|F_{if}(\boldsymbol{q})|^2\delta(E_f - E_i \pm \hbar\omega(\boldsymbol{q})). \quad (2.119)$$

After replacing the summation in (2.119) by integration one arrives at [179]

$$W_{if} = \frac{2\pi}{\hbar}\frac{V}{(2\pi)^3}\int q^2 \sin\theta \,\mathrm{d}q\,\mathrm{d}\theta\,\mathrm{d}\varphi(n_{\boldsymbol{q}}+\frac{1}{2}\pm\frac{1}{2})|\alpha(\boldsymbol{q})|^2|F_{if}(\boldsymbol{q})|^2\delta(E_f-E_i\pm\hbar\omega(\boldsymbol{q})) \quad (2.120)$$

and

$$W_{if} = \Theta(\pm(E_i - E_f))(n_{\boldsymbol{q}_s} + \frac{1}{2} \pm \frac{1}{2})\frac{D_A^2 q_s^3}{\hbar\rho v_s^2}\int \sin\theta\mathrm{d}\theta\mathrm{d}\varphi|F_{if}(\boldsymbol{q}_s)|^2, \quad (2.121)$$

where $q_s = |E_i - E_f|/(\hbar v_s)$, $\Theta(x)$ is the step function and (θ, φ) are the polar coordinates of the vector $\boldsymbol{q}_s$.

2.7.2 Polaron spectrum in quantum dots

In this section it will be shown how one can relatively efficiently find polaron states in quantum dots. Even when one is interested in electron transport only, knowledge of the polaron spectrum can be useful to check whether the approximations introduced in the treatment of the interaction with phonons are appropriate. The approach of Ref. [180] is mainly followed here.

In order to find polaron states, one in principle needs to diagonalise the full Hamiltonian (Eq. (2.103)). Assuming there are N possible electronic states, and that there are M phonon modes (where M is a large number obtained by discretisation of continuous phonon wave vector $\boldsymbol{q}$) that can be occupied with at most K phonons, the dimension of the Hamiltonian matrix would be $N \cdot (K+1)^M$ and such an eigenvalue problem would clearly be intractable. It has however been shown in Ref. [180] that a transformation can be made among phonon modes after which only N^2 modes will remain coupled to electronic degrees of freedom. In order to achieve this, one first introduces the operators

$$\hat{A}_{ij} = \sum_{\boldsymbol{q}} M_{ij}(\boldsymbol{q})\hat{b}_{\boldsymbol{q}}. \quad (2.122)$$

The Hamiltonian $\hat{H}_{e-ph}$ then takes the form

$$\hat{H}_{e-ph} = \sum_{ij} \left(\hat{A}_{ij} \hat{a}_i^+ \hat{a}_j + \hat{A}_{ij}^+ \hat{a}_j^+ \hat{a}_i \right) \tag{2.123}$$

and therefore only new N^2 phonon modes interact with electrons. However the transformation (2.122) also changes $\hat{H}_{ph}$ which is no longer diagonal.

As a next step, a new transformation will be performed which diagonalises $\hat{H}_{ph}$. One can formally look at the operators introduced by (2.122) as vectors in vector space with basis vectors $\hat{b}_{\boldsymbol{q}}$. In such a space, $\hat{A}_{ij}$ are not orthonormalised, however one can perform a Gram-Schmidt orthonormalisation procedure to orthonormalise them, yielding new N^2 operators $\hat{B}_\alpha$ related to $\hat{A}$-operators by

$$\hat{A}_{ij} = \sum_\alpha t_{ij,\alpha} \hat{B}_\alpha. \tag{2.124}$$

The transformation connecting the operators $\hat{B}$ and $\hat{b}$ is unitary since it is a transformation connecting two orthonormal basis. One can then easily verify the relation

$$\sum_\lambda \hat{B}_\lambda^+ \hat{B}_\lambda = \sum_{\boldsymbol{q}} \hat{b}_{\boldsymbol{q}}^+ \hat{b}_{\boldsymbol{q}} \tag{2.125}$$

and therefore, assuming dispersionless LO phonon modes, $\hat{H}_{ph}$ is diagonal in $\hat{B}$-operators as well. Explicit form of $\hat{H}_{e-ph}$ in terms of $\hat{B}$-operators can then be obtained by substituting (2.124) in (2.123). One therefore has to solve the eigenvalue problem of the matrix of size $N \cdot (K+1)^{N^2}$, which is feasible for small N.

2.8 Nonequilibrium Green's functions theory of transport

The transition rates between quantum dot states, derived in previous sections of this Chapter, can be used to form rate equations for populations of quantum dot energy levels, from which populations, and consequently observable quantities, such as absorption or current, can be found. Such an approach is good not only for the basic understanding of the physics of quantum dot

devices, but can be also used for quantitative predictions, as will be shown in subsequent chapters.

However, there are limitations to such an approach. Since only populations of energy levels are considered, and not the coherences, coherent effects are not properly taken into account. Additionally, broadening of the absorption or gain spectrum can be taken into account only in an *ad hoc* manner by replacing the delta functions with appropriate line shapes. Polaron shifts of energy levels are also not included. Despite the fact that these limitations are not severe for modelling of the existing devices, there is a not only theoretical need, for the development of more systematic approach, that will take into account all the mentioned effects.

Two theoretical approaches satisfying this condition have been so far employed in the literature to analyse the transport and optical properties of semiconductor nanostructures. These are *density matrix formalism* and the *nonequilibrium Green's functions formalism*.

Within the density matrix approach [181,182], the main quantities are the electron density matrices $\rho_{\alpha\beta}(t) = \langle \hat{a}_\alpha(t)^+ \hat{a}_\beta(t) \rangle$, where the expectation value is taken with respect to the initial state of the system. The Heisenberg picture is used, therefore the operators depend explicitly on time. When one forms the equation of motion for the density matrix, higher order density matrices involving expectation values of products of several operators appear, and the system of equations is therefore not closed. One therefore arrives at an infinite hierarchy of equations for higher-order density matrices, which needs to be truncated at some point.

On the other hand, within the nonequilibrium Green's functions approach [183,184], the central quantities are expectation values of operators at different times, such as the retarded Green's function

$$G^R_{\alpha\beta}(t_1, t_2) = -i\Theta(t_1 - t_2)\langle\{\hat{a}_\alpha(t_1), \hat{a}^+_\beta(t_2)\}\rangle, \tag{2.126}$$

the advanced Green's function

$$G^A_{\alpha\beta}(t_1, t_2) = i\Theta(t_2 - t_1)\langle\{\hat{a}_\alpha(t_1), \hat{a}^+_\beta(t_2)\}\rangle = G^R_{\beta\alpha}(t_2, t_1)^*, \tag{2.127}$$

and the lesser Green's function

$$G^{<}_{\alpha\beta}(t_1,t_2) = i\langle \hat{a}^{+}_{\beta}(t_2)\hat{a}_{\alpha}(t_1)\rangle. \tag{2.128}$$

As can be seen from (2.128), the lesser function at equal times represents populations and coherences of the states, in terms of which other relevant physical quantities can be expressed. In order to find the retarded and the lesser function, one has to solve their dynamical equations. These satisfy the Dyson equation

$$i\hbar\frac{\partial G^{R}_{\alpha\beta}(t_1,t_2)}{\partial t_1} - \sum_{\gamma} H_{\alpha\gamma}G^{R}_{\gamma\beta}(t_1,t_2) = \hbar\delta_{\alpha\beta}\delta(t_1-t_2) + \tag{2.129}$$
$$+\sum_{\gamma}\int \mathrm{d}t'\Sigma^{R}_{\alpha\gamma}(t_1,t')G^{R}_{\gamma\beta}(t',t_2),$$

where the Hamiltonian $\hat{H}$ contains the kinetic energy of the electron and single particle potential, while all other interactions, such as electron – phonon, electron – impurity, electron – electron, etc. are contained in the self-energy Σ. The equation for $G^{<}$ can also be written in integro-differential form similar to (2.129), however for certain applications, a more useful form is the integral form given by the Keldysh relation which in the case of the steady state of the system reads

$$G^{<}_{\alpha\beta}(t_1,t_2) = \sum_{\gamma\delta}\int \mathrm{d}t'\mathrm{d}t'' G^{R}_{\alpha\gamma}(t_1,t')\Sigma^{<}_{\gamma\delta}(t',t'')G^{A}_{\delta\beta}(t'',t_2). \tag{2.130}$$

It is essential for the description of any physical system to arrive at appropriate expressions for self-energies, as these are the quantities that contain all interactions in the system. A systematic way of doing this is via the diagrammatic techniques of field theory where the time ordered Green's function [175] is expanded in a sum of infinitely many diagrams representing interactions in all orders [175]. In the case of the electron – phonon interaction in the system with translational invariance [185], when one restricts to second order in the expressions for self-energies (the so called Born approximation) these

expressions read [175, 183, 184]

$$\Sigma^R_{\alpha\beta}(t_1,t_2) = i\sum_{\gamma\delta,\boldsymbol{q}} M_{\beta\delta}(\boldsymbol{q})^* M_{\alpha\gamma}(\boldsymbol{q}) \left[g^R_{\gamma\delta}(t_1,t_2) D^R(\boldsymbol{q},t_1,t_2) + \right. \tag{2.131}$$
$$\left. + g^<_{\gamma\delta}(t_1,t_2) D^R(\boldsymbol{q},t_1,t_2) + g^R_{\gamma\delta}(t_1,t_2) D^<(\boldsymbol{q},t_1,t_2) \right],$$

$$\Sigma^<_{\alpha\beta}(t_1,t_2) = i\sum_{\gamma\delta,\boldsymbol{q}} M_{\beta\delta}(\boldsymbol{q})^* M_{\alpha\gamma}(\boldsymbol{q}) g^<_{\gamma\delta}(t_1,t_2) D^<(\boldsymbol{q},t_1,t_2), \tag{2.132}$$

where the free electron Green's functions are denoted by lowercases g, and D^R and $D^<$ are the phonon retarded and lesser Green's functions defined as

$$D^R(\boldsymbol{q},t_1,t_2) = -i\Theta(t_1-t_2)\langle[\hat{A}_{\boldsymbol{q}}(t), \hat{A}^+_{\boldsymbol{q}}(t')]\rangle \tag{2.133}$$

and

$$D^<(\boldsymbol{q},t_1,t_2) = -i\langle \hat{A}^+_{\boldsymbol{q}}(t_2)\hat{A}_{\boldsymbol{q}}(t_1)\rangle, \tag{2.134}$$

where $\hat{A}_{\boldsymbol{q}} = \hat{b}_{\boldsymbol{q}} + \hat{b}^+_{-\boldsymbol{q}}$. One can significantly improve the Born approximation by replacing the free Green's functions g by Green's functions G, which constitutes the self-consistent Born approximation (SCBA). The SCBA takes into account all diagrams up to second order and additionally a certain set of diagrams from all higher orders. Clearly the validity of the Born approximation or the SCBA depends on the system being investigated and the strength of the interaction represented by self-energies.

One is usually mostly interested in the steady state of the system. In that case, Green's functions and self-energies depend only on the difference of their time arguments. One can therefore define the Fourier transform of all these quantities as

$$F(E) = \int \mathrm{d}(t_1-t_2) e^{iE(t_1-t_2)/\hbar} F(t_1-t_2). \tag{2.135}$$

The integro-differential Dyson equation then takes a simple algebraic form

$$\sum_\gamma \left[E\delta_{\alpha\gamma} - \left(H_{\alpha\gamma} + \Sigma^R_{\alpha\gamma}(E) \right) \right] G^R_{\gamma\beta}(E) = \delta_{\alpha\beta} \tag{2.136}$$

and the Keldysh relation reads

$$G^<_{\alpha\beta}(E) = \sum_{\gamma\delta} G^R_{\alpha\gamma}(E)\Sigma^<_{\gamma\delta}(E)G^A_{\delta\beta}(E). \tag{2.137}$$

The relation between the retarded and advanced function in the energy domain is

$$G^R_{\alpha\beta}(E) = G^A_{\beta\alpha}(E)^*. \tag{2.138}$$

While Dyson's equation and the Keldysh relation have acquired a much simpler form in the energy domain, this is not the case for the expressions for self-energies, which read

$$\Sigma^R_{\alpha\beta}(E) = i\sum_{\gamma\delta,\boldsymbol{q}} M_{\beta\delta}(\boldsymbol{q})^* M_{\alpha\gamma}(\boldsymbol{q}) \frac{1}{2\pi}\int \mathrm{d}E' \left[G^R_{\gamma\delta}(E-E')D^R(E') + \right. \tag{2.139}$$
$$\left. + G^<_{\gamma\delta}(E-E')D^R(E') + G^R_{\gamma\delta}(E-E')D^<(E')\right],$$

$$\Sigma^<_{\alpha\beta}(E) = i\sum_{\gamma\delta,\boldsymbol{q}} M_{\beta\delta}(\boldsymbol{q})^* M_{\alpha\gamma}(\boldsymbol{q}) \frac{1}{2\pi}\int \mathrm{d}E' G^<_{\gamma\delta}(E-E')D^<(E'). \tag{2.140}$$

The phonon Green's functions in the energy domain are given by

$$D^R(E) = \frac{1}{E - E_{LO} + i\Gamma} - \frac{1}{E + E_{LO} + i\Gamma}, \tag{2.141}$$

$$D^<(E) = -i\left[(N_{LO}+1)\frac{2\Gamma}{(E+E_{LO})^2+\Gamma^2} + N_{LO}\frac{2\Gamma}{(E-E_{LO})^2+\Gamma^2}\right], \tag{2.142}$$

where Γ is the LO phonon linewidth determined by its anharmonic decay rate and N_{LO} is the phonon occupation number

$$N_{\mathrm{LO}} = \frac{1}{e^{\frac{\hbar\omega_{\mathrm{LO}}}{k_{\mathrm{B}}T}} - 1}. \tag{2.143}$$

Chapter 3

Electronic structure calculation of square based pyramidal quantum dots

3.1 Introduction

A range of theoretical approaches has been used so far to calculate the energy levels in self-assembled quantum dots - the effective mass [160, 186–188], $\boldsymbol{k}\cdot\boldsymbol{p}$ [126–129] and the pseudopotential method [117,189]. They are usually implemented in such a way to be able to treat a quantum dot of arbitrary shape. Different quantum dot shapes (such as pyramid [190], lens [191] and disk [192]) of self-assembled quantum dots are often reported, most of them being highly symmetric. An idea therefore naturally arises to exploit this symmetry in the energy level calculations.

In quantum dots with cylindrical symmetry, symmetry considerations have been applied to effectively reduce the geometry of the problem from three dimensional to two dimensional, both in the effective mass and the $\boldsymbol{k}\cdot\boldsymbol{p}$ method (within the axial approximation) [163]. The possible symmetries of the states in hexagonal III-nitride quantum dots have recently been determined [193]. The symmetry of the pyramid has been used in the effective mass calculation [164] to reduce the size of the corresponding Hamiltonian matrix, however in none of the $\boldsymbol{k}\cdot\boldsymbol{p}$ calculations of pyramidal quantum dots has the explicit use of the symmetry of the Hamiltonian been reported.

Therefore, in this Chapter, a method will be presented that exploits the

symmetry in the 8-band $\boldsymbol{k}\cdot\boldsymbol{p}$ calculation of the electronic structure of square based pyramidal quantum dots based on materials with zincblende crystal symmetry. The method presented is then applied to calculate the electron and hole states in a periodic array of vertically stacked square based pyramidal self-assembled InAs/GaAs quantum dots for different values of the period of the structure and in the presence of an external axial magnetic field.

3.2 The plane wave method

In the presence of an axial magnetic field the total 8-band $\boldsymbol{k}\cdot\boldsymbol{p}$ Hamiltonian is a sum of the kinetic part of the Hamiltonian $\hat{H}_k$ (Eq. (2.20)) including the minimal gauge substitution (see Sec. 2.5.3), the strain part $\hat{H}_s$ (Eq. (2.38)), and the Zeeman part $\hat{H}_Z$ (Eq. (2.76))

$$\hat{H} = \hat{H}_k + \hat{H}_s + \hat{H}_Z. \tag{3.1}$$

The state of the system within the framework of the 8-band $\boldsymbol{k}\cdot\boldsymbol{p}$ method is given as a sum of slowly varying envelope functions $\psi_i(\boldsymbol{r})$ multiplied by the bulk Bloch functions $|i\rangle$ (Eq. (2.19)), i.e.

$$|\Psi\rangle = \sum_{i=1}^{8} \psi_i(\boldsymbol{r})|i\rangle. \tag{3.2}$$

The eigenvalue problem of the 8-band $\boldsymbol{k}\cdot\boldsymbol{p}$ Hamiltonian $\hat{H}$ can therefore be written as

$$\sum_{j=1}^{8} \hat{H}_{ij}\psi_j(\boldsymbol{r}) = E\psi_i(\boldsymbol{r}). \tag{3.3}$$

The plane wave method is based on embedding the quantum dot in a box of sides L_x, L_y and L_z (Fig. 3.1) and assuming the envelope functions are a linear combination of plane waves

$$\psi_i(\boldsymbol{r}) = \sum_{\boldsymbol{k}} A_{i,\boldsymbol{k}} \exp\left(i\boldsymbol{k}\cdot\boldsymbol{r}\right), \tag{3.4}$$

with the coefficients $A_{i,\boldsymbol{k}}$ to be determined. The wave vectors taken in a summation are given by

$$\boldsymbol{k} = 2\pi\left(\frac{m_x}{L_x}, \frac{m_y}{L_y}, \frac{m_z}{L_z}\right), \tag{3.5}$$

where $m_x \in \{-n_x, \ldots, n_x\}$, $m_y \in \{-n_y, \ldots, n_y\}$, $m_z \in \{-n_z, \ldots, n_z\}$. The number of plane waves taken is thus $N = 8(2n_x + 1)(2n_y + 1)(2n_z + 1)$, where $2n_t + 1$ is the number of plane waves per dimension t ($t \in \{x, y, z\}$). Due to the symmetry of the pyramid, the embedding box sides L_x and L_y are taken to be equal ($L_x = L_y$), as well as the number of plane waves per dimensions x and y ($n_x = n_y$).

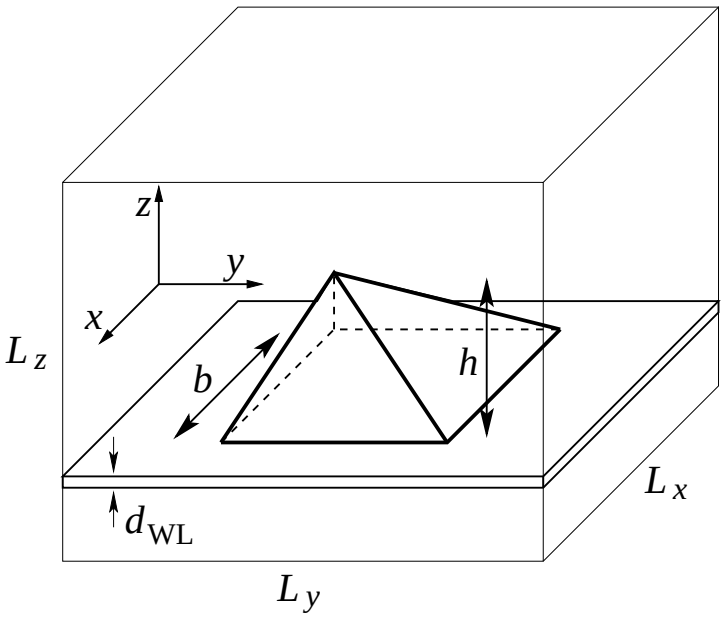

Figure 3.1: Quantum dot geometry. The width of the base is b, the height h, the wetting layer width d_{WL}. The embedding box sides are L_x, L_y and L_z. The center of the pyramid base is taken as the origin of the coordinate system.

After multiplying Eq. (3.3) from the left by $\frac{1}{(2\pi)^3}\int_V \mathrm{d}^3\boldsymbol{r}\exp\left(-i\boldsymbol{q}\cdot\boldsymbol{r}\right)$, where the integration goes over the volume of the embedding box, using (3.4) and the identity

$$\int_V \mathrm{d}^3\boldsymbol{r}\exp\left[2i\pi\left(\frac{m_x x}{L_x}+\frac{m_y y}{L_y}+\frac{m_z z}{L_z}\right)\right] = L_x L_y L_z \delta_{m_x,0}\delta_{m_y,0}\delta_{m_z,0}, \qquad (3.6)$$

one arrives at

$$\sum_{j,\boldsymbol{k}} h_{ij}(\boldsymbol{q},\boldsymbol{k})A_{j,\boldsymbol{k}} = EA_{i,\boldsymbol{q}}, \qquad (3.7)$$

where

$$h_{ij}(\boldsymbol{q},\boldsymbol{k}) = \frac{1}{V}\int_{\mathrm{V}} \mathrm{d}^3\boldsymbol{r}\,\exp\left(-i\boldsymbol{q}\cdot\boldsymbol{r}\right)\hat{H}_{ij}\exp\left(i\boldsymbol{k}\cdot\boldsymbol{r}\right). \tag{3.8}$$

The explicit expressions for the Hamiltonian matrix elements are given in Appendix A.

In order to find the energy levels and the wavefunctions in the quantum dot, the eigenvalue problem (3.7) should be solved. The direct application of this approach would lead to an eigenvalue problem of a matrix of size $N \times N$. However, it is possible to exploit the symmetry of the system to block diagonalise the corresponding matrix, as will be done in Sec. 3.3.

3.3 The symmetry of the model

The main idea is to transform the plane wave basis in such a way that in a new, symmetrised basis, the matrix acquires block diagonal form, see Fig. 3.2. This is mathematically a nontrivial task as the operators of rotation act both on the envelope functions and Bloch functions. In order to achieve this, one has first to establish what is the symmetry group of the model. As a second step, one has to represent operators of the symmetry group. When this is accomplished, the results of mathematical group theory can be used to adapt the plane wave basis to symmetry.

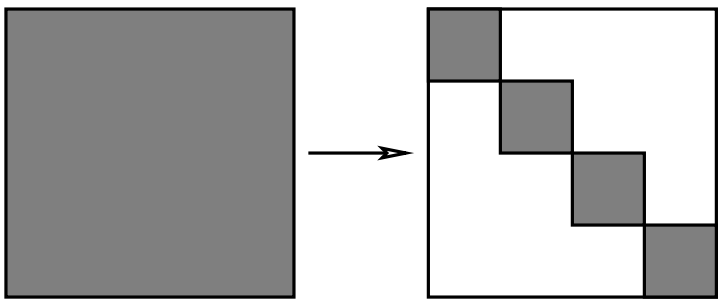

Figure 3.2: Hamiltonian matrix in the plane wave basis (left), and in the new symmetrised basis (right).

The symmetry group of the quantum dot physical system is the intersection of the geometrical symmetry of the dot shape and the symmetry of the zincblende bulk crystal. The symmetry of the model of the quantum dot physical system therefore depends on the model used to describe the underlying bulk structure.

The symmetry of a pyramidal InAs/GaAs quantum dot when atomistic structure is considered which captures the full symmetry of the crystal lattice (as is done for example in the empirical pseudopotential method) is C_{2v} and is lower than the symmetry of the dot's geometrical shape [189]. On the other hand, the 8-band $\boldsymbol{k}\cdot\boldsymbol{p}$ model does not capture the full symmetry of the system and the symmetry group of the InAs/GaAs pyramidal quantum dot model is the C_{4v} group. One should note that this is not an inherent limitation of the envelope function methods, as for example, within the 14-band $\boldsymbol{k}\cdot\boldsymbol{p}$ model, the symmetry would be C_{2v}.

Additionally, one has to establish how the strain part of the Hamiltonian affects the symmetry of the model. When the strain distribution is incorporated in the 8-band $\boldsymbol{k}\cdot\boldsymbol{p}$ method, the continuum mechanical model preserves the C_{4v} symmetry, while the valence force field model, due to its atomistic nature, breaks it [126, 128].

Since in this work, the 8-band $\boldsymbol{k}\cdot\boldsymbol{p}$ method with the strain taken into account via the continuum mechanical model is used, the symmetry group of the model is C_{4v}. The fact that the 8-band $\boldsymbol{k}\cdot\boldsymbol{p}$ model does not capture the full symmetry of the system is often emphasised as its drawback from the fundamental point of view [189]. However if the amount of physical information provided by 8-band $\boldsymbol{k}\cdot\boldsymbol{p}$ model is satisfactory for a particular purpose, as has been established in Chapter 2, this drawback can be turned into a strength from the computational point of view, by exploiting the symmetry of the system in the calculation. In this work, only the C_4 symmetry will be exploited since the presence of an external axial magnetic field reduces the symmetry from C_{4v} to C_4.

3.3.1 Representation of the symmetry group operators

The generator of the rotation group is the total angular momentum $\hat{F}_z$ and therefore the representations of the elements of the group are given by the operators $\hat{D}(R(\varphi)) = \exp(-i\varphi\hat{F}_z)$, where $\varphi \in \{k\pi/2\}$ ($k \in \{0, 1, \ldots, 7\}$) and $R(\varphi)$ is a rotation by an angle φ. In order to find how the operators $\hat{D}(R(\varphi))$ act on the states (Eq. (3.2)), it is enough to find how $\hat{D}(R(\pi/2))$ acts on the states since $\hat{D}(R(k\pi/2)) = \hat{D}(R(\pi/2))^k$. The total angular momentum $\hat{F}_z$ is a sum of the total angular momentum of the Bloch function $\hat{J}_z$ and the orbital angular momentum of the envelope function $\hat{L}_z$, i.e. $\hat{F}_z = \hat{J}_z + \hat{L}_z$ [194]. The action of the operator $\hat{D}(R(\pi/2))$ on state $|\Psi\rangle$ is composed of a rotation of the envelope functions in real space generated by its orbital angular momentum $\hat{L}_z$ and a rotation of the Bloch function generated by its total angular momentum $\hat{J}_z$

$$\hat{D}(R(\pi/2))|\Psi\rangle = \sum_{i=1}^{8} \left[\exp(-i\frac{\pi}{2}\hat{L}_z)\psi_i(\boldsymbol{r})\right] \left[\exp(-i\frac{\pi}{2}\hat{J}_z)|i\rangle\right]. \tag{3.9}$$

Since the basis of the Bloch states $|i\rangle$ is the eigenbasis of $\hat{J}_z$ it follows that

$$\exp(-i\hat{J}_z\pi/2)|i\rangle = \exp(-iJ_z(i)\pi/2)|i\rangle, \tag{3.10}$$

where $J_z(i)$ is the eigenvalue of the $z-$component of the total angular momentum of Bloch function $|i\rangle$ ($J_z(1) = -1/2$, $J_z(2) = 1/2$, $J_z(3) = 1/2$, $J_z(4) = 3/2$, $J_z(5) = -3/2$, $J_z(6) = -1/2$, $J_z(7) = -1/2$, $J_z(8) = 1/2$). Thus the operator $\hat{D}(R(\pi/2))$ acts on the state $|\Psi\rangle$ as

$$\hat{D}(R(\pi/2))|\Psi\rangle = \sum_{i=1}^{8} \psi_i(y, -x, z)\exp(-iJ_z(i)\pi/2)|i\rangle. \tag{3.11}$$

By assuming the envelope functions as a linear combination of a finite number of plane waves, one has already reduced the otherwise infinite Hilbert space of the model to the Hilbert space $\mathcal{H}$ of dimension N formed by linear combination of plane waves multiplied by the Bloch functions. The basis of the space $\mathcal{H}$ is given by

$$|\boldsymbol{k}, i\rangle = \exp(i\boldsymbol{k}\cdot\boldsymbol{r})|i\rangle, \tag{3.12}$$

where $\boldsymbol{k} = 2\pi\left(\frac{m_x}{L_x}, \frac{m_y}{L_y}, \frac{m_z}{L_z}\right)$, $m_x \in \{-n_x, \ldots, n_x\}$, $m_y \in \{-n_y, \ldots, n_y\}$, $m_z \in \{-n_z, \ldots, n_z\}$ and $i \in \{1, 2, \ldots, 8\}$.

Next, one wishes to represent the operator $\hat{D}(R(\pi/2))$ in the plane wave basis of the space $\mathcal{H}$. For that, one needs to know how $\hat{D}(R(\pi/2))$ acts on the basis vectors. Using (3.11) and (3.12) one gets

$$\hat{D}(R(\pi/2))|(k_x, k_y, k_z), i\rangle = \exp(-iJ_z(i)\pi/2)|(-k_y, k_x, k_z), i\rangle. \tag{3.13}$$

At this point, one can explicitly verify that $\hat{D}(R(\pi/2))$ commutes with the Hamiltonian of the model, and therefore the assumed group is indeed the symmetry group of the model. One can note that for $(k_x, k_y) = (0, 0)$ the action of $\hat{D}(R(\pi/2))$ on the basis vector is just a phase shift and the orbit of action of the group elements is just a one dimensional space (it will be denoted as $\mathcal{H}_{(0,0,k_z),i}$), while for $(k_x, k_y) \neq (0, 0)$ the orbit is a four dimensional space (that will be denoted as $\mathcal{H}_{(k_x,k_y,k_z),i}$, where $k_x > 0$ and $k_y \geq 0$ to avoid multiple counting of the same space) with the basis

$$\begin{aligned} |b1\rangle &= |(k_x, k_y, k_z), i\rangle, \\ |b2\rangle &= |(-k_y, k_x, k_z), i\rangle, \\ |b3\rangle &= |(-k_x, -k_y, k_z), i\rangle, \\ |b4\rangle &= |(k_y, -k_x, k_z), i\rangle. \end{aligned} \tag{3.14}$$

In the space $\mathcal{H}_{(0,0,k_z),i}$ the representation $\hat{D}$ reduces to a one dimensional representation defined by

$$\hat{D}_{(0,0,k_z),i}(R(\pi/2)) = \exp(-iJ_z(i)\pi/2), \tag{3.15}$$

while in the space $\mathcal{H}_{(k_x,k_y,k_z),i}$ it reduces to a four dimensional representation which is given in the basis from Eq. (3.14) by

$$\hat{D}_{(k_x,k_y,k_z),i}(R(\pi/2)) = \exp(-iJ_z(i)\pi/2) \begin{bmatrix} 0 & 0 & 0 & 1 \\ 1 & 0 & 0 & 0 \\ 0 & 1 & 0 & 0 \\ 0 & 0 & 1 & 0 \end{bmatrix}. \tag{3.16}$$

Since the spaces $\mathcal{H}_{(k_x,k_y,k_z),i}$ and $\mathcal{H}_{(0,0,k_z),i}$ are invariant for the representation $\hat{D}$, it is given by an orthogonal sum

$$\hat{D} = \bigoplus_{k_x,k_y,k_z,i} \hat{D}_{(k_x,k_y,k_z),i} + \bigoplus_{k_z,i} \hat{D}_{(0,0,k_z),i}. \tag{3.17}$$

From Eqs. (3.15) and (3.16) one finds that the characters (defined as the trace of operators $\hat{D}$) of the representation of the group elements are given by

$$\chi\left(\hat{D}_{(k_x,k_y,k_z),i}(R(k\pi/2))\right) = \begin{cases} 4 & k = 0 \\ -4 & k = 4 \\ 0 & k \in \{1,2,3,5,6,7\} \end{cases} \tag{3.18}$$

and

$$\chi\left(\hat{D}_{(0,0,k_z),i}(R(k\pi/2))\right) = \exp(-iJ_z(i)k\pi/2). \tag{3.19}$$

The characters of the irreducible double valued representations of the group C_4 are given by $\chi\left(A_{m_f}(R(k\pi/2))\right) = \exp(ikm_f\pi/2)$, where

$$m_f \in \{-3/2, -1, -1/2, 0, 1/2, 1, 3/2, 2\}$$

and $k \in \{0, 1, \ldots, 7\}$. One finds from (3.18) that

$$\hat{D}_{(k_x,k_y,k_z),i} = A_{1/2} + A_{-1/2} + A_{3/2} + A_{-3/2} \tag{3.20}$$

and from (3.19) obviously

$$\hat{D}_{(0,0,k_z),i} = A_{-J_z(i)}. \tag{3.21}$$

Eqs. (3.20) and (3.21) were obtained using the formula that the apperance of the irreducible representation A_{m_f} in the reduction of representation $\hat{D}$ is [136]

$$a_{m_f} = \frac{1}{8}\sum_{k=0}^{7} \chi\left(A_{m_f}(R(k\pi/2))\right)^* \chi\left(\hat{D}_{(k_x,k_y,k_z),i}(R(k\pi/2))\right). \tag{3.22}$$

Using (3.20) and (3.21), it follows from (3.17) that

$$\hat{D} = N_1 A_{1/2} + N_1 A_{-1/2} + N_2 A_{3/2} + N_2 A_{-3/2}, \tag{3.23}$$

where

$$N_1 = 8n_x(n_y + 1)(2n_z + 1) + 3(2n_z + 1) \tag{3.24}$$

and

$$N_2 = 8n_x(n_y + 1)(2n_z + 1) + 2n_z + 1. \tag{3.25}$$

3.3.2 The symmetry adapted basis

Projection operators [136] were then used to find the symmetry adapted basis. These operators have the property that they project an arbitrary state to a state of given symmetry. They are given by

$$\hat{P}_{A_{m_f}}((k_x,k_y,k_z),i) = \frac{1}{8}\sum_{k=0}^{7} \chi\left(A_{m_f}(R(k\pi/2))\right)^* \hat{D}_{(k_x,k_y,k_z),i}(R(k\pi/2)), \quad (3.26)$$

while

$$\hat{P}_{A_{m_f}}((0,0,k_z),i) = 1. \quad (3.27)$$

The explicit forms of the projection operators are derived from (3.26) and (3.16) and in the basis (3.14) are equal to

$$\begin{aligned}
\hat{P}_{A_{-3/2}}(1) = \hat{P}_{A_{-3/2}}(6) &= \hat{P}_{A_{-3/2}}(7) = \hat{P}_{A_{-1/2}}(5) = \\
= \hat{P}_{A_{1/2}}(4) &= \hat{P}_{A_{3/2}}(2) = \hat{P}_{A_{3/2}}(3) = \hat{P}_{A_{3/2}}(8) = M_1, \\
\hat{P}_{A_{-3/2}}(2) = \hat{P}_{A_{-3/2}}(3) &= \hat{P}_{A_{-3/2}}(8) = \hat{P}_{A_{-1/2}}(1) = \\
= \hat{P}_{A_{-1/2}}(6) &= \hat{P}_{A_{-1/2}}(7) = \hat{P}_{A_{1/2}}(5) = \hat{P}_{A_{3/2}}(4) = M_2, \\
\hat{P}_{A_{-3/2}}(4) = \hat{P}_{A_{-1/2}}(2) &= \hat{P}_{A_{-1/2}}(3) = \hat{P}_{A_{-1/2}}(8) = \\
= \hat{P}_{A_{1/2}}(1) &= \hat{P}_{A_{1/2}}(6) = \hat{P}_{A_{1/2}}(7) = \hat{P}_{A_{3/2}}(5) = M_3, \\
\hat{P}_{A_{-3/2}}(5) = \hat{P}_{A_{-1/2}}(4) &= \hat{P}_{A_{1/2}}(2) = \hat{P}_{A_{1/2}}(3) = \\
= \hat{P}_{A_{1/2}}(8) &= \hat{P}_{A_{3/2}}(1) = \hat{P}_{A_{3/2}}(6) = \hat{P}_{A_{3/2}}(7) = M_4, \quad (3.28)
\end{aligned}$$

where (k_x,k_y,k_z) was omitted in all brackets for brevity and where the matrices M_1, M_2, M_3 and M_4 are given by

$$M_1 = \frac{1}{4}\begin{bmatrix} 1 & -1 & 1 & -1 \\ -1 & 1 & -1 & 1 \\ 1 & -1 & 1 & -1 \\ -1 & 1 & -1 & 1 \end{bmatrix}, \quad M_2 = \tfrac{1}{4}\begin{bmatrix} 1 & -i & -1 & i \\ i & 1 & -i & -1 \\ -1 & i & 1 & -i \\ -i & -1 & i & 1 \end{bmatrix},$$

$$M_3 = \frac{1}{4}\begin{bmatrix} 1 & 1 & 1 & 1 \\ 1 & 1 & 1 & 1 \\ 1 & 1 & 1 & 1 \\ 1 & 1 & 1 & 1 \end{bmatrix}, \quad M_4 = \tfrac{1}{4}\begin{bmatrix} 1 & i & -1 & -i \\ -i & 1 & i & -1 \\ -1 & -i & 1 & i \\ i & -1 & -i & 1 \end{bmatrix}. \quad (3.29)$$

The elements of the symmetry adapted basis are finally given as:

$$
\begin{aligned}
|A_{1/2},(0,0,k_z),i\rangle &= |(0,0,k_z),i\rangle && i\in\{1,6,7\}\\
|A_{1/2},(k_x,k_y,k_z),i\rangle &= \tfrac{1}{2}\left(|b1\rangle+|b2\rangle+|b3\rangle+|b4\rangle\right) && i\in\{1,6,7\}\\
|A_{1/2},(k_x,k_y,k_z),i\rangle &= \tfrac{1}{2}\left(|b1\rangle-i|b2\rangle-|b3\rangle+i|b4\rangle\right) && i\in\{2,3,8\}\\
|A_{1/2},(k_x,k_y,k_z),i\rangle &= \tfrac{1}{2}\left(|b1\rangle-|b2\rangle+|b3\rangle-|b4\rangle\right) && i=4\\
|A_{1/2},(k_x,k_y,k_z),i\rangle &= \tfrac{1}{2}\left(|b1\rangle+i|b2\rangle-|b3\rangle-i|b4\rangle\right) && i=5,
\end{aligned}
\tag{3.30}
$$

$$
\begin{aligned}
|A_{-1/2},(0,0,k_z),i\rangle &= |(0,0,k_z),i\rangle && i\in\{2,3,8\}\\
|A_{-1/2},(k_x,k_y,k_z),i\rangle &= \tfrac{1}{2}\left(|b1\rangle+|b2\rangle+|b3\rangle+|b4\rangle\right) && i\in\{2,3,8\}\\
|A_{-1/2},(k_x,k_y,k_z),i\rangle &= \tfrac{1}{2}\left(|b1\rangle-i|b2\rangle-|b3\rangle+i|b4\rangle\right) && i=4\\
|A_{-1/2},(k_x,k_y,k_z),i\rangle &= \tfrac{1}{2}\left(|b1\rangle-|b2\rangle+|b3\rangle-|b4\rangle\right) && i=5\\
|A_{-1/2},(k_x,k_y,k_z),i\rangle &= \tfrac{1}{2}\left(|b1\rangle+i|b2\rangle-|b3\rangle-i|b4\rangle\right) && i\in\{1,6,7\},
\end{aligned}
\tag{3.31}
$$

$$
\begin{aligned}
|A_{-3/2},(0,0,k_z),i\rangle &= |(0,0,k_z),i\rangle && i=4\\
|A_{-3/2},(k_x,k_y,k_z),i\rangle &= \tfrac{1}{2}\left(|b1\rangle+|b2\rangle+|b3\rangle+|b4\rangle\right) && i=4\\
|A_{-3/2},(k_x,k_y,k_z),i\rangle &= \tfrac{1}{2}\left(|b1\rangle-i|b2\rangle-|b3\rangle+i|b4\rangle\right) && i=5\\
|A_{-3/2},(k_x,k_y,k_z),i\rangle &= \tfrac{1}{2}\left(|b1\rangle-|b2\rangle+|b3\rangle-|b4\rangle\right) && i\in\{1,6,7\}\\
|A_{-3/2},(k_x,k_y,k_z),i\rangle &= \tfrac{1}{2}\left(|b1\rangle+i|b2\rangle-|b3\rangle-i|b4\rangle\right) && i\in\{2,3,8\},
\end{aligned}
\tag{3.32}
$$

$$
\begin{aligned}
|A_{3/2},(0,0,k_z),i\rangle &= |(0,0,k_z),i\rangle && i=5\\
|A_{3/2},(k_x,k_y,k_z),i\rangle &= \tfrac{1}{2}\left(|b1\rangle+|b2\rangle+|b3\rangle+|b4\rangle\right) && i=5\\
|A_{3/2},(k_x,k_y,k_z),i\rangle &= \tfrac{1}{2}\left(|b1\rangle-i|b2\rangle-|b3\rangle+i|b4\rangle\right) && i\in\{1,6,7\}\\
|A_{3/2},(k_x,k_y,k_z),i\rangle &= \tfrac{1}{2}\left(|b1\rangle-|b2\rangle+|b3\rangle-|b4\rangle\right) && i\in\{2,3,8\}\\
|A_{3/2},(k_x,k_y,k_z),i\rangle &= \tfrac{1}{2}\left(|b1\rangle+i|b2\rangle-|b3\rangle-i|b4\rangle\right) && i=4.
\end{aligned}
\tag{3.33}
$$

The Hamiltonian matrix elements between basis elements having different symmetry are equal to zero implying that in this basis the Hamiltonian matrix is block diagonal with four blocks (Fig. 3.2) of sizes $N_1\times N_1$, $N_1\times N_1$, $N_2\times N_2$

and $N_2 \times N_2$, respectively. The time necessary to diagonalise the matrix of size $N \times N$ scales approximately as N^3. Therefore the block diagonalisation obtained reduces the computational time approximately by a factor of 16. Since all the basis vectors of the symmetry adapted basis are linear combinations of one or four vectors of the plane wave basis, it follows that Hamiltonian matrix elements in the symmetry adapted basis can be expressed as linear combinations of one, four or sixteen Hamiltonian matrix elements in the plane wave basis. Therefore all the elements of the four blocks are given by analytical formulae that can be easily derived from the analytical formulae for the matrix elements in the plane wave basis given in Appendix A.

It can be proved by considering the two dimensional double valued irreducible representations of the group C_{4v} [136] that states with the same absolute value of m_f are degenerate in pairs (the Kramer's degeneracy). This degeneracy is lifted in the presence of external axial magnetic field B when the symmetry reduces from C_{4v} to C_4 and the time reversal symmetry relation $E_{m_f}(B) = E_{-m_f}(-B)$ holds then.

3.3.3 Piezoelectric effect

It has been pointed out [195, 196] that piezoelectric effects in single dots of realistic sizes are small, changing the eigen-energies of the ground state of the system by about $\sim 1\,\mathrm{meV}$, and can be ignored as a first approximation. It has also been shown that in a vertically stacked double quantum dot the influence of a piezoelectric field is more important since the piezoelectric potential generated by the two dots adds up in the regions above and below the dots, while it is almost cancelled out in the region between the dots. Consequently, it is expected that in a periodic array of vertically stacked quantum dots considered in Sec. 3.4 the piezoelectric potential in the region between the dots would be almost cancelled out and that the influence of piezoelectric effect on eigen-energies would be small.

Therefore the piezoelectric potential that breaks the symmetry of the sys-

tem from C_4 to C_2 can be treated as a perturbation. It belongs to the A_2 representation of the C_4 group and therefore only the matrix elements between the states with $\Delta m_f = 2$ are non zero. Consequently, the piezoelectric potential doesn't change the energies in the first order of the perturbation theory and second order perturbation theory is needed to take the piezoelectric effect into account.

3.3.4 Notation of states

The following notation for the electron states is introduced: ne_{m_f}, where n is a positive integer labelling the states with given m_f in increasing order of their energy. Since the quantum number m_f originates from the double valued irreducible representations of the group C_4 whose elements are generated by the total angular momentum, its physical interpretation is that it represents the total quasi-angular momentum. The hole states will be labelled by nh_{m_f}, with the same meaning of the symbol as for the electron case, except that n labels the states in decreasing order of their energy, as is natural for holes.

One can verify that after calculating the matrix elements of interaction with an electromagnetic field in the dipole approximation (2.69) between states with a well defined symmetry, the following selection rules are obtained: If the light is $z-$polarised then $\Delta m_f = 0$, while if the light is $\sigma^{\pm}$ circularly polarised then $\Delta m_f = \pm 1$ (where by definition $3/2 + 1 = -3/2$ and $-3/2 - 1 = 3/2$).

3.4 Results

The method presented was applied to the calculation of the electronic structure of periodic arrays of vertically stacked pyramidal self-assembled quantum dots (Fig. 3.3). The dimensions of the dots in an array were taken to be equal to those estimated for the structure reported in Ref. [197] - the base width $b = 18\,\mathrm{nm}$, the height $h = 4\,\mathrm{nm}$, the wetting layer width $d_{\mathrm{WL}} = 1.7\,\mathrm{ML}$, while the period of the structure in $z-$direction L_z was varied in the interval from

$L_z = h + d_{\mathrm{WL}}$ where the dots lie on top of one another to $L_z = 16\,\mathrm{nm}$.

The dimensions of the embedding box $L_x = L_y = 2b$ were taken and 13 plane waves per dimension ($n_x = n_y = n_z = 6$) were enough to obtain convergence of the order 1 meV for all the states considered. The calculations have therefore been performed with $n_x = n_y = n_z = 5$ which leads to matrices of size $\sim 2600 \times 2600$ that can be routinely diagonalised on single processor machines using standard LAPACK [198] routines.

A comment is necessary at this time about the meaning of the choice of the box size in the calculation. A choice of the box size of the dimensions L_x, L_y, and L_z and the application of the plane wave method implies that it is actually the state of three dimensional superlattice with periods L_x, L_y, and L_z that is modelled. If one wishes to model a single dot, L_x, L_y, and L_z have to be sufficiently large, and if one wishes to model a one dimensional quantum dot superlattice, as is the case in this Chapter, L_x and L_y have to be large. It is currently known (and has also been confirmed in Sec. 3.4.2) that carrier wavefunctions decay exponentially away from the dot, and therefore a box whose sides are approximately twice larger than the dot dimensions is sufficiently large for unstrained structures, as has been demonstrated for example in Ref. [199]. However, the strain decays more slowly, with a power law, and a larger box would be necessary for calculations of strained structures. For larger boxes, it follows that a larger number of plane waves becomes necessary, which significantly slows down the calculation. On the other hand, self-assembled quantum dots within one layer are usually not isolated and a dot feels the strain field from neighbouring dots. Although the dots within a layer are not arranged in a perfect two dimensional superlattice, the superlattice model still gives an estimate of the strain field of neighbouring dots.

The material parameters were taken from Ref. [3] and are summarised in Appendix C. According to Bloch's theorem, the $k-$th component of the state spinor is given by

$$\Psi_k(\boldsymbol{r}) = \exp(iK_z z)\psi_k(\boldsymbol{r}), \tag{3.34}$$

where $k \in \{1, 2, \ldots, 8\}$ and $\psi_k(\boldsymbol{r})$ is periodic in the $z-$direction with the period L_z. Therefore, the matrix elements in the four blocks of the Hamiltonian matrix for calculating $E(K_z)$ are given by linear combinations of the elements obtained by the same formulae from Sec. 3.2 except that k_z and q_z should be replaced by $k_z + K_z$ and $q_z + K_z$, respectively. Since the relation $E(K_z) = E(-K_z)$ holds, only the states with $K_z \geq 0$ will be considered. The InAs unstrained conduction band edge is taken as the energy reference level.

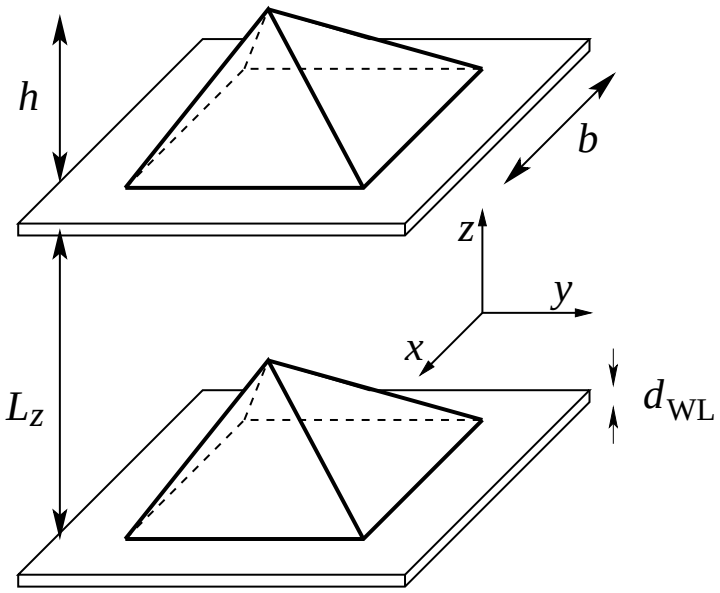

Figure 3.3: Geometry of a periodic array of pyramidal quantum dots. The width of the pyramid base is b, the height h, the wetting layer width d_{WL}, the period of the structure is L_z.

The small piezoelectric effect was assumed to be negligible in the calculation. In order to check this assumption it was included in the framework of second order perturbation theory (Sec. 3.3). Its influence on the state energies was of the order of 1 meV and less, confirming the assumption.

3.4.1 Quantum mechanical coupling and strain distribution

Two main factors influence the electronic structure of the periodic array of quantum dots: the strain distribution and quantum mechanical coupling.

The influence of quantum mechanical coupling is intuitively clear - as the distance between the dots increases the coupling is weaker implying smaller miniband widths. Due to their large effective mass, heavy-holes are the least influenced by coupling and the minibands of dominantly heavy-hole like states are narrow, while the minibands of electron and light-hole states are much wider.

On the other hand, the strain distribution is complex and in principle all six components of the strain tensor influence the electronic structure. Still, the most important are hydrostatic strain $e_h = e_{11} + e_{22} + e_{33}$ that determines the position of the electron and hole levels and biaxial strain $e_b = e_{33} - \frac{1}{2}(e_{11} + e_{22})$ whose main influence is on the splitting of the light and heavy-hole states. The bigger the value of hydrostatic strain, the lower the conduction band states are in energy and the higher the valence band states are in energy. When the biaxial strain is negative, the light-holes tend to have higher energy than heavy-holes, while when it is positive the situation is opposite. Having the importance of those two components of strain in mind, it has been investigated first how they change when the distance between the dots in an array is varied. It has been found that as the distance between the dots increases, the hydrostatic strain in the dots decreases. On the other hand, for small values of the period, the biaxial strain is negative, while for larger values it changes sign and increases further.

3.4.2 Energy levels in the conduction band

The dependence of the miniband minima and maxima on the period of the structure is given in Fig. 3.4. This behaviour is expected. When the dots

are close, they are strongly coupled and the minibands are wide, while as L_z increases the coupling is weaker and the energy spectrum becomes discrete. For large values of the period when the miniband width practically vanishes, one can still see a rising trend in energy. This rise is caused by a still decreasing value of hydrostatic strain. This leads to the conclusion that the range of strain effects is larger than the range of quantum mechanical coupling.

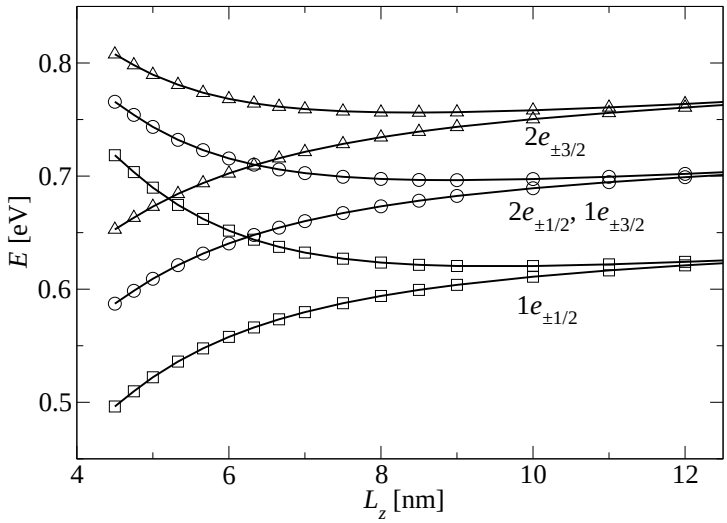

Figure 3.4: The conduction miniband minima and maxima dependence on the period of the structure L_z. The $1e_{\pm 1/2}$ miniband is represented by squares, the $1e_{\pm 3/2}$ and $2e_{\pm 1/2}$ miniband by circles, the $2e_{\pm 3/2}$ miniband by triangles.

The ground miniband has $|m_f| = 1/2$ symmetry, while the first and second excited miniband having different symmetries $|m_f| = 1/2$ and $|m_f| = 3/2$ are nearly degenerate. Their difference in energy is less than 1 meV, too small to be seen on the graph. A comment should be given about the near degeneracy of those two states. It has been a practice in the literature to say that these two states are exactly degenerate in the absence of a piezoelectric effect and that the piezoelectric effect breaks the degeneracy of these states. This is indeed true if the carrier energy spectrum in the quantum dot is modelled by a simple one band Schrödinger equation. The symmetry group is then C_{4v}, consisting

of transformations in real space generated by the orbital angular momentum $\hat{L}_z$ and the first and second excited state transform according to the same two dimensional irreducible representation of C_{4v}, implying their degeneracy. However, when the 8-band $\boldsymbol{k} \cdot \boldsymbol{p}$ model, which is inherently spin-dependent, is used, the Hamiltonian no longer commutes with the rotations generated by orbital angular momentum, but the total angular momentum. In the case when the symmetry of the 8-band $\boldsymbol{k} \cdot \boldsymbol{p}$ Hamiltonian is used, the symmetry group is the C_4 group that has only the one dimensional irreducible representations and there is no *a priori* reason for the states with different absolute values of m_f to be degenerate.

In order to explain the near degeneracy of the states with different symmetry, the 8-band $\boldsymbol{k} \cdot \boldsymbol{p}$ Hamiltonian was further investigated and it has been checked that it would still commute with the transformations in real space generated by orbital angular momentum if the valence band spin-orbit splitting would be set to zero. Since the influence of valence band spin-orbit splitting on the levels in the conduction band is not substantial, the degeneracy of the two states is small. This implies that the origin of splitting of the first and the second excited state is not just the piezoelectric effect but also the valence band spin-orbit splitting.

All the minibands shown in Fig. 3.4 exhibit minima at $K_z = 0$ and maxima at $K_z = \pi/L_z$ for all values of the period L_z. For small values of the period L_z there is an energy overlap between different minibands, while the minibands are completely separated for larger values of L_z. There is no crossing between states of different symmetry.

3.4.3 Energy levels in the valence band

The miniband minima and maxima dependence on the period of the structure are given in Fig. 3.5 for the three highest minibands in the valence band. Due to the combined effects of strain, mixing of light and heavy-holes and quantum mechanical coupling between the dots, the hole minibands exhibit a

more complex structure than the electron minibands.

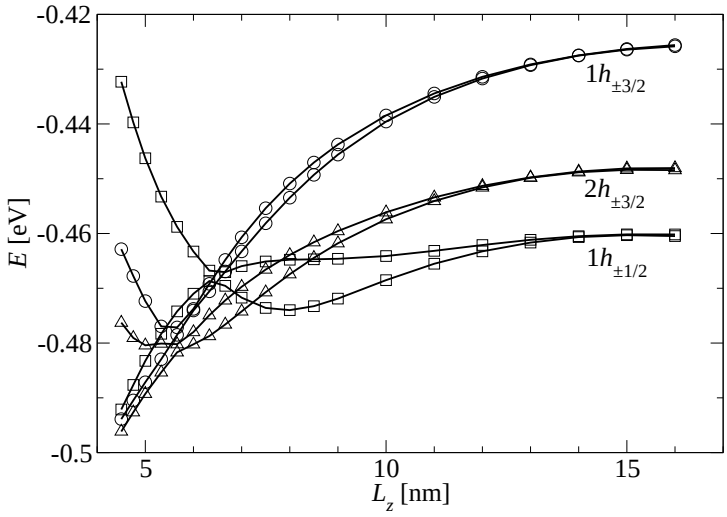

Figure 3.5: The miniband minima and maxima dependence on the period of the structure L_z. The $1h_{\pm 1/2}$ miniband is represented by squares, the $1h_{\pm 3/2}$ miniband by circles and the $2h_{\pm 3/2}$ miniband by triangles.

In order to explain such behaviour it should be noted first that the effective potential felt by carriers depends on K_z. One can define the effective potential as the value obtained by diagonalising the Hamiltonian with $k_x = k_y = 0$ and $k_z = K_z$. The z-dependence of electron, light, heavy and split-off hole $K_z = 0$ and $K_z = \pi/L_z$ effective potentials at the pyramid axis for a few different values of L_z is shown in Fig. 3.6.

Since the effective mass of the light-holes is small, the light-hole effective potential is substantially different for $K_z = 0$ and $K_z = \pi/L_z$, while in the case of heavy-holes that difference is much smaller. As can be seen from Fig. 3.6, as the period of the structure increases, the effective potential felt by $K_z = 0$ light-holes decreases, while quite oppositely the effective potential felt by heavy-holes increases. Both of these trends are an expected consequence of the increase in the value of the biaxial strain. Consequently, in the range of low values of L_z the hole states with $K_z = 0$ are dominantly of the light-

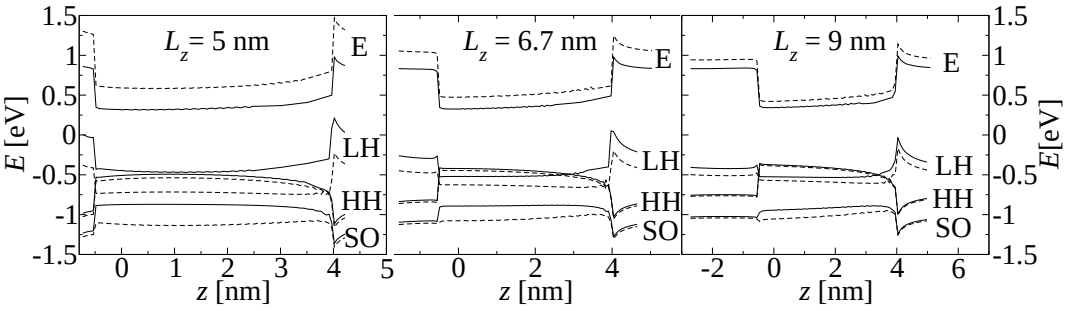

Figure 3.6: Effective potentials at three different values of the period L_z at $K_z = 0$ (full lines) and $K_z = \pi/L_z$ (dashed lines) for electrons (E), light-holes (LH), heavy-holes (HH) and split-off holes (SO).

hole type, while the states with $K_z = \pi/L_z$ are dominantly heavy-hole like. The states with $K_z = \pi/L_z$ remain of the heavy-hole type across the whole investigated interval of L_z and their energy therefore increases with increasing L_z. The energy of the light-hole $K_z = 0$ states decreases with increasing L_z and at the same time their heavy-hole content increases. As a consequence of two different energy trends for $K_z = 0$ and $K_z = \pi/L_z$ the miniband width decreases for all the states until a certain point where the energy of the $K_z = 0$ state becomes less than the energy of the $K_z = \pi/L_z$ state. This point, where the inversion of the sign of the miniband effective mass occurs is different for different states, for the $1h_{\pm 1/2}$ state it occurs around $L_z = 6.5\,\mathrm{nm}$, while for the $1h_{\pm 3/2}$ and $2h_{\pm 3/2}$ states it occurs around $L_z = 5.8\,\mathrm{nm}$. The light-hole content of the $K_z = 0$ states decreases with increasing L_z and eventually they become dominantly heavy-hole like. This light to heavy-hole transition occurs at $L_z = 7.5\,\mathrm{nm}$ for the $1h_{\pm 1/2}$ state, at $L_z = 5.5\,\mathrm{nm}$ for the $1h_{\pm 3/2}$ state and $L_z = 5.0\,\mathrm{nm}$ for the $2h_{\pm 3/2}$ state. Since the energy of the light-hole states decreases with increasing L_z and the energy of the heavy-hole states increases, the position of the light to heavy- hole transition corresponds approximately to the position of the energy minima of $K_z = 0$ states, as can be verified from Fig. 3.5. One can further observe that the ground hole state for $L_z \leq 6.5\,\mathrm{nm}$

is $1h_{\pm 1/2}$ having $|m_f| = 1/2$ symmetry, while for $L_z > 6.5\,\mathrm{nm}$ it is $1h_{\pm 3/2}$ having $|m_f| = 3/2$ symmetry. Therefore at the critical point $L_z = 6.5\,\mathrm{nm}$, an interesting effect of a simultaneous change of ground hole state symmetry, a change of the sign of the effective mass and a change of the ground state type from light to heavy-hole like, is observed.

The split-off band certainly influences the exact positions of the energy levels, however, being far in energy from the light and heavy-hole bands it doesn't influence the overall behaviour described in the previous paragraph. This is verified by the fact that the spin orbit band content of the hole states is typically of the order of 5%.

As far as the spatial localisation of the wavefunctions is concerned, one would expect from the effective potential profiles given in Fig. 3.6 that dominantly light-hole states would be confined outside the dots and dominantly heavy-hole states inside the dots. However, the states are of light-hole type only when the dots are very close to each other and the effective potential well is then too narrow to confine the hole. Therefore, the light-hole like states are spread both inside and outside the dots. When the distance between the dots increases and light to heavy-hole transitions take place, the hole state becomes localised inside the dots.

3.4.4 Influence of external axial magnetic field

The magnetic field dependences of the miniband minima and maxima of the conduction and valence band states for the structure with the period $L_z = 6\,\mathrm{nm}$ are shown in Figs. 3.7 and 3.8, respectively. As already mentioned, Kramer's degeneracy is broken in a magnetic field. The relation $E_{m_f}(B) = E_{-m_f}(-B)$ holds, thus only the $B \geq 0$ part of the dependence is shown on the graphs.

The magnetic field splitting between $1e_{+3/2}$ and $1e_{-3/2}$ states, as well as between $2e_{-1/2}$ and $2e_{+1/2}$ states is significant because the mesoscopic angular momentum [200] of those states is different from zero. However, the splitting between the $1e_{-1/2}$ and the $1e_{+1/2}$ states and between the $2e_{+3/2}$ and the $2e_{-3/2}$

is much smaller, too small to be seen on the graph (of the order of few meV). There is no crossing between states of different symmetry. The $1e_{+1/2}$ and $1e_{-1/2}$ minibands overlap with $2e_{-1/2}$ and $1e_{-3/2}$ minibands for $B = 0$ but as the magnetic field is increased this overlap vanishes (for $B \gtrsim 12\,\mathrm{T}$). The energy separation of the minibands has an important effect on the dynamical characteristics of the structure since it suppresses all the one particle energy conserving scattering mechanisms between those minibands (like ionised impurity scattering) and with further separation even suppresses the mechanisms with energy exchange (like acoustic phonon and longitudinal optical phonon scattering).

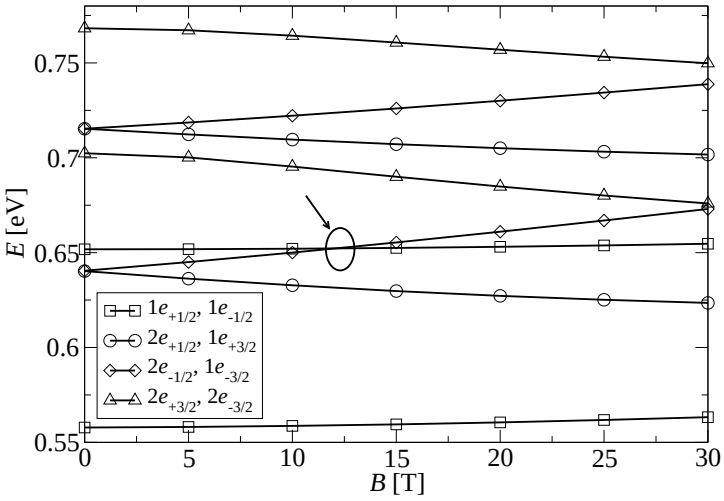

Figure 3.7: Magnetic field dependence of miniband minima and maxima for $1e_{-3/2}$, $1e_{-1/2}$, $1e_{+1/2}$, $1e_{+3/2}$, $2e_{-3/2}$, $2e_{-1/2}$, $2e_{+1/2}$ and $2e_{+3/2}$ states. The position where different minibands separate is marked.

The splitting between the hole states is also of the order of a few meV, however since the energy difference between different states is also small, this splitting is enough to cause crossings between states of different symmetry. It is further found from Fig. 3.8 that the minibands $1h_{-3/2}$ and $1h_{+3/2}$ that are degenerate at $B = 0$ become completely separated already at $B \gtrsim 3\,\mathrm{T}$

and the same effect for $2h_{-3/2}$ and $2h_{+3/2}$ occurs at $B \gtrsim 23\,\mathrm{T}$. Although the magnetic field splitting is the most pronounced for the $1h_{-1/2}$ and $1h_{+1/2}$ states, the effect of the separation of those minibands occurs at magnetic fields larger than 30 T, which is a consequence of a larger miniband width than in the previous cases. Apart from separation of the minibands, the magnetic field can also concatenate otherwise nonoverlapping minibands. It is seen in Fig. 3.8 that $1h_{+1/2}$ and $1h_{-3/2}$ start to overlap at $B \sim 11\,\mathrm{T}$ and that for $B \gtrsim 22\,\mathrm{T}$ the range of energies of $1h_{-3/2}$ becomes a subset of the range of energies of $1h_{+1/2}$ miniband.

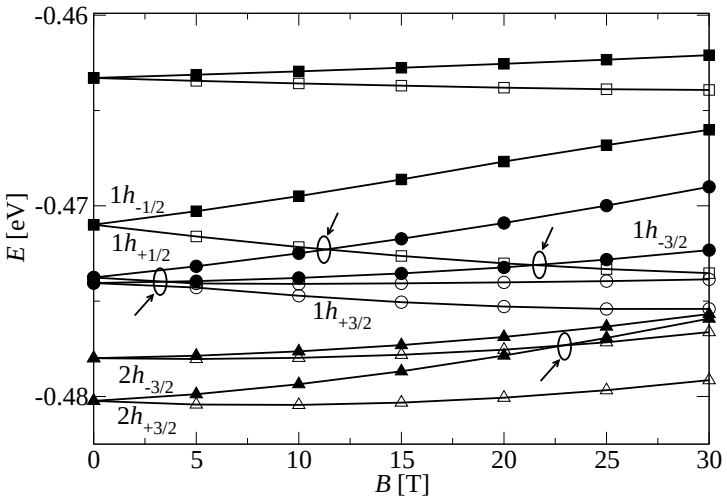

Figure 3.8: Magnetic field dependence of miniband minima and maxima for $1h_{-3/2}$ (full circles), $1h_{+3/2}$ (empty circles), $1h_{-1/2}$ (full squares), $1h_{+1/2}$ (empty squares), $2h_{-3/2}$ (full triangles) and $2e_{+3/2}$ (empty triangles) states. The positions where different minibands separate or concatenate are marked.

3.5 Conclusion

In conclusion, a symmetry based method for the calculation of electronic states in pyramidal InAs/GaAs quantum dots was developed. The corresponding Hamiltonian matrix obtained by the plane wave method was block diago-

nalised into four matrices of approximately equal size, which enabled significantly faster calculation of energy levels within the plane wave method. The symmetry considerations not only enabled more efficient calculation of the electronic structure but also give more insight about the physics of the system by introducing the quantum number of total quasi-angular momentum and giving the selection rules for interaction with an electromagnetic field. The method developed was applied to calculate the electronic structure of a periodic array of vertically stacked pyramidal self-assembled quantum dots. It was found that as the distance between the dots is increased, at a certain critical point the ground hole state simultaneously changes symmetry from $|m_f| = 1/2$ to $|m_f| = 3/2$ and type from light to heavy-hole. The influence of magnetic field on the energy levels is in general less pronounced than the influence of quantum mechanical coupling and strain but nevertheless it can be used for fine tuning of the properties of the structure since its increase or decrease is able to separate energy overlapping minibands.

The work presented in this Chapter was published in Physical Review B [201].

Chapter 4

Symmetry based calculation of single-particle states and intraband absorption in hexagonal GaN/AlN quantum dots

4.1 Introduction

Wide band-gap III-nitride materials attracted significant research attention in the 1990s which led to the demonstration of commercially attractive emitters in the blue and ultra-violet spectral range [202]. Further improvements in GaN based optoelectronic devices [203] have been achieved by using GaN quantum dots [204–206] in the active region. GaN quantum dots have also been shown to be promising for the realisation of solid state quantum computing [207, 208]. In the last few years, intraband transitions in the telecommunications wavelength range (1.3-1.55 μm) in GaN/AlGaN low dimensional heterostructures at room temperature have been demonstrated [209–212]. Due to ultrafast electron dynamics caused by enhanced interaction with longitudinal optical phonons these transitions can be exploited for realising detectors and optical modulators operating at high bit-rates. Theoretical proposals also suggest the possibility of operation of GaN quantum well based unipolar devices in the Reststrahlenband ($\sim 34\,\mu$m) where III-As based unipolar devices cannot operate [213, 214]. Most recently, intersubband luminescence from GaN quantum wells was observed [215].

Having all these possible applications of GaN heterostructures and particu-

larly quantum dots in mind, there have been several theoretical studies of their electronic structure [144, 216–221]. The energy levels of GaN/AlGaN hexagonal quantum dots taking into account the strain distribution as well as the internal electric fields generated due to spontaneous and piezoelectric polarisation were calculated in Ref. [144] using the plane wave expansion method within the framework of the $\boldsymbol{k}\cdot\boldsymbol{p}$ model and in Refs. [216] and [217] using the tight-binding approach. Spherical unstrained GaN quantum dots have also been studied theoretically [218, 219]. However, although the electronic states in III-nitride dots have been symmetry classified in Ref. [193], the hexagonal symmetry of the dots hasn't yet been exploited in the calculation of the single-particle states. So far, the intraband absorption in III-nitride quantum dots was treated within the simple quantum well approach only [211]. No theoretical studies of intraband absorption taking into account a fully three dimensional nature of electron confinement have been reported.

Along this line, the aim of this Chapter is to extend the method developed in Chapter 3 to exploit the symmetry in the calculation of energy levels of hexagonally shaped III-nitride quantum dots within the framework of the $\boldsymbol{k}\cdot\boldsymbol{p}$ method. Furthermore, the symmetry based method developed is applied to study intraband transitions in these dots theoretically.

4.2 Theoretical framework

The 8-band $\boldsymbol{k}\cdot\boldsymbol{p}$ Hamiltonian for semiconductors with wurtzite crystal structure [143] can be block diagonalised into two 4-band Hamiltonians for carriers with opposite values of spin assuming the spin-orbit splitting Δ_{so} is zero. The state of the electron is then of the form

$$|\Psi\rangle = \sum_{l=1}^{4} \psi_l(\boldsymbol{r})|l\rangle, \tag{4.1}$$

where $\psi_l(\boldsymbol{r})$ are the slowly varying envelope functions of electron states ($l = 1$), heavy-hole states ($l = 2$ and $l = 3$), and light-hole states ($l = 4$), and $|l\rangle$ the corresponding Bloch functions given by (2.25). The 4-band Hamiltonian is of

the form

$$\hat{H} = \hat{H}_k + \hat{H}_s + V_p I_4, \tag{4.2}$$

where $\hat{H}_k$ is the kinetic part of the Hamiltonian (Eq. (2.26)), $\hat{H}_s$ is the strain part (Eq. (2.39)), V_p is the potential induced due to spontaneous and piezoelectric polarisations present in III-nitride materials [222] and I_4 is the 4×4 unity matrix.

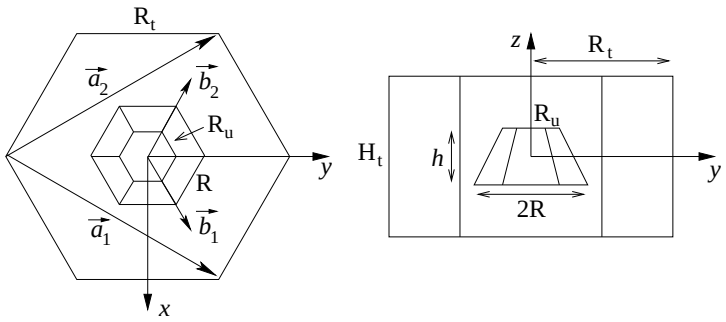

Figure 4.1: Schematic view of a truncated hexagonal pyramid quantum dot with upper base radius R_u, lower base radius R and height h embedded in a hexagonal prism with radius R_t and height H_t – top view (left) and side view (right). The primitive vectors of the corresponding Bravais lattice ($\boldsymbol{a}_1$ and $\boldsymbol{a}_2$) and its reciprocal lattice ($\boldsymbol{b}_1$ and $\boldsymbol{b}_2$) are also shown in the figure.

In the plane wave expansion method, the dot is conventionally embedded in a rectangular box and the plane waves that form the basis of functions periodic on a cubic lattice are taken. However, in this work, due to the hexagonal shape of the dots, it seems more natural to embed the dot in a hexagonal prism and take the plane waves that form the basis of functions periodic on a hexagonal lattice in the expansion. Hence, let the dot be embedded in a hexagonal prism with side length R_t and height H_t, as shown in Fig. 4.1. The primitive vectors

of the Bravais lattice corresponding to the hexagonal lattice are given by

$$\begin{aligned} \boldsymbol{a}_1 &= R_t \left(\frac{\sqrt{3}}{2} \boldsymbol{e}_x + \frac{3}{2} \boldsymbol{e}_y \right), \\ \boldsymbol{a}_2 &= R_t \left(\frac{-\sqrt{3}}{2} \boldsymbol{e}_x + \frac{3}{2} \boldsymbol{e}_y \right), \\ \boldsymbol{a}_3 &= H_t \boldsymbol{e}_z. \end{aligned} \tag{4.3}$$

The primitive vectors of the reciprocal lattice $\boldsymbol{b}_j$ $(j = 1, 2, 3)$ satisfy the condition $\boldsymbol{a}_i \cdot \boldsymbol{b}_j = 2\pi\delta_{ij}$ and are therefore given by

$$\begin{aligned} \boldsymbol{b}_1 &= \frac{4\pi}{3R_t} \left(\frac{\sqrt{3}}{2} \boldsymbol{e}_x + \frac{1}{2} \boldsymbol{e}_y \right), \\ \boldsymbol{b}_2 &= \frac{4\pi}{3R_t} \left(-\frac{\sqrt{3}}{2} \boldsymbol{e}_x + \frac{1}{2} \boldsymbol{e}_y \right), \\ \boldsymbol{b}_3 &= \frac{2\pi}{H_t} \boldsymbol{e}_z. \end{aligned} \tag{4.4}$$

The envelope functions are then assumed in the form

$$\psi_l(\boldsymbol{r}) = \sum_{\boldsymbol{k}} A_{l,\boldsymbol{k}} e^{i\boldsymbol{k}\cdot\boldsymbol{r}}, \tag{4.5}$$

where the summation is performed over $\boldsymbol{k}$ vectors of the form

$$\boldsymbol{k} = m_1 \boldsymbol{b}_1 + m_2 \boldsymbol{b}_2 + m_3 \boldsymbol{b}_3, \tag{4.6}$$

where m_1, m_2 and m_3 are integers.

After putting (4.5) into the Hamiltonian eigenvalue problem

$$\sum_{j=1}^{4} \hat{H}_{ij} \psi_j(\boldsymbol{r}) = E \psi_i(\boldsymbol{r}), \tag{4.7}$$

one arrives at the eigenvalue problem of the Hamiltonian matrix

$$\sum_{j,\boldsymbol{k}} h_{ij}(\boldsymbol{q}, \boldsymbol{k}) A_{j,\boldsymbol{k}} = E A_{i,\boldsymbol{q}}, \tag{4.8}$$

where

$$h_{ij}(\boldsymbol{q}, \boldsymbol{k}) = \frac{1}{V} \int_V \mathrm{d}^3\boldsymbol{r} \exp\left(-i\boldsymbol{q}\cdot\boldsymbol{r}\right) \hat{H}_{ij} \exp\left(i\boldsymbol{k}\cdot\boldsymbol{r}\right) \tag{4.9}$$

are the Hamiltonian matrix elements (the integration is performed over the volume of the embedding hexagonal prism V). They can all be expressed as a linear combination of elements E_i as given in Appendix A.

The elements of the Hamiltonian matrix due to the presence of spontaneous and piezoelectric polarisation are given by [144]

$$h_{ij}^{p}(\boldsymbol{q},\boldsymbol{k}) = \frac{(2\pi)^3}{V}\frac{i|e|}{(\boldsymbol{q}-\boldsymbol{k})^2\varepsilon_0\varepsilon_r}(\boldsymbol{q}-\boldsymbol{k})\cdot\boldsymbol{P}(\boldsymbol{q}-\boldsymbol{k})\delta_{ij}, \tag{4.10}$$

where ε_r is the static dielectric constant, $\boldsymbol{P}(\boldsymbol{q})$ is the Fourier transform of the sum of the spontaneous and piezoelectric polarisation vectors $\boldsymbol{P} = \boldsymbol{P}^{sp} + \boldsymbol{P}^{pz}$. The spontaneous polarisation vector is given by $\boldsymbol{P}^{sp} = P^{sp}\boldsymbol{e}_z$, while the piezoelectric polarisation components are related to strain tensor components by (2.44). The Fourier transform $\boldsymbol{P}(\boldsymbol{q})$ can therefore be calculated in a similar way as the kinetic and strain Hamiltonian matrix elements.

The optical absorption cross section is calculated using (2.68), with the inhomogeneous broadening due to size inhomogeneity of the quantum dot ensemble taken into account by replacing the delta function in Fermi's Golden rule, with a Gaussian given by (2.67). The matrix element (2.69) can be expressed in terms of the coefficients in the plane wave expansion

$$\mathcal{M}_{if}^{\boldsymbol{\epsilon}} = V\sum_{l,\boldsymbol{q}}\sum_{j,\boldsymbol{k}} A_{l,\boldsymbol{q}}^{i*}A_{j,\boldsymbol{k}}^{f}G_{lj}(\boldsymbol{q},\boldsymbol{k}), \tag{4.11}$$

where

$$G_{lj}(\boldsymbol{q},\boldsymbol{k}) = \frac{1}{AV}\int_V \mathrm{d}^3\boldsymbol{r}\exp\left(-i\boldsymbol{q}\cdot\boldsymbol{r}\right)\hat{H}'_{lj}\exp\left(i\boldsymbol{k}\cdot\boldsymbol{r}\right) \tag{4.12}$$

are the Fourier transforms of the perturbation Hamiltonian matrix elements that can also be calculated analytically.

4.3 Symmetry considerations

The symmetry of the hexagonal quantum dot system when the location of every atom is taken into account is C_{3v} and is lower than the symmetry of the dot geometrical shape [189, 193]. In a similar manner as in the case of pyramidal quantum dots made of material of zincblende symmetry, the symmetry of the

8-band $\boldsymbol{k}\cdot\boldsymbol{p}$ model applied to a quantum dot is C_{6v}, being higher than the full atomistic symmetry. The strain part of the Hamiltonian doesn't break that symmetry when the strain distribution is taken into account via the continuum mechanical model [126], as is done here. The spontaneous polarisation is directed along the $z-$axis and obviously preserves the symmetry. In contrast to square based pyramidal InAs/GaAs quantum dots, where piezoelectric effects reduce the symmetry [201] from C_{4v} to C_{2v}, the piezoelectric potential in the dots considered here is C_{6v} symmetric and doesn't affect the symmetry. Consequently, the symmetry of the model is C_{6v}. In this work, only the C_6 symmetry will be exploited as the presence of an external axial magnetic field reduces the symmetry from C_{6v} to C_6, and although magnetic field effects will not be considered in this Chapter, the symmetry adapted basis derived is general enough to be used in such situations as well.

The 4-band Hamiltonian commutes with the rotations around the z-axis by $\varphi_k = k\cdot 2\pi/6$ ($k\in\{0,1,\ldots,11\}$) which are generated by the operator of $z-$component of the total angular momentum $\hat{F}_z$, which is a sum of orbital angular momentum of the envelope function $\hat{L}_z$ and total angular momentum of the Bloch function $\hat{J}_z$. The action of the generator of the double valued representation of the rotation group

$$\hat{D}(R_{\varphi_1}) = e^{-i\hat{F}_z\varphi_1} \tag{4.13}$$

on the basis vectors of Hilbert space

$$|\boldsymbol{k},i\rangle = e^{i\boldsymbol{k}\cdot\boldsymbol{r}}|i\rangle, \tag{4.14}$$

(where $\boldsymbol{k}$ vectors are given by (4.6) and $i\in\{1,2,3,4\}$) is given by

$$\hat{D}(R_{\varphi_1})|\boldsymbol{k},i\rangle = e^{i\boldsymbol{k}'\cdot\boldsymbol{r}}e^{-iJ_z(i)\varphi_1}|i\rangle, \tag{4.15}$$

where $J_z(1)=1/2$, $J_z(2)=3/2$, $J_z(3)=-1/2$, $J_z(4)=1/2$ and the $\boldsymbol{k}$-vector is rotated by φ_1 around the $z-$axis

$$\boldsymbol{k}' = R_{\varphi_1}\boldsymbol{k} = (m_1-m_2)\boldsymbol{b}_1 + m_1\boldsymbol{b}_2 + m_3\boldsymbol{b}_3, \tag{4.16}$$

or in the cartesian coordinates

$$\begin{aligned} k'_x + ik'_y &= e^{i\varphi_1}(k_x + ik_y), \\ k'_z &= k_z. \end{aligned} \tag{4.17}$$

The orbit of action of the group elements on the basis vectors when $(m_1, m_2) = (0, 0)$ is a one dimensional space $\mathcal{H}_{(0,0,m_3),i}$. The labelling introduced of the form $(m_1, m_2, m_3), i$ will also be used in the rest of the text to label the reduction of representation $\hat{D}$ to the space $\mathcal{H}_{(m_1,m_2,m_3),i}$, as well as to label the group projectors and the elements of the symmetry adapted basis belonging to this space. In $\mathcal{H}_{(0,0,m_3),i}$ the representation $\hat{D}$ reduces to

$$\hat{D}_{(0,0,m_3),i}(R_{\varphi_1}) = e^{-iJ_z(i)\varphi_1}. \tag{4.18}$$

On the other hand, when $(m_1, m_2) \neq (0, 0)$ the orbit is a 6-dimensional space $\mathcal{H}_{(m_1,m_2,m_3),i}$ (with $0 \leq m_2 < m_1 \leq n_1 = n_2$ to avoid multiple counting of the same space, and $|m_3| \leq n_3$, where n_1, n_2 and n_3 are positive integers.) spanned by the vectors $|bl\rangle = |R_{l\varphi_1}\boldsymbol{k}, i\rangle$ ($l \in \{0, 1, \ldots, 5\}$). The operator $\hat{D}(R_{\varphi_1})$ in this basis reads

$$\hat{D}_{(m_1,m_2,m_3),i}(R_{\varphi_1}) = e^{-iJ_z(i)\varphi_1} \begin{bmatrix} 0 & 1 \\ I_5 & 0 \end{bmatrix}, \tag{4.19}$$

where I_5 is the 5×5 unity matrix. The characters of the group elements in this representation are then given by

$$\chi(\hat{D}_{(m_1,m_2,m_3),i}(R_{l\varphi_1})) = 6\delta_{l,0} - 6\delta_{l,6} \tag{4.20}$$

and

$$\chi(\hat{D}_{(0,0,m_3),i}(R_{l\varphi_1})) = e^{-iJ_z(i)l\varphi_1}. \tag{4.21}$$

Consequently one finds the reduction of the representation in these spaces to its irreducible double valued representations A_{m_f} whose characters are given by $\chi\left(A_{m_f}(R_{l\varphi_1})\right) = \exp(-ilm_f\varphi_1)$ (where $m_f \in \{-5/2, -2, -3/2, \ldots, 5/2\}$ and $l \in \{0, 1, \ldots, 11\}$):

$$\hat{D}_{(0,0,m_3),i} = A_{J_z(i)} \tag{4.22}$$

and

$$\hat{D}_{(m_1,m_2,m_3),i} = A_{-5/2} + A_{-3/2} + A_{-1/2} + A_{1/2} + A_{3/2} + A_{5/2}. \tag{4.23}$$

From (4.22) and (4.23), one gets that the reduction of $\hat{D}$ to the irreducible representations is given by

$$\hat{D} = N_{-5/2}A_{-5/2} + N_{-3/2}A_{-3/2} + N_{-1/2}A_{-1/2} + N_{1/2}A_{1/2} + N_{3/2}A_{3/2} + N_{5/2}A_{5/2}, \tag{4.24}$$

where $N_{1/2} = 6n_3\,[2 + 2n_1(n_1+1)]$, $N_{-1/2} = N_{3/2} = 6n_3\,[1 + 2n_1(n_1+1)]$ and $N_{-3/2} = N_{5/2} = N_{-5/2} = 12n_3n_1(n_1+1)$. The projection operators [136] are given by

$$\hat{P}_{A_{m_f}}((0,0,m_3),i) = 1 \tag{4.25}$$

and

$$\hat{P}_{A_{m_f}}((m_1,m_2,m_3),i) = \frac{1}{12}\sum_{l=0}^{11} \chi\left(A_{m_f}(R_{l\varphi_1})\right)^* \hat{D}_{(m_1,m_2,m_3),i}(R_{l\varphi_1}). \tag{4.26}$$

After explicit calculation one gets

$$\hat{P}_{A_{m_f}}((m_1,m_2,m_3),i) = M(e^{i\varphi_1(J_z(i)-m_f)}), \tag{4.27}$$

where $M(u)$ is the matrix defined by

$$M(u) = \begin{bmatrix} 1 & u & u^2 & u^3 & u^4 & u^5 \\ u^5 & 1 & u & u^2 & u^3 & u^4 \\ u^4 & u^5 & 1 & u & u^2 & u^3 \\ u^3 & u^4 & u^5 & 1 & u & u^2 \\ u^2 & u^3 & u^4 & u^5 & 1 & u \\ u & u^2 & u^3 & u^4 & u^5 & 1 \end{bmatrix}. \tag{4.28}$$

The elements of the symmetry adapted basis are finally given by

$$\begin{aligned} |A_{1/2},(0,0,m_3),1\rangle &= |(0,0,m_3),1\rangle, \\ |A_{3/2},(0,0,m_3),2\rangle &= |(0,0,m_3),2\rangle, \\ |A_{-1/2},(0,0,m_3),3\rangle &= |(0,0,m_3),3\rangle, \\ |A_{1/2},(0,0,m_3),4\rangle &= |(0,0,m_3),4\rangle, \end{aligned} \tag{4.29}$$

where $-n_3 \leq m_3 \leq n_3$ and

$$|A_{m_f}, (m_1, m_2, m_3), i\rangle = \frac{1}{\sqrt{6}} \sum_{l=0}^{5} e^{il\varphi_1(m_f - J_z(i))} |bl\rangle, \tag{4.30}$$

where $0 \leq m_2 < m_1 \leq n_1 = n_2$, $-n_3 \leq m_3 \leq n_3$, $i \in \{1, 2, 3, 4\}$ and $m_f \in \{-5/2, -3/2, -1/2, 1/2, 3/2, 5/2\}$.

In this basis, the Hamiltonian matrix is block diagonal with 6 blocks of approximately equal size (more precisely, the sizes of the blocks are $N_{1/2}$, $N_{-1/2} = N_{3/2}$ and $N_{-3/2} = N_{5/2} = N_{-5/2}$, see equation (4.24)). Since all the elements of the symmetry adapted basis are linear combinations of the elements of the plane wave basis, all the elements of the 6 blocks of the Hamiltonian matrix can be expressed in terms of the elements of the Hamiltonian matrix in the plane wave basis. The computational time necessary to diagonalise 6 blocks is approximately 36 times smaller than the time necessary within the straightforward plane wave approach.

Apart from reducing the computational time within the plane wave method, the method presented introduces the quantum number m_f which can be interpreted as the total quasi-angular momentum. The selection rules for the interaction with electromagnetic radiation in the dipole approximation have then been derived as: $\Delta m_f = 0$ for $z-$polarised light and $\Delta m_f = \pm 1$ for in-plane polarised light (where by the definition $5/2 + 1 = -5/2$ and $-5/2 - 1 = 5/2$). These rules are very restrictive, and although the quantum dots allow for the absorption of radiation of any polarisation in contrast to quantum wells, these transitions are allowed only for certain pairs of states. The same notation for labelling of states as in Chapter 3 is introduced.

4.4 Results

The method presented was first applied to the calculation of electron and hole energy levels in an ideally periodic array of hexagonal truncated pyramidal GaN/AlN quantum dots. In a realistic case the number of quantum dot layers is finite and therefore the strain distribution and the effective potential are

not strictly periodic. It is also difficult to achieve identical size of the dots in all layers. Nevertheless, in a quantum dot superlattice containing several tens of quantum dot layers one certainly expects that the results obtained within the periodic model can be used as a very good approximation of the actual system. The dot radius was taken to be $R = 9.0\,\text{nm}$, the height $h = 3.7\,\text{nm}$, the upper base radius $R_u = 3.5\,\text{nm}$ and the diameter of the embedding box $2R_t = 30.0\,\text{nm}$. The period of the superlattice was varied over the interval from $H_t = 4.3\,\text{nm}$, when the dots almost lie on top of one another, to $H_t = 12.3\,\text{nm}$. Material parameters in the calculation were taken from Ref. [4] and are summarised in Appendix C. The unstrained AlN conduction band edge was taken as the reference level.

The number of plane waves used in the calculation was $n_1 = n_2 = 12$ and $n_3 = 10$. In order to check that this number of plane waves is enough, the calculation of energy levels has been performed with different number of plane waves used. Three sets of calculations were done - in the first set both $n_1 = n_2$ and n_3 were set to the same value n, which was then varied, in the second $n_1 = n_2$ were set to 12 and n_3 to the value n that was varied, and finally n_3 was set to 10 and $n_1 = n_2$ were varied. The results of the test are shown in Fig. 4.2. The energies of the ground state and the excited state to which the absorption of $z-$polarised radiation is dominant, are presented in the figure. As expected, more plane waves are needed to achieve the same level of precision in the calculation of excited states than in the case of the ground state. One can see that already for $n_1 = n_2 = n_3 \sim 7 - 8$ the errors become of the order 10 meV, which may be a sufficient precision having in mind the large values of band offset in the investigated material system and the uncertainties in the values of III-nitride band parameters. The number of plane waves chosen for the rest of the calculations provides convergence to better than 1 meV for the ground state in the conduction band and the convergence of the order of 1 meV for those excited states in the conduction band that are mainly responsible for the absorption of $z-$polarised radiation. The number of plane waves necessary

to obtain a certain degree of precision in GaN/AlN quantum dots is therefore larger than for the same precision in InAs/GaAs quantum dots. The main reason for this is the presence of an effective triangular potential well that localises the electrons near the top of the dot, and the holes near the bottom of the dot (Fig. 4.6). The wavefunctions are therefore localised in a small area of space and therefore plane waves with higher wave numbers are necessary to accurately represent them.

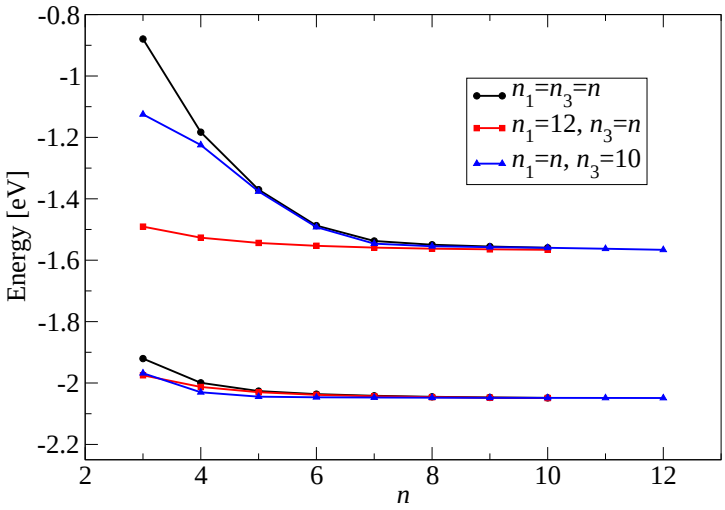

Figure 4.2: The results of the convergence test. Dependence of the energy of the ground state ($1e_{1/2}$) and $4e_{1/2}$ state on the number of plane waves used. Superlattice period is $H_t = 8.3\,\mathrm{nm}$.

The effective electron potential on the z-axis defined as $V_e = H_{11}(k = 0)$, the heavy-hole potential defined as $V_{hh} = H_{22}(k = 0)$, and the light-hole potential defined as $V_{lh} = H_{44}(k = 0)$ are shown in Figs. 4.3 and 4.4. One can see that significant changes in the effective potentials occur when varying the period of the structure, which therefore influence considerably the electronic structure of the quantum dot superlattice.

The electron and hole energy levels, when the period is varied in the above interval, are shown in Fig. 4.5. For each value of m_f, the first few energy

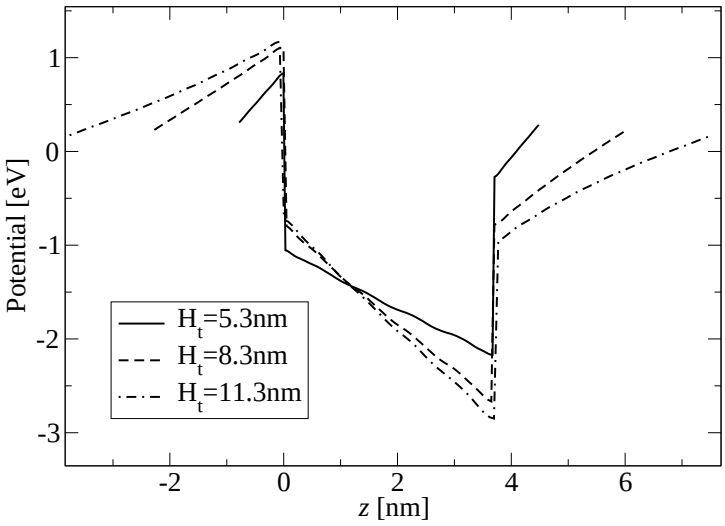

Figure 4.3: The effective potential on the z-axis experienced by electrons for three different values of the period H_t.

levels in the conduction band and the highest energy level in the valence band are shown. A very weak dispersion with the superlattice Bloch wave vector K_z was found and therefore only $K_z = 0$ states are presented. To illustrate this effect, the wavefunctions of the electron and hole ground states when the period is equal to $H_t = 5.3\,\text{nm}$ are shown in Fig. 4.6. One can see that there is no overlap between the states of neighbouring periods and hence no electronic coupling. Therefore, even in the case of dots that almost lie on top each other, electronic coupling is almost negligible. The origin of such a weak electronic coupling between dots in a superlattice is the strong internal electric field (see Figs. 4.3 and 4.4) that creates a deep triangular potential well at the top of the dot for electrons (and at the bottom of the dot for holes) which prevents interaction between neighbouring dots. Another effect caused by the electric field that can be also verified from Fig. 4.6 is the localisation of the electron states at the top of the dot and hole states at the bottom of the dot, as previously reported by others [144, 223].

The energy levels with $m_f = -1/2$ and $m_f = 3/2$ are degenerate. The

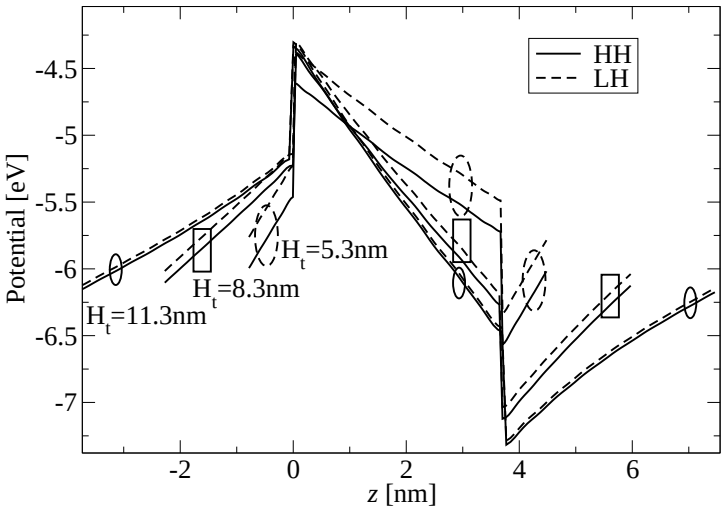

Figure 4.4: The effective potential on the z-axis experienced by light- (LH) and heavy-holes (HH) for three different values of the period H_t.

same holds for $m_f = -3/2$ and $m_f = 5/2$. The origin of these degeneracies is the fact that the used 4-band Hamiltonian also commutes with the operators of rotations and reflections in *real* space, that form the single valued representation of the C_{6v} group. The mentioned degeneracy then stems from two dimensional irreducible representations of the C_{6v} group.

One can see from Fig. 4.5 that as the superlattice period increases, the effective energy gap of the structure decreases, in contrast to the behaviour observed in InAs/GaAs. Such a behaviour is governed by the changes in the value of the internal electric field. As the distance between the dots increases, the field in the dot also becomes larger, the effective electron and hole potential wells are therefore deeper (Figs. 4.3 and 4.4) and consequently both electron and hole states are more confined.

The type of hole states is further discussed: When the superlattice period is small ($H_t \sim 5\,\mathrm{nm}$), the effective potential for light-holes is significantly larger than for heavy-holes (Fig. 4.4) and despite the smaller light-hole effective mass, they are more strongly confined and therefore the hole ground state is of light-

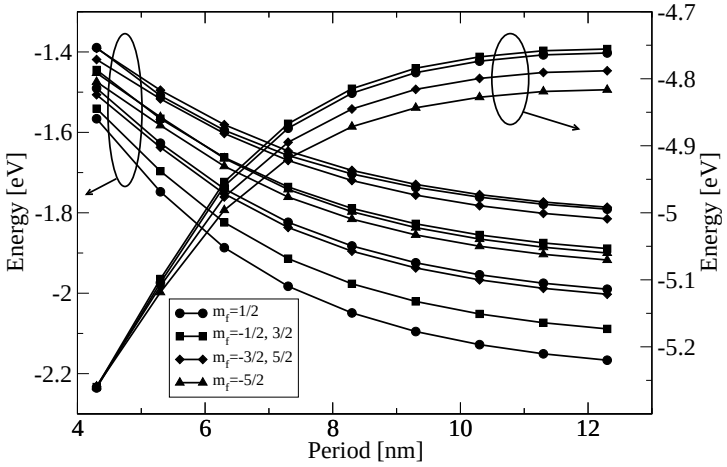

Figure 4.5: The dependence of electron (left axis) and hole (right axis) energy levels on the superlattice period. For each value of m_f, the first few energy levels in the conduction band and the highest energy level in the valence band are shown.

hole type. However, when the period increases, the difference between the light and heavy-hole effective potentials becomes smaller, and due to the larger effective mass, the hole ground state becomes of the heavy-hole type. In the intermediate region, one finds that the ground hole state is a mixed light- and heavy-hole state. However, this region is very narrow and although interesting effects in the optical spectrum due to hole mixing can be expected, it would be very hard to access this region experimentally. As far as excited hole states are concerned, due to the above mentioned effects, when the period increases the heavy-hole character of the states also prevails.

As the ground electron state has $m_f = 1/2$ and selection rules for the absorption of $z-$polarised radiation only allow the transitions with $\Delta m_f = 0$, it follows that the peak positions in the $z-$polarised radiation absorption spectrum will be determined by the positions of the energy levels having $m_f = 1/2$ symmetry. The dependence of the positions of the $m_f = 1/2$ energy levels on the period of the structure is given in Fig. 4.7. One can see that the first

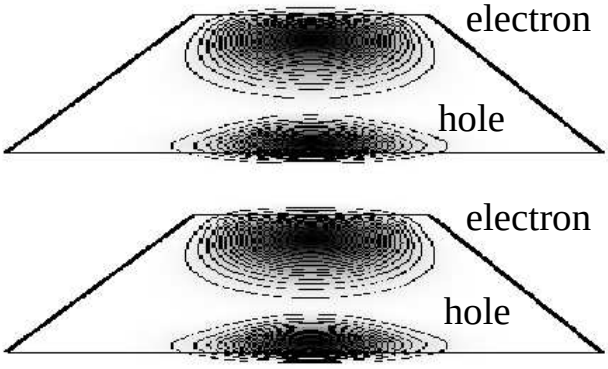

Figure 4.6: Wavefunction moduli squared in the yz-plane of the electron and hole ground states when the period is equal to $H_t = 5.3\,\mathrm{nm}$.

three well separated energy levels (labelled as 1, 2 and 3) are followed by three groups of closely spaced levels (labelled as G1, G2 and G3).

Although the symmetry allows transitions from the ground state to any of the $m_f = 1/2$ states, it turns out that only some of these transitions have significant values of matrix elements. The intraband optical absorption spectrum from the ground state for $z-$polarised radiation is shown in Fig. 4.8. The standard deviation σ of the Gaussian linewidth on each of the transitions was taken to be equal to 10% of the transition energy, which is approximately the experimental value in Ref. [211]. The strongest absorption occurs for the transition from the ground state to the states from the G1 group, as the matrix elements for these transitions are the largest, Fig. 4.9 (among them the strongest is the transition to $4e_{1/2}$). The absorption maximum at $H_t = 8.3\,\mathrm{nm}$ occurs at 490 meV, and is followed by a weaker line with a maximum at 860 meV originating from the transitions to the G3 group of states. These results are in reasonable agreement with the experimental results of Ref. [211], where for the same value of the period and for dots of similar size the strongest absorption occurs at 520 meV or 590 meV for two different samples investigated there, and is followed by two weaker lines at 730 meV and 980 meV or 850 meV and

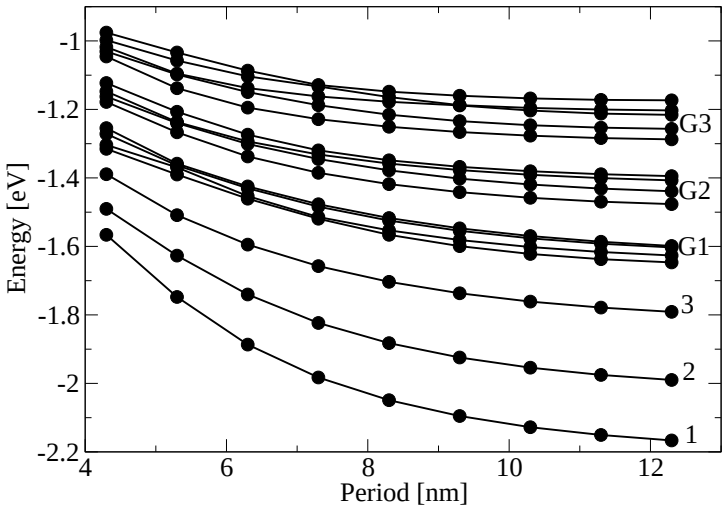

Figure 4.7: The dependence of the $m_f = 1/2$ electron energy levels on the period of the structure.

970 meV.

The wavefunctions of the first four states with $m_f = 1/2$ are shown in Fig. 4.10. The absorption of $z-$polarised radiation from $1e_{1/2}$ is strongest towards $4e_{1/2}$, although both $2e_{1/2}$ and $3e_{1/2}$ have excellent spatial overlap with $1e_{1/2}$ as well. In order to explain why the absorption matrix element is much larger on the $1e_{1/2} \rightarrow 4e_{1/2}$ transition, one may notice that the states $1e_{1/2} - 3e_{1/2}$ are nearly symmetric with respect to reflections through the plane normal to the $z-$axis, denoted in Fig. 4.10 by a dashed line. If that symmetry was exact, the transitions between those states due to the interaction with $z-$polarised radiation would be strictly forbidden, but since it is only approximate the matrix elements of those transitions have relatively small values. As seen from Fig. 4.10, the state $4e_{1/2}$ is asymmetric with respect to the mentioned plane and its spatial overlap with the ground state is still good, therefore the strongest absorption occurs for the $1e_{1/2} \rightarrow 4e_{1/2}$ transition.

The optical cross section for the absorption of $x-$polarised radiation from the ground state is shown in the inset of Fig. 4.8. Symmetry imposed selection

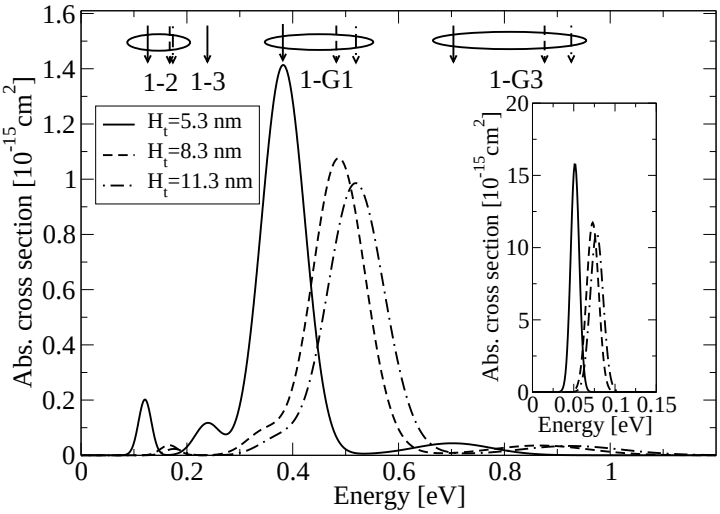

Figure 4.8: Intraband optical absorption spectrum from the ground state for $z-$polarised radiation for three different values of the structure period. The corresponding spectrum for $x-$polarised radiation is shown in the inset.

rules generally allow transitions to any state having $m_f = -1/2$ or $m_f = 3/2$, but in reality the spectrum is entirely dominated by the transition from the ground state (having $m_f = 1/2$) to the degenerate pair of first excited states (having m_f=$-1/2$, $3/2$). The wavefunctions of the $1e_{1/2}$ and $1e_{-1/2,3/2}$ states are presented in Fig. 4.11. The spatial overlap is good and there are no approximate selection rules that would inhibit the transition between these states as in the previous case. The transitions to higher states contribute much less to the absorption due to a reduced spatial overlap with the ground state resulting in smaller matrix elements (Fig. 4.9) and an increased transition energy. As the dot shape investigated is not cylindrical but hexagonal, the absorption of in-plane polarised radiation should in principle depend on the polarisation vector. However, it has been found that the change of absorption for different directions of the polarisation vector in the $xy-$plane is less than 1% and therefore the results shown in the inset of Fig. 4.8 are valid for any direction of in-plane polarised radiation.

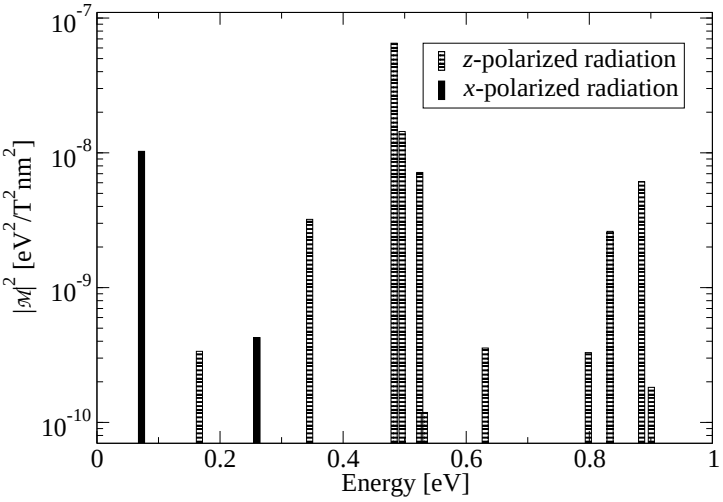

Figure 4.9: Optical absorption matrix elements $|\mathcal{M}|^2$ vs. energy for different intraband transitions from the ground state to excited states when the period is equal $H_t = 8.3\,\mathrm{nm}$.

4.5 Conclusion

In conclusion, a symmetry based method for the calculation of single particle states in hexagonal GaN/AlN quantum dots within the framework of the $\boldsymbol{k}\cdot\boldsymbol{p}$ model has been developed. The method has been applied to calculate the electron and hole states in a quantum dot superlattice. It has been found that changes in the electronic structure when the period of the structure is varied are caused by changes in the internal electric field and not by the electronic coupling, which was found to be negligible. The changes in strain distribution mainly determine the type of hole states. Furthermore, intraband absorption in the conduction band was studied. Selection rules for interaction with electromagnetic radiation were derived and the absorption spectra from the ground state for different polarisations of incident radiation were calculated. The absorption spectrum for in-plane polarised light is dominated by the transition to two degenerate first excited states, while for $z-$polarised light it is determined by the absorption to a group of excited states located $\sim 500\,\mathrm{meV}$ above

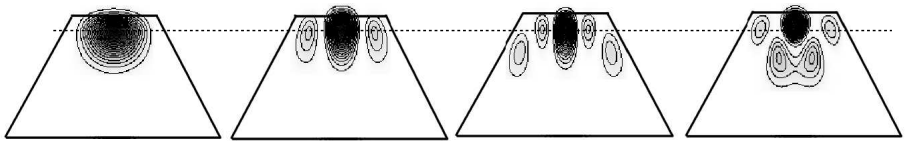

Figure 4.10: Wavefunction moduli squared in the yz-plane of the first four electron states with $m_f = 1/2$ when the period is equal to $H_t = 8.3\,\mathrm{nm}$. The states $1e_{1/2}$, $2e_{1/2}$, $3e_{1/2}$ and $4e_{1/2}$ are shown respectively from left to right.

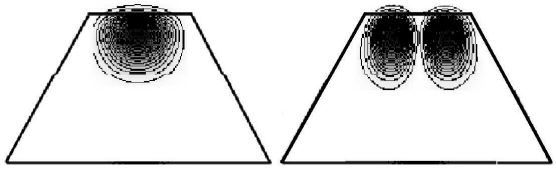

Figure 4.11: Wavefunction moduli squared in the yz-plane of the $1e_{1/2}$ (left) and $1e_{-1/2,3/2}$ (right) states.

the ground state having the same symmetry as the ground state. Such a result is in overall agreement with the available experimental data on intraband absorption in the conduction band in GaN/AlN quantum dots.

The work presented in this Chapter was published in Journal of Physics: Condensed Matter [224].

Chapter 5

Proposal of an optically pumped intersublevel laser

5.1 Introduction

Despite the fact that intraband optical transitions in semiconductor nanostructures are the subject of intensive research due to their applications for sources and detectors of mid- and far-infrared radiation (see Sec. 1.3.2), the possibility of having an optically pumped laser based on intersublevel transitions in quantum dots has not been analysed, prior to the work reported here. In this Chapter, the first theoretical proposal of such a laser based on pyramidal InAs/GaAs quantum dots, emitting at $\lambda \approx 14.6\,\mu$m, is presented. A theoretical model of the laser active region is developed and applied to calculate the pumping flux and temperature dependence of the gain. Furthermore, appropriate waveguides for both edge and surface emission are designed. In comparison with similar lasers based on quantum wells, the proposed laser has the advantage that in-plane polarised emission is possible and a lower pumping flux is needed due to the longer carrier lifetimes in quantum dots.

5.2 Theoretical model

The developed theoretical model starts from the energy level and wavefunction calculation, from which the transition rates among different quantum dot states are obtained. These are subsequently used to form the rate equations, from

which the populations of the energy levels in steady state conditions are found. Finally, from the populations obtained, the temperature and flux dependence of the gain can be calculated.

The energy levels and wavefunctions of the pyramidal InAs/GaAs quantum dots were calculated using the method described in Chapter 3. In the calculation of the energy levels, the small piezoelectric potential that reduces the symmetry from C_4 to C_2 was treated within second order perturbation theory. The dependence of the positions of the first seven energy levels on dot size for quantum dots considered in this work (whose dimensions are given in Table 5.1) is shown in Fig. 5.1.

Table 5.1: The calculated values of the pump λ_p and the emission wavelength λ_e, gain g_{77} at the temperature of $T = 77\,\mathrm{K}$ and g_{300} at $T = 300\,\mathrm{K}$, at the pumping flux $\Phi = 10^{24}\,\mathrm{cm}^{-2}\mathrm{s}^{-1}$ for several different quantum dots. The width of the quantum dot base is b and the height h.

b [nm]	h [nm]	λ_p [μm]	λ_e [μm]	g_{77} [cm^{-1}]	g_{300} [cm^{-1}]
14	6	5.7	13.5	513	218
15	7	5.9	14.6	574	243
16	8	6.2	15.5	577	186
17	8.5	6.5	16.5	561	167
18	9	6.8	17.6	577	211
19	9.5	7.1	18.9	537	202
20	10	7.4	20.1	441	170

The optical absorption cross section was calculated as described in Secs. 2.5.1 and 4.2. The 2σ Gaussian linewidth was taken equal to 12% of the transition energy, which is a typical value in quantum dot infrared pho-

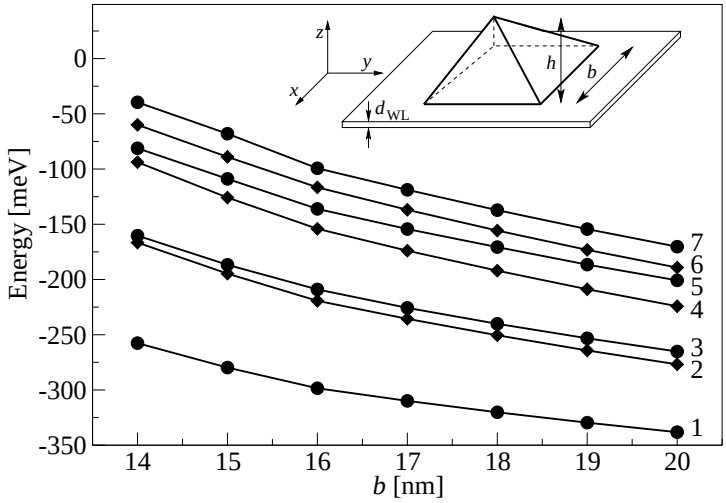

Figure 5.1: The dependence of the first seven energy levels on dot size for quantum dots whose dimensions are given in Table 5.1. The unstrained GaAs conduction band edge was taken as the reference energy level. The states with the quantum number $m_f = \pm 1/2$ are represented with circles and states with $m_f = \pm 3/2$ with diamonds. Lines are given only as a guide to the eye. The inset: Quantum dot geometry. The base width is b, the height h, the wetting layer width d_{WL}.

todetectors based on bound-to-bound transitions [225, 226].

Next, the processes which lead to electron transitions between different energy levels are examined.

The transition rate between states due to the interaction with LO phonons is given by (2.117). From Eq. (2.110), the electron – LO phonon coupling strength is given by

$$g^2 = \sum_{\boldsymbol{k}} (N_{\mathrm{LO}} + \frac{1}{2} \pm \frac{1}{2}) |\alpha(\boldsymbol{k})|^2 |F_{if}(\boldsymbol{k})|^2. \tag{5.1}$$

The summation in (5.1) is performed over phonon wave vectors given by (3.5). With the envelope functions of the final and initial state given by

$$\psi_j^{f(i)}(\boldsymbol{r}) \;=\; \sum_{\boldsymbol{k}} A_{j,\boldsymbol{k}}^{f(i)} \exp\left(i\boldsymbol{k}\cdot\boldsymbol{r}\right), \tag{5.2}$$

for such values of the wave vectors the form factor can be simplified from

$$F_{if}(\boldsymbol{q}) = \sum_{j=1}^{8} \sum_{\boldsymbol{k}_i} \sum_{\boldsymbol{k}_f} \int_V \mathrm{d}^3\boldsymbol{r} A^{f\,*}_{j,\boldsymbol{k}_f} A^{i}_{j,\boldsymbol{k}_i} \exp\left[i(\boldsymbol{q} + \boldsymbol{k}_i - \boldsymbol{k}_f) \cdot \boldsymbol{r}\right] \quad (5.3)$$

to

$$F_{if}(\boldsymbol{q}) = V \sum_{j=1}^{8} \sum_{\boldsymbol{k}_i} A^{f\,*}_{j,\boldsymbol{k}_i+\boldsymbol{q}} A^{i}_{j,\boldsymbol{k}_i}. \quad (5.4)$$

Some of the calculated LO phonon interaction transition rates for quantum dots whose dimensions are given in Table 5.1 are shown in Fig. 5.2.

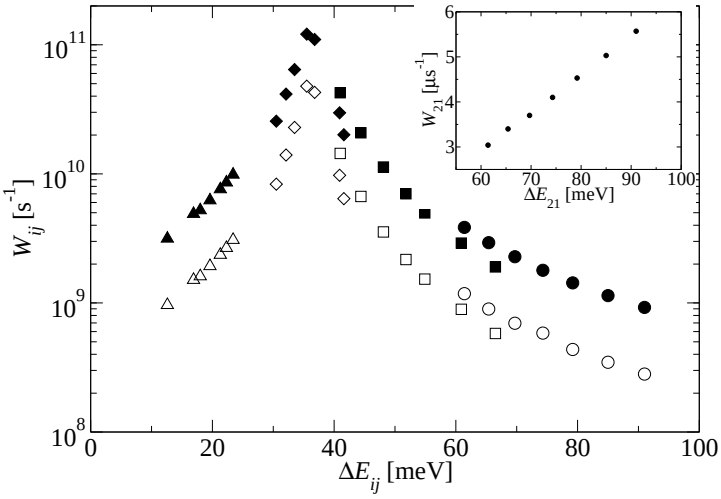

Figure 5.2: Energy dependence of the calculated LO phonon interaction transition rates W_{ij} on the transitions: $2 \rightarrow 1$ at $T = 77\,\mathrm{K}$ (circles) and $T = 300\,\mathrm{K}$ (full circles), $4 \rightarrow 3$ at $T = 77\,\mathrm{K}$ (squares) and $T = 300\,\mathrm{K}$ (full squares), $7 \rightarrow 5$ at $T = 77\,\mathrm{K}$ (diamonds) and $T = 300\,\mathrm{K}$ (full diamonds), $5 \rightarrow 4$ at $T = 77\,\mathrm{K}$ (triangles) and $T = 300\,\mathrm{K}$ (full triangles) for quantum dots whose dimensions are given in Table 5.1. The inset: Energy dependence of spontaneous radiative emission rate on the transition $2 \rightarrow 1$.

The weaker electron – LA phonon scattering transition rate was calculated using Fermi's Golden rule as described in Sec. 2.7.1. Acoustic phonon scattering is only significant when the states are closely spaced in energy ($< 10\,\mathrm{meV}$), as for example are states 2 and 3 in Fig. 5.3, while for larger energy separations the interaction with LO phonons is dominant.

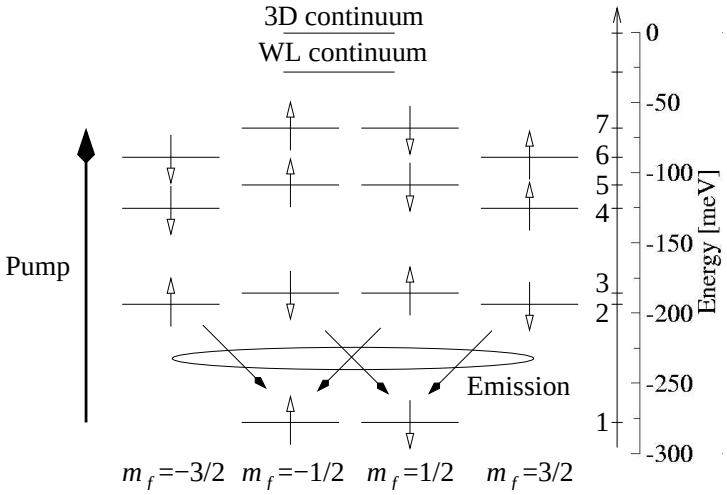

Figure 5.3: The scheme of energy levels of the pyramidal quantum dot. The base width is $b = 15\,\mathrm{nm}$, the height $h = 7\,\mathrm{nm}$, the wetting layer width $d_{WL} = 1.7\,\mathrm{ML}$. The quantum number of total quasi-angular momentum m_f as well as the spin of each state is given. The unstrained GaAs conduction band edge was taken as the reference energy. The position of the wetting layer continuum and 3D continuum states is indicated, as well.

The transition rate from initial state i to final state f due to spontaneous emission of photons is given by Eq. (2.75). The spontaneous radiative emission transition rates on the transition $2 \rightarrow 1$ for quantum dots whose dimensions are given in Table 5.1 are shown in the inset of Fig. 5.2. It has been found that the transition rates in the system due to spontaneous emission are less than $10\,\mu\mathrm{s}^{-1}$ and are thus significantly smaller than the transition rates due to interaction with phonons, hence they were neglected.

Electron – hole scattering, which is considered to be the dominant mechanism in interband quantum dot lasers [11], is not present in this unipolar device. Since it is assumed that the electrons are excited only to bound states (this assumption will be justified in Sec. 5.3), the relaxation processes assisted by the Coulomb interaction between bound and wetting layer carriers [227] do not exist either. Consequently, electron-electron scattering has no effect

on rate equations, because in the system with discrete energy levels, due to energy conservation the transition of an electron from state i to state f must be compensated by the transition of another electron from state f to state i.

The rate equations for the system considered then yield

$$\begin{aligned}\frac{\mathrm{d}n_i}{\mathrm{d}t} &= \sum_{j\neq i} W_{ji} n_j \left(1-\frac{1}{2}n_i\right) - \sum_{j\neq i} W_{ij} n_i \left(1-\frac{1}{2}n_j\right) - \\ &\quad - \sum_j \sigma_{ij}^p(\omega_p)(n_i-n_j)\Phi, \end{aligned} \tag{5.5}$$

where $0 \leq n_i \leq 2$ is the occupancy of level i including electrons of both spin, W_{ij} is the total transition rate from state i to state j due to interaction with phonons, $\sigma_{ij}^p(\omega_p)$ is the optical cross section between states i and j at the pump wavelength for radiation polarised in the same way as the pump and Φ is the optical pump flux. The effect of final state blocking is included via the terms $\left(1-\frac{1}{2}n_i\right)$ that represent the probability that the final state is empty. It is assumed that the doping is such that there are n_d electrons per quantum dot on average, i.e. $\sum_i n_i = n_d$.

The rate equations (5.5) have been formulated for the cold cavity limit when there is no radiation in the cavity corresponding only to subthreshold conditions, i.e. stimulated emission of radiation is not included. The gain calculated from such a model is sufficient to determine whether there will be lasing or not, and the larger its value, the larger the intensity of the emitted radiation. However, if one wants to calculate the value of the intensity of emitted radiation, it is necessary to couple this equation with the equations for the electromagnetic field distribution within the cavity, which was not the subject of this work.

The dots considered here are in the strong confinement regime where the electron-electron interaction energy (which is of the order of $\sim 10\,\mathrm{meV}$ per electron pair [228]) is much smaller than the effective confinement potential (which is $\sim 500\,\mathrm{meV}$). It is therefore expected that the single particle approach adopted here for the calculation of energy levels and the rate equations model should be valid when the dots are occupied by a small number of electrons

($n_d \sim 1-3$). This conclusion can also be supported by the results in Ref. [229] where the excitation spectrum of the quantum dot is almost the same in the range $n_d \sim 1-3$. Having all this in mind, a value of $n_d = 2$ was chosen in Sec. 5.3 to obtain a large value of gain on the one hand and to be sure of the validity of the model presented on the other hand.

The gain at the angular frequency ω for stimulated emission of radiation polarised in the direction $\boldsymbol{\varepsilon}$ is

$$g_{\boldsymbol{\varepsilon}}(\omega) = \sum_{\substack{i,j \\ E_i > E_j}} \sigma_{ij}^{\boldsymbol{\varepsilon}}(\omega)(n_i - n_j)N_t, \tag{5.6}$$

where $\sigma_{ij}^{\boldsymbol{\varepsilon}}(\omega)$ is the optical cross section for interaction with radiation polarised in the direction $\boldsymbol{\varepsilon}$ and N_t is the number of quantum dots per unit volume.

5.3 Results

5.3.1 Active region

A quantum dot with a base width $b = 15\,\mathrm{nm}$, height $h = 7\,\mathrm{nm}$, and a wetting layer of width $d_{\mathrm{WL}} = 1.7\,\mathrm{ML}$, which is a typical representative of the dots grown in experiments [11, 158], was considered first. It was assumed that the doping density is such that the dots are occupied with $n_d = 2$ electrons on average, as already mentioned. The material parameters for the calculation of the energy levels were taken from Ref. [3], the parameters for the calculation of transition rates due to interaction with phonons were taken from Ref. [2] (these are summarised in Appendix C) and the temperature dependence of the LO phonon lifetime was taken from Ref. [178]. The energy level scheme and the geometry of the dot considered is presented in Fig. 5.3.

Most optically pumped lasers use three-level or four-level schemes. It will however be shown that a somewhat more complicated scheme is required to obtain significant values of population inversion in the quantum dots investigated.

The standard three-level scheme would include pumping of electrons from level 1 to level 3, followed by fast depopulation of level 3 to level 2 in order to obtain a population inversion between levels 2 and 1. However, levels 2 and 3 are close in energy and therefore it is questionable whether selective pumping from level 1 to level 3 can be achieved in a real ensemble of quantum dots [1]. One should further note that electrons from level 1 cannot be pumped to level 4 or 6 due to selection rules for quantum number m_f and spin conservation.

Another possible pumping scheme would be to pump from level 1 to level 5. Electrons from level 5 then relax into levels 2 and 3 either directly or via level 4. In order to obtain a significant population inversion between levels 2 or 3, and level 1, the transition rate from level 5 to levels 2 and 3 should be much larger than the transition rate from levels 2 and 3 to level 1. However, these transition rates are of the same order of magnitude, the former being just slightly larger, hence the calculation has shown that only a small population inversion between levels 2 and 1 of approximately $\Delta n_{21} = n_2 - n_1 \approx 0.2$ electrons per dot at $T = 77\,\mathrm{K}$ is possible. The main mechanism that prevents larger values of population inversions Δn_{21} or Δn_{31} is backfilling of level 1 by unavoidable stimulated emission of photons by electrons from level 5 (at the rate $\sigma_{15}\Phi(1 - \frac{n_1}{2})n_5$).

Therefore, the following scheme which gives the largest values of gain among all the schemes explored is proposed. The electrons are optically pumped from level 1 to level 7. The distance between levels 5 and 7 is close to an LO phonon energy and consequently the transition rate between these two levels exceeds all other LO phonon interaction transition rates by more than an order of magnitude, enabling a fast depopulation of level 7. Consequently, the occupancy of level 7 in steady state is small and thus the undesirable stimulated emission from level 7 to level 1 is almost completely avoided in this scheme. The main difference between this and the previous scheme is that in this scheme there exists a fast depopulation mechanism from the level to

[1] Nevertheless, such an approach was proposed in a separate theoretical work (supported by certain experimental results) by other researchers [230], reported after the work presented here, and is shown to be promising.

which the electrons are being pumped, which prevents backfilling of level 1 by stimulated emission of photons. Almost all the electrons from level 7 therefore go into level 5, which implies that level 6 remains almost unpopulated. The electrons are further distributed to levels 2–4 and if the pump flux is sufficiently large, a population inversion between any of the levels 2–5 and level 1 occurs. As will be shown later, the largest population inversion occurs between levels 2 and 1, as well as between 3 and 1. Since the transition linewidth is of the same order of magnitude as the energy difference between states 2 and 3, laser emission is caused by both transitions $2 \rightarrow 1$ and $3 \rightarrow 1$. Due to selection rules on the transition $1 \rightarrow 7$, the pump needs to be $z-$polarised, while the emitted radiation is in-plane polarised, since the selection rules on both transitions $2 \rightarrow 1$ and $3 \rightarrow 1$ allow only such emission. Therefore, a laser based on these transitions can operate either as an edge emitter or as a surface emitter.

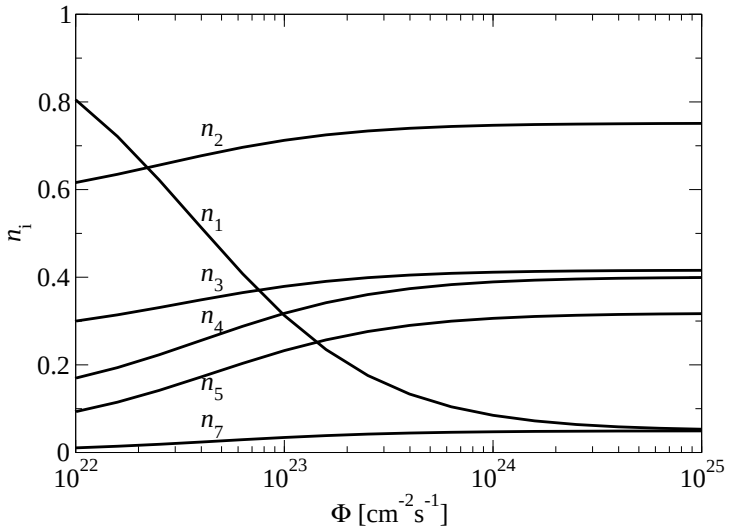

Figure 5.4: Flux dependence of state occupancies n_i at a temperature $T = 77\,\mathrm{K}$ for the quantum dot shown in Fig. 5.3.

The rate equations were solved under steady state conditions to find the population inversion and gain. The flux dependence of state occupancies n_i at a temperature $T = 77\,\mathrm{K}$ are shown in Fig. 5.4. The population inversion

between level 1 and any of the levels 2–5 appears at $\Phi \approx 2 \cdot 10^{23}\,\mathrm{cm}^{-2}\mathrm{s}^{-1}$. All the curves reach saturation at approximately $\Phi = 10^{24}\,\mathrm{cm}^{-2}\mathrm{s}^{-1}$. There are more electrons in levels 2 and 3 than in levels 4 and 5 since the transition rates from levels 4 and 5 to levels 2 and 3 are larger than the transition rates from levels 2 and 3 to level 1. This implies that the population inversion is strongest between levels 2 and 1 and the gain is therefore a maximum at the wavelength of $14.6\,\mu$m, corresponding to the transition between levels 1 and 2. The pump wavelength is $\lambda_p \approx 5.9\,\mu$m. When the curves reach saturation, there is a population inversion of approximately 0.7 electrons per dot between levels 1 and 2 and 0.3 electrons between levels 1 and 3. Both of them contribute significantly to the gain for in-plane polarised radiation at $\lambda_e \approx 14.6\,\mu$m, which is calculated to be $g = 574\,\mathrm{cm}^{-1}$. The calculation shows that the dependence of the optical cross section on the direction of polarisation in the xy-plane is weak and the above value of gain can be considered as the gain for any polarisation direction of in-plane polarised radiation. It should be mentioned that this is due to the fact that the wavefunctions in the absence of the piezoelectric effect were used in the calculation. Polarisation dependence of $1 \rightarrow 2$ and $1 \rightarrow 3$ transitions in InAs/GaAs quantum dots has been established both experimentally and theoretically (see for example Refs. [231, 232]). The origin of this dependence is the orientation of the wavefunctions of states 2 and 3 along the diagonals of the pyramid base, while the wavefunctions used in the calculations are C_4 symmetric. However, in the pumping scheme presented here, both 2 and 3 act as upper laser levels and one is interested in the properties of total emission from levels 2 and 3 to 1, when the individual contributions from levels 2 and 3 are added, and their polarisation is averaged.

It was assumed that the distance between quantum dot planes is $L_z = 50\,\mathrm{nm}$ and the surface density of dots was $N_s = 10^{11}\,\mathrm{cm}^{-2}$, which implies a quantum dot density of $N_t = N_s/L_z = 2 \cdot 10^{16}\,\mathrm{cm}^{-3}$. At this point, one can *a posteriori* justify the approximation that the continuum states are weakly occupied. One can see from Fig. 5.4 that among the bound states only the levels

1–5 are significantly occupied. As the highest among them is 80 meV below the wetting layer continuum states (see Fig. 5.3), the electrons cannot be thermally excited to the continuum. The excitation to the continuum due to undesired absorption of pump photons by electrons from levels 2–5 is also negligible since the corresponding transition matrix elements between the bound and continuum states are very small.

In order to emphasise the advantages of a quantum dot intersublevel optically pumped laser over its quantum well counterpart, these results are compared with the theoretical results for optimised optically pumped quantum well lasers with smooth potential profile [233, 234], emitting at a similar wavelength $\lambda \approx 15.5\,\mu$m as the device proposed here. At a pumping flux of $\Phi = 10^{24}\,\mathrm{cm^{-2}s^{-1}}$ and a temperature $T = 77\,\mathrm{K}$ the gain of the structure from Ref. [233] is less than $1\,\mathrm{cm^{-1}}$, while the gain of the proposed structure is greater than $500\,\mathrm{cm^{-1}}$. An order of magnitude larger flux is required there to obtain the same gain of $g \approx 570\,\mathrm{cm^{-1}}$. Finally, the gain vs. flux curve in Ref. [233] and [234] reaches saturation at $\Phi > 10^{26}\,\mathrm{cm^{-2}s^{-1}}$, two orders of magnitude larger than in this work. In an experimentally realised optically pumped quantum well intersubband laser [50] the lasing threshold flux is $\Phi \approx 4 \cdot 10^{25}\,\mathrm{cm^{-2}s^{-1}}$. On the other hand, the threshold flux predicted in this paper using the values of losses estimated in Sec. 5.3.2 is of the order $\Phi \sim 5 \cdot 10^{22}\,\mathrm{cm^{-2}s^{-1}}$.

The temperature dependence of the population inversions between any of the levels 2–5 and level 1 $\Delta n_{i1} = n_i - n_1$ ($i \in \{2, 3, 4, 5\}$) at $\Phi = 10^{24}\,\mathrm{cm^{-2}s^{-1}}$ is given in Fig. 5.5. An increase of Δn_{31} in the low temperature part of the graph is a consequence of the proximity of levels 2 and 3. The distribution of electrons between levels 2 and 3 here is in favour of the lower level 2. As the temperature increases, electrons become more evenly distributed between levels 2 and 3, thus increasing the population of level 3. When this trend reaches saturation, the decrease of Δn_{31} with temperature is caused by an increase in the population of the ground state. Due to an increase in the carrier

relaxation rates to the ground state with temperature, the pumping flux is no longer sufficient to entirely depopulate the ground state at higher temperatures. Therefore, the population inversions Δn_{21} and Δn_{31} responsible for the gain decrease with temperature, but even at room temperature significant values of population inversions and gain are achievable.

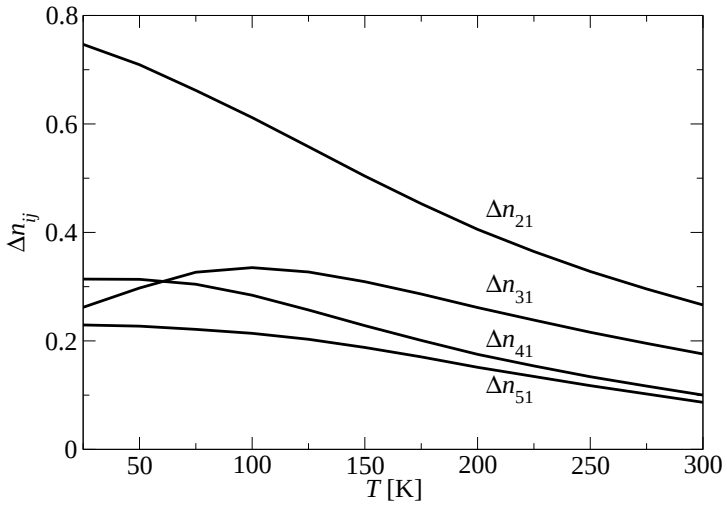

Figure 5.5: Temperature dependence of population inversions $\Delta n_{i1} = n_i - n_1$ ($i \in \{2, 3, 4, 5\}$) at the pumping flux $\Phi = 10^{24}\,\mathrm{cm}^{-2}\mathrm{s}^{-1}$ for the quantum dot shown in Fig. 5.3.

In order to show that the dot analysed is by no means an exception in view of the possibility of achieving significant values of gain, several other dots of different sizes have been investigated. The size, as well as the values of gain, the pump and the emission wavelength of the dots at the pumping flux $\Phi = 10^{24}\,\mathrm{cm}^{-2}\mathrm{s}^{-1}$ and the temperatures of $T = 77\,\mathrm{K}$ and $T = 300\,\mathrm{K}$ are shown in Table 5.1. All the dots considered have values of gain larger than $400\,\mathrm{cm}^{-1}$ at $T = 77\,\mathrm{K}$, and larger than $150\,\mathrm{cm}^{-1}$ at room temperature, and are thus obviously suitable for the active region of the laser in the proposed scheme.

The calculated gain profiles for several different quantum dots with base-to-height ratio $b/h = 2$ at $T = 77\,\mathrm{K}$ and $\Phi = 10^{24}\,\mathrm{cm}^{-2}\mathrm{s}^{-1}$ are shown in Fig. 5.6. In larger dots, the splitting between levels 2 and 3 is larger and the

depopulation of level 3 to level 2 due to LA phonon scattering is much smaller. Consequently, the electrons are more evenly distributed between levels 2 and 3, which results in a wider lineshape with two peaks and smaller values of peak gain for the larger dots, as shown in Fig. 5.6. This effect explains the decrease of gain as the dot size increases for larger ($b \sim 18-20\,\mathrm{nm}$) dots at $T = 77\,\mathrm{K}$ and consequently a smaller value of gain (see Table 5.1) for the dot with $b = 20\,\mathrm{nm}$ compared with other dots.

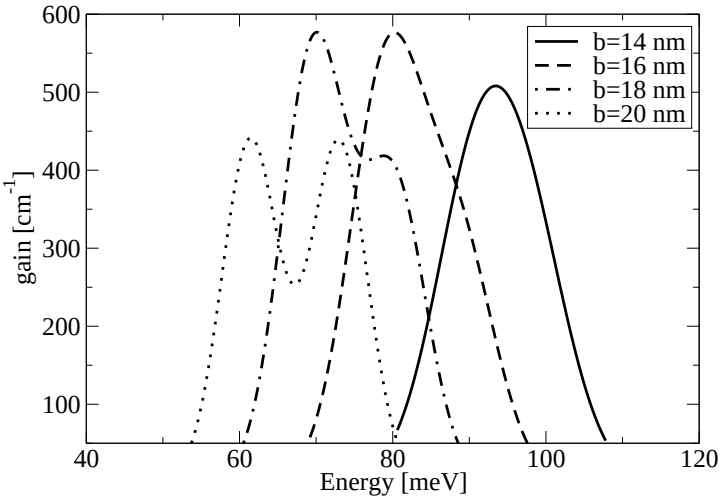

Figure 5.6: The calculated gain profile for several different quantum dots with base-to-height ratio $b/h = 2$ at the temperature $T = 77\,\mathrm{K}$ and the pumping flux $\Phi = 10^{24}\,\mathrm{cm}^{-2}\mathrm{s}^{-1}$.

It should also be mentioned that either significantly smaller dots or dots with significantly larger base to height ratio than those investigated here cannot accommodate the required number of energy levels, and are not suitable for the proposed pumping scheme.

5.3.2 Waveguide and cavity design

The next thing to consider is the design of an appropriate waveguide, or of the resonator cavity, for either edge or surface emission, respectively. Since all the carriers in the proposed scheme are bound to quantum dots, the free carrier

absorption can be neglected.

The waveguide for an edge emitting device may comprise a $5\,\mu$m thick AlAs cladding layer, a $1\,\mu$m thick GaAs core layer, 40 periods of quantum dot layers (total thickness of $2\,\mu$m) and a $2\,\mu$m thick GaAs cap layer. For $\lambda = 14.6\,\mu$m this waveguide supports a single TM mode whose overlap with the active region is $\Gamma_{TM} = 52\%$ and a single TE mode whose overlap is $\Gamma_{TE} = 48\%$. These have been calculated using the method described in Ref. [235], where in the absence of free carrier absorption the equations reduce to a simple one dimensional Schrödinger equation. Assuming the reflectivity $R \approx 0.29$ at the waveguide cleaved facets, the mirror losses for $l \approx 1\,$mm long waveguide are $\alpha_M = -1/l \cdot \ln R \approx 13\,\mathrm{cm}^{-1}$. The modal gain Γg is thus much larger than the losses, implying that edge emission from this laser is possible.

With the gain for normally incident light, the quantum dot based structure enables one to achieve a VCSEL (Vertical Cavity Surface Emitting Laser) configuration, which would require an appropriate resonator. In view of rather short lengths of the active medium (thickness of the quantum dot stack), the resonator must have only small losses. VCSELs operating at visible or near-infrared wavelengths perform very well and offer numerous advantages over edge emitters, but none has been fabricated for long wavelengths (13–21 μm), and this may be a quite challenging task. Here, a couple of possible routes of their realisation are briefly discussed.

One possibility might be to employ a cavity comprising two Bragg mirrors, based on GaAs/AlAs quarter-wavelength multilayer stacks. The mirror reflectivity is calculated from [236]

$$R = \frac{n_1^{2N} - n_2^{2N}}{n_1^{2N} + n_2^{2N}}, \tag{5.7}$$

where n_1 and n_2 are the refractive indices of GaAs and AlAs ($n_1 \approx 3.3$, $n_2 \approx 2.9$), and N is the number of bilayers. Assuming the active layer completely fills the resonator, and satisfies the proper phase condition $d = \lambda/(2n_1) \approx 2.2\,\mu$m, i.e. comprising 44 layers of quantum dots, with interlayer spacing of $L_z = 50\,$nm, one finds that the gain, even at room temperature, would exceed the

equivalent mirror losses $\alpha_M = -1/d \cdot \ln R$ of an $N = 30$, or even $N = 20$ Bragg stack. A practical difficulty with this approach is that the total width of the semiconductor layers is about 100 μm, which makes it somewhat impractical for the whole structure to be grown by the rather slow mathod of MBE (the growth time might take a few days). A way out might be to employ the much faster Liquid Phase Epitaxy (LPE) for the lower Bragg stack, polish the surface to prepare it for quantum dots growth, use MBE next, and finally make the upper Bragg stack by LPE. While the Bragg mirror performance might not be affected by the $\sim$0.05 μm layer width tolerance / roughness inherent to LPE (because the $\lambda/4$ layer widths here are large), it is not quite clear whether the growth speed-up, at the expense of increased complexity, would make this approach practical.

The reasons for the Bragg mirrors being so thick are the large operating wavelength, and the relatively small contrast between the GaAs and AlAs refractive indices. While there is no cure for the former, the latter can be enhanced by wet-oxidation of AlAs layers into Al_2O_3, the technique used for Bragg mirrors in the near-infrared [237]. With the smaller refractive index of Al_2O_3 one finds that just $N = 7$ or 8 would suffice for lasing. It is not known, however, what losses Al_2O_3 formed in this way would present to the 13–21 μm radiation.

5.4 Conclusion

In conclusion, a theoretical model of the active region of an optically pumped intersublevel quantum dot laser is presented. The population of energy levels, and consequently the population inversion and gain were extracted from a rate equations model where both LO and LA phonon interaction were considered. The waveguide and cavity for edge and surface emission are proposed as well. The results predict laser emission in the spectral range $13 - 21\,\mu$m, depending on the dots size. The predicted threshold pumping flux, required to obtain laser action is much smaller than in quantum well based intersubband lasers,

which is due to the longer carrier lifetimes in quantum dots.

The work presented in this Chapter was published in IEEE Journal of Quantum Electronics [238].

Chapter 6

Absorption spectrum of quantum dot infrared photodetectors

6.1 Introduction

Following the experimental success in the field of QDIPs, there have been several theoretical studies of intraband absorption in QDIPs aimed at understanding the detection process and assigning the experimental peaks to transitions between certain states. In these studies, the energy levels and wavefunctions in quantum dots, and then the absorption spectra, have been calculated using mostly the 1-band effective mass approach [81, 226, 239–241], but also the 8-band $\boldsymbol{k} \cdot \boldsymbol{p}$ method [242]. In InAs/GaAs, the most commonly used material system, the large lattice mismatch induces a strong strain field and the small energy gap of InAs causes significant band-mixing; effects that the 1-band method can hardly take into account. The 8-band $\boldsymbol{k} \cdot \boldsymbol{p}$ method is therefore obviously a more realistic model, however the simpler and faster effective mass method is almost exclusively used [81, 226, 239–241], and the question arises whether it may still perform well enough to be useful for modelling the intraband absorption spectrum.

In this Chapter, calculations of the absorption spectrum, obtained by the two methods, will be presented for several experimentally realised QDIPs. The aim is not to compare the methods themselves, as it is well known that $\boldsymbol{k} \cdot \boldsymbol{p}$ performs better in a wider range of relevant energies than the effective mass

method. The idea is rather to provide a quantitative estimate of how much can one rely on the quantitative predictions of the widely used effective mass approach.

In most of the QDIPs reported in the literature, the dots have the shape of a lens [81], cone [80] or truncated cone [64,243], all belonging to the class of cylindrically symmetric dots. Therefore, the symmetry of the dot shape will again be exploited in the calculation. In contrast to pyramidal quantum dots whose symmetry group is discrete, the symmetry group of cylindrically symmetric dots is continuous. It is therefore manifested in a simpler form via separation of variables and reduction of the problem from three dimensional to two dimensional, as has been previously demonstrated in the literature [163, 186]. The results obtained in the calculation will be compared with experimental results.

It should be emphasised that the absorption spectrum calculation is not sufficient to fully understand the photocurrent spectrum. The contribution of the carrier absorbed from the ground state to an excited state to the photocurrent depends on the position of the final state. Clearly, carriers absorbed to continuum states are more likely to contribute to photocurrent, than the carriers absorbed to bound states, which need additionally to be thermally excited or to tunnel to continuum states in order to contribute to photocurrent. The positions of the peaks of the absorption spectrum should match the experimental photocurrent peaks, however the peak intensities of the two spectra differ. The model presented in Chapter 8 is able to treat the photocurrent spectrum, as well.

6.2 Theoretical models of absorption

6.2.1 Parabolic quantum dot model of absorption

The simplest model which is sufficient to qualitatively understand the quantum dot intraband absorption spectrum is the parabolic dot model, where

the potential is assumed in a separable form $V(\boldsymbol{r}) = V_1(x,y) + V_2(z)$, where $V_1(x,y) = \frac{1}{2}m^*\omega^2(x^2+y^2)$ is the potential of a two dimensional harmonic oscillator, and $V_2(z)$ is the potential of a quantum well with infinitely high barriers. The solutions are of the form $\Psi(\boldsymbol{r}) = h_{n_x}(x)h_{n_y}(y)\psi_{n_z}(z)$, where $h_n(t)$ is the wavefunction of a one dimensional harmonic oscillator and $\psi_{n_z}(z)$ are solutions of Schrödinger equation with potential $V_2(z)$ (corresponding to energies ε_{n_z}). The eigenenergies are then of the form $E(n_x, n_y, n_z) = \hbar\omega(n_x + n_y + 1) + \varepsilon_{n_z}$. The factor $\hbar\omega$ corresponds to the transition energy from the ground to first excited state and for modelling realistic quantum dots it should be set to $\hbar\omega \sim 40 - 70\,\mathrm{meV}$. Typical quantum dots are wide in the xy-plane (diameters of the order of 20 nm and more) and have very small height (of the order of 3 nm) in the $z-$direction, therefore the effective potential well representing the $z-$direction confinement is narrow (see Fig. 6.1, left). In a typical case therefore $\varepsilon_1 - \varepsilon_0$ is of the order of at least 100 meV.

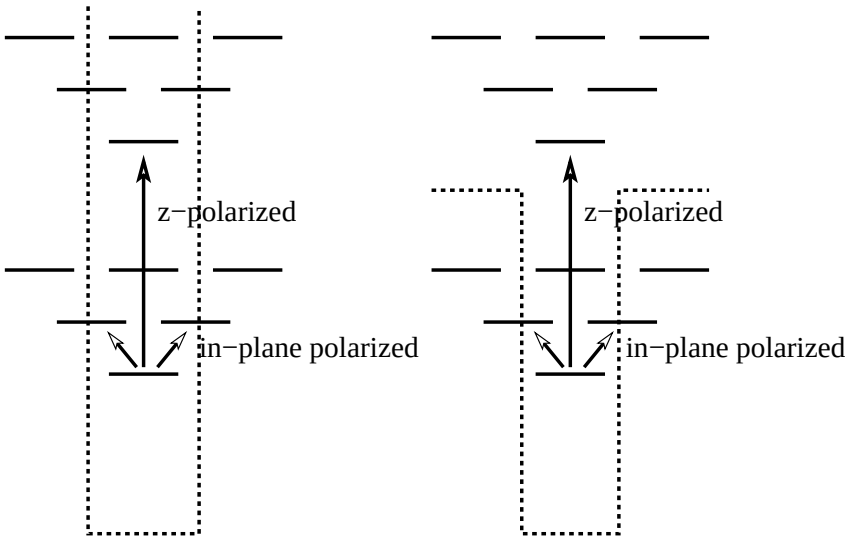

Figure 6.1: Scheme of energy levels and allowed optical transitions in a parabolic quantum dot model with infinite potential barriers (left) and finite potential barriers (right). Only the levels with $n_x + n_y \leq 2$ and $n_z \leq 2$ are shown.

The optical absorption matrix elements on the transitions between states are proportional to the matrix elements of coordinate operators, therefore by calculating the latter, one obtains the following selection rules on the transitions between states:

- $\Delta n_x = \pm 1$, $\Delta n_y = 0$, $\Delta n_z = 0$, for $x-$polarised radiation,
- $\Delta n_y = \pm 1$, $\Delta n_x = 0$, $\Delta n_z = 0$, for $y-$polarised radiation,
- $\Delta n_x = 0$, $\Delta n_y = 0$, for $z-$polarised radiation.

The transitions from the ground state are of primary importance for QDIPs. From the selection rules obtained, one concludes that only the transition to a pair of degenerate first excited states is allowed for in-plane polarised radiation, while in the case of $z-$polarised radiation, only the transitions to higher excited states are allowed, as demonstrated in Fig. 6.1. In a more realistic model where $V_2(z)$ is the potential of a well with finite barriers (Fig. 6.1, right), it may happen that the well can accommodate only one state, and that the absorption of $z-$polarised radiation may be allowed to continuum states only.

Although the model presented considers the quantum dot bandstructure in a very simplified manner, it is excellent for understanding the results of more realistic models. The strict selection rules from this model are then relaxed and strictly forbidden transitions become weakly allowed. Nevertheless, qualitatively, the absorption spectrum retains the same features as in this model.

6.2.2 Effective mass model of absorption

An improved approach is to use the effective mass method, with a realistic dot shape. In order to keep the simplicity of the approach and avoid the calculation of the three dimensional strain distribution in quantum dots, one is attracted to use the effective mass and band offset parameters that take the effects of strain into account on average. These parameters should in principle be different for each quantum dot, however usually a single value for a given

quantum dot material system is used. This approach has often been followed in the literature [81, 226, 239–241].

Within the framework of the effective mass method the Hamiltonian is given by

$$\hat{H} = \hat{\boldsymbol{k}} \frac{\hbar^2}{2m^*(\boldsymbol{r})} \hat{\boldsymbol{k}} + V(\boldsymbol{r}) + |e| F \hat{z}, \tag{6.1}$$

where $\hat{k}_i$ ($i \in \{1, 2, 3\}$) is the differential operator $\hat{k}_i = -i\frac{\partial}{\partial x_i}$, $\boldsymbol{F} = F\boldsymbol{e}_z$ is the electric field oriented along the $z-$direction, $m^*(\boldsymbol{r})$ is the position-dependent effective mass and $V(\boldsymbol{r})$ is the position-dependent potential, both assumed constant within the dot and within the matrix (and within the well in the case of quantum dots-in-a-well structure). The modified values of the effective mass in the dot of $m^* = 0.04\, m_0$ [160] and the conduction band offset $V_0 = 450\,\text{meV}$ [196] are used to take the averaged effect of strain into account.

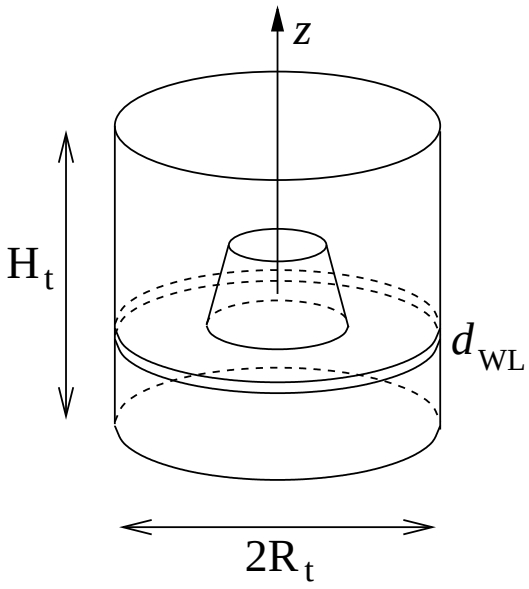

Figure 6.2: Schematic view of a quantum dot in an embedding cylinder of radius R_t and height H_t. The wetting layer width is d_{WL}.

The wavefunction expansion method (see Sec. 2.6.1) in a cylindrical basis was used to find the eigenenergies and the corresponding wavefunctions. The

mathematical details omitted in Sec. 2.6.1 are given here. The method is based on embedding the dot in a cylinder of radius R_t and height H_t (see Fig. 6.2) and assuming the wavefunction is a linear combination of the expansion basis functions

$$\psi(\boldsymbol{r}) = \sum_{nl} A_{nl} b_{nml}(r, z, \varphi), \tag{6.2}$$

with the coefficients A_{nl} ($n \in \{1, \ldots, n_{max}\}$ and $l \in \{-l_{max}, \ldots, l_{max}\}$) to be determined. The basis functions b_{nml} are given by

$$b_{nml}(r, z, \varphi) = f_{nm}(r) g_l(z) \Phi_m(\varphi), \tag{6.3}$$

where

$$\begin{aligned} f_{nm}(r) &= \frac{\sqrt{2}}{R_t} \frac{J_m(k_{nm} r)}{\left| J_{|m|+1}(k_{nm} R_t) \right|}, \\ g_l(z) &= \frac{1}{\sqrt{H_t}} e^{i \frac{2\pi}{H_t} l z}, \\ \Phi_m(\varphi) &= \frac{1}{\sqrt{2\pi}} e^{i m \varphi}, \end{aligned} \tag{6.4}$$

where l and m are integers and n is a positive integer. J_m is a Bessel function of order m and $k_{nm} R_t$ is its n-th zero. Due to the cylindrical symmetry of the dots, the Hamiltonian commutes with the $z-$component of the orbital angular momentum, whose eigenvalue m is then a good quantum number and therefore in (6.2) the summation needs to be performed over n and l only.

After substituting the expansion (6.2) into the Hamiltonian eigenvalue problem one arrives at an eigenvalue problem of the Hamiltonian matrix

$$\sum_{n'l'} H_{nml,n'ml'} A_{n'l'} = E A_{nl}, \tag{6.5}$$

where

$$H_{nml,n'm'l'} = \int_V b^*_{nml} \hat{H} b_{n'm'l'} \, r \, \mathrm{d}r \, \mathrm{d}z \, \mathrm{d}\varphi \tag{6.6}$$

and the integration is performed over the volume of the embedding cylinder. The one-band Hamiltonian contains only terms of the form of T_1, T_2 and T_3 (see Appendix B) and their corresponding Hamiltonian matrix elements can be evaluated as shown in Appendix B.

The matrix element for absorption of electromagnetic radiation (Eq. (2.69)) is equal to

$$\mathcal{M}_{if}^{\boldsymbol{\varepsilon}} = \sum_{nl} \sum_{n'l'} A_{nl}^{i*} A_{n'l'}^{f} G(nl, n'l'), \tag{6.7}$$

where the superscripts i and f refer to the initial and final state and the perturbation Hamiltonian matrix elements

$$G(nl, n'l') = \frac{1}{A} \int_V b_{nml}^* \hat{H}' b_{n'ml'} \, r \, \mathrm{d}r \, \mathrm{d}z \, \mathrm{d}\varphi \tag{6.8}$$

are of the form of T_5 (see Appendix B) and can be therefore calculated in a similar manner. From the last two expressions, the selection rules can easily be established: $\Delta m = 0$ for absorption of $z-$polarised radiation and $|\Delta m| = 1$ for in-plane polarised radiation.

6.2.3 8-band $\boldsymbol{k} \cdot \boldsymbol{p}$ model of absorption

The 8-band $\boldsymbol{k} \cdot \boldsymbol{p}$ Hamiltonian is a sum of the kinetic part of the Hamiltonian $\hat{H}_k$ (Eq. (2.20)), the strain part $\hat{H}_s$ (Eq. (2.38)), and the diagonal term $|e|Fz$ due to a constant electric field F directed along the $z-$axis. The piezoelectric effect was neglected here, as it has been shown that it is small in cylindrical quantum dots lacking sharp features [244].

The symmetry of the kinetic part of the 8-band $\boldsymbol{k} \cdot \boldsymbol{p}$ Hamiltonian $\hat{H}_k$ applied to cylindrically symmetric quantum dots is equal to the intersection of the symmetry of the geometrical shape of the dot and the symmetry of the 8-band $\boldsymbol{k} \cdot \boldsymbol{p}$ Hamiltonian applied to the zincblende crystal lattice. Since the crystal symmetry is lower than cylindrical it turns out that the system considered is only C_4 symmetric. However, the deviations of the Hamiltonian from the cylindrically symmetric form are only slight and one often employs the axial approximation [155, 163] (where one explicitly takes $\gamma_2 = \gamma_3 = \frac{1}{2}(\gamma_2 + \gamma_3)$ in and only in the R-terms in Eq. (2.20)) in which $\hat{H}_k$ becomes exactly axially symmetric. This is highly desirable as such an approximation effectively reduces the problem from three dimensional to two dimensional and therefore significantly reduces the computational cost, without influencing the accuracy.

Such an approximation is therefore used in this work, too. Furthermore, the strain part $\hat{H}_s$ also slightly deviates from the cylindrically symmetric form and it would also have to be modified to be able to exploit the cylindrical symmetry and reduce the computational complexity. A slightly different approach is used here. The wavefunctions are assumed in the form they would have if the Hamiltonian was exactly cylindrically symmetric, and therefore its parts that deviate from symmetry give a zero contribution in the Hamiltonian matrix elements given by Eq. (6.11).

Since the 8-band model inherently takes into account the spin-orbit interaction, the good quantum number in this case is the quantum number m_f (where m_f is half integer) of the $z-$component of the total angular momentum [163] (rather than just the orbital angular momentum) given as a sum of the orbital angular momentum of the envelope function and total angular momentum of the Bloch function. The envelope functions of the quantum state having m_f can then be assumed in the form

$$\psi_i(\boldsymbol{r}) = \sum_{nl} A_{inl} b_{nm(i)l}(r, z, \varphi), \tag{6.9}$$

where $m(i) = m_f - m_j(i)$ and $m_j(i)$ is the eigenvalue of the z-component of the total angular momentum of the Bloch function $|i\rangle$. After inserting the envelope function expansion of (6.9) into the Hamiltonian eigenvalue problem one arrives at

$$\sum_{i'n'l'} H_{inm(i)l,i'n'm(i')l'} A_{i'n'l'} = E A_{inl}, \tag{6.10}$$

where

$$H_{inml,i'n'm'l'} = \int_V b^*_{nml} \hat{H}_{ii'} b_{n'm'l'}\, r\, \mathrm{d}r\, \mathrm{d}z\, \mathrm{d}\varphi. \tag{6.11}$$

The 8-band Hamiltonian contains terms of the form T_1–T_{10} (see Appendix B), whose corresponding Hamiltonian matrix elements are given in Appendix B.

The strain was modelled using the continuum mechanical model and the strain distribution was found using the finite element method in a manner that was described in Sec. 2.6.2, where the size of the system of linear equations was reduced by a factor of approximately 8 by noting that only the displacements

in, for example, the region $0 \leq y \leq x$ can be considered, as the rest of them can then be deduced using symmetry properties of the system. A nonuniform mesh for the finite element calculation was chosen to be more dense in the region around the dot.

The absorption matrix element is in this case given by

$$\mathcal{M}_{if}^{\boldsymbol{\varepsilon}} = \sum_{inl} \sum_{i'n'l'} A_{inl}^{i*} A_{i'n'l'}^{f} G(inl, i'n'l'), \tag{6.12}$$

where the superscripts i and f refer to the initial and final state and the perturbation Hamiltonian matrix elements

$$G(inl, i'n'l') = \frac{1}{A} \int_V \mathrm{d}^3\boldsymbol{r} b_{nm(i)l}^{*} \hat{H}' b_{n'm(i')l'} \tag{6.13}$$

are of one of the forms T_1, T_4 and T_5 (see Appendix B) and can be therefore calculated in a similar manner. After explicit calculation one can straightforwardly derive the selection rules: $\Delta m_f = 0$ for $z-$polarised radiation and $|\Delta m_f| = 1$ for in-plane polarised radiation.

6.3 Results

The two methods described in Sec. 6.2 have been applied to calculate the optical absorption matrix elements and the intraband absorption spectra for quantum dots of several different shapes and sizes reported for experimentally realised QDIPs. In typical QDIP operating conditions only the ground state is significantly occupied as the occupation of the excited states would lead to a much larger dark current. The intraband absorption spectrum is therefore calculated by adding the contributions from transitions from the ground state to each of the excited states (bound or continuum). The material parameters in the calculation were taken from Ref. [3] and are summarised in Appendix C. The standard deviation of the Gaussian lineshape was taken to be equal to 10% of the transition energy in the case of the transitions to bound states and 20% in the case of the transitions to continuum states. These are the typical values observed in the experiments [64, 80, 81]. In further discussion

the states obtained within the framework of the 8-band model will be labelled as ne_{m_f}, which represents the $n-$th electron state having the quantum number of the $z-$component of total angular momentum m_f (note that for each state ne_{m_f}, there is another state ne_{-m_f} with the same energy), and in a similar manner the state obtained by the effective mass method ne_m represents the $n-$th electron state having the quantum number of the $z-$component of orbital angular momentum m (note that for each state ne_m there also is an ne_{-m} state of the same energy). The dimensions of the embedding cylinder taken in all calculations are $R_t = 40\,\text{nm}$, $H_t = 50\,\text{nm}$, while the number of basis functions is determined from $n_{max} = 10$ and $l_{max} = 20$. It has been assumed in all calculations that a 0.5 nm wide wetting layer is present beneath each dot.

Since the choice of the embedding cylinder dimensions is arbitrary one has to check whether an increase in its dimensions leads to changes in the calculated spectrum. This is especially important when the transitions to continuum states dominate the spectral response, as the continuum states are artificially discretised by embedding the quantum dot in a cylinder of finite size. Furthermore, it also has to be checked whether the number of basis functions taken in the calculation is sufficiently large. Such tests were performed by increasing each of the parameters R_t, H_t, n_{max} and l_{max}, while keeping the rest of them constant. No observable changes in the absorption spectra occurred during these tests.

It has also been checked that for all structures considered in this Chapter the changes in absorption spectra with electric field are only slight and therefore the spectrum obtained at zero bias can be considered as representative of the spectrum for any value of the field. More specifically, in the range of fields typically used in QDIPs $-50\,\text{kV/cm} < F < 50\,\text{kV/cm}$, the positions of the absorption peaks change by less than 5% for all the structures considered (see Fig. 6.3 as an example). Clearly, these peaks cannot be observed in the responsivity spectra at zero bias, but only when the bias is sufficient that the absorbed carriers can form a photocurrent.

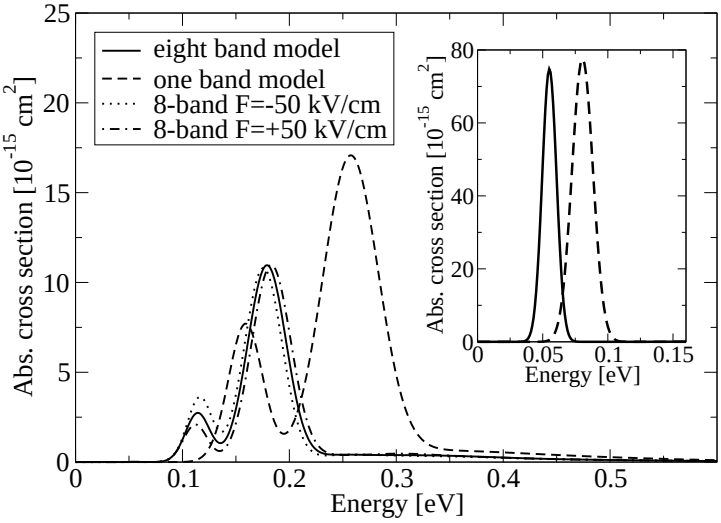

Figure 6.3: The intraband optical absorption spectrum for a quantum dot of conical shape with the diameter $D = 25\,\mathrm{nm}$ and height $h = 7\,\mathrm{nm}$ for the case of $z-$polarised radiation. The corresponding spectrum for in-plane polarised radiation is shown in the inset. The absorption spectrum of $z-$polarised radiation calculated using the 8-band model at the fields of $F = -50\,\mathrm{kV/cm}$ and $F = 50\,\mathrm{kV/cm}$ is shown as well.

Firstly, the absorption spectrum obtained by the two methods for a quantum dot of conical shape with the diameter $D = 25\,\mathrm{nm}$ and height $h = 7\,\mathrm{nm}$, is presented. The dimensions chosen are those which are approximately reported for quantum dots in a QDIP structure in Ref. [80] (the structure labelled as S-GaAs therein) based on the combination of atomic force microscopy and cross-sectional transmission electron microscopy measurements [80, 245]. The quantum dot is assumed to be of pure InAs as the growth conditions reported in Ref. [80] are such that intermixing between InAs and GaAs is minimised. The optical absorption spectrum in the case of $z-$polarised radiation is shown in Fig. 6.3. The two peaks in the spectrum originate from the transitions between bound states $1e_{1/2} \rightarrow 3e_{1/2}$ and $1e_{1/2} \rightarrow 5e_{1/2}$ ($\boldsymbol{k}\cdot\boldsymbol{p}$ model based labelling of states), i.e. $1e_0 \rightarrow 2e_0$ and $1e_0 \rightarrow 3e_0$ (effective mass model based labelling

of states). The states $2e_{1/2}$ and $4e_{1/2}$ have opposite values of spin from $1e_{1/2}$ and transitions to them are therefore forbidden due to spin selection rules. The transitions to continuum states give a much smaller contribution to the spectrum. One can see from Fig. 6.3 that the results obtained by the two methods are qualitatively similar, however there are significant quantitative differences. The effective mass method gives larger values of transition energies and predicts stronger absorption. Since both the one and eight band method predict approximately the same position of the ground state with respect to the GaAs continuum (305 meV in one band vs. 295 meV in $\boldsymbol{k}\cdot\boldsymbol{p}$), one can ascribe these differences to non-parabolicity effects that are not properly taken into account within the simple effective mass approach. The one band model therefore underestimates the effective mass of the excited states which leads both to larger intersublevel energies and larger absorption matrix elements. The corresponding absorption spectrum for in-plane polarised incident radiation is presented in the inset of Fig. 6.3. There is a single peak in the spectrum which is due to the transition from the ground state $1e_{\pm 1/2}$ to a pair of nearly degenerate first excited states $2e_{\mp 1/2}$, $1e_{\pm 3/2}$. As in the case of $z-$polarised radiation, the peak position energy obtained by one band model is larger, which can be attributed to the same cause. The matrix elements of the dominant transition calculated within the effective mass method are larger. However, the difference between the transition energies (on the relative scale) is more prominent than in the case of $z-$polarised radiation, which therefore leads to only a slightly larger value of the peak absorption cross section within the effective mass model.

Next, the theoretical results obtained by the two methods are compared with the experimental results from Ref. [80] (Fig. 7a therein). One should have in mind that due to uncertainty in the determination of the dot size, as well as due to possible effects of In segregation and interdiffusion, any comparison between theoretical and experimental results should be taken with caution. The experimental intraband photocurrent spectrum exhibits the main peak at 175 meV and a much smaller peak at 115 meV, in excellent agreement with the

results obtained for $z-$polarised incident radiation within the 8-band model where the corresponding peaks occur at 179 meV and 114 meV, respectively. As already mentioned, the effective mass method gives peak positions at larger energies, which is only in qualitative agreement with the experimental results.

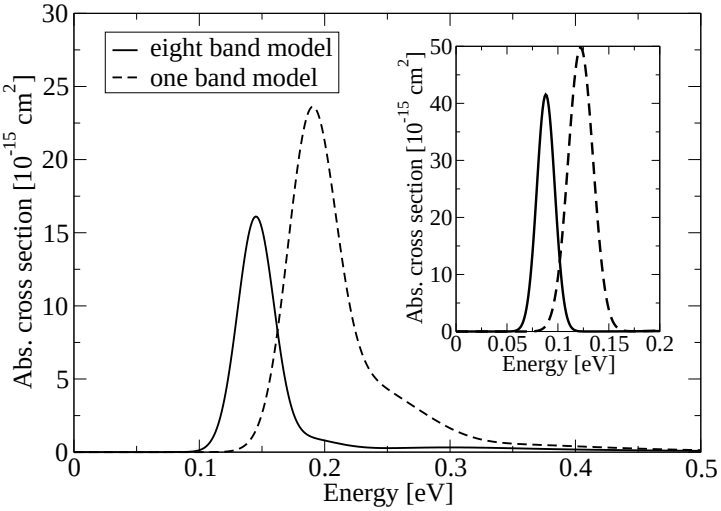

Figure 6.4: The intraband optical absorption spectrum for a quantum dot in the shape of a truncated cone with the diameter of $D = 15\,\text{nm}$, height $h = 7\,\text{nm}$ and base angle of $\alpha = 60^0$, with $In_{0.15}Ga_{0.85}As$ layers of thickness $d = 6\,\text{nm}$ positioned both under and above the dot, surrounded by GaAs barriers, in the case of $z-$polarised radiation. The corresponding spectrum for the in-plane polarised radiation is shown in the inset.

The intraband spectrum for the quantum dot in the shape of a truncated cone with the diameter of $D = 15\,\text{nm}$, height $h = 7\,\text{nm}$ and base angle of $\alpha = 60^0$ with $In_{0.15}Ga_{0.85}As$ layers of thickness $d = 6\,\text{nm}$ positioned both under and above the dot and surrounded by GaAs barriers, is analysed next. The dimensions were chosen to approximately match the dimensions of the quantum dots-in-a-well structure studied in Ref. [64] (the structure labelled as F therein). The optical absorption spectrum for $z-$polarised radiation is given in Fig. 6.4, while the inset shows the spectrum for the in-plane polarised radiation. In

this case, there is a single peak for $z-$polarised radiation originating from $1e_{1/2} \rightarrow 3e_{1/2}$ ($1e_0 \rightarrow 2e_0$) transition ($2e_{1/2}$ has opposite value of spin to $1e_{1/2}$), while the same states as in the previous case are responsible for absorption of in-plane polarised radiation. Similarly to the previous structure considered, the effective mass approach predicts larger peak absorption energies and stronger absorption, which may be attributed to the same effect, as the positions of the ground state with respect to the continuum, calculated by the two methods, are again almost the same (270 meV in eight band vs. 280 meV in one band model). The experimental results in Ref. [64] give the peak spectral response wavelength at 9.5 μm (Fig. 2 therein, curve labelled as F), the $\boldsymbol{k} \cdot \boldsymbol{p}$ method predicts the value of 8.6 μm, while the effective mass method gives 6.5 μm. The discrepancy between the results obtained by the $\boldsymbol{k} \cdot \boldsymbol{p}$ method and the experiment is most likely due to the effects of intermixing of InAs and GaAs during growth at elevated temperatures.

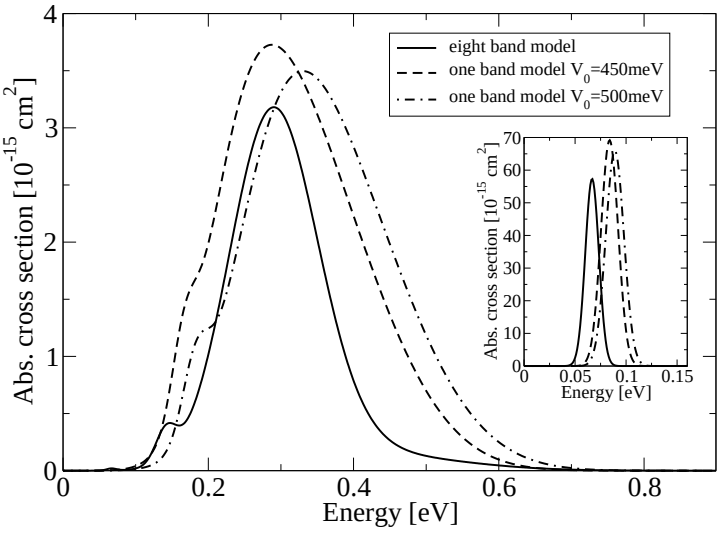

Figure 6.5: The intraband optical absorption spectrum for quantum dots in the shape of a lens with the diameter of $D = 20\,\text{nm}$, height $h = 3\,\text{nm}$ for $z-$polarised radiation. The corresponding spectrum for in-plane polarised radiation is shown in the inset.

Finally, a lens-shaped quantum dot is studied, with a diameter $D = 20\,\mathrm{nm}$ and a height $h = 3\,\mathrm{nm}$. Quantum dots of similar shape and size were reported in several experiments [60, 71, 79, 81] and this is therefore one of the most typical shapes of InAs/GaAs self-assembled quantum dots. The intraband optical absorption spectrum calculated by the two methods is shown in Fig. 6.5. The effective mass calculation was performed with two different values of the conduction band offset $V_0 = 450\,\mathrm{meV}$ and $V_0 = 500\,\mathrm{meV}$, because the calculated hydrostatic strain profile suggested that a larger value of V_0 than the conventional one (of 450 meV) should be used. Furthermore, the position of the ground state with respect to the onset of the GaAs continuum, calculated using the value $V_0 = 500\,\mathrm{meV}$ is approximately the same as in the case of the $\boldsymbol{k} \cdot \boldsymbol{p}$ method (approximately 230 meV), in contrast to the smaller value of 190 meV when the conventional value of V_0 is used.

The dominant line in the absorption spectrum for in-plane polarised incident radiation stems again from the transition to a pair of (nearly) degenerate excited states. The position of the peak, at 66 meV, calculated within the $\boldsymbol{k} \cdot \boldsymbol{p}$ framework is within the range of experimentally observed values 55−85 meV [60, 81], while the effective mass method gives somewhat larger values. On the other hand, the main peak in the spectrum for $z-$polarised radiation originates from transitions to resonance states in the continuum. In this case, the absorption spectrum calculated by the two methods gives almost the same peak position of 280 meV, when the same value of the conduction band offset is chosen as in the previous cases. The overestimation of intraband energies, due to the neglect of non-parabolicity effects, exists in the effective mass method in this case too, but it is compensated by the underestimation of the ground state position with respect to the continuum. When a larger value of the conduction band offset is taken, which puts the ground states at the same position, the peak calculated within the effective mass method appears at a larger energy. On the other hand, the experimental results in Refs. [60, 71, 79, 81] give the peaks in the range 150–300 meV.

The results obtained suggest that the in-plane polarised radiation causes non-negligible transitions only between the ground and first excited state, these being located in the region 40–80 meV in the far-infrared. On the other hand, $z-$polarised radiation causes the transition in the $\sim 100-300\,\mathrm{meV}$ region in the mid-infrared. The best way to understand the origin of such behaviour is via a simplified model presented in Sec. 6.2.1. Such behaviour can be altered only if the dot dimension in the $z-$direction becomes comparable to the in-plane dimensions. These results are in agreement with previous theoretical calculations that addressed the issue of polarisation dependence of intraband absorption [81,226,246]. Recent experimental studies [71,72,81,247,248] have also identified the mid-infrared response to originate from z-polarised radiation, although some earlier studies suggested it is nearly polarisation independent [249]. On the other hand, the mid-infrared response has been observed on many occasions in experiments performed in normal-incidence geometry [59,63,64,69,77–80,250]. This would contradict the results previously mentioned if one assumed ideally in-plane polarised radiation in these experiments. However, several effects (such as off-normal axis experimental missalignment, light scattering, etc.) can cause a certain degree of $z-$polarisation in the radiation interacting with the dots, and cause the response in the mid-infrared ($\sim 100-300\,\mathrm{meV}$). For example, the polarisation dependent measurements reported in Ref. [81] have assigned the mid-infrared response measured in normal-incidence geometry in Ref. [79] to $z-$polarised radiation. It has also been emphasised in Ref. [71] that the mid-infrared response results reported in the literature in the normal-incidence geometry are indeed due to $z-$polarised radiation.

In view of the fact that one of the expected advantages of QDIPs over QWIPs is the ability to detect radiation of any polarisation, these results are somewhat discouraging. The absorption of $z-$polarised radiation causing transition taking place to some higher excited state (possibly even in the continuum) can certainly be observed in photocurrent spectrum. However, in-plane

polarised radiation causing transition to well bound first excited state(s) can hardly cause a strong photocurrent response.

6.4 Conclusion

A simulation of several typical InAs/GaAs QDIP structures reported in the literature and a systematic comparison of the two methods used to calculate the intraband absorption has been given. The results obtained by the two methods are in qualitative agreement – the transition from the ground state to the pair of first excited states is responsible for absorption of in-plane polarised radiation, while the absorption of $z-$polarised radiation is due to the transition to a higher excited bound state in the case of larger dots and due to the transition to resonance states in the continuum in the case of small and flat dots. On the other hand, quantitatively, the effective mass method overestimates both the transition energies and the optical absorption cross sections. Therefore, while the simple and fast effective mass method can be quite useful for general understanding of intraband absorption and assignment of the experimental peaks to different transitions, the $\boldsymbol{k}\cdot\boldsymbol{p}$ method is more appropriate for a study aiming to provide quantitative predictions.

The work presented in this Chapter was published in Semiconductor Science and Technology [251].

Chapter 7

Quantum dots-in-a-well infrared photodetectors

7.1 The effect of well width

The difficulties in controlling the size and shape of self-assembled quantum dots make it very hard to engineer these devices and produce a QDIP for a specified, user-defined detection wavelength. The so called quantum dots-in-a-well (DWELL) infrared photodetectors [64, 77, 78], where an InAs quantum dot layer is embedded in an $In_{0.15}Ga_{0.85}As$ quantum well (see Fig. 7.1), have a special place among different types of QDIPs. They have been introduced with the motivation to tailor the operating wavelength by changing the well width, which would therefore lead to a recipe for producing a QDIP with the desired spectral response. Such expectations were recently confirmed experimentally [64,78] where tailoring of 2–3 μm in the long wavelength atmospheric window (8–12 μm) has been achieved by varying the well width by 3–5 nm.

Current thought, based on experimental results, is therefore that it is the modification of the energy levels and the corresponding wavefunctions, due to the change of well width, that shifts the spectral response peak. A theoretical study quantifying this effect would therefore be very useful as it might provide a recipe for the well width necessary to obtain the desired detection wavelength. However, it has been pointed out in Ref. [64, 78] that unintentional changes in dot size may also shift the operating wavelength. Furthermore, one

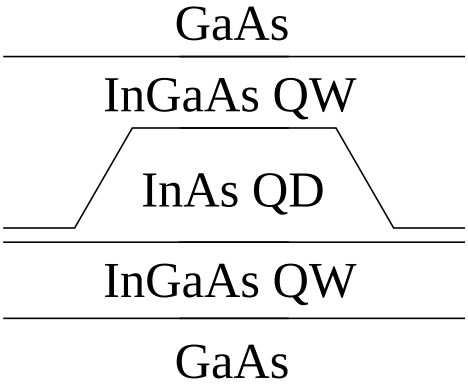

Figure 7.1: Scheme of an InAs quantum dot embedded in an $In_{0.15}Ga_{0.85}As$ quantum well.

cannot exclude the possibility of change in the dot composition due to the effects of interdiffusion and segregation [252]. Uncertainties in the experimental determination of the dot size and composition make it very difficult to establish which of the above effects is dominant - the effect of the intentional change of well width or the effect of unintentional changes in dot size or composition. Clearly, it would be highly desirable that the effect of intentional control of well width prevails. In this section, a theoretical study is performed quantifying the above effects with the aim of understanding the origin of the experimentally observed wavelength tailoring in DWELLs.

The calculation of the optical absorption spectrum was performed within the framework of the 8-band $\boldsymbol{k} \cdot \boldsymbol{p}$ method as described in Chapter 6. The inhomogeneity of the quantum dot ensemble was taken into account assuming a Gaussian lineshape on each of the transitions with a standard deviation equal to 10% of the transition energy, which is approximately equal to the experimental values for the dominant transitions in Refs. [64, 78].

The optical absorption spectrum was first calculated for a quantum dot of the shape of a truncated cone with a diameter of 15 nm, height 7 nm, base angle 60^0, and a 6 nm wide $In_{0.15}Ga_{0.85}As$ layer positioned above the dot layer, which are approximately the dimensions of the DWELL structures reported in

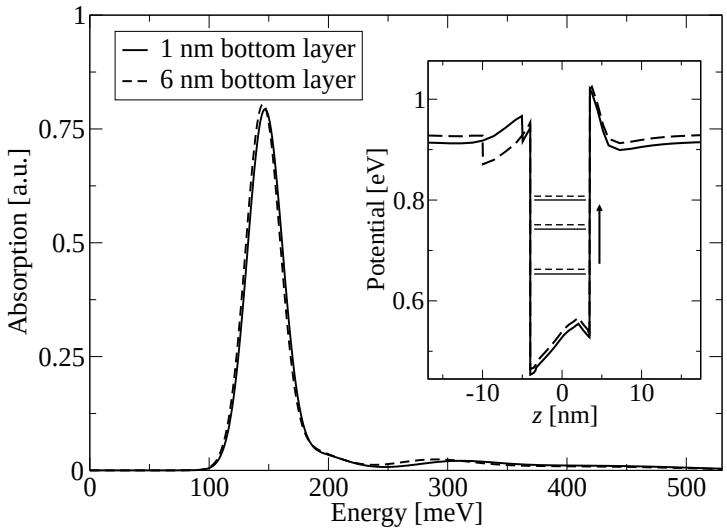

Figure 7.2: Absorption spectrum of a DWELL structure with a quantum dot of the shape of a truncated cone with a diameter of 15 nm, height 7 nm, base angle 60^0, a 6 nm wide $In_{0.15}Ga_{0.85}As$ layer positioned above the dot layer and 1 nm (full line) or 6 nm (dashed line) wide layer under the dot. The inset: Effective potential profile along the z-axis and the first three $|m_f| = 1/2$ energy levels for the same structure.

Ref. [64]. The width of the $In_{0.15}Ga_{0.85}As$ layer under the dot was varied from 1 nm to 6 nm, as in the experiment [64]. In all calculations a 0.5 nm wide wetting layer was also assumed. The results of these calculations are shown in Fig. 7.2. The peak of the spectrum is in both cases positioned around 8.5 μm with a relative difference between the positions of the two peaks of only 2%, while in the experiment the spectral response peak wavelength is red-shifted from 7 μm to 9.5 μm (i.e. by about 30%) when the layer width is increased in the above interval (Fig. 2 in Ref. [64]). This gives the first indication that the shift in the operating wavelength cannot be explained in terms of the effect of the well width. The transition from the ground state (having $|m_f| = 1/2$) to the third $|m_f| = 1/2$ state dominates the spectrum. Both states are bound (270 meV and 125 meV below the continuum respectively), and the influence of the well width on their positions and separation is very weak. It is generally

expected that the effect of the well width should be more pronounced when the level to which the absorption is maximal has its energy within the range of the quantum well confinement potential (roughly within 15% of the conduction band offset below the continuum in the case of $In_{0.15}Ga_{0.85}As$ well). The same type of calculation was therefore performed for quantum dots of different height and In composition in the dot, in order to investigate the effect for different positions of that level. These calculations also allow quantification of the sensitivity of the peak absorption wavelength on the changes in dot size or composition.

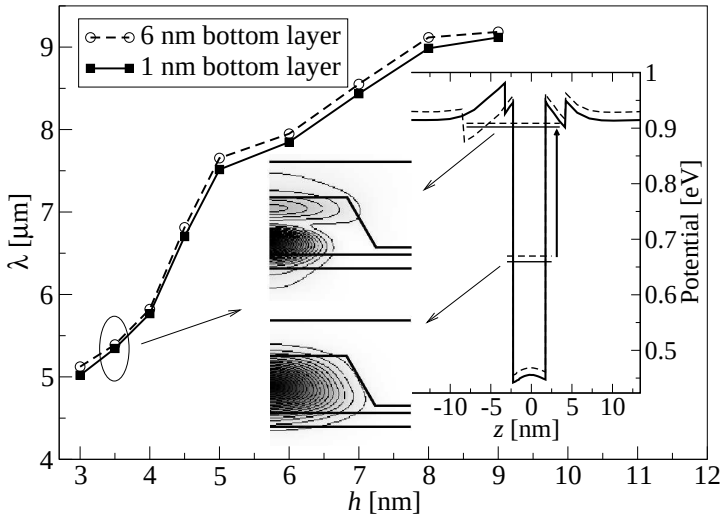

Figure 7.3: The operating wavelength of a DWELL structure from Fig. 7.2 for different quantum dot heights, for the case of 1 nm thick bottom layer (full line) and 6 nm thick bottom layer (dashed line). The right inset: Effective potential profile along the z-axis, the ground state and the state to which absorption is maximal when the dot height is h=3.5 nm. The left inset: The wavefunctions of the two states in the case of a 1 nm bottom layer.

The change in the detector operating wavelength when the height of the quantum dot is varied from 3 nm to 9 nm is shown in Fig. 7.3. One can see that throughout the whole investigated interval of dot heights the change in the peak absorption wavelength is less than 3% when the bottom layer width

is changed from 1 nm to 6 nm. For small values of dot height ($h \lesssim 4$nm), the absorption to the state which is within the range of the quantum well confinement potential is dominant. Nevertheless, as seen from the right inset in Fig. 7.3, the influence of the well on the position of this state is weak. When the bottom layer width is 1 nm the wavefunction of the state is largely confined to the dot volume, which provides a large overlap with the ground state and strong absorption. An increase in the bottom layer width induces a change proportional to the probability that the wavefunction is located in the interval from 1 to 6 nm beneath the wetting layer, and since this is small (see the left inset in Fig. 7.3), the change in the state energy is small, too. The change of well width has a much stronger influence on states that are less confined to the dot. However, such states have a poor overlap with the ground state and do not significantly contribute to the absorption. Consequently, the influence of the well width on the absorption spectrum is weak.

The dependence of the detection wavelength on the In content in the dot is given in Fig. 7.4. For smaller values of In content in the dot (for example $x = 0.65$) the absorption in the case of a 1 nm bottom layer is maximal towards a resonant state in the continuum (see the right inset in Fig. 7.4), which is less confined to the dot than the corresponding state when the In content is larger. The increase in well width then has a larger impact on that state, shifting it down and correspondingly red-shifting the absorption peak (see the left inset in Fig. 7.4), and therefore the difference between the operating wavelengths in the case of a 1 and a 6 nm bottom layer increases as the In molar content in the dot decreases. However, even in the extreme case of $x = 0.5$ the relative difference between the operating wavelengths is just 10%, which is well below the experimentally observed value of 30%.

From the results obtained, a conclusion can be drawn that tailoring of the detection wavelength in DWELL structures cannot be explained if one assumes that the dot remains of the same size and with the same composition. In fact, the pure effect of well width plays only a minor role in shifting the

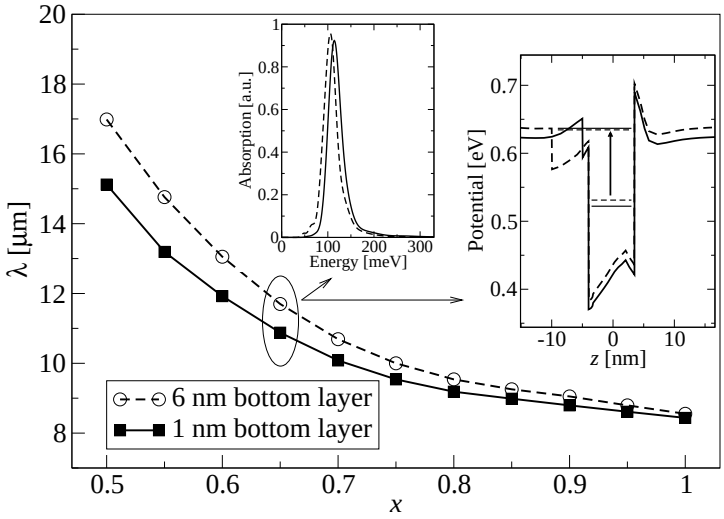

Figure 7.4: Dependence of the operating wavelength λ of a DWELL structure from Fig. 7.2 on In composition in the dot x. The absorption spectrum when the In molar content in the dot is $x = 0.65$ is given in the left inset, while the right inset shows the effective potential profile along the z-axis, the ground state and the state to which the absorption is maximal. The results are given for the case of 1 nm (full line) and 6 nm thick bottom layer (dashed line).

detection peaks. The observed changes in the operating wavelength can then be explained only in terms of unintentional modification of the quantum dot size because of changed growth conditions or composition due to the effects of interdiffusion or segregation. From Fig. 7.4 one can see that in the range of In content around $x = 1$ the changes in wavelength with the composition are only slight and that only extremely large changes in x, which are highly unlikely in the experiment, would be sufficient to explain the experimental shifts. On the other hand, variations in the size of the dot can induce more pronounced changes in the position of the peak of the spectrum, as is evident from Fig. 7.3. For example, a slight decrease in the size of the dots from 5 nm to 4 nm changes the wavelength by 26%, which is the value comparable to the experimentally observed ones. Bearing in mind that the shifts originating from the pure effect of well width and the changes in dot composition are

significantly smaller, the dot size variations can be safely identified as the main source of wavelength tailoring. All the calculations reported have also been performed for a fixed value of bottom layer width, while varying the top layer from 1 nm to 6 nm. The magnitude of the observed shifts was similar, indicating that the conclusions drawn are valid in this case too.

In conclusion, theoretical calculations of the absorption spectrum of DWELL structures have been performed for a range of dot sizes, compositions and the embedding well widths. From these calculations it has been shown that experimentally observed detection wavelength shifts cannot be explained as an effect of intentional changing the well width, and that they rather originate from the unintentional changes in quantum dot dimensions.

The work presented in this section was published in Applied Physics Letters [253].

7.2 Intraband Stark effect in DWELL structures

The effect of pre-growth tailoring of QDIP detection wavelength was investigated in Sec. 7.1. It would be certainly more attractive if one were able to tune the detection wavelength of a particular structure, by means of external fields, for example. In principle both static electric and magnetic fields could be used. However, as shown in Chapter 3, large magnetic fields (of the order of at least $\sim$10T) are necessary to provide a significant effect on the quantum dot energy levels, which is an approach which is certainly not attractive from the commercial point of view. On the other hand, external bias is already necessary for QDIP operation, and therefore it would be highly advantageous if the Stark shift created by the electric field could be used at the same time for control of the operating wavelength.

It has indeed been shown that the spectral response of a QDIP may be voltage dependent [64, 254, 255]. However, the voltage controllability of QDIP response reported in Refs. [64, 254, 255] stems from the changes in relative response of different peaks in the photocurrent spectrum with applied bias. It

is not a consequence of the Stark effect as individual peaks remain at approximately the same position. The Stark shift on interband transition in QDs has been reported in Ref. [256]. Relatively large fields of ∼300 kV/cm were necessary to cause a shift of ∼10 meV. On the other hand, in QDIP structures an order of magnitude smaller fields are typically used which makes it difficult to observe the intraband Stark shift.

As already emphasised in Chapter 6, self-assembled quantum dots typically have much larger dimensions in the lateral direction than in the growth direction. As a consequence, mid-infrared intraband absorption transitions involving higher energy states (which contribute to the photoresponse) are strongest for radiation polarised in the $z-$direction. Transitions take place between the ground state and excited states which arise due to confinement predominantly in the growth direction. A significant Stark effect for these transitions is possible if there is a large z-component of the dipole moment, i.e. if there is a difference of the z-coordinate of the centroids of the two states. As quantum dot heights are small (a few nanometers), this difference becomes small as well. In order to increase the difference between the centroids of the two states, one can displace the excited state by embedding the dot in a well. In order for this effect to be efficient the excited state should be above the quantum well confinement potential. This makes dots-in-a-well structures more suitable for observing the Stark shift than conventional quantum dot structures. The transition then takes place between the ground state of the dot, and an excited state which is a mixed quantum dot - quantum well state, which will for simplicity be called quantum well state.

In this section, the results of the modelling of the DWELL structures where the intraband Stark effect was observed, will be reported. The structures were grown and characterised at the University of Sheffield. The DWELL structures comprised InAs dots placed within an 8 nm $In_{0.15}Ga_{0.85}As$ quantum well, with 1 nm of the well below the dots and 7 nm above. The dots in the structure S_1 were obtained by depositing 2.9 monolayers (MLs) of InAs, where in the case

of S_2 2.2 MLs were deposited. The experimental dependence of the transition energy on applied bias is given in Fig. 7.5. The absorption does not contribute significantly to the photocurrent at zero and low (<0.4V) negative or positive biases because of the low electron escape probability from the quantum well state. Shifts of 15% energy are measured between +1V and −1V for the 2.9 ML sample.

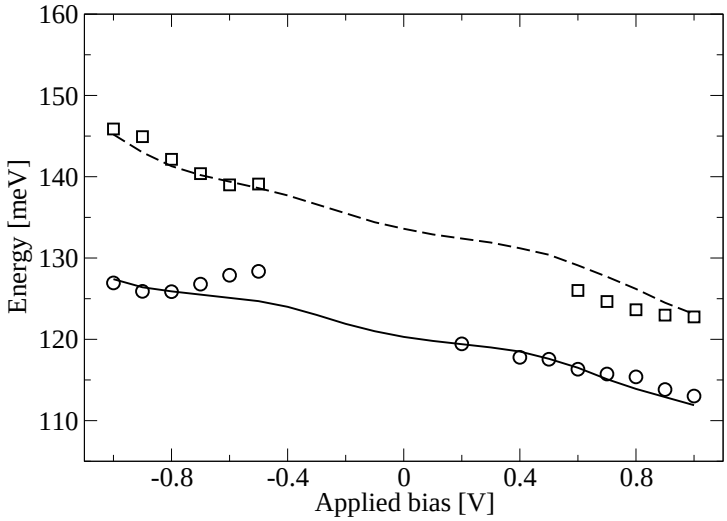

Figure 7.5: The transition energy dependence on applied bias: for 2.9 ML sample – experimental (open squares) and calculated (dashed line), and for 2.2 ML sample – experimental (open circles) and calculated (solid line).

The calculation was performed assuming dots of truncated conical shape with base diameter D, height if the dot were not truncated H, actual height h, and indium content in the dot x. In the simulations, these parameters were varied in the range where the calculated absorption spectrum exhibits a maximum in the same spectral region as the experimental spectrum: h was varied in the interval 4-7 nm; x from 0.6 to 0.75, D in the range 15-22 nm, and H was set to 10 nm. The best fit for the dependence of the transition energy on bias was obtained when $h = 4\,\mathrm{nm}$, $x = 0.7$, $D = 17\,\mathrm{nm}$, as shown in Fig. 7.5 (dashed line). In order to verify the importance of the presence of the embedding well for the observation of the Stark shift, an additional

calculation was performed for the same structure but without the embedding well. The calculated Stark shift was only 6% in this case, compared to 15% in the previous case.

It is known that for the transition between two truly discrete states one obtains the quadratic dependence of the transition energy on the electric field (including the terms up to second order of perturbation theory). However, in this case the transition takes place between a truly discrete bound state and a quasi-continuum density of states. The maximum of the absorption spectrum is then determined by complex changes in the density of states and does not follow a simple quadratic trend, as shown in Fig. 7.5. The continuum density of states is represented by a discrete set of states which is a consequence of embedding the dot in a cylinder of finite size. It has been checked that the embedding cylinder is large enough so that the calculated absorption spectrum and the position of its maximum have converged. In the calculation which involves discretised continuum states the position of the maximum is determined by the interplay of the bias dependences of energies of several states, as well as by the relative contribution to the absorption spectrum of each of these states.

In Fig. 7.6 the wavefunctions of the ground and the excited state to which the absorption is maximal when the bias is equal to -0.6V and $+0.6$V, as well as the on-axis potential profile with the energies of the states that mostly contribute to the absorption, are shown. One can see from the wavefunctions shown in Fig. 7.6 that the ground state wavefunction is weakly influenced by the electric field, while the influence of the electric field on the wavefunction of higher energy quasi-bound states which mostly contribute to the absorption is much stronger.

The 2.2 ML sample exhibits a similar photoresponse as 2.9 ML sample with the transition occurring at a lower energy due to the shallower confinement potential and a smaller bias dependent shift of the photoresponse ($\sim$11%). This indicates that S_2 has a smaller separation between the centroids of the quantum dot ground and quantum well state. Detailed information about the

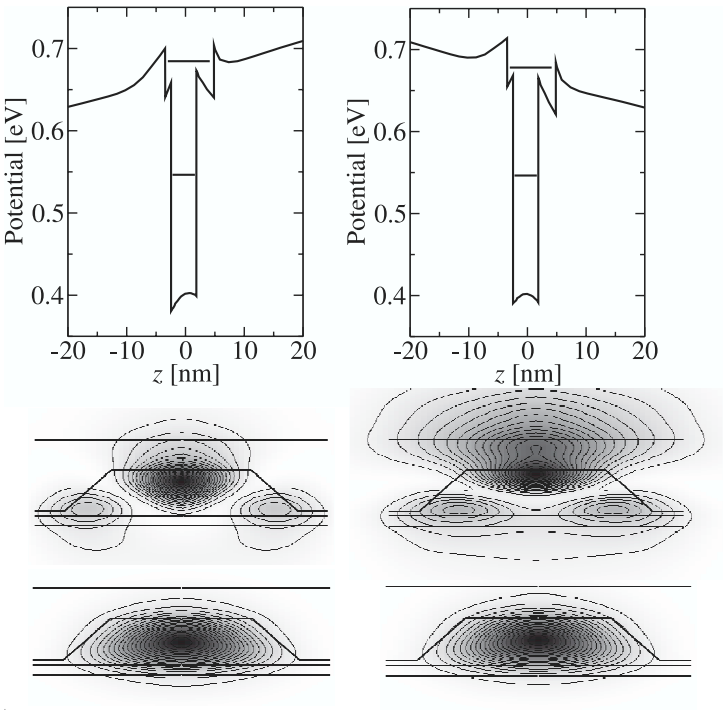

Figure 7.6: The calculated potential profile along the z-axis (top) and contour plots of wavefunction moduli of the ground state (bottom) and the state to which absorption is maximal (middle) in the case of dot dimensions that best fit the 2.9 ML sample for -0.6V (left) and $+0.6$V (right).

quantum dot structure would be necessary to introduce a non-uniform indium profile in the simulation, however an agreement with experimental results can be obtained using a larger QD height ($h = 6\,\mathrm{nm}$). The dots are then placed in the middle part of the well and the asymmetry of the system is smaller. The best fit to the experimental results (Fig. 7.5, solid line) is obtained when $h = 6\,\mathrm{nm}$, $x = 0.66$, $D = 17\,\mathrm{nm}$. Therefore the most probable explanation for the observed differences in the photoresponse of the two samples is an increased In content in the dot for S_1, leading to an increased transition energy and a decrease of the dot height for S_1, leading to an increased Stark shift. Whilst additional structural investigations would be necessary to unambiguously identify the origin of the increased Stark shift, the results clearly show that the

bias dependent spectral shift of the photoresponse is sensitive to quantum dot growth parameters and may be controlled by varying the asymmetry of the DWELL system.

In conclusion, it has been shown that DWELL structures are more favourable in terms of achieving significant values of Stark shift, in comparison to conventional quantum dot structures. It should however be emphasised that not every DWELL structure is suitable for observing the Stark shift. Numerous DWELL structures used as trial structures in fitting the experimental results, where the dominant optical transition takes place to a bound state, showed only a weak Stark shift, being no larger than the Stark shift of the same structure without the embedding well.

Chapter 8

Transport in quantum dot infrared photodetectors

8.1 Introduction

The realisations of the variety of different QDIP structures have initiated the development of several theoretical approaches with different levels of complexity to understand the performance of QDIPs. As the detection is based on the process of absorption of incident radiation, a significant amount of theoretical work was focused on calculation of the intraband optical matrix elements within the one band effective mass approach [81, 226, 239–241] or the 8-band $\boldsymbol{k} \cdot \boldsymbol{p}$ method [242, 251, 253]. Some theoretical efforts have also been made to model the current under dark or light conditions [76, 257–263]. In these models, the current is deduced from the analysis of the processes of carrier capture, thermal escape and photoexcitation. However, the rates of these processes are calculated using parameters that were either taken phenomenologically [257–259], deduced from experiment or obtained by fitting [76]. None of these models aims to predict the dependence of relevant QDIP output parameters, such as responsivity or dark current on the choice of material system used or on the quantum dot size and composition, which it is highly desirable to know in order to optimise the QDIP characteristics. Recently, the effects of interdot coupling [264] and Pauli correlations [265] in QDIPs were also studied theoretically. Deeper understanding of the underlying QDIP physics can

also be achieved by obtaining information about carrier distribution among various quantum dot and continuum energy levels, which is hard to access experimentally.

In this Chapter, a theoretical model of vertical electron transport in quantum dot infrared photodetectors is therefore presented. The model starts from the energy level and wavefunctions calculation, followed by evaluation of intra- and inter-period transition rates, from which a system of nonlinear rate equations is formed. From its steady state solution in dark or light conditions, the populations of the energy levels and consequently the dark current and responsivity are calculated. The details of the model are presented in Sec. 8.2, while the results obtained by its application to one of the reported InAs/GaAs QDIP structures [80] are given in Sec. 8.3.

8.2 Theoretical model

QDIPs consist of periodically arranged layers of quantum dots (see Fig. 8.1a), with the period typically equal to $L_z = 50\,\text{nm}$ chosen to minimise the dark current channel via transport between bound states of quantum dots in neighbouring periods. At such a value of the quantum dot period, the quantum dots are not vertically aligned, and the whole structure is not strictly periodic in the $z-$direction. Nevertheless, as a reasonably good approximation, the vertical arrangement and the periodicity of the structure will be assumed in the model as shown in Fig. 8.1b. The processes that determine the dark and light current are the excitation of carriers from the bound quantum dot states to resonant continuum states mainly localised in the quantum dot region, their subsequent transport via the continuum states to the next period, and the possible capture of carriers from the continuum by quantum dots, but not the direct transport between quantum dot bound states of neighbouring periods. Therefore, it is not expected that the transport properties of QDIPs are dependent on the details of the quantum dot arrangement, hence the simplest possible periodic arrangement is chosen in the model.

In order to prevent high values of dark current, quantum dots used in QDIPs are typically either doped at a relatively low level to populate just the ground state or undoped. It is therefore reasonable to assume a uniform electric field throughout the structure as the formation of electric field domains [266, 267] is expected to occur only at high doping densities.

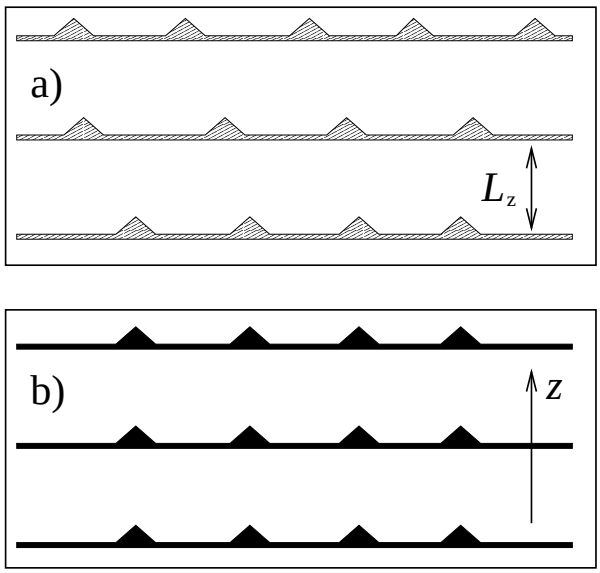

Figure 8.1: Schematic view of three QDIP periods: a) a realistic structure, b) the structure used in the modelling. The period of the structure in the growth direction z is equal to L_z.

8.2.1 Modelling the electronic structure

The energy states of a quantum dot superlattice subjected to a uniform electric field possess the property of shift-invariance. For each state assigned to a certain period of the superlattice (called the central period in the text), there is a set of corresponding states obtained by translating the wavefunction in the growth direction by multiples of the superlattice period. The corresponding eigenenergies are shifted by multiples of the potential drop due to the electric field over one period (see Fig. 8.2). Therefore, it is enough to find the energy

levels assigned to one period only, and the others are then obtained by exploiting the shift-invariance property. The states assigned to the central period are obtained by solving the Hamiltonian eigenvalue problem in the region of space containing $2N+1$ periods (central period, N periods to the left and N periods to the right, see Fig. 8.3) and selecting only the eigenstates whose probability of finding a carrier in the central period is larger than in any of the other $2N$ periods. In the calculations, a value of $N = 2$ was taken based on large value of superlattice period compared to quantum dot size and previous experience with simulations of QWIPs [268, 269].

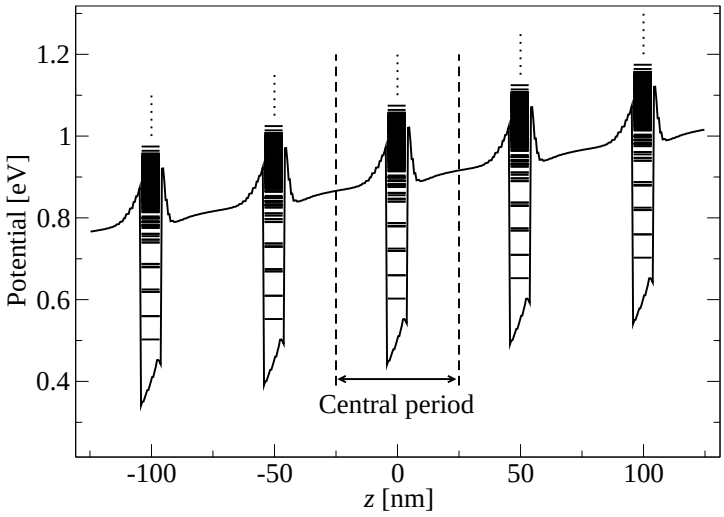

Figure 8.2: The effective potential profile along the z-axis for the analysed structure subjected to an electric field $F = 10\,\mathrm{kV/cm}$ and the corresponding energy levels assigned to each of the five periods.

The 8-band strain dependent $\boldsymbol{k}\cdot\boldsymbol{p}$ Hamiltonian is used to model the single-particle states in the conduction band, as described in Chapter 6. The strain distribution was modelled using the continuum mechanical model and was found using the finite element method as described in Sec. 2.6.2. Due to the periodicity of the structure, periodic boundary conditions in the growth direction were imposed, therefore the strain tensor components need to be found in a single period only.

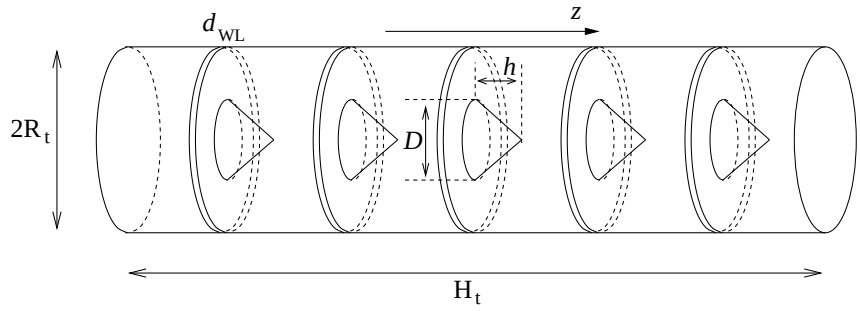

Figure 8.3: The region of space in which the Hamiltonian eigenvalue problem is solved, consisting of $2N + 1$ periods ($N = 2$). The radius of the embedding cylinder is R_t and its length H_t. It is assumed that quantum dots have conical shape with diameter D and height h. The wetting layer width is d_{WL}.

8.2.2 Carrier interaction with phonons and electromagnetic radiation

Due to the discrete nature of states in quantum dots, transition rates between electronic states due to interaction with LO phonons have previously been considered to be vanishingly small unless the energy levels are separated by the energy of an LO phonon [91], as already mentioned in Sec. 1.3.2. Furthermore, LA phonons, due to their small energy, cause transitions only between closely spaced energy levels. These expectations led to the predictions of extremely low dark currents and very small capture rates in QDIPs due to inhibited carrier dynamics. Consequently, QDIPs were expected to have excellent characteristics. However, it is currently thought that the electron – LO phonon interaction in quantum dots cannot be taken into account within the framework of first order perturbation theory and should be considered in the strong coupling regime [93,94], when the entangled electron – LO phonon states called polarons are formed, as discussed in more detail in Sec. 2.7.1. The transition rate between states caused by polaronic decay is then given by Eq. (2.117).

The envelope functions of the initial and final state are given as

$$\psi_j^{(i)}(\boldsymbol{r}) = \sum_{nl} A_{jnl}^{(i)} b_{nm(j)l}(r,z,\varphi), \tag{8.1}$$

$$\psi_{j'}^{(f)}(\boldsymbol{r}) = \sum_{n'l'} A_{j'n'l'}^{(f)} b_{n'm'(j')l'}(r,z,\varphi), \tag{8.2}$$

where $m(j) = m_f - m_j(j)$ and $m'(j') = m'_f - m_j(j')$ with m_f and m'_f being the z-components of the total angular momentum of the initial and final state, respectively. One of the very convenient features of the wavefunction expansion method is that the electron – phonon interaction form factor can be evaluated without the numerically demanding three dimensional integration. Instead, one finds that it can be expressed in terms of the expansion coefficients as

$$F_{if}(\boldsymbol{q}) = \sum_{j=1}^{8} \sum_{nl,n'l'} A_{jnl}^{(i)*} A_{jn'l'}^{(f)} f_1(q_z,\Delta l) f_2(m_f,m'_f,n,n',q_r,j), \tag{8.3}$$

where

$$f_1(q_z,\Delta l) = \frac{1}{H_t} \frac{e^{i\left(q_z+\frac{2\pi}{H_t}\Delta l\right)H_t/2} - e^{-i\left(q_z+\frac{2\pi}{H_t}\Delta l\right)H_t/2}}{i\left(q_z+\frac{2\pi}{H_t}\Delta l\right)} \tag{8.4}$$

is an analytic function of its arguments, while

$$f_2(m_f,m'_f,n,n',q_r,j) = \tfrac{1}{2\pi}\int_0^{2\pi} \mathrm{d}\varphi \int_0^{R_t} r\mathrm{d}r e^{i\Delta m_f \varphi} \times$$
$$\times e^{i(q_x\cos\varphi + q_y \sin\varphi)r} f_{nm(j)}(r) f_{n'm'(j)}(r), \tag{8.5}$$

where $\Delta l = l' - l$, $\Delta m_f = m'_f - m_f$, and

$$q_r = \sqrt{q_x^2 + q_y^2}.$$

The function f_2 does not depend on the wavefunctions and can be tabulated once for all arguments before evaluating the form factors. Finally, since $F_{if}(\boldsymbol{q})$ depends on the radial and the z-component of the wave vector only (and not on the φ-component), the summation (integration) over $\boldsymbol{q}$ in Eq. (5.1) can be simplified from three dimensional to two dimensional.

The weaker electron – LA phonon scattering was calculated using Fermi's Golden rule (see Sec. 2.7.1). Since $F_{if}(\boldsymbol{q}_s)$ does not depend on φ, the two dimensional integration in Eq. (2.121) can be reduced to one dimensional.

Other possible types of scattering were not included in the calculation and the reasons for that are now discussed. As under normal operating conditions, only the ground state of the QD is significantly populated and the populations of the wetting layer and the continuum states are small; all the processes originating from the Coulomb interaction among carriers, being proportional to the carrier density, can therefore be neglected. These are, for example, the relaxation of bound states assisted by the Coulomb interaction between bound and wetting layer carriers [227, 270], or Coulomb scattering among the carriers in the continuum or wetting layer. Coulomb scattering between bound states is also suppressed as in a system with discrete energy levels it is difficult to achieve the resonance imposed by the condition of energy conservation, as already emphasised in Chapter 5. This is also the case for ionised impurity scattering in the case of structures with a doped active region, although in this work the structure with an undoped active region was considered. It has been shown in Chapter 5 that the relaxation rates due to spontaneous emission of photons are much smaller than the other relaxation rates in the system. Finally, in a realistic device, a number of defects are present, depending on the quality of growth. The defects are another potential source of scattering, and as they are not included in the model, it is expected that the results of the model should be valid in the limit of high-quality samples with low defect density.

The interaction with incident electromagnetic radiation was treated in a standard manner within the dipole approximation and Fermi's Golden rule. In a similar manner as the form factors, the absorption matrix elements can be expressed in terms of the expansion coefficients, as given by Eq. (6.12).

8.2.3 The transport model

The energy levels of a quantum dot superlattice will be denoted as $i = (M, P)$ representing the P-th level in ascending order of energies among the levels belonging to the period M. The populations of energy levels and the current

in the device will be found from the semiclassical (Boltzmann equation) model, which due to the discreteness of the energy levels reduces to the following system of rate equations:

$$\begin{aligned}\frac{\mathrm{d}n_i}{\mathrm{d}t} &= \sum_{j\neq i} W_{ji} n_j \left(1-\frac{1}{2}n_i\right) - \sum_{j\neq i} W_{ij} n_i \left(1-\frac{1}{2}n_j\right) - \\ &\quad - \sum_j \sigma_{ij}^p(\omega)(n_i-n_j)\Phi, \end{aligned} \tag{8.6}$$

where the same notation as in Chapter 5 is used.

Due to the periodicity of the structure the relations

$$\begin{aligned} n_{(M,P)} &= n_{(L,P)}, \\ W_{(M,P),(L,Q)} &= W_{(M+K,P),(L+K,Q)}, \\ \sigma_{(M,P)(L,Q)} &= \sigma_{(M+K,P)(L+K,Q)} \end{aligned} \tag{8.7}$$

hold [268, 269, 271]. After exploiting them, the system of equations (8.6) is reduced and contains only the occupations of levels assigned to a central period. Furthermore, in the spirit of the nearest neighbours approximation introduced in Sec. 8.2.1, only the transitions with $|M-L| \leq N$ are considered. As usual, the system of rate equations should be supplemented by the condition imposing the total number of particles in the system. It is therefore assumed that there are n_d electrons per quantum dot on the average, i.e. $\sum_P n_{(M,P)} = n_d$. In order to obtain a finite system of equations, one also has to limit the number of levels per period, i.e. take into account only the states with $P < P_{\max}$. It has been checked for each field that the number of states taken in the calculation was sufficient. Due to the presence of closely spaced discretised continuum states, the number $P_{\max}$ is of the order of several hundred which makes the computation rather demanding, as a large number of transition rates among each pair of states has to be calculated.

As the carrier transition rates in QDIPs are much larger than the frequencies of external excitations, one is mainly interested in the steady-state response ($\mathrm{d}/\mathrm{d}t = 0$). Nevertheless, the rate equations are solved by time integration of the system of equations (8.6), starting from an initial condition that all carriers

are in the ground state and performing the integration until a steady state is reached. Such a method is extremely reliable in terms of convergence unlike the methods for solving a large system of nonlinear equations [272].

After the system of equations (8.6) is solved, the current in steady-state conditions is found by selecting a certain reference plane normal to the growth direction and keeping track of the amount of charge that passes through that plane in a unit of time. Let p_i be the probability that the electron in state i is located to the left of the reference plane. The contribution to the current from the transitions from level i to level f is then given by

$$J_{if} = \; -|e|\,(W_{if} + \sigma_{if}\Phi)\,n_i\left(1 - \tfrac{n_f}{2}\right)\left[p_i(1-p_f) - p_f(1-p_i)\right]. \qquad (8.8)$$

The first term in square brackets in Eq. (8.8) accounts for the carriers that were initially on the left side of the reference plane and pass to the right side, while the second term considers the carriers that were on the right and pass to the left and clearly gives the contribution to current of an opposite sign to the previous one. The total current is calculated by adding the contributions of the current from all the transitions considered.

The probability of finding an electron whose wavefunction is given by Eq. (8.1) in a region of space $a \leq z \leq b$

$$p = \int_{a\leq z\leq b} \mathrm{d}^3\boldsymbol{r} \sum_{i=1}^{8} |\psi_i(\boldsymbol{r})|^2 \qquad (8.9)$$

can also be expressed in terms of the expansion coefficients as

$$p = \sum_{nll'} \sum_{i} A^*_{inl} A_{inl'} \int_a^b \mathrm{d}z\, g_l(z)^* g_{l'}(z), \qquad (8.10)$$

where the last integral is evaluated analytically. This expression is used both for the current calculation according to Eq. (8.8) and assigning a certain period to the state as described in Sec. 8.2.1.

8.3 Results

The model presented in Sec. 8.2 has been applied to the simulation of the InAs/GaAs QDIP structure reported in Ref. [80] (the structure labelled as S-

GaAs therein). The quantum dots are assumed to be of conical shape with the diameter $D = 25\,\text{nm}$ and height $h = 7\,\text{nm}$. A combination of atomic force microscopy and cross-sectional transmission electron microscopy measurements reported in Refs. [80] and [245] has shown that such shape and dimensions are a very good approximation for the dots in the QDIP structure considered. A wetting layer with the width of $d_{\text{WL}} = 0.5\,\text{nm}$ is considered as well. The same set of material parameters for the InAs/GaAs material system as in previous chapters was taken.

The calculated energy levels, as well as the effective potential profile on the z-axis for the structure analysed subjected to an electric field $F = 10\,\text{kV/cm}$ are shown in Fig. 8.2. Due to the relatively large size of the dots, there is a significant number of bound energy levels. The ground state is strongly bound and positioned 300 meV below the continuum in agreement with the experimental results obtained from photoluminescence and photoluminescence excitation studies [80]. The ground state has the $z-$component of total angular momentum $|m_f| = 1/2$, while the other bound states have $|m_f| \leq 9/2$ and are shown in Fig. 8.4. The calculations have shown that the change in the energy level structure of the bound states with electric field is small and therefore the structure shown in Figs. 8.2 and 8.4 can be considered to be a typical representation of the position of energy levels for any field. It can be seen that the states are grouped into five groups according to their energies with energy gaps in between. While the model presented in Sec. 8.2 treats all the states on equal footing regardless of whether such grouping occurs or not, the groups will be labelled with G_1–G_5 and will be used in the discussion to build an intuitive picture of the microscopic processes in the device.

8.3.1 The dark conditions

The calculated dark current density–electric field characteristics at three different temperatures are given in Fig. 8.5. For comparison with experimental results where current voltage characteristics are reported, a mesa area of

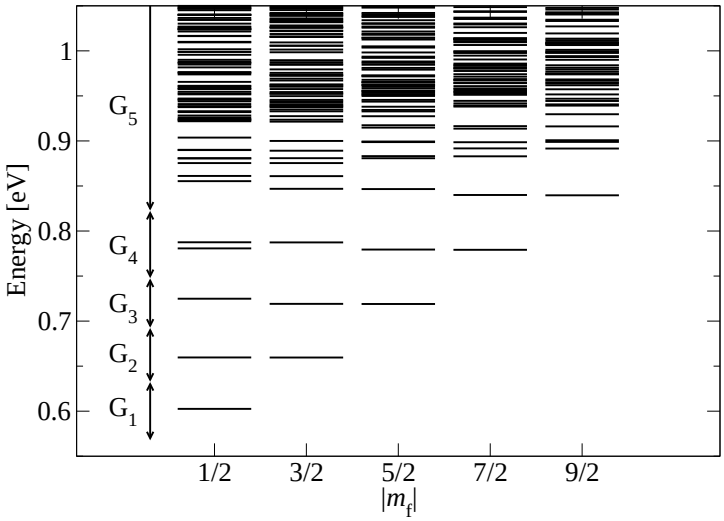

Figure 8.4: Quantum dot energy levels and the quantum number of the $z-$component of their total angular momentum at $F = 10\,\mathrm{kV/cm}$. According to their energy the states are grouped in five groups G_1-G_5.

$A = 5 \times 10^{-4}\,\mathrm{cm}^2$ in accordance with the reported mesa diameter of 250 μm is assumed, and a uniform electric field distributed along the 340 nm long structure is taken. A realistic quantum dot density of $6 \times 10^{10}\,\mathrm{cm}^{-2}$ is taken and it is assumed that there are $n_d = 1$ electrons per dot on average, which is a typical quantum dot occupation number in the case when relatively small voltages are applied in n^+-i-n^+ structures [228]. The comparison with the experiment should be taken with caution as the reported QDIP structure consists of 5 periods only and it is possible that the effects of contacts, not taken into account in this model of a periodic structure, might become important in such cases. Nevertheless, one certainly expects the same trends and at least the same order of magnitude of dark current. The inset in Fig. 8.5 shows that an overall good agreement between the theoretical and experimentally measured results at $T = 77\,\mathrm{K}$ is found, especially bearing in mind that the current changes by seven orders of magnitude in the range of electric fields investigated. It can also be seen that the expected exponential increase of current with field, followed by its saturation is obtained, as well as an increase of current with temper-

ature. The microscopic origin of these expected results will be presented in what follows.

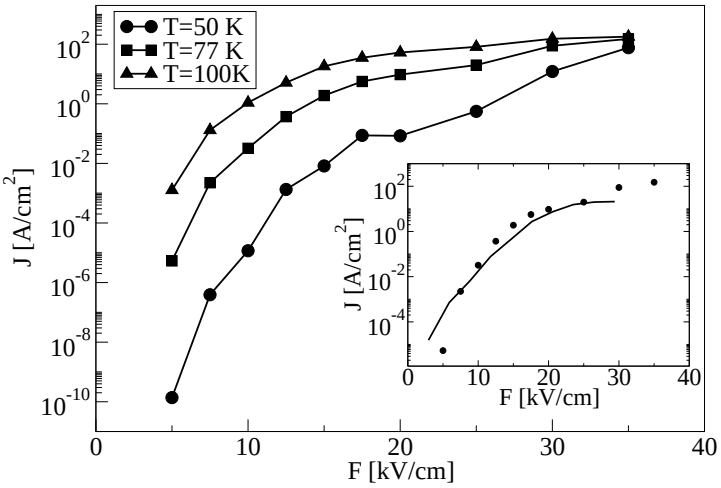

Figure 8.5: Calculated dependence of the dark current density on the electric field at the temperatures $T = 50\,\mathrm{K}$ (circles), $T = 77\,\mathrm{K}$ (squares) and $T = 100\,\mathrm{K}$ (triangles). The inset gives a comparison of the experimental dark current results at $T = 77\,\mathrm{K}$ (line) and calculated values (points).

The carrier distribution among various energy levels at $T = 77\,\mathrm{K}$ is shown in Fig. 8.6. At small values of the electric field the carriers appear to be thermalised and the distribution resembles the equilibrium one. Most of the carriers are then in the ground state. At medium fields the majority of carriers still remain in the ground state, however the nonequilibrium distribution becomes clearly evident with some of the continuum states being more populated than certain bound states. Finally, large values of the electric field significantly increase the population in the continuum and at the same time the occupancy of the ground state falls. The effect of temperature (at a fixed electric field) on the carrier population is similar to the effect of electric field – larger temperatures promote more carriers to the continuum and eventually deplete the ground state.

In order to identify the main carrier transport channels causing the presence

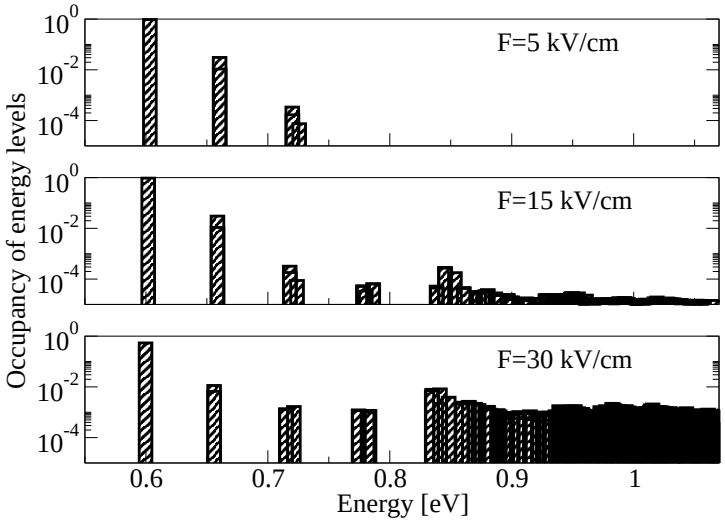

Figure 8.6: Occupancies of energy levels at three different values of electric field at a temperature of $T = 77\,\mathrm{K}$.

of carriers in the continuum and consequently the dark current in the device, the transition rates between different quantum dot states are analysed. The main transition mechanism is due to interaction with LO phonons, while the interaction with LA phonons that carry only a small amount of energy ($\lesssim$ 5 meV) mainly causes the redistribution of carriers within the same group of states, but cannot cause transitions between states from different groups. In order to participate in the current, the carriers must eventually be excited to the continuum (group G_5, see Fig. 8.4) states. The carriers are naturally in the ground (G_1 group) state and only the excitations such as temperature and higher electric fields can populate higher states.

At low values of electric field, the main carrier route to the continuum is via a sequence of transitions $G_1 \rightarrow G_2$, $G_2 \rightarrow G_3$, $G_3 \rightarrow G_4$ and finally $G_4 \rightarrow G_5$. The transitions between non-adjacent groups of bound states, (such as $G_1 \rightarrow G_3$, $G_1 \rightarrow G_4$ or $G_2 \rightarrow G_4$), as well as direct excitations to G_5 states are much less probable due to the larger energy difference (and hence the smaller transition rates) between the levels. When the electric field is increased, the continuum states from the left neighbouring periods (Fig. 8.2)

start to penetrate the quantum dots of the central period. As the field increases the energy of these states decreases and the overlap with the bound states of the central period increases, providing additional channels for carrier excitation to the continuum states. This firstly affects the transition rate from G_4 to G_5, as shown in Fig. 8.7, which increases since the carriers can now be excited not only to the continuum states assigned to the central period, but also to the continuum states of the neighbouring periods with smaller energy distance from G_4 and the overlap which is still sufficient to increase the transition rates. As the electric field is further increased, additional paths of direct carrier excitation to the continuum, such as G_3 to G_5, and at larger fields even G_2 to G_5, are opened and the dark current is therefore significantly increased.

The influence of temperature on the carrier excitation into the continuum is more transparent. The transition rates to higher states in all the paths mentioned, being proportional to the number of LO phonons, increase with temperature (as seen for example from Fig. 8.7) and therefore the number of carriers excited to the continuum and the dark current increase.

8.3.2 The light conditions

The results of the simulation of the mid-infrared (100–250 meV) optical response of the structure investigated, are now presented. Under normal QDIP operating conditions the carriers are mostly in the ground state, and the main origin of the optical response is the absorption of carriers from the ground state.

The calculation shows that significant absorption of the in-plane polarised radiation from the ground state may occur only on transitions to G_2 states and is located in the far-infrared region. The carriers excited to G_2 states in such a manner have a low probability of escaping to the continuum and forming a photocurrent and the structure considered has therefore a poor response to in-plane polarised radiation. Consequently, the transitions in the mid-infrared region may only be due to $z-$polarised radiation and from here the transitions

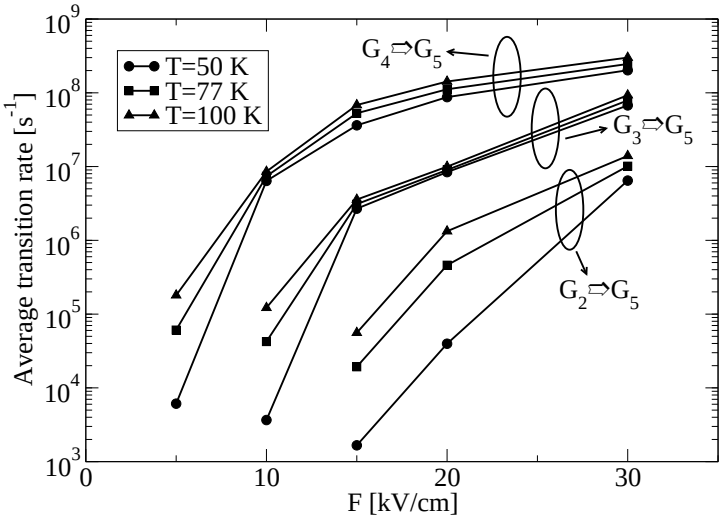

Figure 8.7: The dependence of the average carrier transition rates from the states in groups G_2 to G_4 to the continuum (group G_5) on the electric field at the temperatures $T = 50\,\mathrm{K}$ (circles), $T = 77\,\mathrm{K}$ (squares) and $T = 100\,\mathrm{K}$ (triangles).

due to this polarisation are addressed.

The energy dependence of the optical matrix elements for the absorption of z-polarised radiation from the ground state at an electric field of $F = 10\,\mathrm{kV/cm}$ is shown in Fig. 8.8. It can be also considered as the representative graph for any value of the electric field, as the dominant bound to bound transition matrix elements are weakly influenced by the operating bias. The carriers from the ground state are mainly absorbed to the state of the same symmetry from the G_4 group and to a smaller extent to the state from the G_3 group.

The QDIP responsivity at the angular frequency of incident radiation ω is defined as

$$R(\omega) = \frac{J(\Phi) - J(\Phi = 0)}{\hbar\omega\Phi}. \tag{8.11}$$

In the simulation, the standard deviation of the Gaussian linewidth due to size inhomogeneity of the quantum dot ensemble was taken to be equal to 10% of the transition energy, which is approximately the experimental value of the

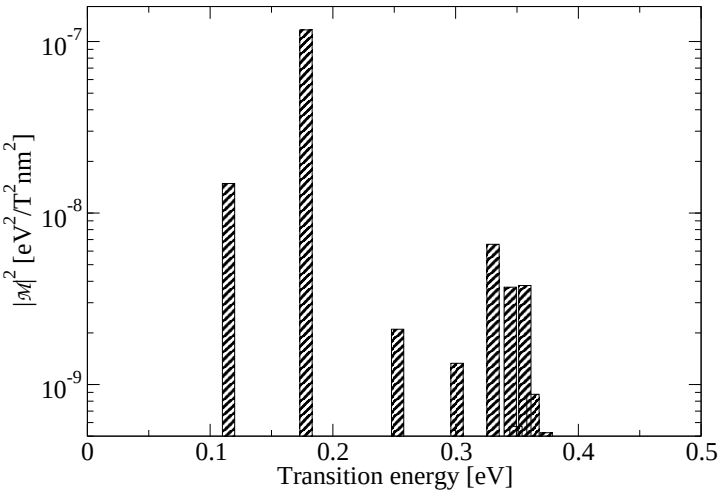

Figure 8.8: The energy dependence of the optical matrix elements for absorption of z-polarised radiation from the ground state at an electric field of $F = 10\,\mathrm{kV/cm}$.

dominant transition in Ref. [80]. The spectral responsivity curves at several different values of the electric field and a temperature of $T = 77\,\mathrm{K}$ are presented in Fig. 8.9. All of them exhibit a main peak around 180 meV originating from the absorption from the ground state to the state from the G_4 group, while at higher values of the electric field another peak at an energy around 115 meV occurs, due to a transition to the state from the G_3 group. The positions of the peaks are in agreement with experiment [80] where the strong peak at 175 meV is accompanied by the weaker one at 115 meV. The peak responsivity mainly increases with electric field as one might expect, but at large values of the electric field it starts to drop. These features can be understood as follows. The carriers that are absorbed from the ground to a state from the G_4 group need to be promoted to the continuum to cause photocurrent. The transition rate from G_4 to the continuum states increases with field, as already explained in Sec. 8.3.1 and shown in Fig. 8.7, causing the photocurrent to increase. However at larger values of electric field the population of the ground state falls (see Fig. 8.6), therefore there are less carriers that can be absorbed, causing the

photocurrent to decrease, see Fig. 8.9. The smaller peak due to absorption to the G_3 state is not present at low fields due to the small probability of further promotion of carriers from the G_3 states to the continuum. At larger fields, when the transition path $G_3 \rightarrow G_5$ is activated (Fig. 8.7), this peak starts to appear.

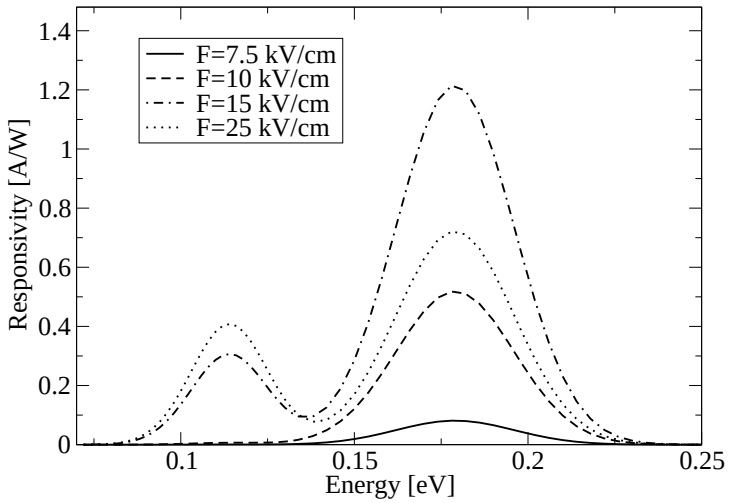

Figure 8.9: The dependence of responsivity on the energy of photons of incident radiation at a temperature of $T = 77\,\mathrm{K}$ and an electric field of $F = 7.5\,\mathrm{kV/cm}$ (full line), $F = 10\,\mathrm{kV/cm}$ (dashed line), $F = 15\,\mathrm{kV/cm}$ (dashed-dotted line), and $F = 25\,\mathrm{kV/cm}$ (dotted line).

The spectral responsivity curves for different temperatures at two values of the electric field are given in Fig. 8.10. The influence of temperature on the responsivity can be understood in a similar manner as the influence of electric field. At smaller values of electric field, the responsivity increases with temperature, as the carriers absorbed to the state from G_4 group are more likely to be promoted to the continuum at higher temperatures. On the other hand, at larger values of the electric field when the ground state starts to be depleted, higher temperature additionally reduces the number of carriers in the ground state, causing less carriers to be absorbed from the ground state and consequently a smaller photocurrent.

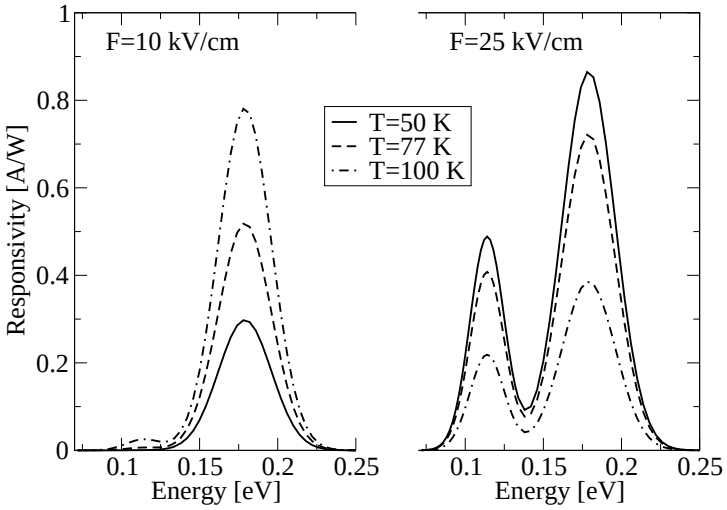

Figure 8.10: The dependence of responsivity on the energy of photons of incident radiation at the temperatures $T = 50\,\mathrm{K}$ (full line), $T = 77\,\mathrm{K}$ (dashed line) and $T = 100\,\mathrm{K}$ (dashed-dotted line) and the values of electric field of $F = 10\,\mathrm{kV/cm}$ (left) and $F = 25\,\mathrm{kV/cm}$ (right).

It is more difficult to give a fair comparison of the theoretical and experimental responsivity results than in the case of the dark current. In the model, an ideally $z-$polarised excitation, performing a single pass through the QDIP active region, is considered. The experiment reported in Ref. [80] was performed in normal incidence geometry, when the incident radiation is certainly not ideally $z-$polarised, as already discussed, and a quantitative comparison of the actual value of the responsivity would require a more detailed analysis of the coupling of the optical field with the active region of the QDIP structure. It can still be said that the results for the responsivity of the order of $R \sim 1\,\mathrm{A/W}$ are consistent with the experimental results. Since only a part of the radiation interacting with the dots is $z-$polarised, one certainly expects that the simulated responsivity would overestimate the experimental one. Indeed, from the photocurrent spectra and the optical excitation power reported in Ref. [80], one may estimate the experimental responsivity to be of the order $R \sim (0.1-1)\,\mathrm{A/W}$ for different values of voltage. Furthermore, the simulation

also predicts a fall of responsivity at higher voltages, as observed in the experiment. The temperature of $T = 77\,\mathrm{K}$ was identified in the experiment as the optimal temperature in terms of the maximisation of the responsivity. In the simulation the responsivity at low voltages increases with temperature, and at high voltages decreases with temperature, one should therefore expect that there is an intermediate region where it exhibits a nonmonotonic behaviour. However, for none of the values of the electric field used in the simulation was such a behaviour observed, implying that the simulation probably predicts a steeper transition between the two regimes than in reality.

A further insight into the origin of the photocurrent can be obtained by analysing the distribution of the photoexcited carriers. The difference between the state occupancies under light and dark conditions for three values of the electric field at $T = 77\,\mathrm{K}$ is given in Fig. 8.11. At a field of $F = 5\,\mathrm{kV/cm}$, most of the carriers photoexcited to G_4 states relax back to the lower states, rather than escaping into the continuum. The carriers absorbed from the ground state are then distributed among G_2–G_4 states. At a higher field of $F = 15\,\mathrm{kV/cm}$, the carriers photoexcited to G_4 have a significant probability to make a transition to the continuum states. Most of the carriers absorbed from the ground state are therefore distributed among continuum levels, as can be seen from Fig. 8.11. The same also holds for the field of $F = 30\,\mathrm{kV/cm}$, but due to a drop in the occupation of the ground state under dark conditions, the total number of absorbed carriers is smaller than at $F = 15\,\mathrm{kV/cm}$.

8.4 Conclusion

In conclusion, a microscopic model of electron transport in vertical conductivity QDIPs was developed. The model considers the transitions between various quantum dot bound and continuum states to evaluate the current under dark or light conditions, without resorting to any fitting parameters. The model was applied to one of the experimentally reported QDIP structures. A very good agreement with the dark current experimental results was found in the

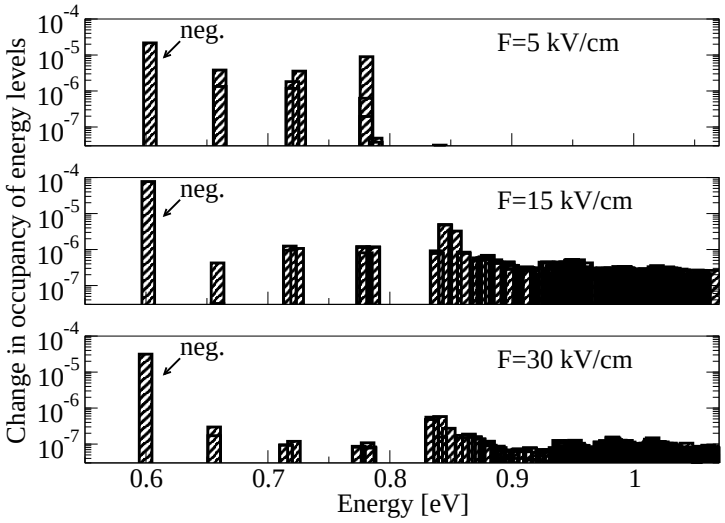

Figure 8.11: The change in the occupancies of energy levels due to the optical flux excitation of $\Phi = 10^{18}\,\mathrm{cm}^{-2}\mathrm{s}^{-1}$ at the peak responsivity photon energy at three different values of electric field and a temperature of $T = 77\,\mathrm{K}$. Only absolute values of the changes are presented and the negative (neg.) quantities are therefore marked.

range of voltages where the current changes by as much as seven orders of magnitude. The simulations also predict most of the experimentally observed trends in responsivity.

The proposed model should therefore serve as a useful tool in the analysis of the characteristics of existing QDIP devices, providing a better understanding of their performance and enabling researchers to find the way for possible device improvements. More importantly, as the model does not contain any fitting parameters, it can be used to predict the performance of new types of QDIP devices and suggest whether such devices would perform better than the existing ones. Finally, the model gives a deeper insight into internal QDIP physics, extracting important information about carrier excitation paths to the continuum and carrier distribution both under dark and light conditions.

The work presented in this Chapter was published in Journal of Applied Physics [273].

Chapter 9

Nonequilibrium Green's functions theory of transport in quantum dot cascades

9.1 Introduction

In recent years, a significant experimental interest has been put into the possibility of the development of intraband lasers based on quantum dots [102–104]. Due to the truly discrete electronic spectrum of quantum dots, most of the undesired scattering and relaxation processes are suppressed, and such devices are expected to have two orders of magnitude lower threshold currents than the corresponding quantum well based devices, as already discussed in Sec. 1.3.2.

Several encouraging experimental results towards the realisation of this type of device have been obtained. In Ref. [102], electroluminescence has been observed from the structure consisting of InAs quantum dots embedded in a GaAs/AlAs quantum well based cascade structure, based on the transition from the quantum well state to the quantum dot ground state. The transition from the ground state of AlInAs quantum dots to subbands of GaAlAs/GaAs quantum wells was the origin of emission reported in Ref. [103]. On the other hand, electroluminescence from the transition between the dot states of InGaAs quantum dots in a GaAsN/GaAs superlattice, was achieved in Ref. [104]. Electroluminescence from the transition between the dot states in a single layer of InAs quantum dots in a superlattice was also observed [274,275]. However, the lack of precise controlability of quantum dot geometry is probably the main

reason why lasing has not yet been achieved. Nevertheless, improvements in technology will, at some point, certainly make such devices feasible.

The physics of such quantum dot devices is essentially different from quantum well devices that possess a continuous spectrum. Polaron effects are known to be important [270] and one can also expect that due to reduced phase space for decoherence, coherent processes are relevant. Therefore, there is an obvious need for the development of an appropriate theoretical framework, capable of treating such processes. After the initial theoretical proposals of quantum dot cascade lasers [92, 99], only a few theoretical studies of this type of devices were reported. Their luminescence spectra was investigated in Ref. [100]. The structures based on a quantum dot superlattice were proposed and analysed in Ref. [101]. However, a detailed transport model through such structures has not yet been developed. Therefore, in this Chapter, a nonequilibrium Green's functions theory of steady-state transport through periodic arrays of single or multiple quantum dots is presented and applied to several structures.

It should be mentioned that the interest in this Chapter is in transport through bound states of *closely stacked* quantum dots, as the transport in quantum cascade lasers takes place through these states. In Chapter 8, QDIPs were also modelled as periodic arrays of quantum dots. However, the period of the structure in QDIPs is large and the transport takes place through continuum states there, which makes the physical situation essentially different.

9.2 Theoretical approach

The current in the steady state through an array of identical quantum dots will now be calculated within the nonequilibrium Green's functions formalism described in Sec. 2.8.

As a first step in application of the formalism to a given physical system, one has to choose the basis of states to represent the Green's functions. Any complete basis can be used in principle since a physical theory must be independent of its choice. Here, a basis of states localised mainly to one period

is chosen. Such a choice enables one to make a tight-binding approximation where interactions with nearest neighbours only are considered. Additionally, such a basis gives an excellent insight into the carrier transport in real space. Due to the periodicity of the structure, the basis states are labelled as (ν, n), where ν is the index of the state assigned to period n. In the case when only ground states are important, the first index can be suppressed. The basis states are calculated as follows.

The electronic miniband structure of a quantum dot superlattice is solved using the eight band $\boldsymbol{k} \cdot \boldsymbol{p}$ method with strain distribution taken into account via continuum elasticity theory, as described in more detail in Chapter 6. As a result of this step one obtains the quantum dot superlattice eight component spinors $|\Psi_{\nu K_z}(\boldsymbol{r})\rangle$, satisfying the Bloch condition

$$|\Psi_{\nu K_z}(\boldsymbol{r} + L_z \boldsymbol{e}_z)\rangle = e^{iK_z L_z} |\Psi_{\nu K_z}(\boldsymbol{r})\rangle, \tag{9.1}$$

where ν is the miniband index, L_z the period of the structure, and K_z the superlattice wave vector. The phase of the spinors was fixed by imposing the condition that the value of the dominant spinor component at a particular point in space is real and positive.

The spinors obtained are then used to construct Wannier states that are localised to a certain period. The Wannier state originating from miniband ν, localised to period n is given by

$$|\Psi_{\nu n}\rangle = \frac{L_z}{2\pi} \int_{-\pi/L_z}^{\pi/L_z} \mathrm{d}K_z e^{-inK_z L_z} |\Psi_{\nu K_z}\rangle. \tag{9.2}$$

In order to obtain states with even better localisation, the eigenvalue problem of the operator of z-coordinate is solved in the manifold of states spanned by $|\Psi_{\nu n}\rangle$, $n \in \{-N, \ldots, N\}$. The $(N+1)$-th eigenvector then corresponds to the basis state $(\nu, 0)$. The states (ν, n), when $n \neq 0$ are then obtained by making a translation in real space by nL_z.

Once the basis of states is chosen, one can proceed to calculate the relevant Green's functions represented in that basis and afterwards the current in the structure. As shown in Sec. 2.8, in the steady state of the system, one obtains

an algebraic system of equations for Green's functions in the energy domain, containing the Dyson equation (2.136), the Keldysh relation (2.137), and the expressions for self-energies. The system of equations is closed by imposing the periodic condition for all Green's functions and self-energies

$$G_{(\nu,n),(\mu,m)}(E) = G_{(\nu,n+1),(\mu,m+1)}(E + V_F), \tag{9.3}$$

where V_F is the potential drop over one period of the structure, and introducing a tight-binding approximation by considering only the Green's functions and self-energies with $|n - m| \leq K$.

Self-energies are modelled using the SCBA. Within the SCBA, self-energies due to interaction with LO phonons are given by (2.139) and (2.140). These take into account the anharmonic decay of LO phonons, which is known to be important for the proper description of relaxation processes in quantum dots [95]. The justification of application of the SCBA to electron – LO phonon interaction self-energies in the system studied here will be given in Sec. 9.3. In the expressions for self-energies, only the electron – phonon interaction form factors between states with $|n - m| \leq K$ are assumed to be nonvanishing, in the spirit of the tight-binding approximation.

Self-energy terms due to interaction with acoustic phonons are given by the formulae which have the same form as in the case of LO phonons. These can be simplified to avoid a demanding integration in the energy domain, assuming acoustic phonons are stable. They then read [184]

$$\Sigma^R_{\alpha\beta}(E) = \sum_{\gamma\delta,\boldsymbol{q}} M^*_{\beta\delta}(\boldsymbol{q}) M_{\alpha\gamma}(\boldsymbol{q}) \quad \left[(N_{\boldsymbol{q}} + 1) G^R_{\gamma\delta}(E - E_{\boldsymbol{q}}) + N_{\boldsymbol{q}} G^R_{\gamma\delta}(E + E_{\boldsymbol{q}}) + \right.$$
$$\left. + \tfrac{1}{2} G^<_{\gamma\delta}(E - E_{\boldsymbol{q}}) - \tfrac{1}{2} G^<_{\gamma\delta}(E + E_{\boldsymbol{q}}) \right], \tag{9.4}$$

$$\Sigma^<_{\alpha\beta}(E) = \sum_{\gamma\delta,\boldsymbol{q}} M^*_{\beta\delta}(\boldsymbol{q}) M_{\alpha\gamma}(\boldsymbol{q}) \left[N_{\boldsymbol{q}} G^<_{\gamma\delta}(E - E_{\boldsymbol{q}}) + (N_{\boldsymbol{q}} + 1) G^<_{\gamma\delta}(E + E_{\boldsymbol{q}}) \right], \tag{9.5}$$

where $E_{\boldsymbol{q}}$ is the energy of an acoustic phonon. The principal value integrals appearing in the expression for the retarded self-energy have been neglected, as is often done in the literature [276].

An additional self-energy term representing the nonuniformity of quantum dots can also be included, as described in Sec. 9.7.

The interest here will be in the limit of low doping and carrier densities where interaction with ionised impurities and electron – electron interaction can be neglected, and there is no formation of electric field domains. In this region, current depends linearly on the number of carriers. Therefore, the values of current presented on figures in this Chapter have been normalised by dividing it by the total occupancy of states in one quantum dot (or double quantum dot in Sec. 9.8). Current density J can then be obtained by multiplying the current by sheet carrier density $J = N_{\mathrm{S}} I$.

The system of algebraic equations for Green's functions and self-energies was solved in a manner that is now described. The overall strategy consisted of two steps. In the first step, the spectral properties of the system are found by solving the Dyson equation and neglecting the lesser Green's functions in the expression for the retarded self-energy. This step provides a good initial guess for the retarded functions for a fully self-consistent procedure in the second step.

- For the first step, an initial guess for the retarded Green's function is chosen in the form of the free particle function broadened by the width σ as $G^R_{\alpha\beta}(E) = \frac{\delta_{\alpha\beta}}{E - E_\alpha + i\sigma}$, where E_α is the ground energy of miniband α. The retarded self-energy is then calculated by not including the terms with lesser Green's function. Next, the retarded Green's functions are calculated from the Dyson equation by solving the appropriate system of linear equations. The former two steps are repeated until convergence is achieved.

- In the second step, a fully self-consistent procedure is performed. An initial guess for the lesser Green's functions is taken in the form

$$G^<_{\alpha\beta}(E) = 2\pi i \, g(E - E_\alpha, \sigma) \, n_\alpha \delta_{\alpha\beta}, \tag{9.6}$$

  where g is the Gaussian (2.67), and n_α is the initial guess for expected

values of state populations given by the thermal distribution of carriers. An initial guess for the retarded Green's functions is provided from the result of the first step of the calculation. Retarded and lesser self-energies are then calculated. Next, the retarded Green's function is found from Dyson's equation, and finally the lesser Green's function is calculated from the Keldysh relation. These three steps constitute one iteration of the self-consistent procedure which is repeated until convergence is achieved. In order to improve the stability of the self-consistent procedure, the lesser and retarded functions for the next iteration are calculated from their average value in the previous two iterations, as is usually done in self-consistent calculations. After each iteration the lesser Green's functions are adjusted to enable the total number of particles to be equal to a given predefined value.

When the current – field characteristic is calculated, i.e. when the same calculation is performed for different values of the electric field, the results obtained for the previous value of the field can be used as an initial guess, instead of performing the first step described above. With this approach the number of iterations necessary decreases significantly from several tens ($\sim 30-50$) to just a few ($\sim 5-6$).

It should be mentioned that due to the assumption of dispersionless LO phonon modes, the integral in the expression for self-energy does not depend on $\boldsymbol{q}$. Therefore, the terms $M_{\alpha\beta\gamma\delta} = \sum_{\mathrm{q}} M^*_{\beta\delta}(\boldsymbol{q}) M_{\alpha\gamma}(\boldsymbol{q})$ can be calculated only once before the self-consistent procedure, rather than in each iteration.

When the self-energies due to the interaction with acoustic phonons are concerned, due to assumption of isotropic dispersion relation these take the form

$$\int d^3\boldsymbol{q} M^*_{\beta\delta}(\boldsymbol{q}) M_{\alpha\gamma}(\boldsymbol{q}) f(|q|). \tag{9.7}$$

The integral over spherical coordinates θ and φ for each $|q|$ can therefore be calculated before the self-consistent procedure. However, the integral over $|q|$ must be calculated in each iteration.

The populations of the energy levels and coherences between states can finally be calculated by performing an integration of lesser Green's functions over the whole energy domain. The current through the structure can also be calculated as described in Sec. 9.4.

9.3 Validation of the self-consistent Born approximation

The main approximation in the model described is the use of the self-consistent Born approximation (SCBA), which therefore needs to be validated.

The SCBA was used in Ref. [277] to describe the transport through two quantum dots coupled to contacts in the presence of the electron – LO phonon interaction. The electron – phonon interaction matrix elements $M_{\alpha\alpha\alpha\alpha}$ used in Ref. [277] were of the order $\sim 0.001 \times E_{\mathrm{LO}}^2$, implying a weak interaction where the SCBA is fully justified, and it has been argued in Ref. [277] that polaron effects become important when $M_{\alpha\alpha\alpha\alpha}$ approaches E_{LO}^2, which is expected to be the regime of strong electron – phonon coupling, beyond the reach of SCBA.

In Ref. [270], polaron relaxation in InGaAs quantum dots assisted by the presence of wetting layer states was treated within the random-phase approximation (in which only $G^R D^<$ term in the expression for the retarded self-energy is considered, and therefore involves neglection of additional terms in comparison to the SCBA). It has been pointed out there that the RPA is expected to be valid in the presence of continuum states provided by the wetting layer, which has been verified by the comparison with the first term in the cumulant expansion [270].

On the other hand, in Ref. [180] the problem of interaction of quantum dot carriers with dispersionless LO phonon modes was treated, as outlined in Sec. 2.7.2, and the conclusion was reached that the SCBA cannot reproduce the exact solution of the idealised model given by a series of delta functions. This is a consequence of the fact that the SCBA sums only a limited number of diagrams in the expansion, while a full summation is needed to reproduce

delta functions.

None of the previous works just mentioned [180, 270, 277] gives a definite answer on whether the SCBA is a good approximation in the system considered here. Numerical calculation of the $M_{\alpha\alpha\alpha\alpha}$ matrix element (where α is the ground state) gives the value of $\sim 0.07 \times E_{\mathrm{LO}}^2$, which is larger than the value used in Ref. [277] but still significantly smaller than E_{LO}^2. The validity of the RPA in Ref. [270] was established for a quantum dot system with a significant number of carriers present in the wetting layer continuum, while here the interest is mainly in transport through bound quantum dot states. In contrast to Ref. [180] where a single quantum dot interacting with dispersionless LO phonons only is considered, other interactions are included in the system considered here, such as anharmonic terms leading to LO phonon decay, the interaction with acoustic phonons, the tunnelling interaction with neighbouring dots of a quantum dot array, as well as an additional term due to nonuniformity of the quantum dot ensemble.

In order to validate the use of the SCBA, it will be established here that for InAs/GaAs quantum dots, the polaron shift of the ground state, as well as the polaron splitting when the energy difference between the ground and first excited state is set to an LO phonon resonance, are accurately calculated in the SCBA. This gives confidence that the positions of the peaks of Green's functions are correct. The physical properties of the system depend not only on the positions of the peaks but also on their linewidths. One therefore has to establish that the linewidths originate from real interactions in the system, rather than from the effect described in Ref. [180]. This will be done *a posteriori* by showing that the calculated linewidths are significantly larger than the ones arising due to artificial broadening of the spectrum of electrons interacting with dispersionless LO phonons only.

A comparison of the polaron shifts in the spectrum calculated by exact diagonalisation of the Hamiltonian given in Eq. (2.103) as described in Sec. 2.7.2, and by the Green's function method, for different electron – phonon interac-

tion strengths, is given in Fig. 9.1. The calculations were performed for a lens shaped single InAs/GaAs quantum dot of diameter 20 nm and height 5 nm, which is representative of typical self-assembled quantum dots obtained in experiments. The electronic structure of quantum dots was calculated using the eight band strain dependent $\boldsymbol{k} \cdot \boldsymbol{p}$ model in the axial approximation, as described in more detail in Chapter 6. The electronic states obtained that way were subsequently used as input for both calculations. The strength of the electron – phonon interaction was artificially varied by multiplying the electron – phonon interaction Hamiltonian (2.123) by a constant whose value is given on $x-$axis in Fig. 9.1.

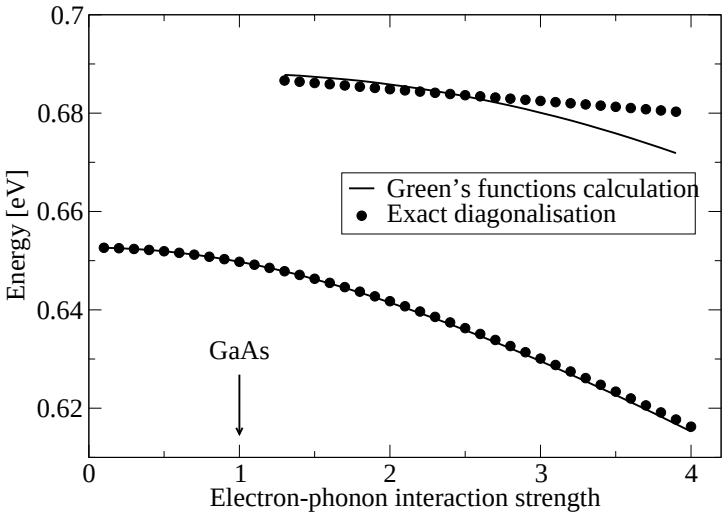

Figure 9.1: The dependence of the energy of the ground state and its first phonon replica of a single InAs/GaAs quantum dot on the electron – LO phonon interaction strength. A comparison of the results obtained by exact diagonalisation of the electron – LO phonon interaction Hamiltonian (circles) and by the Green's function calculation in the SCBA (full line) is given.

In order to provide a fair comparison, in both calculations, only the ground and the pair of nearly degenerate first excited states were taken into account, and only the electron – LO phonon interaction was considered. The energies of the polaron states that contain a contribution from the purely electronic

ground state of more than 10% are represented by circles in Fig. 9.1. The Green's function calculation was performed by self-consistently iterating between Eqs. (2.136) and (2.139), where a temperature of $T = 77\,\mathrm{K}$ was assumed. In Fig. 9.1 the positions of the maximum of the spectral function $A_{11}(E) = -2\mathrm{Im}G^{\mathrm{R}}_{11}(E)$, and its replica when its peak value is at least 10% of the main maximum peak value are shown with a full line. The Green's functions of the ground and first excited state are given in Fig. 9.2. One can see from Fig. 9.1 that excellent agreement for the polaron shift of the ground state obtained by the two methods is obtained throughout the whole interval of electron – phonon interaction strengths investigated. On the other hand, for larger interaction strengths (say larger than 2.5) the positions of the replica start to differ. Further presentations will show that this replica is important for the description of carrier transport. Therefore, the conclusion arising from the results presented in Fig. 9.1 is that the application of the SCBA can be expected to give reliable prediction of polaron shifts up to the electron – phonon interaction strength being 2.5 times larger than the strength in the InAs/GaAs material system which is of central interest here.

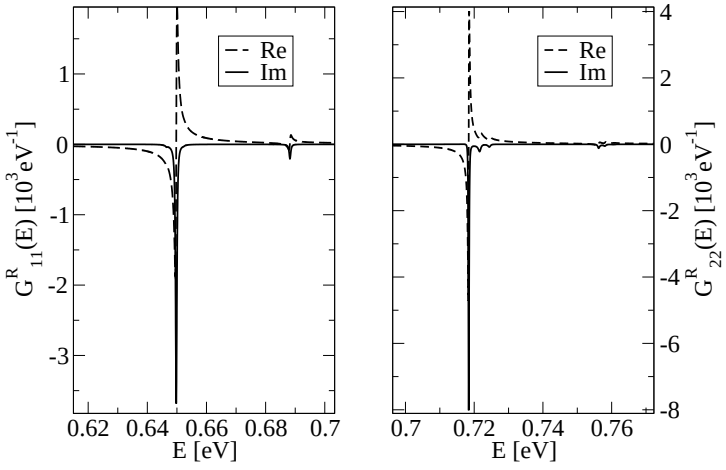

Figure 9.2: Real (dashed line) and imaginary (full line) part of the Green's function of the ground state (left) and first excited state (right).

It is shown next that the SCBA also accurately predicts the amount of

polaron splitting when two levels are at an LO phonon resonance. For that purpose, a numerical experiment is performed where the energies of the pair of first excited states are shifted in opposite directions by the same amount ΔE, which is varied. The electron – phonon interaction matrix elements are kept constant. The polaron energy levels that contain a contribution from at least one of the electronic states larger than 10% are shown by circles in Fig. 9.3, while the maxima of spectral functions A_{ii} whose peak values are at least 10% of the main peak value are represented by diamonds, squares and triangles, for $i = 1$, $i = 2$ and $i = 3$, respectively. The results obtained by the SCBA are in excellent agreement with the results obtained by direct diagonalisation.

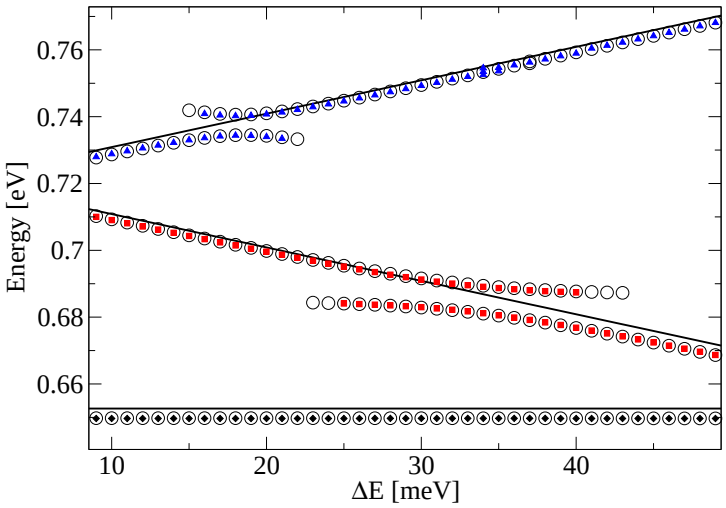

Figure 9.3: Dependence of the polaron energy levels obtained by direct diagonalisation (circles) and the maxima of the spectral functions $A_{ii}(E)$ obtained in the SCBA (diamonds $i = 1$, squares $i = 2$ and triangles $i = 3$) on the artificial shift ΔE. The corresponding single-particle levels are shown by full lines.

9.4 Transport in an ideal superlattice of quantum dots

The electron current through an array of quantum dots can be expressed in terms of the expectation value of the velocity operator as

$$I = -\frac{|e|}{L}\left\langle \frac{\mathrm{d}\hat{Z}}{\mathrm{d}t} \right\rangle, \tag{9.8}$$

where L is the total length of the structure in the $z-$direction and $\hat{Z}$ is the coordinate operator of all the electrons in the system in the Heisenberg picture. From its equation of motion one gets

$$\frac{\mathrm{d}\hat{Z}}{\mathrm{d}t} = \frac{i}{\hbar}\left[\hat{H}, \hat{Z}\right], \tag{9.9}$$

where $\hat{H}$ is the total Hamiltonian of the system. Bearing in mind that all interaction terms commute with $\hat{Z}$, as emphasised in Ref. [278], one obtains the following expression for the current

$$I = -\frac{|e|}{L}\frac{i}{\hbar}\left\langle \sum_{\alpha\beta}\left[\hat{H}_0, \hat{z}\right]_{\alpha\beta}\hat{a}^{+}_{\alpha}\hat{a}_{\beta} \right\rangle, \tag{9.10}$$

where $\hat{H}_0$ is the Hamiltonian of an electron in the superlattice potential, $\hat{z}$ its coordinate operator, $\hat{a}^{+}$ and $\hat{a}$ are electron creation and annihilation operators and the summation takes place over a complete basis of states of the system. Using the definition of the lesser Green's function one gets

$$I = -\frac{|e|}{L\hbar}\sum_{\alpha\beta}\left[\hat{H}_0, \hat{z}\right]_{\alpha\beta} G^{<}_{\beta\alpha}. \tag{9.11}$$

By exploiting the periodicity of the structure, it follows

$$I = -\frac{|e|}{L_z\hbar}{\sum_{\beta}}' \sum_{\alpha}\left[\hat{H}_0, \hat{z}\right]_{\alpha\beta} G^{<}_{\beta\alpha}, \tag{9.12}$$

where L_z is the period of the structure, and the summation over β takes place over the states of one period only (called the central period). In view of the nearest neighbour approximation, the summation over α then takes place over the states in the central period and its few nearest neighbours only.

The current given by the expression (9.12) was interpreted in Ref. [278] to be entirely coherent, where the scattering events only redistribute the carriers in energy domain. Following that interpretation, the origin of all resonances, presented in the sections that follow, can be explained in terms of oscillations of coherence between ground states of neighbouring periods, when the external field is varied. However, such an interpretation would not give an insight into the origin of the mentioned coherence oscillations. It has also been pointed out in Ref. [278] that in the basis of Wannier-Stark states coherences are created by scattering, leading to a well known picture of scattering induced transport between Wannier-Stark ladder of states.

A very useful view of how coherences are created by scattering comes from the interpretation of the Keldysh relation. The interpretation in the time domain [184] considers $\Sigma^<$ as a scattering event, which is then propagated by G^R and G^A to a moment of time when coherence $G^<$ is observed. Following a similar interpretation that can be given in the energy domain and the fact that current is entirely determined by coherences, one can determine the origin of current in the structure, as follows. In the case when $\alpha = \gamma$, $\delta = \beta$ and $\gamma \neq \delta$, the contribution to current from $G^<_{\alpha\beta}(E)$ originates from a scattering event (represented by $\Sigma^<_{\gamma\delta}(E)$) creating coherence at energy E, which will be observed only if there is available density of states (information about which is contained in $G^R_{\alpha\gamma}(E)$ and $G^A_{\delta\beta}(E)$) at that energy. On the other hand, when $\alpha = \gamma$, $\delta \neq \beta$ and $\gamma = \delta$, the current originates from a coherent propagation $G^A_{\delta\beta}$, which will be observed providing there are carriers scattered into $\gamma = \delta$ (the term $\Sigma^<_{\gamma\delta}(E)$) and available density of states at $\alpha = \gamma$ (the term $G^R_{\alpha\gamma}(E)$). The same interpretation of a coherent origin of current can be given in the case $\alpha \neq \gamma$, $\delta = \beta$ and $\gamma = \delta$. Other cases where the current originates from a combination of scattering and coherent propagation are also possible, but it is expected that these, being higher order processes, give a much smaller contribution. The results of the calculation presented here will indeed show that this is the case.

The current-field characteristics were calculated for a quantum dot array consisting of quantum dots whose dimensions are given in Sec. 9.3 for several different values of the period of the structure. The results of the calculation for different temperatures when the period is equal to $L_z = 10\,\mathrm{nm}$ are given in Fig. 9.4. It was necessary to take into account two nearest neighbours ($K = 2$) in the calculation to obtain convergent results. Self-energies due to the interaction with LO and acoustic phonons were both included in the calculation. Only the states originating from the ground miniband were considered at $T = 77\,\mathrm{K}$ and $T = 150\,\mathrm{K}$ since these are the only ones that are significantly populated then, while it was necessary to include a pair of first excited states at $T = 300\,\mathrm{K}$.

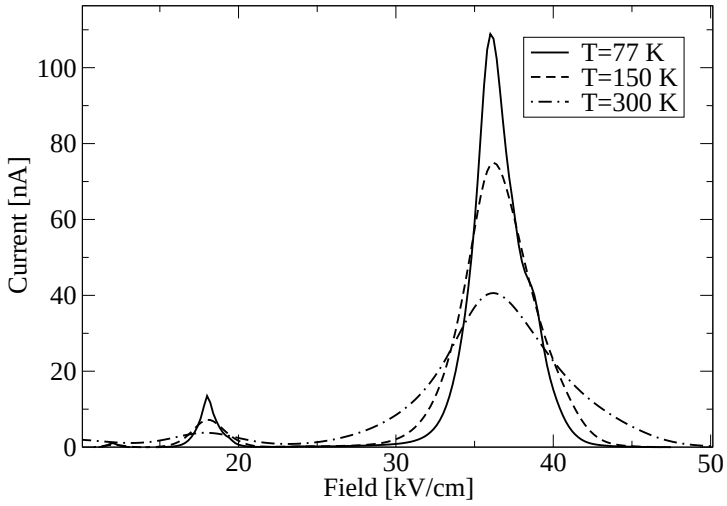

Figure 9.4: Current – electric field characteristics of a quantum dot superlattice at temperatures $T = 77\,\mathrm{K}$ (full line), $T = 150\,\mathrm{K}$ (dashed line) and $T = 300\,\mathrm{K}$ (dashed-dotted line) when the period is $L_z = 10\,\mathrm{nm}$.

9.5 The main current peak

The main peak arises when the potential drop over one period V_F is equal to LO phonon energy E_{LO}. The second peak appears at $V_F = \frac{1}{2}E_{\mathrm{LO}}$ at all

temperatures, while there is also a third peak at $V_F = \frac{1}{3}E_{\mathrm{LO}}$ present at lower temperatures. The origin of these resonances, as well as the nature of the electron transport at resonances will be investigated in what follows.

The most similar physical system where resonances of this kind were investigated are quantum well superlattices in an external axial magnetic field. It has been predicted [279–281] that optical phonon resonances occur whenever $nE_C + pV_F + qE_{LO} = 0$ (Stark-cyclotron-phonon resonance), and elastic resonances (Stark-cyclotron) when $nE_C + pV_F = 0$ (where E_C is the cyclotron energy). The observation of Stark-cyclotron resonances was reported in Ref. [282]. A special case of both of these, so called Stark-magneto-phonon resonances that occur when $nE_C = pV_F = qE_{LO}$ was recently measured in Refs. [283] and [284]. The resonances predicted in the results reported here are in full analogy with Stark-cyclotron-phonon resonances or Stark-magneto-phonon resonances in the case of quantum well superlattices in a magnetic field.

On the other hand, phonon-assisted transport through a double quantum dot was theoretically investigated in Ref. [277]. A weak LO phonon peak was obtained which is a consequence of the fact that a weak LO phonon interaction strength was assumed.

The focus will be given on the case of low temperatures when only the ground state is occupied. The results of the calculation were transformed to a Wannier-Stark basis which is more useful for the physical interpretation of the results. In that case, one can show using the properties of translational invariance and the identity $G^<_{\alpha\beta} = -G^{<}_{\beta\alpha}{}^*$ that in the Wannier-Stark basis, the expression (9.12) reduces to

$$I = \frac{e^2F}{\hbar}\sum_{\alpha>0}\alpha\cdot 2\mathrm{Re}\left(z_{0\alpha}G^<_{\alpha 0}\right). \tag{9.13}$$

For $L_z = 10\,\mathrm{nm}$, the current is entirely determined by the $\alpha = 1$ term, i.e. by the coherence between two ground states of neighbouring periods $G^<_{10}(E)$. In order to understand the origin of the current, one therefore has to investigate the origin of this coherence. It should be mentioned that the fact that $G^<_{10}(E)$

determines the current does not necessarily imply that nearest neighbour approximation is sufficient. Indeed, in this particular case, convergent results are obtained with second nearest neghbour approximation $K = 2$.

The dominant contribution to $G^<_{10}(E)$ when $V_F = E_{\mathrm{LO}}$ comes from the $G^R_{11}(E)\Sigma^<_{10}(E)G^A_{00}(E)$ term in Keldysh relation. The corresponding Green's functions and self-energies are presented in Fig. 9.5. $G^<_{10}(E)$ exhibits a maximum at the energy of level 0, originating from the maxima of the scattering $\Sigma^<_{10}(E)$ term and the $G^A_{00}(E)$ term. In view of the interpretation of the Keldysh relation presented, the origin of the current at this value of the field is LO phonon scattering from level 1 to level 0, represented by the $\Sigma^<_{10}(E)$ term. By expressing $G^<_{10}$ in the energy domain as

$$G^<_{10} = \frac{1}{2\pi}\int \mathrm{d}E G^<_{10}(E) \tag{9.14}$$

and substituting into (9.13) one can also spectrally resolve the current flow between periods 1 and 0. The maximum of the spectrally resolved current appears at the energy of the ground state of period 0, confirming the fact that the current flows into level 0, as demonstrated in the left part of Fig. 9.6.

When one increases the electric field, the scattering $\Sigma^<_{10}(E)$ term decreases as 1 and 0 are no longer set to an LO phonon resonance. One should note that first phonon replica in the spectral density of states $A_{00}(E) = -2\mathrm{Im}G^R_{00}(E)$ (see Fig. 9.6) is separated from the main maximum by an energy larger than E_{LO}, as a consequence of the polaron shift, as demonstrated in Sec. 9.3. Consequently, the resonance between the level 1 and phonon replica of level 0 occurs at a higher field, which in this particular case corresponds to a potential drop per period of $V_F = 38.3\,\mathrm{meV}$ rather than $V_F = E_{\mathrm{LO}} = 36\,\mathrm{meV}$. Around this resonance, the nature of the electron transport is significantly different than at an LO phonon resonance. The dominant contribution to coherence $G^<_{10}(E)$, shown in Fig. 9.7, now comes from the $G^R_{11}(E)\Sigma^<_{11}(E)G^A_{10}(E)$ term. Therefore, the current originates from coherent propagation represented by $G^A_{10}(E)$, which now exhibits a pronounced maximum at the energy of level 1. The coherence $G^<_{10}(E)$, and hence the current exhibit a maximum at the energy of level 1 (see

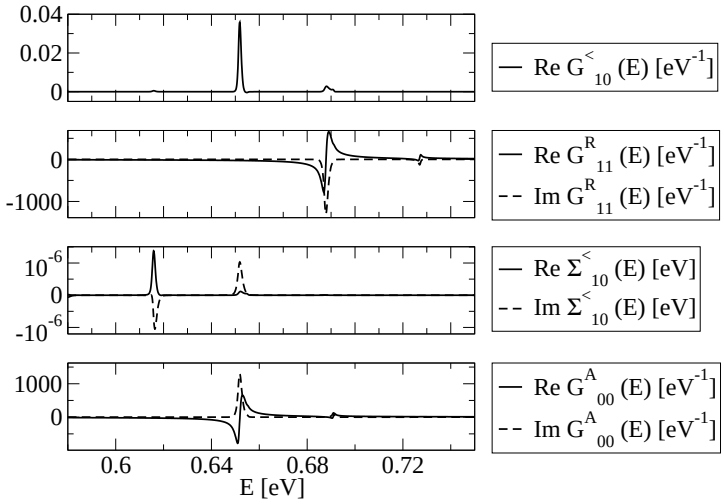

Figure 9.5: Green's functions and self-energies of the dominant contribution $G^R_{11}(E)\Sigma^<_{10}(E)G^A_{00}(E)$ to coherence $G^<_{10}(E)$, and hence the current, at LO phonon resonance ($V_F = E_{\rm LO}$) when the period is $L_z = 10\,$nm.

Fig. 9.7), confirming the interpretation that the transport channel at this value of the field is coherent tunnelling to phonon replica, as shown schematically by horizontal arrows in the right part of Fig. 9.6.

At the period length of 10 nm and smaller, the two resonances cannot be distinguished as their separation is smaller than their width. However, at a larger value of the period when the linewidth decreases, the peaks become distinguishable, as shown in the left part of Fig. 9.8. The doublet structure of the current peak is a transport signature of polaron effects, its width being a measure of the electron – phonon interaction strength.

At this point, one can make an additional *a posteriori* justification of the SCBA, as mentioned in Sec. 9.3. The width of the spectral functions presented in Figs. 9.5 and 9.6 is significantly larger than the width of the spectral functions presented in Fig. 9.2. Therefore, the appropriate linewidths do come from the interactions in the system rather than from artifacts of the SCBA.

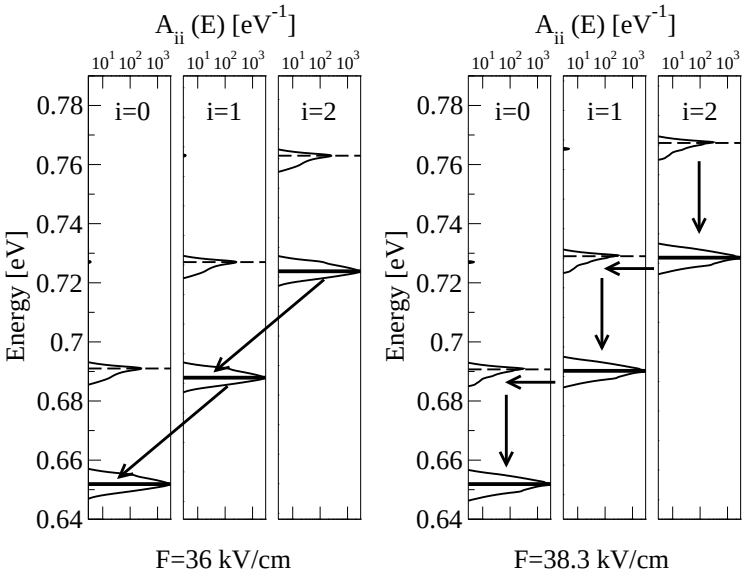

Figure 9.6: Schematic view of current transport at the field of $F = 36\,\mathrm{kV/cm}$ corresponding to LO phonon resonance $V_F = E_{\mathrm{LO}}$ (left) and at $F = 38.3\,\mathrm{kV/cm}$ corresponding to resonance of the phonon replica with the ground state of neighbouring period (right). Corresponding density of states given by the spectral function $A_{ii}(E) = -2\mathrm{Im}G^R_{ii}(E)$ presented in logarithmic scale, is shown for each state. The dominant current transport channel in both cases is marked by arrows.

9.6 Other resonances

The discussion will now be concentrated to a peak appearing at $V_F = \frac{1}{2}E_{\mathrm{LO}}$. While one might expect that $\alpha = 2$ term in (9.13) is of importance here, this is not the case, i.e. $G^<_{10}(E)$ mainly determines the current, as already mentioned. The dominant contribution to it comes in this case both from the scattering $G^R_{11}(E)\Sigma^<_{10}(E)G^A_{00}(E)$ term and coherent $G^R_{11}(E)\Sigma^<_{11}(E)G^A_{10}(E)$ term, where each of these becomes dominant at appropriate energy, as demonstrated in Fig. 9.9. In order to understand such behaviour, one should note that the peaks in the spectral function $A_{ii}(E)$ appear not only at the energy of state i and its phonon replica, but also at energies of other states and their replicae.

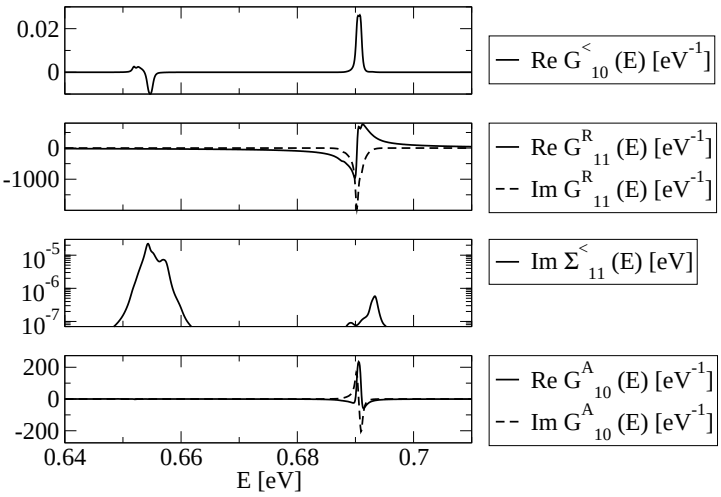

Figure 9.7: Green's functions and self-energies of the dominant contribution $G^R_{11}(E)\Sigma^<_{11}(E)G^A_{10}(E)$ to coherence $G^<_{10}(E)$, at a field of $F = 38.3\,\mathrm{kV/cm}$, corresponding to resonance of phonon replica with the state of the neighbouring period. The period of the structure is $L_z = 10\mathrm{nm}$.

This is a consequence of the fact that in the presence of interaction Wannier-Stark states are no longer the eigenstates of the Hamiltonian of the system. The interaction then couples different Wannier-Stark states, with peaks appearing in the density of states as a consequence. Resonances in transport then appear when the peaks in the density of states of different periods overlap. In this particular case, the peak at $\frac{1}{2}E_{\mathrm{LO}}$ above the ground state of period i, being a consequence of LO phonon coupling with the ground state of period $(i-1)$, becomes resonant with the ground state of period $(i+1)$. The scattering contribution to current between periods i and $i-1$ therefore comes from the LO phonon scattering from the density of states at $\frac{1}{2}E_{\mathrm{LO}}$ above the ground state of period i to ground state of period $i-1$. On the other hand, the coherent contribution comes from tunnelling from the ground state of period i to the density of states at $\frac{1}{2}E_{\mathrm{LO}}$ above the ground state of period $i-1$. These two contributions are schematically illustrated in Fig. 9.10. One therefore sees that the transport between the ground state of period i and the ground state

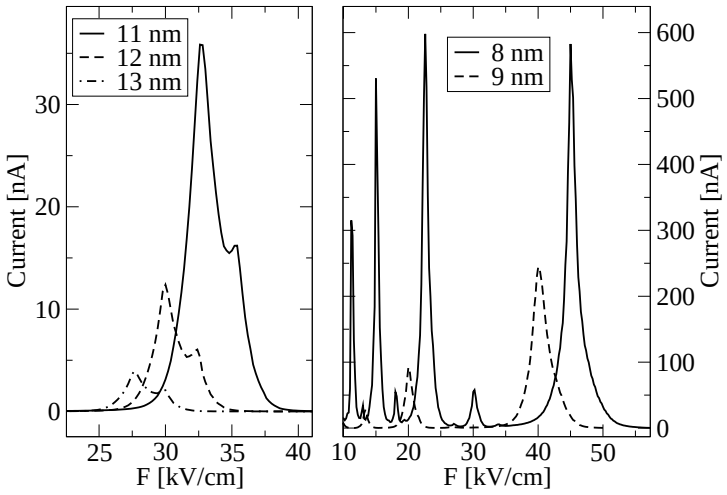

Figure 9.8: Current – field characteristics for different values of the period, when the temperature is $T = 77\,\mathrm{K}$. Convergent results are obtained with $K = 4$ when $L_z = 8\,\mathrm{nm}$, $K = 3$ when $L_z = 9\,\mathrm{nm}$, and $K = 1$ when $L_z \geq 11\,\mathrm{nm}$.

of period $i-2$ which are at LO phonon resonance takes place by a sequence of two events: tunnelling event represented by horizontal arrows in Fig. 9.10 and scattering event represented by diagonal arrows. As the two types of events follow each other, they yield the same contributions to $G^<_{10}$, as demonstrated in Fig. 9.9.

When the dots in a superlattice are closer, additional peaks in the transport appear. For example when the period is 8 nm, clearly visible peaks at $V_F = E_{\mathrm{LO}}$, $\frac{1}{2}E_{\mathrm{LO}}$, $\frac{1}{3}E_{\mathrm{LO}}$, $\frac{1}{4}E_{\mathrm{LO}}$, and even $\frac{2}{3}E_{\mathrm{LO}}$ and $\frac{2}{5}E_{\mathrm{LO}}$, can be seen in Fig. 9.8.

9.7 Nonuniformities of the quantum dot ensemble

The discussion so far has addressed ideally periodic quantum dot arrays. However, real quantum dot ensembles are nonuniform and in a real experiment, one cannot expect to obtain the results predicted by the theory assuming ideal periodicity. On the other hand, the inclusion of quantum dot nonuniformity in the theory requires detailed information about the quantum dot size distribution and is obviously sample dependent. In order to estimate the influence of

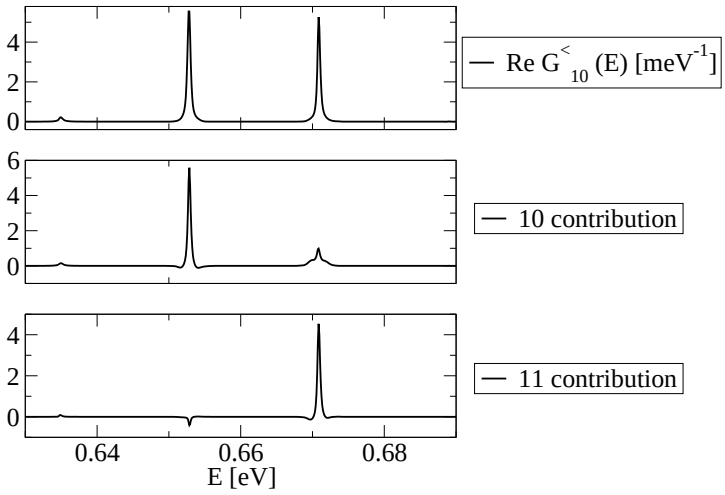

Figure 9.9: The coherence $G^{<}_{10}(E)$, at $V_F = \frac{1}{2}E_{\mathrm{LO}}$, as well as dominant contributions to it $G^{R}_{11}(E)\Sigma^{<}_{11}(E)G^{A}_{10}(E)$ (termed as 11 contribution) and $G^{R}_{11}(E)\Sigma^{<}_{10}(E)G^{A}_{00}(E)$ (termed as 10 contribution).

nonuniformities, additional self-energies were included in the theory according to the following approach.

Let V be the additional potential due to the difference between the potential of a real ensemble of dots and an ideal dot superlattice. Within the SCBA, the contribution to self-energy from this potential is given by

$$\Sigma^{<,R}_{\alpha\beta}(E) = \sum_{\gamma\delta}\langle V_{\alpha\gamma}V_{\delta\beta}\rangle G^{<,R}_{\gamma\delta}(E). \tag{9.15}$$

The average value $\langle V_{\alpha\gamma}V_{\delta\beta}\rangle$ contains information about the quantum dot nonuniformities, and it should be in principle evaluated from the information provided by the experimental dot size distribution, which is sample dependent. For the purpose of an estimate which could be utilised regardless of the details of the dot distribution, a simple phenomenological approach is adopted here. It is assumed that $\langle V_{\alpha\gamma}V_{\delta\beta}\rangle = U^2$ when states α, β, γ and δ belong to the same period, and $\langle V_{\alpha\gamma}V_{\delta\beta}\rangle = 0$ otherwise, where U is a constant roughly representing the standard deviation of the position of quantum dot energy levels due to nonuniformities. This approach therefore assumes zero overlap of

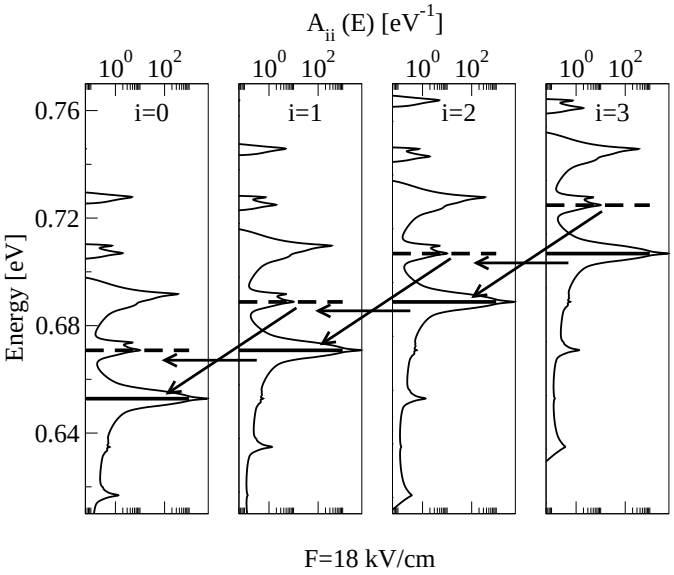

Figure 9.10: Schematic view of current transport at the field of $F = 18\,\mathrm{kV/cm}$ corresponding to $V_F = \frac{1}{2}E_{\mathrm{LO}}$. Corresponding density of states given by the spectral function $A_{ii}(E) = -2\mathrm{Im}G^R_{ii}(E)$, presented in logarithmic scale, is shown for each state. The dominant current transport channels are marked by arrows.

the matrix elements of the V-operator between the states of different periods, which is a reasonable assumption. Additionally, it assumes there is no correlation between the influence of nonuniformities on the states of different periods. Finally, the most severe assumption which makes this approach be only an estimate is that U is independent of α, β, γ and δ, when these belong to the same period. However, when the transport takes place through ground states only, and therefore only one state per period is involved, as is the case here, this approximation becomes justified as well.

The current – field characteristics for several different values of U at $T = 150\,\mathrm{K}$ and $L_z = 10\,\mathrm{nm}$ are presented in Fig. 9.11. As expected, an increase in U leads to broadening of the current peaks, with weaker peaks eventually vanishing. The main peak however, although broadened, remains clearly distinguishable.

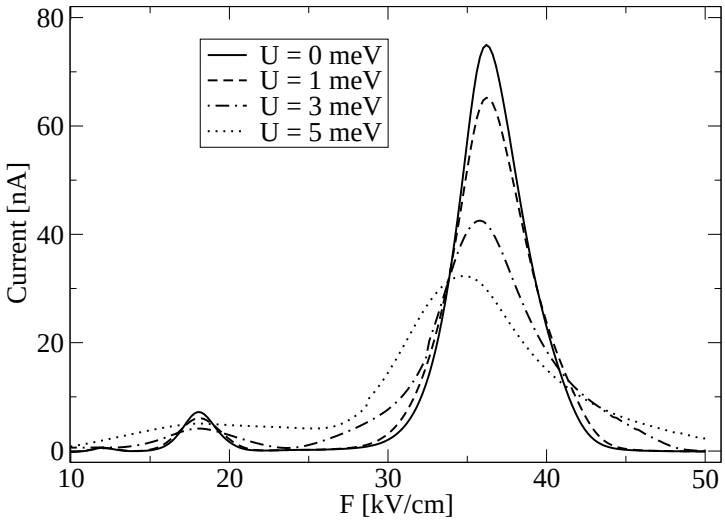

Figure 9.11: Current – field characteristics for several values of phenomenological nonuniformity parameter U at $T = 150\,\mathrm{K}$, when the period of the structure is $L_z = 10\,\mathrm{nm}$.

It is also interesting to estimate how nonuniformity affects the doublet structure of the main current peak. The I–F curve at $T = 77\,\mathrm{K}$ with different nonuniformity parameters is presented in the left panel of Fig. 9.12. One can conclude that already a weak nonuniformity of $U \sim 0.5\,\mathrm{meV}$ broadens the stronger peak of the doublet in such a way that the weaker peak vanishes. Therefore, in InAs/GaAs material system the doublet structure could be observable only in extremely highly uniform samples. On the other hand, InAs/GaAs is a system with weak polar coupling and one can expect a more favourable situation in systems with stronger coupling. The right panel of Fig. 9.12 presents the current – field curve when the LO phonon interaction strength is multiplied by a factor of 2. In this case, the doublet structure remains observable even for nonuniformities of several meV. Therefore, although InAs/GaAs is not the most appropriate system for observing the signature of polaronic effects in electron transport, one can expect the effect to be observable in other systems.

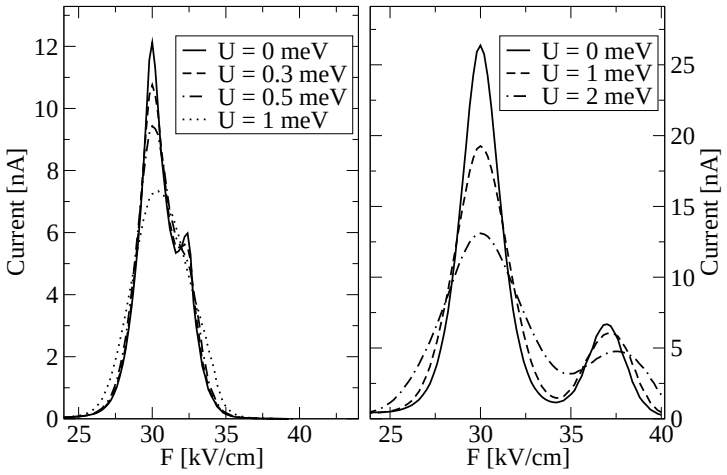

Figure 9.12: Current – field characteristics for several values of the phenomenological nonuniformity parameter U at $T = 77\,\mathrm{K}$, when the period of the structure is $L_z = 12\,\mathrm{nm}$ (left panel). The same result when electron – LO phonon interaction Hamiltonian is multiplied by a factor of 2 is shown in the right panel.

9.8 Transport in a prototype of a quantum dot cascade laser structure

In this section, the method developed in the previous sections of this Chapter, will be applied to design a quantum dot cascade laser structure and evaluate its characteristics. From a purely theoretical point of view, quantum dots provide additional degrees of freedom in design in comparison to quantum wells, as both the dimensions in the growth and lateral directions can be varied in principle. However, controllability of the dot dimensions is not that mature, and a realistic design should therefore be as simple as possible. The design principle for the structure presented here is shown in Fig. 9.13. One period of the structure consists of two dots A and B of different sizes. The barrier between the dots is thin enough to provide significant electronic coupling between the dots. The state originating mainly from dot A is designed to be the upper laser level and the state originating from dot B is the lower laser

level. In order to get population inversion in the structure, the depopulation rate of the lower laser level (transition $B_2 \rightarrow A_1$ in Fig. 9.13) should be faster than its population rate (transition $A_2 \rightarrow B_2$ in Fig. 9.13). This is achieved by engineering the energy of the $B_2 \rightarrow A_1$ transition to be close to one LO phonon energy, while the lasing transition ($A_2 \rightarrow B_2$) energy is significantly smaller than that. Electronic coupling between the dots provides wavefunction overlap sufficient both for large values of the optical matrix element on the lasing transition and large transition rate on the lower laser level depopulation transition.

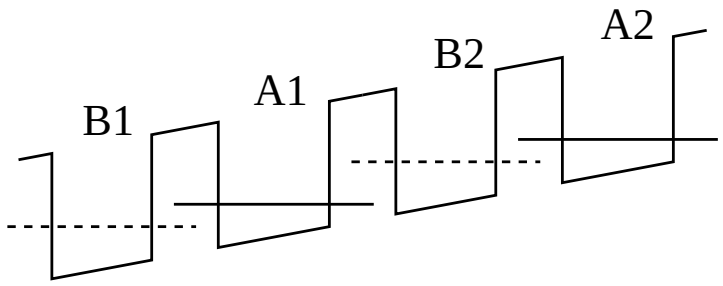

Figure 9.13: Energy levels scheme of a quantum dot cascade structure. Two periods of the structure are presented.

The above conditions are fulfilled when the dot dimensions are chosen as follows. Lens-shaped InAs/GaAs quantum dots are assumed, with the dot diameters set to $D = 20\,\mathrm{nm}$. The height of the dot A is set to $h_\mathrm{A} = 5\,\mathrm{nm}$ and the height of the dot B to $h_\mathrm{B} = 4.5\,\mathrm{nm}$. All barriers between the dots are set to 3 nm. The field-current characteristics of the structure at temperatures $T = 77\,\mathrm{K}$ and $T = 150\,\mathrm{K}$ around the design field are presented in Fig. 9.14. Two levels per period were included in the simulation and $K = 2$ was taken.

The imaginary part of the lesser Green's function $G^<_{ii}(E)$ related to populations of energy levels is presented in Fig. 9.15, when the field is $F = 32\,\mathrm{kV/cm}$. The presence of a population inversion between the upper and lower laser level is evident from the figure. The calculated population inversion between the upper and lower laser level at this field is 56% at $T = 77\,\mathrm{K}$ and 53% at

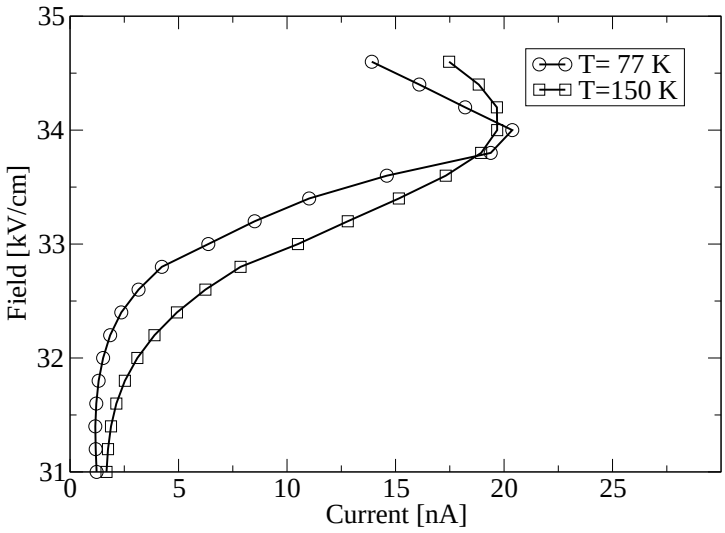

Figure 9.14: Field-current characteristics of the prototype of a quantum dot cascade laser structure at temperatures $T = 77\,\mathrm{K}$ and $T = 150\,\mathrm{K}$.

$T = 150\,\mathrm{K}$. The transition energy is equal to 19 meV corresponding to a frequency of 4.6 THz. The gain in the structure should in principle be calculated from the self-consistent procedure as described for example in Ref. [276]. Here, an estimate will be given based on Eqs. (5.6) and (2.68). Calculated value of optical matrix element for $z-$polarised radiation (defined in Eq. (2.69)) on the lasing transition is $|\mathcal{M}| \approx 9.7 \cdot 10^{-5} \frac{\mathrm{eV}}{\mathrm{T \cdot nm}}$. Assuming a Gaussian linewidth with FWHM equal to 12% of the transition energy, one obtains an optical cross section of $\sigma \approx 150 \cdot 10^{-15}\,\mathrm{cm}^2$. The period of the structure is $L_z = 15.5\,\mathrm{nm}$. Assuming the carrier density of $10^{10}\,\mathrm{cm}^{-2}$ and a population inversion of 50%, one obtains a gain of $g \approx 470\,\mathrm{cm}^{-1}$, which is sufficient for lasing since typical waveguide losses in terahertz QCLs are much smaller. The operating current density at this field is equal to $J \approx 15\,\mathrm{A/cm}^2$, being significantly smaller than in terahertz quantum well based QCLs, where the threshold current density is an order of magnitude larger (see for example Refs. [55, 285–289]). It is also important to note that gain is present in the region of positive differential resistivity and therefore stable operation of the device structure should be feasible.

A certain degree of electric field tunability is also predicted as for example in the range of fields from $31 - 34\,\mathrm{kV/cm}$ the transition energy changes by 10%.

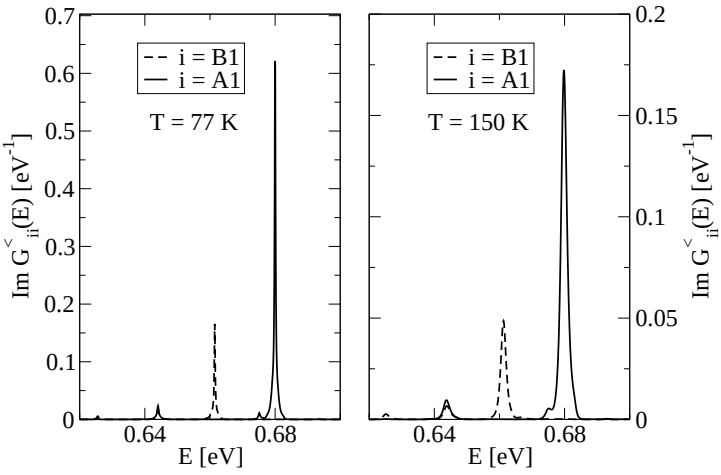

Figure 9.15: Energy distribution of population of the upper (full line) and lower (dashed line) laser level of the prototype of a quantum dot cascade laser structure at the field $F = 32\,\mathrm{kV/cm}$ and temperatures of $T = 77\,\mathrm{K}$ (left) and $T = 150\,\mathrm{K}$ (right).

9.9 Conclusion

Transport through bound states in periodic arrays of closely stacked quantum dots was analysed in this Chapter. An appropriate theoretical framework based on nonequilibrium Green's functions formalism was developed and applied to calculate the current – field characteristics. As expected, the current exhibits a strong peak when the potential drop over a period is equal to the LO phonon energy. The nature of charge transport at this resonance was analysed in detail. It was found that at low temperatures the peak exhibits a doublet structure with one peak originating from LO phonon scattering between states of neighbouring periods and the other one from resonant tunnelling to a phonon replica of the state of the neighbouring period. Therefore the doublet structure can be considered to be a transport signature of polaron effects. The

nonuniformities of the quantum dot ensemble act to suppress the weaker peaks, while the main peak remains present. Finally, a structure with two quantum dots per period was analysed and it was shown that it had promise to perform as a quantum cascade laser.

Chapter 10

Conclusions and suggestions for future work

The main achievements of this thesis from the point of view of device applications can be summarised as follows:

- development of a detailed theory of intraband quantum dot devices,
- implementation of computer codes for the calculation of device characteristics,
- simulation of several existing device structures,
- proposals for new types of devices and their simulation.

In order to achieve this, many fundamental physical questions related to quantum dot properties had to be addressed such as:

- electronic structure and symmetries of states, including the effects of strain, spin-orbit coupling, piezoelectricity and external fields,
- polaron effects,
- optical absorption and selection rules,
- carrier relaxation and thermal excitation,
- transport of carriers through largely separated or closely stacked quantum dots.

Therefore, many of the results presented in this thesis are of more general interest than for intraband devices only. Throughout this concluding Chapter, additional emphasis will therefore be put into underlying the broader nature of the achievements presented.

In Chapter 3, a method for the calculation of electronic structure of square based pyramidal quantum dots based on materials with zincblende crystal structure was developed. The method utilises the symmetry of the model to block diagonalise the matrix obtained in the plane wave representation of the eight-band $\boldsymbol{k} \cdot \boldsymbol{p}$ model. The method arose from the need to significantly speed up the calculation, and therefore to have both a fast and accurate way to determine the energy levels in quantum dots. Although the interest throughout the thesis was mainly on the energy levels in the conduction band relevant for intraband devices, and the method was developed with these applications in mind, a calculation of hole levels in quantum dot superlattices was also performed in Chapter 3. Interesting features in the hole spectrum were observed, being a consequence in the change of strain and consequently the hole character from light- to heavy-hole.

The same overall strategy was applied in Chapter 4 to calculate the electronic structure of hexagonally shaped III-nitride quantum dots. In this case, however, a different basis set of plane waves adapted to a hexagonal, rather than a square lattice, needed to be applied. A simulation of available experimental data on intraband absorption was also performed in this Chapter, giving an insight into the origin of selection rules on intraband absorption in these dots.

In Chapter 5, a theoretical model of an optically pumped quantum dot intraband laser was introduced and a proposal of an appropriate device based on InAs/GaAs quantum dots emitting in the long wavelength mid-infrared part of the spectrum is given. The model starts from a full calculation of single particle wavefunctions, which were subsequently used to evaluate the transition rates between states, from which one can find the populations of energy levels in the steady state, and finally the gain under the given pumping conditions. The main result of this Chapter is that the proposed device should outperform the equivalent quantum well based device by two orders of magnitude. From a broader perspective, these results confirm and illustrate the expected

advantages of quantum dot intraband devices.

Chapter 6 was devoted to the simulation of intraband optical absorption spectra of several existing QDIP structures. Apart from the selection rules imposed by symmetry, additional approximate selection rules, being a consequence of the flat dot shape were established. The main conclusion arising from this Chapter from the methodological point of view, is that it has been established that the widely used one-band effective mass method gives qualitatively good results, but that the 8-band $\boldsymbol{k} \cdot \boldsymbol{p}$ method should be used to make quantitative predictions. It has been also shown theoretically that the response of most QDIP structures is due to $z-$polarised radiation, although many of these experiments are performed in normal-incidence geometry.

In Chapter 7, DWELL detectors were studied. It has been established that contrary to the usual thought, the origin of change of the operating wavelength cannot be due to well width variations only, but rather comes from the unintentional changes in dot dimensions due to changed growth conditions. It is also shown that under certain circumstances, the intraband Stark shift can be observed in these devices, yielding certain prospects for electrically tunable QDIP devices.

A full model of carrier transport in QDIPs was developed in Chapter 8. The model does not contain any fitting parameters and predicts the observable quantities such as dark current and responsivity, starting from the information about quantum dot geometry and the material system used. While modelling of the absorption spectrum only, presented in Chapter 6, is extremely useful in predicting the positions of peaks in the photocurrent spectrum, it cannot predict their relative intensities. The full transport model is capable of doing that, which has been demonstrated by the prediction of the appearance of an additional peak in the photocurrent spectrum at higher biases in agreement with the experimental results for the structure investigated.

With the theoretical framework developed for optically pumped lasers and QDIPs, it remained to develop a theory of quantum dot cascade lasers, to

include all types of intraband devices. Therefore, transport through quantum dot superlattices with closely coupled quantum dots, was investigated in Chapter 9. For the structure with only one quantum dot per period (not capable of producing gain), a doublet structure of the main LO phonon resonance peak was predicted, as a transport signature of polaron effects. Finally, a structure with more quantum dots per period, capable of producing gain, and therefore being a prototype of a quantum dot cascade laser, was also investigated.

The work presented in this thesis gives a comprehensive theory of quantum dot intraband optoelectronic devices, but also opens many other research directions in view of improving the existing models, applying them to different devices, as well as calculation methodology development. Some of these directions are presented in what follows.

- **Investigation into the other material systems for optically pumped lasers.** The optically pumped laser was designed in Chapter 5 in InAs/GaAs quantum dot material system, as the most explored where self-assembled quantum dots are concerned. Other material systems should also be investigated as some of them may offer a larger value of gain. Simpler pumping schemes than the one proposed can be achieved with double or multiple quantum dots, which however increases the growth complexity.

- **The development of nonequilibrium Green's functions theory of the gain properties in steady state in optically pumped lasers.** The present model assumes a Gaussian shape of the gain linewidth as a consequence of nonhomogeneities, which is an approach which should be sufficient for quantum dot ensembles. However, one can also envisage single dot experiments where the linewidth is determined by interactions in the system, and where a detailed lineshape theory would be necessary.

- **Absorption to continuous density of states.** Within the current approach the continuum of states (3D continuum and 2D continuum

provided by the wetting layer and/or embedding quantum well) is artificially discretised by embedding the dot in a box, and it is checked that the box is sufficiently large for the system where line broadening due to nonuniformities of the dot ensemble is taken into account. However, such an approach is not feasible for single dots where one would obtain a discrete spectrum due to discretisation, instead of a continuous one. Therefore, the development of an appropriate method able to treat absorption to continuous density of states is necessary.

- **Simulation of different QDIP structures.** A variety of QDIP structures based on different material systems was reported. The model developed in Chapter 8 enables in principle the treatment of any of these structures. It would be interesting to simulate these, particularly recently emerging structures operating at room temperature [68, 74].

- **Influence of rapid thermal annealing on QDIP performance.** Rapid thermal annealing is an experimental technique where interdiffusion of Ga atoms into the InAs dot is caused, therefore changing the dot potential profile and consequently the energy level structure. The process of interdiffusion can be modelled by solving the diffusion equation for the Ga content in the dot, and further either the absorption spectrum calculation or the full transport simulation can be performed.

- **Design and simulation of photovoltaic quantum dot infrared photodetectors.** For certain applications it is important to have extremely low dark current, while high responsivity is not essential. QDIPs operating at zero bias, therefore called photovoltaic, fulfil this requirement. In order to maximise the responsivity they have to be designed in such a way that the whole system is asymmetric, which can be achieved either with multiple dots per period or by embedding the dots in asymmetric wells.

- **Intraband absorption in quantum dots doped with a single mag-**

netic ion. It has been mentioned in Sec. 1.1 that such quantum dots are currently feasible. Signatures of electron spin – magnetic ion spin interaction, as well as magnetic ion – magnetic ion interaction should be visible in the intraband spectrum of such dots. Furthermore, from the applied point view, these offer the prospect for magnetic field tunable absorption.

- **Designs of quantum dot cascade lasers.** In Chapter 9 it has been demonstrated that quantum dot cascade lasers are feasible. Following the technological advances in quantum dot engineering, an interest will arise in the optimisation of quantum dot cascade laser designs. The theory developed in Chapter 9 can be used to evaluate the quality of such designs.

- **Transport in structures with combined quantum wells and quantum dots.** An alternative approach to quantum dot cascade lasers is to combine injectors consisting of quantum wells with the core of the active region consisting of quantum dots. It is a challenging task to develop a computationally tractable theory of transport in such structures.

- **Application of symmetry to other multiband Hamiltonians and in other basis than plane waves.**

- **Symmetry based calculations of polaron spectrum.**

- **Development of the plane wave methodology for treating single quantum dots.** It has been pointed out in Sec. 3.4 that the plane wave method actually calculates the electronic structure of a 3D quantum dot superlattice and that a very large box is needed if one wants to treat truly single quantum dots, due to the slow strain decay away from the dot. A way has to been found to renormalise the Fourier transform of strain calculated on larger box to the strain on a smaller box that will be used for electronic structure calculations.

Appendix A

Hamiltonian matrix elements in plane wave basis

All the elements in the Hamiltonian matrix in the plane wave basis are Fourier transforms of a linear combination of the elements of the form $E_1 = f(\boldsymbol{r})e_{ij}$, $E_2 = f(\boldsymbol{r})e_{ij}k_l$, $E_3 = f(\boldsymbol{r})x^\alpha y^\beta$, $E_4 = f(\boldsymbol{r})x^\alpha y^\beta k_i$ and $E_5 = f(\boldsymbol{r})x^\alpha y^\beta k_i k_j$, where k_i ($i \in \{1,2,3\}$) is the differential operator $k_i = -i\frac{\partial}{\partial x_i}$, e_{ij} are the components of the strain tensor and $f(\boldsymbol{r})$ is of the form

$$f(\boldsymbol{r}) = f^{QD}\chi_{QD}(\boldsymbol{r}) + f^M(1 - \chi_{QD}(\boldsymbol{r})),$$

where f^{QD} is the value of a material parameter in the quantum dot and f^M its value in the matrix, $\chi_{QD}(\boldsymbol{r})$ is the quantum dot characteristic function equal to 1 inside the dot and 0 outside the dot. Their Fourier transforms (3.8) are within the recipe for ordering of differential and multiplication operators (2.55) thus given by

$$\begin{aligned}
E_1(\boldsymbol{q},\boldsymbol{k}) &= \frac{(2\pi)^3}{V} f^M e_{ij}(\boldsymbol{q}-\boldsymbol{k}) - \frac{(2\pi)^6}{V^2}\Delta f \sum_{\boldsymbol{q}'} \chi_{QD}(\boldsymbol{q}-\boldsymbol{k}-\boldsymbol{q}')e_{ij}(\boldsymbol{q}'), \\
E_2(\boldsymbol{q},\boldsymbol{k}) &= \frac{1}{2}(k_l+q_l)\left[\frac{(2\pi)^3}{V} f^M e_{ij}(\boldsymbol{q}-\boldsymbol{k}) - \right. \\
&\quad \left. -\frac{(2\pi)^6}{V^2}\Delta f \sum_{\boldsymbol{q}'} \chi_{QD}(\boldsymbol{q}-\boldsymbol{k}-\boldsymbol{q}')e_{ij}(\boldsymbol{q}')\right], \\
E_3(\boldsymbol{q},\boldsymbol{k}) &= f^M J_{x^\alpha y^\beta}(\boldsymbol{q}-\boldsymbol{k}) - \frac{(2\pi)^3}{V}\Delta f \chi_{QD}^{x^\alpha y^\beta}(\boldsymbol{q}-\boldsymbol{k}), \\
E_4(\boldsymbol{q},\boldsymbol{k}) &= \frac{1}{2}(k_i+q_i)\left[f^M J_{x^\alpha y^\beta}(\boldsymbol{q}-\boldsymbol{k}) - \frac{(2\pi)^3}{V}\Delta f \chi_{QD}^{x^\alpha y^\beta}(\boldsymbol{q}-\boldsymbol{k})\right],
\end{aligned}$$

$$E_5(\boldsymbol{q},\boldsymbol{k}) \;=\; \frac{1}{2}(k_i q_j + q_i k_j)\left[f^M J_{x^\alpha y^\beta}(\boldsymbol{q}-\boldsymbol{k}) - \frac{(2\pi)^3}{V}\Delta f \chi_{QD}^{x^\alpha y^\beta}(\boldsymbol{q}-\boldsymbol{k})\right],$$

where $\Delta f = f^M - f^{QD}$, $e_{ij}(\boldsymbol{q})$ are Fourier transforms of the strain components given by

$$e_{ij}(\boldsymbol{q}) = \frac{1}{(2\pi)^3}\int_V \mathrm{d}^3\boldsymbol{r}\exp\left(-i\boldsymbol{q}\cdot\boldsymbol{r}\right)e_{ij}(\boldsymbol{r}).$$

$\chi_{QD}^{x^\alpha y^\beta}(\boldsymbol{q})$ is Fourier transform of the quantum dot characteristic functions

$$\chi_{QD}^{x^\alpha y^\beta}(\boldsymbol{q}) = \frac{1}{(2\pi)^3}\int_{QD} \mathrm{d}^3\boldsymbol{r}\, x^\alpha y^\beta \exp\left(-i\boldsymbol{q}\cdot\boldsymbol{r}\right),$$

where the integration goes only over the volume of the quantum dot and

$$J_{x^\alpha y^\beta}(\boldsymbol{q}-\boldsymbol{k}) = \delta_{k_z,q_z}\frac{1}{L_y}\int_{-L_y/2}^{L_y/2} e^{-i(q_y-k_y)y} y^\beta\,\mathrm{d}y \frac{1}{L_x}\int_{-L_x/2}^{L_x/2} e^{-i(q_x-k_x)x}x^\alpha\,\mathrm{d}x,$$

where α and β are non-negative integers from the set

$$(\alpha,\beta) \in \{(0,0);(1,0);(2,0);(0,1);(1,1);(0,2)\}.$$

The center of the pyramid base is taken as the origin of the coordinate system (Fig. 3.1). The analytical formulae from which $e_{ij}(\boldsymbol{q})$ are derived in a crystal with zinblende symmetry are given by (2.93). After integration, the characteristic functions can all be expressed as a linear combination of integrals of the type

$$I_m(q) = \int_0^{b/2} x^m e^{iqx}\,\mathrm{d}x,$$

where $m \in \{0,1,2,3\}$ and can therefore be evaluated analytically. All the integrals $J_{x^\alpha y^\beta}(\boldsymbol{q}-\boldsymbol{k})$ are evaluated analytically, as well.

Appendix B

Hamiltonian matrix elements in cylindrical basis

In order to calculate the Hamiltonian matrix elements in a cylindrical basis, one needs to evaluate expressions of the form

$$U_i = \int_V b^*_{nml}(r,z,\varphi) T_i b_{n'm'l'}(r,z,\varphi)\, r\, \mathrm{d}r\, \mathrm{d}z\, \mathrm{d}\varphi.$$

The one-band Hamiltonian contains the terms of the form

$$\begin{aligned} T_1 &= F(r,z), \\ T_2 &= (k_x^2 + k_y^2)F(r,z), \\ T_3 &= k_z^2 F(r,z), \end{aligned}$$

and therefore after performing the integration one can see that the Hamiltonian matrix elements will only have terms of the form

$$\begin{aligned} U_1 &= \delta_{mm'} \int_0^{R_t} \mathrm{d}r\, r f_{nm} f_{n'm'} F_{l-l'}(r), \\ U_2 &= \delta_{mm'} \int_0^{R_t} \mathrm{d}r \left(r \frac{\mathrm{d}f_{nm}}{\mathrm{d}r} \frac{\mathrm{d}f_{n'm'}}{\mathrm{d}r} + mm' \frac{f_{nm} f_{n'm'}}{r} \right) F_{l-l'}(r), \\ U_3 &= \delta_{mm'} \int_0^{R_t} \mathrm{d}r\, r f_{nm} f_{n'm'} \left(\frac{2\pi}{H_t} \right)^2 ll' F_{l-l'}(r), \end{aligned}$$

where

$$F_{l-l'}(r) = \frac{1}{H_t} \int_{-H_t/2}^{H_t/2} \mathrm{d}z\, e^{-i\frac{2\pi}{H_t}(l-l')z} F(r,z).$$

The explicit form of the functions $F(r,z)$ is

$$F_a(r,z) = P_{\mathrm{QD}} \chi_{\mathrm{QD}}(\boldsymbol{r}) + P_{\mathrm{B}} \chi_{\mathrm{B}}(\boldsymbol{r}) + P_{\mathrm{QW}} \chi_{\mathrm{QW}}(\boldsymbol{r}),$$

and when the external bias is also included additional terms appear, which are of the form

$$F_b(r,z) = |e|Fz.$$

P_{QD}, P_{B} and P_{M} are the values of the material parameter P in the dot, barrier and well respectively and χ_{QD}, χ_{B} and χ_{QW} are functions equal to 1 inside and 0 outside the dot, barrier and quantum well (without the dot) region, respectively. The quantum well term clearly exists only in the case of quantum dots-in-a-well structures. The integral $F_{l-l'}(r)$ can then be performed analytically for each of the quantum dot shapes with cylindrical symmetry. However, in the more general case when the indium composition varies smoothly (for example when the effects of segregation or intermixing occur), $F_a(r,z)$ is not piecewise constant, and the integration in $F_{l-l'}(r)$ has to be performed numerically. This approach was chosen and numerical integration was performed to keep the simulation general enough such that the effects of a smooth variation of indium composition can be included as well.

In addition to the terms of type T_1, T_2, T_3, the elements of the kinetic part of the 8-band Hamiltonian contain the terms

$$\begin{aligned} T_4 &= k_z F(r,z), \\ T_5 &= k_{\mp} F(r,z), \\ T_6 &= k_z k_{\mp} F(r,z), \\ T_7 &= k_{\mp}^2 F(r,z), \end{aligned}$$

where $k_{\pm} = k_x \pm i k_y$. After the integration one finds that the corresponding terms in the Hamiltonian matrix are of the form

$$\begin{aligned} U_4 &= \frac{\pi}{H_t}(l+l')U_1, \\ U_5 &= -\frac{i}{2}\delta_{m,m'\mp 1}\int_0^{R_t} \mathrm{d}r\, r F_{l-l'}(r) \times \\ &\quad \times \left[f_{nm}\left(\frac{\mathrm{d}f_{n'm'}}{\mathrm{d}r} \pm m'\frac{f_{n'm'}}{r}\right) - f_{n'm'}\left(\frac{\mathrm{d}f_{nm}}{\mathrm{d}r} \mp m\frac{f_{nm}}{r}\right)\right], \end{aligned}$$

$$
\begin{aligned}
U_6 &= -i\frac{\pi}{H_t}\delta_{m,m'\mp 1}\int_0^{R_t} \mathrm{d}r\, r F_{l-l'}(r) \times \\
&\quad \times \left[l f_{nm}\left(\frac{\mathrm{d}f_{n'm'}}{\mathrm{d}r} \pm m'\frac{f_{n'm'}}{r}\right) - l' f_{n'm'}\left(\frac{\mathrm{d}f_{nm}}{\mathrm{d}r} \mp m\frac{f_{nm}}{r}\right)\right], \\
U_7 &= \delta_{m\pm 1,m'\mp 1}\int_0^{R_t} \mathrm{d}r\, r F_{l-l'}(r) \times \\
&\quad \times \left(\frac{\mathrm{d}f_{nm}}{\mathrm{d}r} \mp m\frac{f_{nm}}{r}\right)\left(\frac{\mathrm{d}f_{n'm'}}{\mathrm{d}r} \pm m'\frac{f_{n'm'}}{r}\right).
\end{aligned}
$$

The strain part of the Hamiltonian has terms of the type

$$
\begin{aligned}
T_8 &= F(r,z)e_{ij}, \\
T_9 &= F(r,z)e_{ij}k_{\mp}, \\
T_{10} &= F(r,z)e_{ij}k_z,
\end{aligned}
$$

where e_{ij} are the strain tensor components. After performing the integration over φ, one gets

$$
U_8 = \int_0^{R_t} \mathrm{d}r\, r f_{nm} f_{n'm'} \frac{1}{H_t}\int_{-H_t/2}^{H_t/2} \mathrm{d}z\, e^{-i\frac{2\pi}{H_t}(l-l')z}\overline{e}_{ij}(r,z),
$$

where

$$
\overline{e}_{ij}(r,z) = \frac{1}{2\pi}\int_0^{2\pi} \mathrm{d}\varphi\, e^{-i(m-m')\varphi} e_{ij}(r,z,\varphi),
$$

and therefore the term U_8 becomes of the same form as U_1. In a similar manner, the terms U_9 and U_{10} are of the same form as U_5 and U_4.

Appendix C

Material parameters

Material parameters used in this work are summarised in this Appendix.

Table C.1: Material parameters of GaAs relevant for calculations of interaction with phonons [2]

Parameter		GaAs
Acoustic deformation potential [eV]	D_{A}	6.8
Longitudinal sound velocity [km/s]	v_s	5.2
Density of the material $[g/cm^3]$	ρ	5.32
LO phonon energy [meV]	v_s	36
Static dielectric constant	ε_{st}	13.10
High frequency dielectric constant	ε_{∞}	10.9

Table C.2: Material parameters of InAs, GaAs and InGaAs relevant for band-structure calculations [3]

Parameter		InAs	GaAs	boving
Lattice constant [Å]	a	6.0583	5.65325	
Energy gap [eV]	E_g	0.417	1.519	0.477
Spin-orbit splitting [eV]	Δ_{so}	0.39	0.341	0.15
Effective mass at Γ point [m_0]	m^*	0.026	0.067	0.0091
Luttinger parameters	γ_1^L	20.0	6.98	
	γ_2^L	8.5	2.06	
	γ_3^L	9.2	2.93	
	κ^L	1.20	7.68	
Interband matrix element [eV]	E_P	21.5	28.8	-1.48
Chemical valence band offset [eV]	VBO	-0.59	-0.80	-0.38
Deformation potentials [eV]	a_c	-5.08	-7.17	2.61
	a_v	-1.00	-1.16	
	b	-1.8	-2.0	
	d	-3.6	-4.8	
Elastic stiffness constants [GPa]	C_{11}	832.9	1221	
	C_{12}	452.6	566	
	C_{44}	395.9	600	
Piezoelectric constant [C/m^2]	ε_{14}	0.160	0.045	

Table C.3: Material parameters of GaN and AlN relevant for bandstructure calculations (part 1) [4]

Parameter		GaN	AlN
Lattice constant [Å]	a	3.189	3.112
	c	5.185	4.982
Energy gap [eV]	E_g	3.510	6.25
Crystal field splitting [eV]	Δ_{cr}	0.010	-0.169
Spin-orbit splitting [eV]	Δ_{so}	0.017	0.019
Effective mass at Γ point [m_0]	$m^{\parallel}$	0.20	0.32
	$m^{\perp}$	0.20	0.30
Luttinger parameters	A_1	-7.21	-3.86
	A_2	-0.44	-0.25
	A_3	6.68	3.58
	A_4	-3.46	-1.32
	A_5	-3.40	-1.47
	A_6	-4.90	-1.64
Conduction band offset [eV]		1.89	

Table C.4: Materials parameters of GaN and AlN relevant for bandstructure calculations (part 2) [4]

Parameter		GaN	AlN
Hydrostatic deformation potential [eV]	$a_{\parallel}$	-4.9	-3.4
	$a_{\perp}$	-11.3	-11.8
Deformation potentials [eV]	D_1	-3.7	-17.1
	D_2	4.5	7.9
	D_3	8.2	8.8
	D_4	-4.1	-3.9
	D_5	-4.0	-3.4
	D_6	-5.5	-3.4
Elastic stiffness constants [GPa]	C_{11}	390	396
	C_{12}	145	137
	C_{13}	106	108
	C_{33}	398	373
	C_{44}	105	116
Piezoelectric constants $[C/m^2]$	ε_{15}	0.326	0.418
	ε_{31}	-0.527	-0.484
	ε_{33}	0.895	1.561
Spontaneous polarisation $[C/m^2]$	P_{sp}	-0.034	-0.090
Static dielectric constant	ε_r	9.6	

Appendix D

Computational issues

All computational codes for the calculations presented in this thesis were developed by the author of the thesis, except for the usage of standard numerical packages such as LAPACK [198] and Numerical recipes [174]. The codes were developed for single processor machines in the Fortran 77 programming language. Since the emphasis in the thesis was on the results of the calculation and their interpretation, a few words about the codes will be given in this Appendix.

In Chapters 3 and 5, the code developed for symmetry based 8-band $\boldsymbol{k} \cdot \boldsymbol{p}$ calculations of electronic structure of square based pyramidal quantum dots based on materials with zincblende crystal structure was used. The main part of the code calculates the energy levels and wavefunctions, and additional programs calculate the absorption cross sections, the transition rates due to interaction with phonons, and solve the rate equations. Most of the computational time is spent on diagonlisation of the main Hamiltonian matrix. For the size of matrices typically necessary for energy level precision better than 10 meV, the execution time is of the order of tens of minutes. It is the methodology developed in Chapter 3 that significantly reduced the computational time and memory requirements. Otherwise, within the straightforward plane wave approach, large parallel machines would be necessary for the calculation.

In Chapter 4, the code developed for symmetry based 4-band $\boldsymbol{k} \cdot \boldsymbol{p}$ calculations of electronic structure of hexagonal quantum dots based on materials with wurtzite crystal structure was used. Additional program calculates the

absorption matrix elements using the output of the previous one. Typical execution times of this code are again of the order of 10 minutes.

In Chapters 6, 7, 8, the code developed for one band and 8-band $\boldsymbol{k}\cdot\boldsymbol{p}$ calculations of cylindrically symmetric quantum dots was used. The code consists of programs for finite element strain distribution calculation, the calculation of energy levels and wavefunctions, absorption cross sections, carrier transitions rates, solution of rate equations, and finally current calculation. Due to the reduction of the problem from 3D to 2D, execution times of the electronic structure calculation are of the order of a few minutes only. The finite-element calculation takes about the same time. However, application of the code to QDIPs is very computationally demanding, due to the large number of transition rates that need to be determined. Therefore, the typical execution time necessary to calculate the current at the given value of the field is of the order of a week. The calculation was therefore performed on a multiprocessor computer cluster grinch.

The previous code was extended in Chapter 9 to calculate Wannier states of a quantum dot superlattice and to solve the self-consistent equations for Green's functions and self-energies. Since the calculation was performed with only a small number of states involved, it can be done quite efficiently. For example, with only one state per period involved and in the nearest neighbour approximation, one iteration of the self-consistent procedure takes a few seconds only. However, scaling with the number of states is not favourable.

The code developed for polaron spectrum calculations was also used in Chapter 9.

References

[1] H. Page, C. Becker, A. Robertson, G. Glastre, V. Ortiz, and C. Sirtori, Appl. Phys. Lett. **78**, 3529 (2001).

[2] G. Shkerdin, J. Stiens, and R. Vounckx, J. Appl. Phys. **85**, 3792 (1999).

[3] I. Vurgaftman, J. R. Meyer, and L. R. Ram-Mohan, J. Appl. Phys. **89**, 5815 (2001).

[4] I. Vurgaftman and J. R. Meyer, J. Appl. Phys. **94**, 3675 (2003).

[5] S. M. Reimann and M. Manninen, Rev. Mod. Phys. **74**, 1283 (2002).

[6] W. G. van der Wiel, S. D. Franceschi, J. M. Elzerman, T. Fujisawa, S. Tarucha, and L. P. Kouwenhoven, Rev. Mod. Phys. **75**, 1 (2003).

[7] A. P. Alivisatos, Science **271**, 933 (1996).

[8] X. Michalet, F. F. Pinaud, L. A. Bentolila, J. M. Tsay, S. Doose, J. J. Li, G. Sundaresan, A. M. Wu, S. S. Gambhir, and S. Weiss, Science **307**, 538 (2005).

[9] J. Stangl, V. Holý, and G. Bauer, Rev. Mod. Phys. **76**, 725 (2004).

[10] P. M. Petroff and S. P. DenBaars, Superlattices Microstruct. **15**, 15 (1994).

[11] D. Bimberg, M. Grundmann, and N. N. Ledentsov, *Quantum dot heterostructures* (John Wiley, Chichester, 1999).

[12] L. P. Kouwenhoven, D. G. Austing, and S. Tarucha, Rep. Prog. Phys. **64**, 701 (2001).

[13] S. M. Cronenwett, T. H. Oosterkamp, and L. P. Kouwenhoven, Science **281**, 540 (1998).

[14] D. Goldhaber-Gordon, H. Shtrikman, D. Mahalu, D. Abusch-Magder, U. Meirav, and M. A. Kastner, Nature **391**, 156 (1998).

[15] A. Zrenner, E. Beham, S. Stufler, F. Findeis, M. Bichler, and G. Abstreiter, Nature **418**, 612 (2002).

[16] F. H. L. Koppens, C. Buizert, K. J. Tielrooij, I. T. Vink, K. C. Nowack, T. Meunier, L. P. Kouwenhoven, and L. M. K. Vandersypen, Nature **442**, 766 (2006).

[17] J. R. Petta, A. C. Johnson, J. M. Taylor, E. A. Laird, A. Yacoby, M. D. Lukin, C. M. Marcus, M. P. Hanson, and A. C. Gossard, Science **309**, 2180 (2005).

[18] J. P. Reithmaier, G. Sek, A. Loffler, C. Hofmann, S. Kuhn, S. Reitzenstein, L. V. Keldysh, V. D. Kulakovskii, T. L. Reinecke, and A. Forchel, Nature **432**, 197 (2004).

[19] Y. L. Lim, A. Beige, and L. C. Kwek, Phys. Rev. Lett. **95**, 030505 (2005).

[20] Y. Léger, L. Besombes, J. Fernendez-Rossier, L. Maingault, and H. Mariette, Phys. Rev. Lett. **77**, 107401 (2006).

[21] A. P. Alivisatos, W. W. Gu, and C. Larabell, Ann. Rev. Biomed. Eng. **7**, 55 (2005).

[22] R. D. Schaller and V. I. Klimov, Phys. Rev. Lett. **92**, 186601 (2004).

[23] N. N. Ledentsov, M. Grundmann, F. Heinrichsdorff, D. Bimberg, V. M. Ustinov, A. E. Zhukov, M. V. Maximov, Z. I. Alferov, and J. A. Lott, IEEE J. Select. Topics Quantum Electron. **6**, 439 (2000).

[24] D. Bimberg and N. Ledentsov, J. Phys.: Condens. Matter **15**, 1063 (2003).

[25] R. Dingle and C. H. Henry, U.S. Patent 3982207 (1976).

[26] R. D. Dupuis, P. D. Dapkus, N. Holonyak, Jr., E. A. Rezek, and R. Chin, Appl. Phys. Lett. **32**, 295 (1978).

[27] N. Holonyak, Jr., R. Kolbas, R. D. Dupuis, and P. D. Dapkus, IEEE J. Quantum Electron. **16**, 170 (1980).

[28] W. T. Tsang, Appl. Phys. Lett. **39**, 786 (1981).

[29] Y. Arakawa and H. Sakaki, Appl. Phys. Lett. **40**, 939 (1982).

[30] M. Asada, Y. Miyamoto, and Y. Suematsu, IEEE J. Quantum Electron. **22**, 1915 (1986).

[31] N. Kirstaedter, N. N. Ledentsov, M. Grundmann, D. Bimberg, V. M. Ustinov, S. S. Ruvimov, M. V. Maximov, P. S. Kopev, Z. I. Alferov, U. Richter, P. Werner, U. Gosele, and J. Heydenreich, Electron. Lett. **30**, 1416 (1994).

[32] J. P. Reithmaier *et al.*, J. Phys. D: Appl. Phys. **38**, 2088 (2005).

[33] A. Moritz, R. Wirth, A. Hangleiter, A. Kurtenbach, and K. Eberl, Appl. Phys. Lett. **69**, 212 (1996).

[34] P. Bhattacharya, S. Ghosh, and A. D. Stiff-Roberts, Annu. Rev. Mater. Res. **34**, 1 (2004).

[35] D. J. Mowbray and M. S. Skolnick, J. Phys. D: Appl. Phys. **38**, 2059 (2005).

[36] M. Sugawara, N. Hatori, M. Ishida, H. Ebe, Y. Arakawa, T. Akiyama, K. Otsubo, T. Yamamoto, and Y. Nakata, J. Phys. D: Appl. Phys. **38**, 2126 (2005).

[37] M. Pelton, C. Santori, G. S. Solomon, O. Benson, and Y. Yamamoto, Eur. Phys. J. D **18**, 179 (2002).

[38] C. Santori, M. Pelton, G. S. Solomon, Y. Dale, and Y. Yamamoto, Phys. Rev. Lett. **86**, 1502 (2001).

[39] P. Michler, A. Kiraz, C. Becher, W. V. Schoenfeld, P. M. Petroff, L. D. Zhang, E. Hu, and A. Imamoglu, Science **290**, 2282 (2000).

[40] N. Akopian, N. H. Lindner, E. Poem, Y. Berlatzky, J. Avron, D. Gershoni, B. D. Gerardot, and P. M. Petroff, Phys. Rev. Lett. **96**, 130501 (2006).

[41] R. M. Stevenson, R. J. Young, P. Atkinson, K. Cooper, D. A. Ritchie, and A. J. Shields, Nature **439**, 179 (2006).

[42] P. Harrison, *Quantum Wells, Wires and Dots, 2*$^{\text{nd}}$ *edition* (John Wiley and Sons Ltd., Chichester, England, 2005).

[43] J. H. Davies, *The Physics of Low-Dimensional Semiconductors* (Cambridge University Press, 1998).

[44] C. Gmachl, F. Capasso, D. L. Sivco, and A. Y. Cho, Rep. Prog. Phys. **64**, 1533 (2001).

[45] E. Pickwell and V. P. Wallace, J. Phys. D: Appl. Phys. **39**, 301 (2006).

[46] R. F. Kazarinov and R. A. Suris, Sov. Phys. Semicond. **5**, 707 (1971).

[47] B. F. Levine, K. K. Choi, C. G. Bethea, J. Walker, and R. J. Malik, Appl. Phys. Lett. **50**, 1092 (1987).

[48] B. F. Levine, J. Appl. Phys. **74**, R1 (1993).

[49] H. C. Liu, C. Y. Song, A. J. SpringThorpe, and J. C. Cao, Appl. Phys. Lett. **84**, 4068 (2004).

[50] O. Gauthier-Lafaye, P. Boucaud, F. H. Julien, S. Sauvage, S. Cabaret, J.-M. Lourtioz, V. Thierry-Mieg, and R. Planel, Appl. Phys. Lett. **71**, 3619 (1997).

[51] J. Faist, F. Capasso, D. L. Sivco, C. Sirtori, A. L. Hutchinson, and A. Y. Cho, Science **264**, 553 (1994).

[52] C. Sirtori, P. Kruck, S. Barbieri, P. Collot, J. Nagle, M. Beck, J. Faist, and U. Oesterle, Appl. Phys. Lett. **73**, 3486 (1998).

[53] D. G. Revin, L. R. Wilson, E. A. Zibik, R. P. Green, J. W. Cockburn, M. J. Steer, R. J. Airey, and M. Hopkinson, Appl. Phys. Lett. **85**, 3992 (2004).

[54] R. Teissier, D. Barate, A. Vicet, C. Alibert, A. N. Baranov, X. Marcadet, C. Renard, M. Garcia, C. Sirtori, D. Revin, and J. Cockburn, Appl. Phys. Lett. **85**, 167 (2004).

[55] C. Walther, G. Scalari, J. Faist, H. Beere, and D. Ritchie, Appl. Phys. Lett. **89**, 231121 (2006).

[56] R. Köhler, A. Tredicucci, F. Beltram, H. E. Beere, E. H. Linfield, A. G. Davies, R. C. I. D. A. Ritchie, and F. Rossi, Nature **417**, 156 (2002).

[57] G. Scalari, C. Walther, J. Faist, H. Beere, and D. Ritchie, Appl. Phys. Lett. **88**, 141102 (2006).

[58] D. Pan, Y. P. Zeng, M. Y. Kong, J. Wu, Y. Q. Zhu, C. H. Zhang, J. M. Li, and C. Y. Wang, Electron. Lett. **32**, 1726 (1996).

[59] D. Pan, E. Towe, and S. Kennerly, Appl. Phys. Lett. **73**, 1937 (1998).

[60] S. Maimon, E. Finkman, G. Bahir, S. E. Schacham, J. M. Garcia, and P. M. Petroff, Appl. Phys. Lett. **73**, 2003 (1998).

[61] S. Y. Wang, S. D. Lin, H. W. Wu, and C. P. Lee, Appl. Phys. Lett. **78**, 1023 (2001).

[62] A. D. Stiff, S. Krishna, P. Bhattacharya, and S. Kennerly, Appl. Phys. Lett. **79**, 421 (2001).

[63] E. T. Kim, Z. H. Chen, and A. Madhukar, Appl. Phys. Lett. **79**, 3341 (2001).

[64] S. Raghavan, D. Forman, P. Hill, N. R. Weisse-Bernstein, G. von Winckel, P. Rotella, S. Krishna, S. W. Kennerly, and J. W. Little, J. Appl. Phys. **96**, 1036 (2004).

[65] S. Krishna, J. Phys. D: Appl. Phys. **38**, 2142 (2005).

[66] J. Jiang, K. Mi, S. Tsao, W. Zhang, H. Lim, T. O'Sullivan, T. Sills, M. Razeghi, G. J. Brown, and M. Z. Tidrow, Appl. Phys. Lett. **84**, 2232 (2004).

[67] S. Krishna, D. Forman, S. Annamalai, P. Dowd, P. Varangis, T. Tumolillo, A. Gray, J. Zilko, K. Sun, M. G. Liu, J. Campbell, and D. Carothers, Appl. Phys. Lett. **86**, 193501 (2005).

[68] P. Bhattacharya, X. H. Su, S. Chakrabarti, G. Ariyawansa, and A. G. U. Perera, Appl. Phys. Lett. **86**, 191106 (2005).

[69] L. Fu, P. Lever, K. Sears, H. H. Tan, and C. Jagadish, IEEE Electron Dev. Lett. **26**, 628 (2005).

[70] J. Y. Duboz, H. C. Liu, Z. R. Wasilewski, M. Byloss, and R. Dudek, J. Appl. Phys. **93**, 1320 (2003).

[71] S. Sauvage, P. Boucaud, T. Bruhnes, V. Immer, E. Finkman, and J. M. Gerard, Appl. Phys. Lett. **78**, 2327 (2001).

[72] A. M. Adawi, E. A. Zibik, L. R. Wilson, A. Lemaître, J. W. Cockburn, M. S. Skolnick, M. Hopkinson, and G. Hill, Appl. Phys. Lett. **83**, 602 (2003).

[73] S. D. Gunapala, S. V. Bandara, C. J. Hill, D. Z. Ting, J. K. Liu, S. B. Rafol, E. R. Blazejewski, J. M. Mumolo, S. A. Keo, S. Krishna, Y.-C. Chang, and C. A. Shott, IEEE J. Quantum Electron. **43**, 230 (2007).

[74] H. Lim, S. Tsao, W. Zhang, and M. Razeghi, Appl. Phys. Lett. **90**, 131112 (2007).

[75] C. Kammerer, S. Sauvage, G. Fishman, P. Boucaud, G. Patriarche, and A. Lemaître, Appl. Phys. Lett. **87**, 173113 (2005).

[76] A. D. Stiff-Roberts, X. H. Su, S. Chakrabarti, and P. Bhattacharya, IEEE Photonics Technol. Lett. **16**, 867 (2004).

[77] Z. Ye, J. C. Campbell, Z. Chen, E.-T. Kim, and A. Madhukar, J. Appl. Phys. **92**, 7462 (2002).

[78] G. Ariyawansa, A. G. U. Perera, G. S. Raghavan, G. von Winckel, A. Stintz, and S. Krishna, IEEE Photonics Technol. Lett. **17**, 1064 (2005).

[79] L. Rebohle, F. F. Schrey, S. Hofer, G. Strasser, and K. Unterrainer, Appl. Phys. Lett. **81**, 2079 (2002).

[80] Z. Chen, O. Baklenov, E. T. Kim, I. Mukhametzhanov, J. Tie, A. Madhukar, Z. Ye, and J. C. Campbell, J. Appl. Phys. **89**, 4558 (2001).

[81] F. F. Schrey, L. Rebohle, T. Müller, G. Strasser, K. Unterrainer, D. P. Nguyen, N. Regnault, R. Ferreira, and G. Bastard, Phys. Rev. B **72**, 155310 (2005).

[82] W. Zhang, H. Lim, M. Taguchi, S. Tsao, B. Movaghar, and M. Razeghi, Appl. Phys. Lett. **86**, 191103 (2005).

[83] S. Kim, H. Mohesmi, M. Erdtmann, E. Michel, C. Jelen, and M. Razeghi, Appl. Phys. Lett. **73**, 963 (1998).

[84] J. Jiang, S. Tsao, T. O'Sullivan, W. Zhang, H. Lim, T. Sills, K. Mi, M. Razeghi, G. J. Brown, and M. Z. Tidrow, Appl. Phys. Lett. **84**, 2166 (2004).

[85] J. Szafraniec, S. Tsao, W. Zhang, H. Lim, M. Taguchi, A. A. Quivy, B. Movaghar, and M. Razeghi, Appl. Phys. Lett. **88**, 121102 (2006).

[86] E. Finkman, S. Maimon, V. Immer, G. Bahir, S. E. Schacham, F. Fossard, F. H. Julien, J. Brault, and M. Gendry, Phys. Rev. B **63**, 045323 (2001).

[87] L. Doyennette, L. Nevou, M. Tchernycheva, A. Lupu, F. Guillot, E. Monroy, R. Colombelli, and F. H. Julien, Electron. Lett. **41**, 1077 (2005).

[88] A. Vardi, N. Akopian, G. Bahir, L. Doyennette, M. Tchernycheva, L. Nevou, F. H. Julien, F. Guillot, and E. Monroy, Appl. Phys. Lett. **88**, 143101 (2006).

[89] A. I. Yakimov, A. V. Dvurechenskii, A. I. Nikiforov, and Y. Y. Proskuryakov, J. Appl. Phys. **89**, 5676 (2001).

[90] X. H. Su, J. Yang, P. Bhattacharya, G. Ariyawansa, and A. G. U. Perera, Appl. Phys. Lett. **89**, 031117 (2006).

[91] U. Bockelman and G. Bastard, Phys. Rev. B **42**, 8947 (1990).

[92] N. S. Wingren and C. A. Stafford, IEEE J. Quantum Electron. **33**, 1170 (1997).

[93] T. Inoshita and H. Sakaki, Phys. Rev. B **56**, R4355 (1997).

[94] S. Hameau, Y. Guldner, O. Verzelen, R. Ferreira, G. Bastard, J. Zeman, A. Lemaître, and J. M. Gérard, Phys. Rev. Lett. **83**, 4152 (1999).

[95] X.-Q. Li, H. Nakayama, and Y. Arakawa, Phys. Rev. B **59**, 5069 (1999).

[96] O. Verzelen, R. Ferreira, and G. Bastard, Phys. Rev. B **62**, R4809 (2000).

[97] J. Urayama, T. B. Norris, J. Singh, and P. Bhattacharya, Phys. Rev. Lett. **86**, 4930 (2001).

[98] S. Sauvage, P. Boucaud, R. P. S. M. Lobo, F. Bras, G. Fishman, R. Prazeres, F. Glotin, J. M. Ortega, and J.-M. Gérard, Phys. Rev. Lett. **88**, 177402 (2002).

[99] C.-F. Hsu, J.-S. O, P. Zory, and D. Botez, IEEE J. Select. Topics Quantum Electron. **6**, 491 (2000).

[100] V. M. Apalkov and T. Chakraborty, Appl. Phys. Lett. **78**, 1820 (2001).

[101] I. A. Dmitriev and R. A. Suris, Phys. Status Solidi A **202**, 987 (2005).

[102] S. Anders, L. Rebohle, F. F. Schrey, W. Schrenk, K. Unterrainer, and G. Strasser, Appl. Phys. Lett. **82**, 3862 (2003).

[103] N. Ulbrich, J. Bauer, G. Scarpa, R. Boy, D. Schuh, G. Abstreiter, S. Schmult, and W. Wegscheider, Appl. Phys. Lett. **83**, 1530 (2003).

[104] C. H. Fischer, P. Bhattacharya, and P. C. YU, Electron. Lett. **39**, 1537 (2003).

[105] G. Scalari, S. Blaser, J. Faist, H. Beere, E. Linfield, D. Ritchie, and G. Davies, Phys. Rev. Lett. **93**, 237403 (2004).

[106] P. Hohenberg and W. Kohn, Phys. Rev. **136**, B864 (1964).

[107] W. Kohn and L. J. Sham, Phys. Rev. **140**, A1133 (1965).

[108] M. C. Payne, M. P. Teter, D. C. Allan, T. A. Arias, and J. D. Joannopoulos, Rev. Mod. Phys. **64**, 1045 (1992).

[109] C. S. Garoufalis, A. D. Zdetsis, and S. Grimme, Phys. Rev. Lett. **87**, 276402 (2001).

[110] Z. Zhou, R. A. Friesner, and L. Brus, J. Am. Chem. Soc. **125**, 15599 (2003).

[111] A. Puzder, A. J. Williamson, J. C. Grossman, and G. Galli, J. Am. Chem. Soc. **125**, 2786 (2003).

[112] K. Eichkorn and R. Ahlrichs, Chem. Phys. Lett. **288**, 235 (1998).

[113] I. Vasiliev, S. Öğüt, and J. R. Chelikowsky, Phys. Rev. B **65**, 115416 (2002).

[114] M. L. Cohen and T. K. Bergstresser, Phys. Rev. **141**, 789 (1966).

[115] J. R. Chelikowsky and M. L. Cohen, Phys. Rev. B **14**, 556 (1976).

[116] J. Kim, L.-W. Wang, and A. Zunger, Phys. Rev. B **57**, R9408 (1998).

[117] L. W. Wang, J. Kim, and A. Zunger, Phys. Rev. B **59**, 5678 (1999).

[118] A. J. Williamson and A. Zunger, Phys. Rev. B **59**, 15819 (1999).

[119] L.-W. Wang and A. Zunger, Phys. Rev. B **59**, 15806 (1999).

[120] L.-W. Wang, Phys. Rev. Lett. **88**, 256402 (2002).

[121] T. B. Boykin, Phys. Rev. B **56**, 9613 (1997).

[122] T. Saito, J. N. Schulman, and Y. Arakawa, Phys. Rev. B **57**, 13016 (1998).

[123] S. Lee, J. Kim, L. Jönsson, J. W. Wilkins, G. W. Bryant, and G. Klimeck, Phys. Rev. B **66**, 235307 (2002).

[124] R. Santoprete, B. Koiller, R. B. Capaz, P. Kratzer, Q. K. K. Liu, and M. Scheffler, Phys. Rev. B **68**, 235311 (2003).

[125] W. Sheng, S.-J. Cheng, and P. Hawrylak, Phys. Rev. B **71**, 035316 (2005).

[126] O. Stier, M. Grundmann, and D. Bimberg, Phys. Rev. B **59**, 5688 (1999).

[127] C. Pryor, Phys. Rev. Lett. **80**, 3579 (1998).

[128] H. Jiang and J. Singh, Phys. Rev. B **56**, 4696 (1997).

[129] C. Pryor, Phys. Rev. B **57**, 7190 (1998).

[130] T. B. Bahder, Phys. Rev. B **41**, 11992 (1990).

[131] S. Tomić, A. G. Sunderland, and I. J. Bush, J. Mater. Chem. **16**, 1963 (2006).

[132] J. M. Luttinger, Phys. Rev. **102**, 1030 (1956).

[133] J. M. Luttinger and W. Kohn, Phys. Rev. **97**, 869 (1955).

[134] C. R. Pidgeon and R. N. Brown, Phys. Rev. **146**, 575 (1966).

[135] G. F. Koster, *Properties of the thirty two points groups* (MIT press, Cambridge, Massachusetts, 1963).

[136] J. P. Elliott and P. G. Dawber, *Symmetry in Physics* (Macmillan, London, 1979).

[137] G. Bastard, *Wave Mechanics Applied to Semiconductor Heterostructures* (Les editions de physique, Les Ulis, 1992).

[138] P. O. Löwdin, J. Chem. Phys. **19**, 1396 (1951).

[139] O. Stier, *Electronic and Optical Properties of Quantum Dots and Wires* (Wissenschaft & Technik Verlag, Berlin, 2000).

[140] S. Richard, F. Aniel, and G. Fishman, Phys. Rev. B **70**, 235204 (2004).

[141] S. L. Chuang and C. S. Chang, Phys. Rev. B **54**, 2491 (1996).

[142] R. Beresford, J. Appl. Phys. **95**, 6216 (2004).

[143] E. Berkowicz, D. Gershoni, G. Bahir, E. Lakin, D. Shilo, E. Zolotoyabko, A. C. Abare, S. P. Denbaars, and L. A. Coldren, Phys. Rev. B **61**, 10994 (2000).

[144] A. D. Andreev and E. P. O'Reilly, Phys. Rev. B **62**, 15851 (2000).

[145] V. Mlinar, M. Tadić, and F. M. Peeters, Phys. Rev. B **73**, 235336 (2006).

[146] D. P. Williams, A. D. Andreev, E. P. O'Reilly, and D. A. Faux, Phys. Rev. B **72**, 235318 (2005).

[147] M. G. Burt, J. Phys.: Condens. Matter **4**, 6651 (1992).

[148] B. A. Foreman, Phys. Rev. Lett. **81**, 425 (1998).

[149] B. A. Foreman, Phys. Rev. B **56**, 12748 (1997).

[150] E. P. Pokatilov, V. A. Fonoberov, V. M. Fomin, and J. T. Devreese, Phys. Rev. B **64**, 245328 (2001).

[151] B. A. Foreman, Phys. Rev. B **48**, 496 (1993).

[152] V. Mlinar, M. Tadić, B. Partoens, and F. M. Peeters, Phys. Rev. B **71**, 205305 (2005).

[153] B. A. Foreman, Phys. Rev. B **72**, 165345 (2005).

[154] J. D. Jackson, *Classical Electrodynamics* (John Wiley & Sons, 1999).

[155] Z. Ikonić and V. Milanović, *Poluprovodničke kvantne mikrostrukture (in Serbian)* (University of Belgrade, 1997).

[156] L. R. Ram-Mohan, K. H. Yoo, and R. L. Aggarwal, Phys. Rev. B **38**, 6151 (1988).

[157] M. H. Weiler, R. L. Aggarwal, and B. Lax, Phys. Rev. B **17**, 3269 (1978).

[158] T. Nakaoka, T. Saito, J. Tatebayashi, and Y. Arakawa, Phys. Rev. B **70**, 235337 (2004).

[159] G. A. Baraff and D. Gershoni, Phys. Rev. B **43**, 4011 (1991).

[160] M. A. Cusack, P. R. Briddon, and M. Jaros, Phys. Rev. B **54**, R2300 (1996).

[161] S.-S. Li, J.-B. Xia, Z. L. Yuan, Z. Y. Xu, W. Ge, X. R. Wang, Y. Wang, J. Wang, and L. L. Chang, Phys. Rev. B **54**, 11575 (1996).

[162] S. Tomić, Phys. Rev. B **73**, 125348 (2006).

[163] M. Tadić, F. M. Peeters, and K. L. Janssens, Phys. Rev. B **65**, 165333 (2002).

[164] M. Roy and P. A. Maksym, Phys. Rev. B **68**, 235308 (2003).

[165] C. Pryor, J. Kim, L. W. Wang, A. J. Williamson, and A. Zunger, J. Appl. Phys. **83**, 2548 (1998).

[166] P. N. Keating, Phys. Rev. **145**, 637 (1966).

[167] R. M. Martin, Phys. Rev. B **1**, 4005 (1970).

[168] M. Tadić, F. M. Peeters, K. L. Janssens, M. Korkusiński, and P. Hawrylak, J. Appl. Phys. **92**, 5819 (2002).

[169] A. D. Andreev, J. R. Downes, D. A. Faux, and E. P. O'Reilly, J. Appl. Phys. **86**, 297 (1999).

[170] J. H. Davies, J. Appl. Phys. **84**, 1358 (1998).

[171] J. D. Eshelby, Proc. R. Soc. London, Ser. A **241**, 376 (1957).

[172] B. Jogai, J. Appl. Phys. **88**, 5050 (2000).

[173] A. J. Davies, *The Finite Element Method* (Clarendon Press, Oxford, 1980).

[174] W. H. Press, S. A. Teukolsky, W. T. Vetterling, and B. P. Flannery, *Numerical recipes in Fortran 77* (Cambridge University Press, Cambridge, 1992).

[175] G. Mahan, *Many-Particle Physics* (Kluwer Academic, 2000).

[176] C.-Y. Tsai, L. F. Eastman, Y.-H. Lo, and C.-Y. Tsai, Appl. Phys. Lett. **65**, 469 (1994).

[177] L. F. Register, Phys. Rev. B **45**, 8756 (1992).

[178] A. R. Bhat, K. W. Kim, and M. A. Stroscio, J. Appl. Phys. **76**, 3905 (1994).

[179] E. A. Zibik, L. R. Wilson, R. P. Green, G. Bastard, R. Ferreira, P. J. Phillips, D. A. Carder, J.-P. R. Wells, J. W. Cockburn, M. S. Skolnick, M. J. Steer, and M. Hopkinson, Phys. Rev. B **70**, 161305 (2004).

[180] T. Stauber, R. Zimmermann, and H. Castella, Phys. Rev. B **62**, 7336 (2000).

[181] F. Rossi and T. Kuhn, Rev. Mod. Phys. **74**, 895 (2002).

[182] R. C. Iotti and F. Rossi, Reports on Progress in Physics **68**, 2533 (2005).

[183] H. Haug and A.-P. Jauho, *Quantum kinetics in transport and optics of semiconductors* (Springer, Berlin, 1996).

[184] A. Wacker, Phys. Rep. **357**, 1 (2002).

[185] P. Hyldgaard, S. Hershfield, J. H. Davies, and J. W. Wilkins, Ann. Phys. **236**, 1 (1994).

[186] J. Y. Marzin and G. Bastard, Solid State Commun. **92**, 437 (1994).

[187] M. Califano and P. Harrison, Phys. Rev. B **61**, 10959 (2000).

[188] J. A. Barker and E. P. O'Reilly, Phys. Rev. B **61**, 13840 (2000).

[189] G. Bester and A. Zunger, Phys. Rev. B **71**, 045318 (2005).

[190] J. Oshinowo, M. Nishioka, S. Ishida, and Y. Arakawa, Appl. Phys. Lett. **65**, 1421 (1994).

[191] D. Leonard, M. Krishnamurthy, C. M. Reaves, S. P. Denbaars, and P. M. Petroff, Appl. Phys. Lett. **63**, 3203 (1993).

[192] M. Bayer, P. Hawrylak, K. Hinzer, S. Fafard, M. Korkusinski, Z. R. Wasilewski, O. Stern, and A. Forchel, Science **291**, 451 (2001).

[193] P. Tronc, V. P. Smirnov, and K. S. Zhuravlev, Phys. Status Solidi B **241**, 2938 (2004).

[194] F. B. Pedersen and Y.-C. Chang, Phys. Rev. B **55**, 4580 (1997).

[195] L. R. C. Fonseca, J. L. Himenez, and J. P. Leburton, Phys. Rev. B **58**, 9955 (1998).

[196] M. Grundmann, O. Stier, and D. Bimberg, Phys. Rev. B **52**, 11969 (1995).

[197] G. S. Solomon, J. A. Trezza, A. F. Marshall, and J. S. Harris, Jr., Phys. Rev. Lett. **76**, 952 (1996).

[198] Available at http://www.netlib.org/lapack.

[199] S. S. Li and J. B. Xia, Chin. Phys. Lett. **23**, 1896 (2006).

[200] M. Brasken, M. Lindberg, and J. Tulkki, Phys. Rev. B **55**, 9275 (1997).

[201] N. Vukmirović, D. Indjin, V. D. Jovanović, Z. Ikonić, and P. Harrison, Phys. Rev. B **72**, 075356 (2005).

[202] S. Nakamura and G. Fasol, *The Blue Laser Diode* (Springer, Berlin, 1997).

[203] Y. Arakawava, IEEE J. Select. Topics Quantum Electron. **8**, 823 (2002).

[204] S. Tanaka, S. Iwai, and Y. Aoyagi, Appl. Phys. Lett. **69**, 4096 (1996).

[205] F. Widmann, J. Simon, B. Daudin, G. Feuillet, J. L. Rouvière, N. T. Pelekanos, and G. Fishman, Phys. Rev. B **58**, R15989 (1998).

[206] B. Daudin, F. Widmann, G. Feuillet, Y. Samson, M. Arlery, and J. L. Rouviére, Phys. Rev. B **56**, R7069 (1997).

[207] S. DeRinaldis, I. D'Amico, E. Biolatti, R. Rinaldi, R. Cingolani, and F. Rossi, Phys. Rev. B **65**, 081309(R) (2002).

[208] B. Krummheuer, V. M. Axt, T. Kuhn, I. D'Amico, and F. Rossi, Phys. Rev. B **71**, 235329 (2005).

[209] J. D. Heber, C. Gmachl, H. M. Ng, and A. Y. Cho, Appl. Phys. Lett. **81**, 1237 (2002).

[210] N. Iizuka, K. Kaneko, N. Suzuki, T. Asano, S. Noda, and O. Wada, Appl. Phys. Lett. **77**, 648 (2000).

[211] K. Moumanis, A. Helman, F. Fossard, M. Tchernycheva, A. Lusson, F. H. Julien, B. Damilano, N. Grandjean, and J. Massies, Appl. Phys. Lett. **82**, 868 (2003).

[212] M. Tchernycheva, L. Nevou, L. Doyennette, A. Helman, R. Colombelli, F. H. Julien, F. Guillot, E. Monroy, T. Shibata, and M. Tanaka, Appl. Phys. Lett. **87**, 101912 (2005).

[213] V. D. Jovanović, D. Indjin, Z. Ikonić, and P. Harrison, Appl. Phys. Lett. **84**, 2995 (2004).

[214] N. Vukmirović, V. D. Jovanović, D. Indjin, Z. Ikonić, P. Harrison, and V. Milanović, J. Appl. Phys. **97**, 103106 (2005).

[215] L. Nevou, M. Tchernycheva, F. H. Julien, F. Guillot, and E. Monroy, Appl. Phys. Lett. **90**, 121106 (2007).

[216] V. Ranjan, G. Allan, C. Priester, and C. Delerue, Phys. Rev. B **68**, 115305 (2003).

[217] N. Baer, S. Schulz, S. Schumacher, P. Gartner, G. Czycholl, and F. Jahnke, Appl. Phys. Lett. **87**, 231114 (2005).

[218] A. Bagga, P. K. Chattopadhyay, and S. Ghosh, Phys. Rev. B **68**, 155331 (2003).

[219] A. Bagga, P. K. Chattopadhyay, and S. Ghosh, Phys. Rev. B **71**, 115327 (2005).

[220] V. A. Fonoberov and A. A. Balandin, J. Appl. Phys. **94**, 7178 (2003).

[221] M. Winkelnkemper, A. Schliwa, and D. Bimberg, Phys. Rev. B **74**, 155322 (2006).

[222] V. Fiorentini, F. Bernardini, F. DellaSala, A. DiCarlo, and P. Lugli, Phys. Rev. B **60**, 8849 (1999).

[223] A. D. Andreev and E. P. O'Reilly, Appl. Phys. Lett. **79**, 521 (2001).

[224] N. Vukmirović, Z. Ikonić, D. Indjin, and P. Harrison, J. Phys.: Condens. Matter **18**, 6249 (2006).

[225] E. Towe and D. Pan, IEEE J. Select. Topics Quantum Electron. **6**, 408 (2000).

[226] J.-Z. Zhang and I. Galbraith, Appl. Phys. Lett. **84**, 1934 (2004).

[227] T. R. Nielsen, P. Gartner, and F. Jahnke, Phys. Rev. B **69**, 235314 (2004).

[228] L. R. C. Fonseca, J. L. Jimenez, J. P. Leburton, and R. M. Martin, Phys. Rev. B **57**, 4017 (1998).

[229] A. Wojs and P. Hawrylak, Phys. Rev. B **53**, 10841 (1996).

[230] S. Sauvage and P. Boucaud, Appl. Phys. Lett. **88**, 063106 (2006).

[231] G. A. Narvaez and A. Zunger, Phys. Rev. B **75**, 085306 (2007).

[232] E. A. Zibik, A. D. Andreev, L. R. Wilson, M. J. Steer, R. P. Green, W. H. Ng, J. W. Cockburn, M. S. Skolnick, and M. H. M, Physica E **26**, 105 (2005).

[233] S. Tomić, M. Tadić, V. Milanović, and Z. Ikonić, J. Appl. Phys. **87**, 7965 (2000).

[234] S. Tomić, Z. Ikonić, and V. Milanović, J. Appl. Phys. **91**, 4801 (2002).

[235] J. Stiens, R. Vounckx, I. Veretennicoff, A. Voronko, and G. Shkerdin, J. of Appl. Phys. **81**, 1 (1997).

[236] E. Rosencher and B. Vinter, *Optoelectronics* (Cambridge University Press, Cambridge, 2002).

[237] D. J. Ripin, J. T. Gopinath, H. M. Shen, A. A. Erchak, G. S. Petrich, L. A. Kolodziejski, F. X. Kärtner, and E. P. Ippen, Opt. Commun. **214**, 285 (2002).

[238] N. Vukmirović, Z. Ikonić, V. D. Jovanović, D. Indjin, and P. Harrison, IEEE J. Quantum Electron. **41**, 1361 (2005).

[239] H. Lim, W. Zhang, S. Tsao, T. Sills, J. Szafraniec, K. Mi, B. Movaghar, and M. Razeghi, Phys. Rev. B **72**, 085332 (2005).

[240] X. Han, J. Li, J. Wu, G. Cong, X. Liu, Q. Zhu, and Z. Wang, J. Appl. Phys. **98**, 053703 (2005).

[241] X. D. Jiang, S. S. Li, and M. Z. Tidrow, Physica E (Amsterdam) **5**, 27 (1999).

[242] V. G. Stoleru and E. Towe, Appl. Phys. Lett. **83**, 5026 (2003).

[243] A. Amtout, S. Raghavan, P. Rotella, G. von Winckel, A. Stintz, and S. Krishna, J. Appl. Phys. **96**, 3782 (2004).

[244] M. Tadić and F. M. Peeters, Phys. Rev. B **70**, 195302 (2004).

[245] I. Mukhametzhanov, Z. H. Chen, O. Baklenov, E. T. Kim, and A. Madhukar, Phys. Status Solidi B **224**, 697 (2001).

[246] H. Jiang and J. Singh, Appl. Phys. Lett. **71**, 3239 (1997).

[247] B. Aslan, H. C. Liu, M. Korkusinski, S.-J. Cheng, and P. Hawrylak, Appl. Phys. Lett. **82**, 630 (2003).

[248] H. C. Liu, Opto-Electron. Rev. **11**, 1 (2003).

[249] L. Chu, A. Zrenner, G. Böhm, and G. Abstreiter, Appl. Phys. Lett. **75**, 3599 (1999).

[250] L. Fu, H. H. Tan, I. McKerracher, J. Wong-Leung, C. Jagadish, N. Vukmirović, and P. Harrison, J. Appl. Phys. **99**, 114517 (2006).

[251] N. Vukmirović, Ž. Gačević, Z. Ikonić, D. Indjin, P. Harrison, and V. Milanović, Semicond. Sci. Technol. **21**, 1098 (2006).

[252] G. Biasol, S. Heun, G. B. Golinelli, A. Locatelli, T. O. Mentes, F. Z. Guo, C. Hofer, C. Teichert, and L. Sorba, Appl. Phys. Lett. **87**, 223106 (2005).

[253] N. Vukmirović, D. Indjin, Z. Ikonić, and P. Harrison, Appl. Phys. Lett. **88**, 251107 (2006).

[254] Z. Ye, J. C. Campbell, Z. Chen, E.-T. Kim, and A. Madhukar, J. Appl. Phys. **92**, 4141 (2002).

[255] Z. Chen, E.-T. Kim, and A. Madhukar, Appl. Phys. Lett. **80**, 2490 (2002).

[256] P. W. Fry, I. E. Itskevich, D. J. Mowbray, M. S. Skolnick, J. J. Finley, J. A. Barker, E. P. O'Reilly, L. R. Wilson, I. A. Larkin, P. A. Maksym, M. Hopkinson, M. Al-Khafaji, J. P. R. David, A. G. Cullis, G. Hill, and J. C. Clark, Phys. Rev. Lett. **84**, 733 (2000).

[257] V. Ryzhii, Appl. Phys. Lett. **78**, 3346 (2001).

[258] V. Ryzhii, I. Khmyrova, V. Mitin, M. Stroscio, and M. Willander, Appl. Phys. Lett. **78**, 3523 (2001).

[259] J. Phillips, J. Appl. Phys. **91**, 4590 (2002).

[260] V. Ryzhii, I. Khmyrova, V. Pipa, V. Mitin, and M. Willander, Semicond. Sci. Technol. **16**, 331 (2001).

[261] M. B. El Mashade, M. Ashry, and A. Nasr, Semicond. Sci. Technol. **18**, 891 (2003).

[262] V. Ryzhii, Semicond. Sci. Technol. **11**, 759 (1996).

[263] Y. Matsukura, Y. Uchiyama, R. Suzuki, T. Fujii, and N. Kajihara, Infrared Phys. Technol. **47**, 164 (2005).

[264] V. Apalkov, J. Appl. Phys. **100**, 076101 (2006).

[265] V. M. Apalkov, Phys. Rev. B **75**, 035339 (2007).

[266] Z. Ikonić, P. Harrison, and R. W. Kelsall, IEEE Trans. Electron Devices **53**, 189 (2006).

[267] V. D. Jovanović, D. Indjin, N. Vukmirović, Z. Ikonić, P. Harrison, E. H. Linfield, H. Page, X. Marcadet, C. Sirtori, C. Worrall, H. E. Beere, and D. A. Ritchie, Appl. Phys. Lett. **86**, 211117 (2005).

[268] I. Savić, V. Milanović, N. Vukmirović, V. D. Jovanović, Z. Ikonić, D. Indjin, and P. Harrison, J. Appl. Phys. **98**, 084509 (2005).

[269] V. D. Jovanović, P. Harrison, Z. Ikonić, and D. Indjin, J. Appl. Phys. **96**, 269 (2004).

[270] J. Seebeck, T. R. Nielsen, P. Gartner, and F. Jahnke, Phys. Rev. B **71**, 125327 (2005).

[271] R. C. Iotti and F. Rossi, Phys. Rev. Lett. **87**, 146603 (2001).

[272] I. Savić, Z. Ikonić, V. Milanović, N. Vukmirović, V. D. Jovanović, D. Indjin, and P. Harrison, Phys. Rev. B **73**, 075321 (2006).

[273] N. Vukmirović, Z. Ikonić, I. Savić, D. Indjin, and P. Harrison, J. Appl. Phys. **100**, 074502 (2006).

[274] D. Wasserman and S. A. Lyon, Appl. Phys. Lett. **81**, 2848 (2002).

[275] D. Wasserman, C. Gmachl, S. A. Lyon, and E. A. Shaner, Appl. Phys. Lett. **88**, 191118 (2006).

[276] S.-C. Lee and A. Wacker, Phys. Rev. B **66**, 245314 (2002).

[277] C. Gnodtke, G. Kiesslich, E. Scholl, and A. Wacker, Phys. Rev. B **73**, 115338 (2006).

[278] S.-C. Lee, F. Banit, M. Woerner, and A. Wacker, Phys. Rev. B **73**, 245320 (2006).

[279] R. Ferreira, Phys. Rev. B **43**, 9336 (1991).

[280] V. V. Bryksin and P. Kleinert, Phys. Rev. B **59**, 8152 (1999).

[281] N. H. Shon and H. N. Nazareno, Phys. Rev. B **53**, 7937 (1996).

[282] L. Canali, M. Lazzarino, L. Sorba, and F. Beltram, Phys. Rev. Lett. **76**, 3618 (1996).

[283] D. Fowler, A. Patane, A. Ignatov, L. Eaves, M. Henini, N. Mori, D. K. Maude, and R. Airey, Appl. Phys. Lett. **88**, 052111 (2006).

[284] R. S. Deacon, R. J. Nicholas, and P. A. Shields, Phys. Rev. B **74**, 121306 (2006).

[285] S. Kumar, B. S. Williams, Q. Hu, and J. L. Reno, Appl. Phys. Lett. **88**, 121123 (2006).

[286] B. S. Williams, S. Kumar, Q. Qin, Q. Hu, and J. L. Reno, Appl. Phys. Lett. **88**, 261101 (2006).

[287] H. Luo, S. R. Laframboise, Z. R. Wasilewski, G. C. Aers, H. C. Liu, and J. C. Cao, Appl. Phys. Lett. **90**, 041112 (2007).

[288] A. Benz, G. Fasching, A. M. Andrews, M. Martl, K. Unterrainer, T. Roch, W. Schrenk, S. Golka, and G. Strasser, Appl. Phys. Lett. **90**, 101107 (2007).

[289] M. S. Vitiello, G. Scamarcio, V. Spagnolo, S. S. Dhillon, and C. Sirtori, Appl. Phys. Lett. **90**, 191115 (2007).